Reconstruction of Late Quaternary environmental conditions applying the natural radionuclides ^{230}Th, ^{10}Be, ^{231}Pa and ^{238}U: A study of deep-sea sediments from the eastern sector of the Antarctic Circumpolar Current System

Rekonstruktion von spätquartären Umweltbedingungen mit den natürlichen Radionukliden ^{230}Th, ^{10}Be, ^{231}Pa und ^{238}U: Eine Untersuchung von Tiefseesedimenten aus dem östlichen Sektor des Antarktischen Zirkumpolarstromsystems

---

Martin Frank

Ber. Polarforsch. 186 (1996)
ISSN 0176 - 5027

Martin Frank
Heidelberger Akademie der Wissenschaften
c/o Institut für Umweltphysik
Im Neuenheimer Feld 366
D-69120 Heidelberg

Die vorliegende Arbeit ist die inhaltlich unveränderte Fassung einer Dissertation, die 1995 der Fakultät für Geowissenschaften der Universität Heidelberg vorgelegt wurde.

Contents

Abstract

High resolution radioisotope and proxy element profiles were measured on five sediment cores forming a transect over the eastern part of the Atlantic sector of the Antarctic Circumpolar Current in order to achieve a more detailed reconstruction of sedimentary and paleoenvironmental conditions of this key area for global climate change during the late Quaternary.

Comprehensive previous stratigraphic work which was carried out within the Special Research Project (SFB) 261 of the German Science Foundation (DFG): "Der Südatlantik im Spätquartär: Rekonstruktion von Stoffhaushalt und Stromsystemen", can mostly be corroborated by results of the $^{230}Th_{ex}$ dating method, by which rough average sedimentation rates may be calculated. In addition, a high resolution dating within single isotope stages is shown to be possible applying $^{230}Th_{ex}$ constant flux models, which enable the investigation of short-term paleoenvironmental changes during the last about 300,000 years, corresponding to isotope stages 1-9. Short periods of drastically increased sedimentation rates by up to a factor of 8 are for example determined in the sediments of the Antarctic Zone during the climate optima at the beginning of the Holocene and the beginning of isotope stage 5e, about 125,000 years ago.

By a comparison of the expected and measured accumulation rates of $^{230}Th_{ex}$, which should be constant due to the short residence time of ^{230}Th in the water column of the ocean, lateral sediment redistribution (focusing and winnowing) is quantified and vertical particle rain rates are calculated. It is possible to show that lateral contributions to the sediment accumulation rates locally were up to six times higher than the vertical particle rain rates. During other periods and at other locations only about 25 % of the vertical particle rain were at last deposited. Only the $^{230}Th_{ex}$ normalized vertical particle fluxes represent a correct reconstruction of accumulation rates, which has, for example, a strong impact on estimations of export paleoproductivity that are calculated using accumulation rates of proxies like biogenic barium.

The $^{230}Th_{ex}$ normalized accumulation rates (rain rates) are inserted into a paleoproductivity transfer function, basing on biogenic barium results of a previous study, carried out on the same cores as this study. It is shown that the peak export paleoproductivity occurring in the Antarctic Zone of the ACC during the interglacials was by far not as high as previously assumed. From fluxes of biogenic opal and vertical sediment accumulation rates it is deduced that the high particle flux area, presently located south of the Antarctic Polar Front (Opal Belt) in the Antarctic Zone, was shifted to the north by about 4 to 5° during glacials. The intensity of the glacial particle flux, however, as already deduced from previous investigations, was slightly lower than in the Antarctic Zone during the interglacial periods.

The $^{231}Pa_{ex}$ rain rates are suggested to be a suitable proxy indicator for biogenic particle flux in the past. The rain rates rates of cosmogenic ^{10}Be which yield a pattern just opposite to the expected one, turned out not to be a suitable tracer for biogenic particle flux in the past. As shown by a comparison to the rain rates of terrigenous material, the

scavenging of ^{10}Be seems to be mainly controlled by aluminosilicate deposition originating from aeolian dust flux and ice rafted debris. Nevertheless, biogenic ^{10}Be deposition was increased during the climate optima in the Antarctic Zone sediments.

Changes in the redox conditions of the surface sediments and the deep water are investigated by authigenic ^{238}U concentrations and accumulation rates and Mn/Al ratios.

Assuming that the increased glacial dust flux released additional iron to the surface waters of the transect, the results obtained from the sediments of the Antarctic Zone suggest that a glacial fertilization by detrital input of iron, as recently discussed, was not the case. Altogether, a glacial increase in Southern Ocean productivity and thus a glacial Southern Ocean CO_2 sink seems to be rather unlikely, as previously deduced from other investigations.

Zusammenfassung

Zeitlich hochauflösend wurden an fünf Sedimentkernen eines Transects über den östlichen atlantischen Sektor des Antarktischen Zirkumpolarstromsystems Profile von Radioisotopen und Proxyindikatoren gemessen. Ziel dieser Arbeit war es, eine detailliertere Rekonstruktion der sedimentären Bedingungen und der Paläoumweltbedingungen dieses Schlüsselgebietes für globale Klimaveränderungen im Spätquartär zu ermöglichen.

Umfassende stratigraphische Arbeiten, die im Rahmen des Sonderforschungsbereichs (SFB) 261 der Deutschen Forschungsgemeinschaft (DFG): "Der Südatlantik im Spätquartär: Rekonstruktion von Stoffhaushalt und Stromsystemen" an den Kernen durchgeführt wurden, konnten mit Hilfe der $^{230}Th_{ex}$-Datierungsmethode, die die Berechnung von groben durchschnittlichen Sedimentationsraten ermöglicht, zunächst weitgehend bestätigt werden. Ergänzend ermöglicht die Berechnung von $^{230}Th_{ex}$-Konstant-Fluß-Modellen eine hochauflösende Datierung innerhalb einzelner Isotopenstadien, die es möglich macht, auch kurzzeitige Veränderungen von Paläoumweltbedingungen während der letzten etwa 300000 Jahre, also den Isotopenstadien 1-9, zu erfassen. Drastische Anstiege der Sedimentationsraten um bis zu einem Faktor von 8 konnten während der Klimaoptima des Holozän und am Beginn des Interglazialstadiums 5e vor etwa 125000 Jahren in der Antarktischen Zone südlich der heutigen Position der antarktischen Polarfront festgestellt werden.

Durch einen Vergleich der erwarteten und gemessenen $^{230}Th_{ex}$-Akkumulationsraten, die aufgrund der niedrigen Verweilzeit des ^{230}Th in der Wassersäule konstant sein sollten, kann der Anteil lateralen Sedimenteintrags oder -abtransports (Focusing und Winnowing) quantifiziert werden und vertikale Sedimentakkumulationsraten ("Rain Rates") können berechnet werden. Es wird gezeigt, daß der Anteil an lateral eingetragenem Sediment lokal bis zu sechs mal höher als das tatsächlich vertikal aus der Wassersäule akkumulierte Material war. An anderen Stellen wurden aufgrund des Einflusses von Bodenströmungen nur 25 % des aus der darüberliegenden Wassersäule stammenden Sediments letztendlich abgelagert. Nur die $^{230}Th_{ex}$-normalisierten vertikalen Sedimentakkumulationsraten stellen eine korrekte Rekonstruktion der Akkumulationsraten der Vergangenheit dar, wenn

zum Beispiel die Exportpaläoproduktivität mit Hilfe von Akkumulationsraten von Proxyindikatoren wie biogenem Barium abgeschätzt wird.

Durch Einsetzen der $^{230}Th_{ex}$-normalisierten vertikalen Sedimentakkumulationsraten in die Transferfunktion einer Paläoproduktivitätsstudie, die auf den Akkumulationsraten biogenen Bariums an den gleichen Sedimentkernen basiert, wird gezeigt, daß die Paläoproduktivität aufgrund des lateralen Sedimenteintrags zum Teil wesentlich niedriger war als vorher berechnet. Anhand der Akkumulationsraten biogenen Opals und der vertikalen Sedimentakkumulationsraten kann eine glaziale Nordwärtsverlagerung des biogenen Hochproduktivitätsgebiets, das heute südlich der Polarfront liegt (Opalgürtel), um etw 4 bis 5° abgeleitet werden. Dabei zeigt es sich jedoch, wie auch in anderen Untersuchungen vorher schon festgestellt, daß die Intensität des biogenen Partikelflusses in den Glazialen etwas niedriger als in den Interglazialen südlich der Polarfront war.

Es deutet sich an, daß die "Rain Rates" von $^{231}Pa_{ex}$ aufgrund ihrer relativ guten Übereinstimmung mit anderen Proxyindikatoren geeignete Tracer für den biogenen Partikelfluß der letzten 150000 Jahre sind. Die "Rain rates" des kosmogenen Radionuklids ^{10}Be, die südlich der Polarfront einen Verlauf genau entgegengesetzt zu den Erwartungen zeigen, können nach dieser Arbeit nicht als geeigneter Tracer für biogenen Partikelfluss angesehen werden. Ein Vergleich mit den "Rain Rates" terrigenen Materials legt nahe, daß der adsorptive Abtransport von ^{10}Be aus der Wassersäule, trotz eines großen Angebots an biogenen Partikeln, hauptsächlich von Tonmineralen kontrolliert wird, die durch äolischen Eintrag verstärkt während der Glazialzeiten in den Südatlantik gelangten. Südlich der Polarfront zeigt die Berechnung des Anteils an biogen gebundenem ^{10}Be trotz der erniedrigten Gesamt-^{10}Be-Rain Rates während der Klimaoptima einen Anstieg.

Änderungen der Redoxbedingungen im Tiefenwasser und im Oberflächensediment werden anhand der authigenen ^{238}U-Konzentrationen und der Mn/Al-Verhältnisse untersucht.

Eine glaziale Düngung des Oberflächenwassers durch verstärkten Eintrag von Eisen mit windtransportiertem Staub, die vermutet wird, um eine postulierte höhere biologische Produktivät des glazialen Zirkumantarktischen Ozeans zu erklären, kann zumindest in den Sedimenten, die an der heutigen Position des Opalgürtels abgelagert wurden, nicht nachvollzogen werden. Vielmehr ist eine insgesamt höhere glaziale Produktivität des Zirkumantarktischen Ozeans mit den Ergebnissen dieser Untersuchung nicht zu vereinbaren. Wie auch in anderen Untersuchungen gezeigt, hat der Südatlantik daher wahrscheinlich nicht als die gesuchte fehlende Senke für atmosphärisches CO_2 während der Kaltzeiten fungiert.

1 Introduction

1.1 Motivation of the Study

The global thermohaline conveyor belt is driven by the sinking of cold water masses in the high latitudes forming the main bottom water currents in today's ocean (Broecker and Peng, 1982).

In contrast to the high northern latitude ocean basins, the Southern Ocean with the Antarctic Circumpolar Current system (ACC) is considered the most important linkage for mass and energy exchange between the three main ocean basins. This is a consequence of the geographic situation, which allows a continuous current system to be established around Antarctica. At the frontal systems of the ACC the nutrient rich and cold Antarctic water masses are gradually separated from the nutrient poor and warm water masses of low and middle latitudes. The pattern and the position of the frontal systems which control the distribution of these cold and warm water masses, together with the sea ice extension influence the heat transfer and the budget of the constituents of the world ocean. The production of intermediate and deep water masses, as well as wind stress and wind fields of the atmosphere are influenced. The sea ice distribution controls the spatial and temporal extension of biologically productive areas of the surface waters as well as the albedo and last but not least the CO_2 exchange between atmosphere and ocean is influenced.

Motivated by the above mentioned importance of the Southern Ocean, extensive research has been carried out in the eastern Atlantic sector of the ACC. Within the special research project (SFB) 261: "Der Südatlantik im Spätquartär: Rekonstruktion von Stoffhaushalt und Stromsystemen" various expeditions took place and a large number of sediment cores were collected (see for example the "SFB 261 Arbeits- und Ergebnisbericht 1989-1992" for a summary). One main topic where interest has been focussed on, is the reconstruction of changes of the surface layer of the ocean, which are controlled by the glacial/interglacial paleoclimatic conditions in the Late Quaternary.

It is indispensable for any paleoceanographic reconstruction to achieve a stratigraphy as precise as possible. Today modern mass spectrometers allow the measurement of oxygen isotopes in very small samples of carbonaceous microfossils (mostly foraminifera). This enables the establishment of $\delta^{18}O$ stratigraphies for sediments with very low carbonate content, as it is the case in high southern latitudes.

With the help of transfer functions proxy data of paleo-water temperature, salinity and nutrient content are produced, which allow the reconstruction of the distribution of warm and cold surface water masses, of the position of the frontal systems and of the gradients during the last about 300 kyr. Core sections representing glacial conditions can be identified using the abundances of certain radiolarian species (*Cycladophora davisiana* and *Eucampia antarctica* stratigraphy). The increased abundance of the diatom species *Nitzschia curta* and *Nitzschia cylindrus* are applied for reconstructing the extension of

the sea ice cover (see Gersonde and Pätzold, 1992, for a summary). These biofluctuation stratigraphies of siliceous microfossils (Hays et al., 1976; Burckle and Cooke, 1983; Abelmann and Gersonde, 1988) could be given a reliable time frame by the improved oxygen isotope measurement techniques and may themselves be applied as independent dating tools. The accumulation rates of biogenic opal may, considering some uncertainties concerning dissolution, serve as paleoproductivity proxy (Charles et al. 1991; Mortlock et al., 1991).

The $\delta^{18}O$ records of these high latitude sediments may be obscured by the influence of meltwater and thus may often not be applied without additional stratigraphic information. Additionally, there are large sections which are definitely barren of biogenic carbonate, thus mostly only allowing the calculation of linear sedimentation rates between the major climatic transitions. There were, however, severe changes of the paleoenvironmental conditions and the sedimentation rates within certain climatic stages (Gersonde et al., in prep.). These changes are linked to significant variations of the sea ice distribution and the hydrography of the surface water and thus may help to understand the processes leading to short-term climatic changes in the past, which may have influenced the budget of the constituents of the entire ocean. The interhemispheric comparison of such climate events, as for example the Younger Dryas period, is essential for reconstructing the mechanisms of global climate change.

A high resolution record of the sedimentation rates which is necessary to investigate these short-term changes, can for example be achieved by ^{14}C measurements. This, however, is time consuming and expensive if a large number of samples have to be analyzed and this method is restricted to the last 30,000 to 40,000 years. One of the goals of this study was to address the described dating problems by applying radioisotopic methods:

- Sediments which are either completely barren or which contain sections barren of biogenic carbonate may be roughly dated applying the $^{230}Th_{ex}$ method, thus providing a time frame for other stratigraphic investigations.
- Changes of the concentration of $^{230}Th_{ex}$ in the sediments may be interpreted as changes of dilution with sedimenting particles and thus as changes of the sedimentation rates assuming a constant flux. This constant flux model enables the calculation of a high resolution record of the sedimentation rates, also within previously fixed stratigraphic sections during the last about 300,000 years.

There is a process which may lead to false conclusions when calculating paleo accumulation rates from sediment cores, especially adjacent to topographic elevations or in areas where high bottom water current velocities occur. Sedimenting particles from the surface water may be transported with bottom currents or within the nepheloid layer to other areas and may be deposited there. Additionally sediment particles can be resuspended and transported by bottom currents. These lateral contributions or losses can not be quantified in the deposited sediments because the transport mostly occurs on small scales of distance and no lithological changes are recorded. Accumulation rates calculated for sediments

which laterally received or lost material, are then too high or too low and may lead to incorrect conclusions, for example when evaluating paleoproductivity from the fluxes of C_{org} or biogenic barium. The lateral supply of particles may be more than ten times as high as the vertical contribution, as for example determined in a sediment core from the Indian sector of the Southern Ocean (Francois et al., 1993).

In this context, problems arise from the development and application of modern sonar systems on board of the research ships, like for example "parasound" (Gersonde and Hempel, 1990; Gersonde, 1993). These tools enable the finding of places with a sufficiently thick Quaternary sediment cover. This may, however, also result in some disadvantages, because in areas where apparently only low sedimentation rates and thus a poor time resolution is expected, often no sediment cores are recovered. This is a general problem in areas where intricate topography causes uneven sedimentation of particles. The effect is that sediments are preferentially sampled at locations where lateral contributions (focusing) may have occurred. When balancing mass fluxes and accumulation rates of proxy elements, estimates may be significantly too high. This problem may also be addressed by $^{230}Th_{ex}$ investigations:

- Sediment redistribution effects (focusing and winnowing processes) may be quantified by comparing the measured $^{230}Th_{ex}$ accumulation rates to the expected values from production in the water column. The vertical flux of $^{230}Th_{ex}$ can be considered constant, which means that any significant deviation from this flux may be attributed to lateral import or export of particles loaded with adsorbed $^{230}Th_{ex}$.

Furthermore there is no independent tracer of paleoproductivity for which a masking by dissolution or other disturbing factors can unambiguously be excluded. Therefore, the suitability of the accumulation rates of the particle reactive natural radionuclides ^{10}Be and $^{231}Pa_{ex}$ as tracers for the paleointensity of biogenic particle flux is investigated in this study. Promising attempts have already been made in other areas of the world ocean (c.f. Anderson et al., 1990; Frank et al., 1994) and in the Southern Ocean (Francois et al., 1993; Kumar et al., 1993):

- Are the accumulation rates of ^{10}Be and $^{231}Pa_{ex}$ suitable tracers of paleoproductivity in the Southern Ocean? This is checked by comparison to other tracers of paleoproductivity like biogenic opal and biogenic barium, which are available for the cores of this study.

- Can a glacial northward shift of the frontal zones of the ACC, which was suggested in various studies (Charles et al., 1991; Mortlock et al., 1992; Kumar et al., 1993) be corroborated by the different approaches of this study?

- Finally, is it possible to deduce additional information on the overall paleoproductivity of the Southern Ocean during glacials and interglacials and thus on the probability of the Southern Ocean as glacial CO_2 sink from the results of this study?

1.2 Oceanography

1.2.1 Global Circulation Patterns

The global thermohaline circulation is driven today by the formation of deep water masses from two sources. In the Norwegian-Greenland Sea high saline and oxygen rich North Atlantic Deep Water (NADW) is produced by cooling and subsequent sinking of water masses which were more or less in equilibrium with the atmosphere. It flows southward along the North and South American continents until it enters the Circumpolar Deep Water (CDW) in the Argentine Basin (Reid et al., 1977) after a residence time of about 80 years (Broecker and Peng, 1982). In the Weddell Sea, Antarctic Bottom Water (AABW) is formed by mixing of water masses that were only partly in contact with the atmosphere (see chapter 1.2.2). Consequently AABW is lower in oxygen and rich in nutrients and ^{12}C. Thus, it is the NADW which accounts for the ventilation of the deep ocean basins.

The conveyor belt model (Broecker and Peng, 1982) explains the chemical differences between Atlantic and Pacific deep waters by differences in age: While the NADW is less then 100 years old when it enters the CDW, the Pacific deep water is several hundreds up to 1500 years old. Correspondingly, it is characterized by low oxygen content, more negative $\delta^{13}C$ values and high nutrient and ΣCO_2 concentrations. However, there are indications that the circulation pattern was significantly different through glacial periods of the paleoclimate. One key area for studying these changes is the Southern Ocean because there, changes in deep water supply from the north are expected to have strong consequences.

The $\delta^{13}C$, Cd and Ba sediment profiles measured on benthic foraminfera in the Pacific and Atlantic sectors of the Southern Ocean show that the contrast between the two deep ocean areas was weaker during glacials, suggesting that deep water ventilation was reduced (Boyle and Weaver, 1994). Stronger ventilation was observed for a more intermediate glacial NADW circulation cell which, however, was restricted to the Atlantic basin (Fichefet et al., 1994). According to these authors, the NADW production was reduced by approximately 40 %, whereas the AABW production was slightly increased and penetrated farther north. Charles and Fairbanks (1992) used results from $\delta^{13}C$ studies of benthic foraminifera to reconstruct changes of NADW production and input into the global thermohaline circulation. They observed an abrupt increase of the NADW production at 12.6 to 12.2 kyr B.P., exactly preceding the first large scale melting events of the northern hemisphere ice sheets and suggested that the restarting NADW production was the primary amplifier for glacial/interglacial climate change.

Recent results of Howard and Prell (1994) imply that increased carbonate dissolution in the Southern Ocean during glacials is strongly correlated to a diminished NADW inflow, corroborating earlier results of Raymo et al. (1990). However, the lower input of NADW can not account completely for the total decrease in deep CO_3^{2-} ion concentrations. Yu (1994), on the other hand, deduced from a comparison of last glacial and Holocene $^{231}Pa_{ex}/^{230}Th_{ex}$ ratios of the whole Atlantic Ocean that the intensity of NADW input into the Southern Ocean remained more or less unchanged during the last glacial.

In summary, it is still neither known whether NADW production was completely switched off nor to what extent it was active during the glacials and during the transitions between two stable glacial and interglacial modes of the thermohaline circulation. However, there are more indications at the moment that there was at least a certain percentage of NADW input into the glacial Southern Ocean. Although the two principally used proxies for the investigation of this question, $\delta^{13}C$ and Cd, yield a consistent picture throughout the world's ocean, this is not the case in the southernmost part of the Southern Ocean. Various suggestions for resolving this contradiction have recently been discussed (chapter 1.4), but as long as these do not give a satisfactory and consistent explanation, the role of NADW and the exchange between the Atlantic and the Southern Ocean during glacials cannot be unambiguously resolved.

Water Masses and Currents

NADW	North Atlantic Deep Water	CDW	Circumpolar Deep Water
AABW	Antarctic Bottom Water	AAIW	Antarctic Intermediate Water
LCDW	Lower Circumpolar Deep Water	UCDW	Upper Circumpolar Deep Water
WSDW	Weddell Sea Deep Water	WSBW	Weddell Sea Bottom Water
WDW	Warm Deep Water	WSW	Western Shelf Water
ISW	Ice Shelf Water	AASW	Antarctic Surface Water
SACW	South Atlantic Central Water	SASW	Subantarctic Surface Water
SAC	South Atlantic Current	ACC	Antarctic Circumpolar Current

Fronts and Frontal Zones

STF	Subtropical Front	SAF	Subantarctic Front
APF	Antarctic Polar Front	SAZ	Subantarctic Zone
PFZ	Polar Frontal Zone	AZ	Antarctic Zone

Table 1: Glossary of the applied abbreviations for water masses, fronts and frontal zones of the Southern Ocean.

1.2.2 Present Hydrography of the Southern Atlantic Ocean and the Antarctic Circumpolar Current System (ACC)

The circulation pattern of the Atlantic section of the Southern Ocean is in many respects extraordinary, as shown already by the first investigations in the 1920's and 1930's (Wüst, 1935). The wind driven near-surface circulation of the water masses of the Atlantic sector of the Southern Ocean is dominated by the westward flowing equatorial current system in the north and by the eastward flowing circumpolar current system in the south (c.f. Peterson and Stramma, 1991) (Fig. 1). Nearly zonal isobars in the high latitudes of the

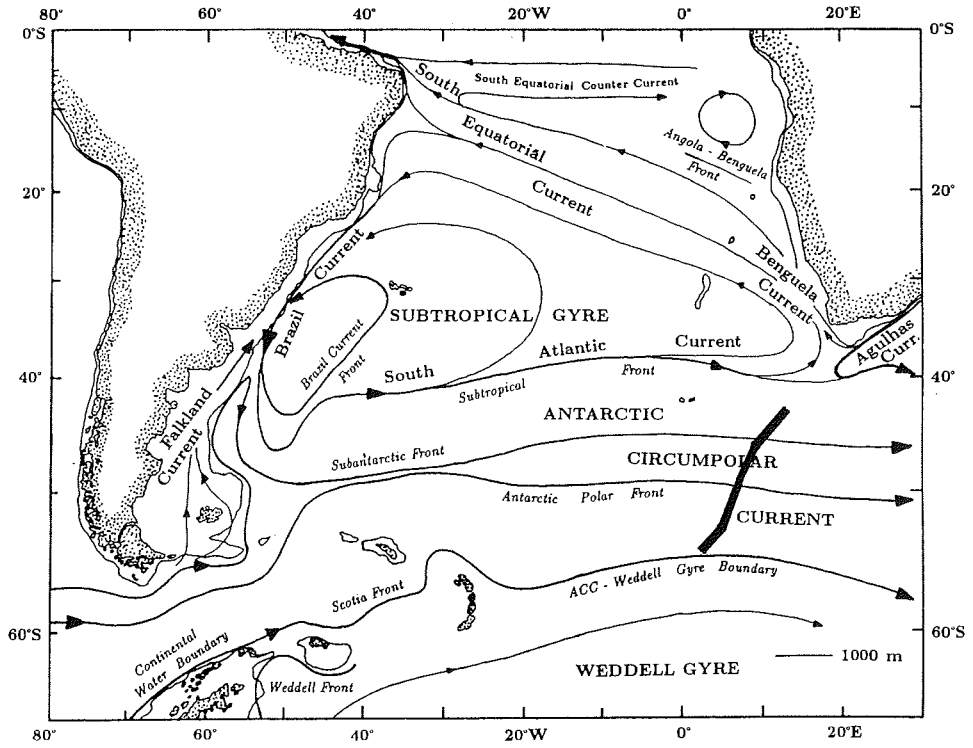

Figure 1: Schematic picture of the large-scale, upper-level geostrophic currents and fronts in the South Atlantic Ocean, from Peterson and Stramma (1991). The bold solid line in the eastern southern Atlantic marks the transect of the sediment cores of this study.

southern Atlantic produce strong westerly winds and drive the ACC, which flows eastward around the Antarctic continent without being disturbed by any bigger landmasses, thus leading to a thermal isolation of Antarctica. The South Atlantic Subtropical Gyre is bounded to the south by the South Atlantic Current (SAC) which itself is separated from the ACC to the south by the Subtropical Front (STF) (Stramma and Peterson, 1990). The STF is characterized by a sharp drop in temperature of 5°C or more. The ACC, which represents the transition zone between highly nutrient enriched cold water masses in the south and warmer nutrient depleted water masses in the north, itself consists of a sequence of zonal jets of geostrophic transport and bands of quiescence (Fig. 2).

These zonal jets, where the main geostrophic transport occurs, define the location of the fronts within the ACC, which from the north to the south are the Subantarctic Front (SAF), the Antarctic Polar Front (APF), and the ACC-Weddell Gyre Boundary (Fig. 1) (Whitworth and Nowlin, 1987; Peterson and Whitworth, 1989). The area between the STF in the north and the SAF in the south is called Subantarctic Zone (SAZ). North of the Polar Front the Polar Frontal Zone (PFZ) and south of it the Antarctic Zone (AZ) complete the transect.

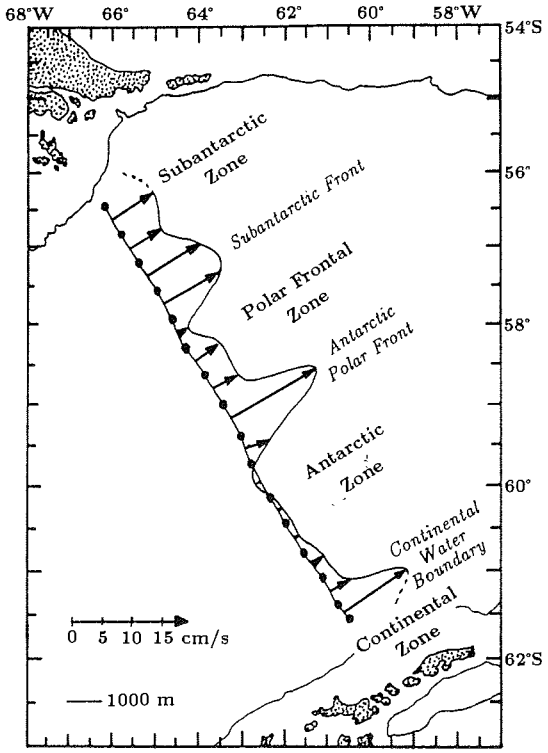

Figure 2: Vertically-averaged geostrophic speeds in the Drake Passage in the upper 2500 m, relative to 2500 m water depth. The solid line marks 1000m water depth, adapted from Peterson et al. (1982) in Peterson and Stramma (1991).

The SAF is characterized by a pronounced salinity and temperature gradient which marks the beginning of the steep northward deepening of the salinity maximum of the Antarctic Intermediate Water (AAIW), which is generated at the surface ocean in the PFZ. A strong southward increase of the concentrations of dissolved nutrients like nitrate (NO_3) and phosphate (PO_4) is also located at the SAF (Fig. 3). The PFZ itself represents a complex zone of mixing north of the APF and is a region of transition between Antarctic and Subantarctic surface waters (Nowlin et al., 1977), where NO_3 and PO_4 concentrations are already high, but dissolved silica (H_4SiO_4) is not.

The APF which has been investigated to a much greater extent than the SAF (see Peterson and Stramma (1991) for an overview), represents the northern boundary between cold near-surface water (-1.5° to 2°C) in the south and warmer water masses in the north (Mosby, 1934) and is about equivalent to the term Antarctic Convergence. Besides a small southward increase in dissolved nutrients, a drastic increase in dissolved silica gives way to an enhanced opal productivity. In the AZ south of the APF the cold Antarctic Surface Water (AASW) is underlain by the huge and relatively homogeneous water mass of the CDW. The ACC-Weddell Gyre Boundary separates the ACC from the clockwise

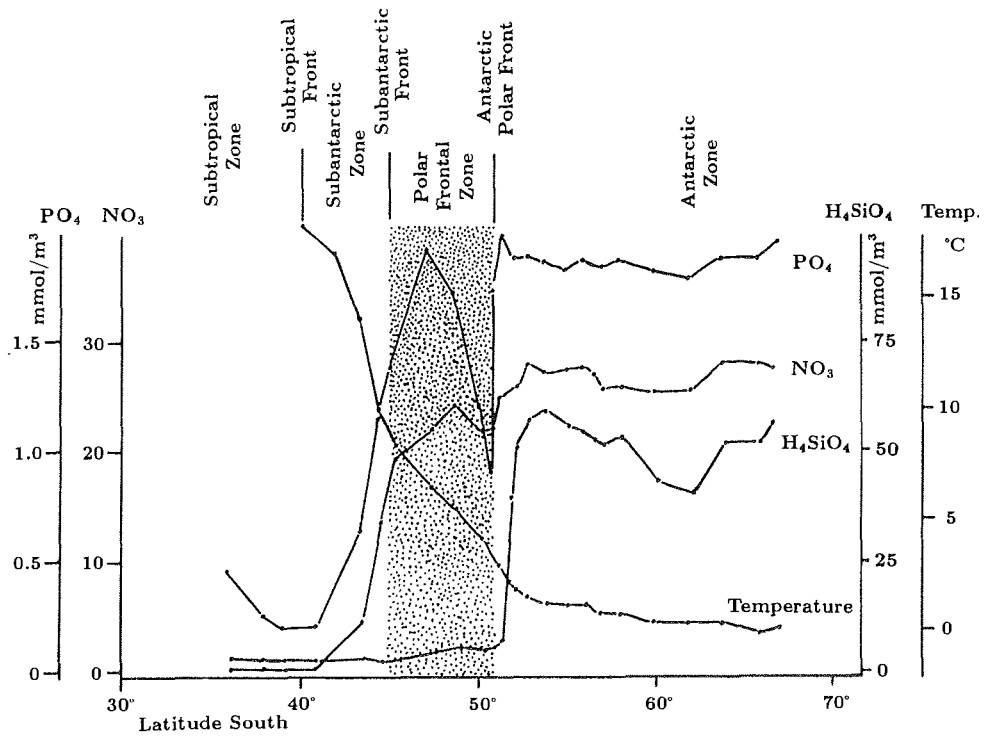

Figure 3: Nutrient concentrations and temperature in the surface water on a NE-SW transect over the ACC from about 14°E to 4°E (from van Bennekom et al., 1988). The shaded area marks the PFZ, where the most pronounced changes occur.

rotating Weddell Gyre, the eastern boundary of which is located at about 20° to 30° E.

Volume transport estimates of the ACC vary between some 200 Sv (10^6 cm^3/s) of eastward flow and even flow in the opposite direction (see Peterson and Stramma (1991) for a summary), while, according to newer results, realistic estimates are somewhere between 90 and 130 Sv, taking into account relatively large interannual variations (Whitworth and Peterson, 1985).

The deep circulation in the Atlantic sector of the Southern Ocean is dominated by the eastward flowing ACC, which in many places extends to the sea floor, and the generally northward flowing AABW. The bulk of the ACC consists of a thick layer of CDW which in the southwest Atlantic is divided into a lower (LCDW) and an upper branch (UCDW) at depths between 1000 and 2000 m by the inflow of NADW (Reid et al., 1977). The high salinity core of the NADW rises towards the south across the ACC (Fig. 4). The deep water is mainly dominated by Weddell Sea Deep Water (WSDW) and the Weddell Sea Bottom Water (WSBW), which is the densest component in the production of AABW (potential temperature θ < -0.8°C (Carmack and Foster, 1975)). WSDW (θ = +0.4 - -0.1°C) is mainly formed in the southern and western Weddell Sea by mixing of Warm

Deep Water (WDW, $\theta = +0.4°C$) derived from LCDW (Whitworth and Nowlin, 1987)) and high saline and cold Western Shelf Water (WSW) at the shelf break (Foster et al., 1987), but also by mixing of WSBW and WDW.

Downslope flowing supercooled Ice Shelf Water (ISW), formed below the Filchner and Ronne Ice Shelves (Foldvik et al., 1985), mixes below about 2000 m with WDW from the east and forms WSBW (Foldvik and Gammelsrød, 1988). WSBW may also form from mixing of WSW and WDW. While WSBW does not leave the Weddell Sea, WSDW flows northward and by mixing with CDW, AABW is formed which can today be identified as far as 35° N in the subtropical North Atlantic (Tucholke et al., 1973).

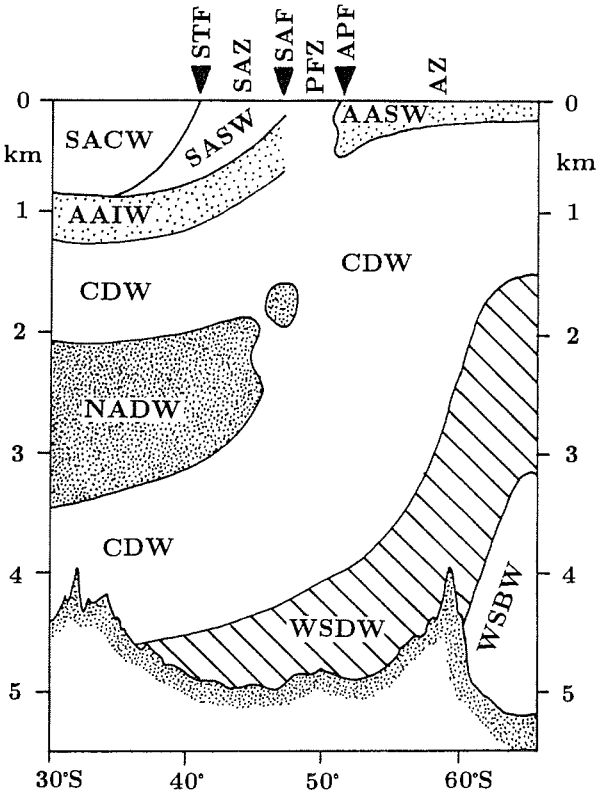

Figure 4: Schematic picture of the vertical distribution of water masses on a N-S profile in the southern South Atlantic Ocean west of the Mid Atlantic Ridge, from Peterson and Whitworth III (1989)

In the central Weddell Gyre the WDW, which represents the intermediate water mass in the Weddell Sea, was shown to be derived from the LCDW (Whitworth and Nowlin, 1987), which on its way around Antarctica has interacted with deep waters from the Pacific, Indian and Atlantic Oceans.

1.3 Paleoclimate

The global climate was subject to major cycles of warming and cooling during the Pleistocene. Applying the theory of Milankovitch (1930), these changes probably have been triggered by cyclic variations of the Earth's orbital parameters precession (23,000 year cycle), obliquity (41,000 year cycle), and excentricity (100,000 year cycle) (Berger et al., 1987; Imbrie et al., 1984, 1992). The control of the seasonal and latitudinal distribution of incident solar radiation is considered the driving mechanism for climate cyclicity, where mainly the 100 kyr (kyr = 1,000 years) cycle seems to have been responsible for the duration of one complete glaciation cycle during the last 500 kyr.

The Pleistocene climate changes have been recorded in the deep-sea sediments of the oceans, where the same cyclicity is found in the $\delta^{18}O$ records of foraminiferal calcite (c.f. Martinson et al., 1987). Another important archive for climate change in the past are the continental ice caps of Greenland and Antarctica, where the atmospheric composition (CO_2, CH_4, etc.) of the last about 200 kyr is preserved in gas inclusions (Barnola et al., 1987; GRIP-members, 1993). CO_2 and CH_4 are the main contributors to the Earth's greenhouse effect. It was shown that increased atmospheric concentrations of these gases occur during warmer global climate and vice versa. Prominent maxima of the CO_2 concentration of the atmosphere were observed during the peak interglacial periods of the paleoclimate (present interglacial and Eemian), which are in good agreement with the preindustrial CO_2 concentration of about 280 ppmV. During the glacials, the atmospheric concentration was lowered by about 90 ppmV. The origin of these changes is not yet completely understood and can neither be explained by changes of the land vegetation nor by lower glacial ocean temperatures. A major point of discussion is the coupling between climate change and CO_2: Are the changes recorded in the ice cores both, in Antarctica and Greenland, a consequence of orbitally forced global climate change or did changes in the concentrations of the greenhouse gases at least trigger for example deglaciation periods (Broecker, 1984)?

It is reasonable to look for the origin of the observed variations in changes of the chemistry and circulation of the largest CO_2 reservoir, the world ocean (c.f. Siegenthaler, 1990), with the underlying oceanic sediments representing the long-term sink of CO_2, with respect to Late Quaternary climate change. Even small variations in oceanic chemistry or biology may cause significant changes in atmospheric CO_2 concentrations because of the fast exchange between the two reservoirs (the turnover time of the entire ocean is in the order of 1000 years (Broecker and Peng, 1982)).

1.4 The Polar Nutrient Hypothesis

Besides physical processes like upwelling, one important mechanism controlling CO_2 exchange between the ocean and the atmosphere and between the surface ocean and the deep-sea is the so called biological pump. Organisms, mainly phytoplankton, living in the euphotic zone of the surface ocean transfer surface water CO_2 to organic matter, which then sinks to the deep-sea. The activity of the biological pump is traditionally thought

to be mainly controlled by nutrient supply (phosphate and nitrate) to the surface waters, which itself is linked to upwelling of deeper waters enriched in nutrients. Surface water nutrient concentrations are normally strongly depleted due to efficient biological removal.

In the Southern Ocean nutrient concentrations are not depleted (c.f. Levitus et al., 1993) suggesting that the biological activity is not limited by nitrate and phosphate and that nutrient utilization is low (High Nutrient Low Chlorophyll (HNLC) area). This led to the hypothesis that the Southern Ocean may represent the missing glacial CO_2 sink. According to multi box modelling approaches of Sarmiento and Toggweiler (1984) and Keir (1988), an increased primary productivity during glacials and thus an enhancement of the efficiency of the biological pump was proposed. The more efficient removal of CO_2 consequently was suggested to decrease surface water pCO_2 and thus also atmospheric pCO_2. The modelling approach of Sarmiento and Toggweiler yielded an atmospheric pCO_2 as low as 165 ppmV if all nutrients were removed.

Martin (1990) suggested iron as the biolimiting factor responsible for the increase of glacial Southern Ocean productivity. He claimed a strongly increased aeolian iron supply to the glacial Southern Ocean, for example originating from the desert areas of Patagonia due to more arid conditions and stronger wind stress. This follows the work of Duce and Tindale (1991) who suggested that about 10 % of the iron contained in the dust particles are leached out in the ocean water column. Recently, further support for the iron hypothesis was gained by a large scale experiment, during which iron was introduced artificially into a patch of equatorial Pacific surface water 500 km from Galapagos. This area, as the Southern Ocean, is a HNLC area, where the productivity of the surface water is not limited by nutrient availability. Instead, it was suggested that herbivore grazing is the controlling factor for keeping chlorophyll levels and thus phytoplankton productivity low (Walsh, 1976; Frost, 1991). Although grazing effects led to a fast return to preexperimental levels and to the effect that by far not all the available nutrients were utilized, there is strong evidence from the iron experiment that the availability of iron may indeed be important in controlling phytoplankton paleoproductivity in HNLC areas: Subsequent to the introduction of the iron, plant biomass was doubled, chlorophyll levels were increased threefold and plant production was increased fourfold after a relatively short period of time (Martin et al., 1994; Kolber et al., 1994).

Such a control may also be deduced from a comparison of the area of artificial iron enrichment to the Galapagos Plume area, where natural phytoplankton productivity and iron concentrations in the surface water are higher. The analysis of various parameters of both areas before the experiment showed that only the iron concentrations were significantly higher in the Plume area and thus may be responsible for the higher productivity. In the Southern Ocean constant geostrophic transport and supply of iron at the APF originating from the Antarctic Peninsula, the Scotia Ridge and the north-eastern Georgian Ridge was recently suggested to be responsible for the intensity of phytoplankton spring blooms (deBaar et al., 1995). These authors compared iron concentrations in the upper 300 m of the water column, pCO_2 and primary productivity in the southern ACC and at the APF. They found increased productivity and a CO_2 undersaturation in the area of the increased iron supply. In contrast, in the southern ACC the upwelling of deep waters

only allowed moderate productivity to develop.

The validity of these hypotheses for the global glacial atmospheric CO_2 decrease may be checked by reconstructing surface water nutrient concentrations of the glacial Southern Ocean: Significantly lowered nutrient concentrations would support the hypothesis and unchanged concentrations consequently would disprove it. The main proxy indicators for surface water nutrient concentrations, which are themselves not recorded in the sediments, are the $\delta^{13}C$ values and the Cd/Ca ratio in planktonic foraminifera.

The use of the $\delta^{13}C$ as a surface water nutrient proxy is based on the kinetic fractionation of the carbon isotopes during the production of organic matter. ^{12}C is enriched in the organic matter and leaves the dissolved inorganic carbon enriched in ^{13}C, while at the same time the phosphate concentration is lowered. The inverse relationship was shown to be linear, allowing the $\delta^{13}C$ in planktonic foraminifera to be applied as a nutrient proxy (Kroopnick, 1985).

The Cd/Ca ratio shows a positive correlation with the phosphate concentrations and thus may also serve as a nutrient proxy (Boyle, 1988b). Both records yield consistent results throughout the world ocean, with the exception of the Southern Ocean: $\delta^{13}C$ results of planktonic foraminifera from Southern Ocean sediments, deposited during the last glacial, show a decrease, both south and north of the present day position of the Antarctic Polar Front (APF), suggesting that there was no decrease in glacial nutrient concentrations but, instead, that there was an increase (Charles and Fairbanks, 1990). The Cd/Ca ratio at the same time does not show any systematic glacial/interglacial changes (Boyle, 1988b; 1992; Keigwin and Boyle, 1989), instead of an expected decrease following the hypothesis, suggesting that surface water phosphate concentrations did not change. This is not only a discrepancy between the two proxies, but also a discrepancy to the hypothesis of a high glacial productivity in the Southern Ocean.

Various attempts were made to explain the contradiction between the two proxies. Mackensen et al. (1994) suggest that a glacial northward shift of the high productivity area, presently located south of the APF, was responsible for at least a part of the observed change in $\delta^{13}C$. Deep convection and thus efficient atmospheric exchange during interglacials is indicated by equal $\delta^{13}C$ values in the planktonic and benthic records and a more stratified water column during glacials is documented by differences in the benthic and planktonic $\delta^{13}C$ records. Just opposite, isotope data of Niebler (1995) from the eastern Atlantic sector of the ACC suggest a stronger stratification of the water column during interglacials. Broecker (1993) appealed to the temperature dependence of the isotope fractionation between atmospheric CO_2 and surface ocean ΣCO_2. Saager (1994) claims that spatial variations in the Cd/PO_4 ratio which are observed today in the world ocean may also have occurred temporarily at the same location, whereas McCorkle et al. (1994) discuss a selective dissolution of Cd and Ca through time. Finally, an increased accumulation of Cd in suboxic sediments, which may also have changed the Cd/PO_4 ratio, is suggested by Van Geen et al. (1995), but none of the explanations has yet proved to be undoubtfully correct.

Recently, the $\delta^{15}N$ value has been introduced as a tool to trace surface water nitrate

utilization (Calvert et al., 1992; Francois et al., 1992). High sedimentary $\delta^{15}N$ values in organic matter indicate an increased nitrate depletion of the surface waters. In contrast to the expectations, Francois et al. (1993) found higher $\delta^{15}N$ values and correspondingly higher nitrate depletion during periods of low particle flux and thus also low export productivity, and vice versa, in a sediment core presently located south of the Subantarctic Front in the Indian sector of the Southern Ocean. They interpreted this feature as a reduction in the rate of nutrient supply to the surface water during the last glacial and deglacial period caused by a stratification of the water column by a meltwater lid.

The accumulation rates of the particulate organic matter may be traced directly by the organic carbon accumulation rate or indirectly by the accumulation rates of biogenic carbonate or biogenic opal. Uncertainties for all three sediment components (biogenic opal, carbonate and C_{org}) arise from the variability of decomposition effects in the water column and in the sediments. Most severe recycling is experienced by the organic carbon. Only about 1 % of the amount produced in the surface water reaches the sediment (see Berger et al. (1987) for a summary), which makes it a questionable tracer for the accumulation rate of organic matter.

Bottom water undersaturated in $CaCO_3$ allows biogenic carbonate to accumulate in the sediments of the Southern Ocean south of the APF only at high elevations. The decay of the high amounts of settling organic matter itself releases CO_2 to the bottom water which consequently dissolves $CaCO_3$. Additionally, there are strong glacial interglacial variations of the depth of the lysocline and CCD, related to mixing patterns of the Southern Ocean (Howard and Prell, 1994) (see chapter 4.5).

Following DeMaster (1981), at present two thirds of the sedimentary biogenic opal are deposited in the Antarctic Ocean forming the opal belt of the Antarctic Zone with sediments consisting of 50-95 weight-% biogenic opal. The biogenic opal consists of frustules of marine plankton (radiolarians and diatoms), which can develop due to the high supply of nutrients and dissolved silica upwelling in the AZ and the PFZ. Investigations with time-series sediment traps in the Atlantic sector of the Southern Ocean showed that the biogenic opal flux is negligible during periods of sea ice cover and that opal flux pulses with a duration of only 2-9 weeks during austral summer account for 70-95 % of the total annual flux. It was shown by Nürnberg (1995) that although the opal accumulation has been high, export paleoproductivity does not reach the values determined at the coastal upwelling areas at the western continental margins off North and South America and Africa (Berger, 1989). However, also biogenic opal is subject to dissolution due to the undersaturation of sea water with respect to silica. Dissolution intensity depends on the sediment accumulation rate: In case of low accumulation rates most of the opal is dissolved in the surface sediment, whereas much more can be preserved when the rates are high, as for example in the high productivity zone south of the APF (Pichon et al., 1992). Nevertheless, changes in opal accumulation may at least deliver relative variations of the organic carbon flux due to their good correlation determined in sediment traps (c.f., Fischer et al., 1988).

In this context the study of the biogenic barium (excess Ba over the lithogenic background) as a measure for opal productivity was introduced because of its higher preser-

vation rates and high resistance against remobilization in oxic sediments (Dymond et al. 1992). Dehairs et al. (1980) found a positive correlation between particulate barium (barite - $BaSO_4$) and primary productivity. With the help of transfer functions the biogenic barium accumulation rates can be translated into paleoproductivity rates (see chapter 4.3.3). The formation of the barite occurs in the sulphate-saturated microenvironments of decaying and settling diatom frustules, thus explaining the very good correlation between biogenic opal and biogenic barium (Bishop, 1988). Biogenic barium has already been applied for tracing biogenic particle fluxes in the Southern Ocean (Shimmield et al. 1994; Frank et al., in press). For a detailed summary on biogenic barium see Dymond et al. (1992), Gingele and Dahmke (1994) and Nürnberg (1995).

Studies of the opal accumulation history of the Southern Ocean suggest that the zone of high opal productivity which is mainly dependent on the sea ice extension and the position of the frontal zones moved northwards during the glacials by about 5° (Charles et al., 1991; Mortlock et al., 1991), resulting in opal accumulation features just opposite to each other in sedimentary profiles north and south of the APF. The same feature was deduced by Kumar et al. (1993) from $^{231}Pa_{ex}/^{230}Th_{ex}$ ratios in two sediment cores north and south of the APF. The total amount of Southern Ocean opal accumulation, however, did not change or was even decreased during glacials (Mortlock et al., 1991).

Results which were achieved by investigations within the SFB 261 led to a somewhat different interpretation concerning a glacial northward shift of the frontal systems. Paleotemperature reconstructions of the surface water did not show a significant shift of the fronts. However, the temperature gradients at the fronts during the climate optima were lowered. Various proxy records show a clearly reduced glacial productivity south of the APF and a higher glacial productivity north of the Polar Front, but the amount was suggested not to be comparable to the interglacial values south of the Polar Front, in accordance to the results of Mortlock et al. (1991)

The main problem with these studies is that the effect of sediment redistribution (focusing and winnowing) related to paleocurrent speeds was not considered, with the exception of the studies of Francois et al. (1993) and Kumar et al. (1993). Additionally, it may be possible that dissolved silica became a biolimiting nutrient in the glacial surface water, thus decoupling organic carbon and silica fluxes (Berger, 1991; Kumar, 1994). In the study of Kumar (1994) it is suggested that this decoupling is visible in the accumulation rate pattern of authigenic uranium north and south of the APF: North of the APF much higher accumulation rates of authigenic uranium, accumulated under reducing conditions for example caused by high accumulation rates of organic matter, than in the Antarctic Zone south of the APF were determined. This pattern which yields opposite results compared to the biogenic opal record is interpreted as being caused by a decoupling of the organic carbon and biogenic opal flux. Further the author infers an overall increased productivity during glacials in the Southern Ocean from the accumulation rates of the authigenic uranium.

Recent modelling invokes a glacial alkalinity increase of the Southern Ocean surface water to explain pCO_2 changes (Boyle, 1988a; Broecker and Peng, 1989). The increase of

CO_2 is suggested to be driven by reductions in NADW inflow into the Southern Ocean leading to an increase in deep water nutrient supply and dissolution of carbonate sediments. Thus the alkalinity increases in the CDW, which upwells in the Southern Ocean. Howard and Prell (1994) suggest that the main driving force for the glacial alkalinity increase was a diminished carbonate productivity and thus also a decreased $CaCO_3/C_{org}$ rain ratio. However, the carbonate preservation signal apparently leads the restarting admixture of NADW.

In summary, there are still various problems and inconsistencies when reconstructing the climatically forced changes in Southern Ocean paleoenvironmental conditions. In the following it is tried to contribute to the understanding and solving of some of these problems by a radionuclide study of Southern Ocean sediments from the eastern Atlantic.

1.5 Radionuclide Geochemistry

1.5.1 ^{10}Be

^{10}Be (T(1/2) = 1.52 Ma (Hofmann et al., 1987)) is produced in the upper atmosphere by cosmic radiation induced spallation of oxygen and nitrogen atoms depending on the geographical latitude (Lal and Peters, 1967) and is then transferred to the Earth's surface by wet and dry precipitation with a residence time in the atmosphere of about 1 year (c.f. Turekian et al., 1983) (Fig 5). The present global average production was calculated to be $1.21 \pm 0.26 \cdot 10^6$ atoms/cm^2 · yr (Monaghan et al., 1985/1986). There are, however, great differences in the estimates of today's ^{10}Be production that range from 0.1 to $1.6 \cdot 10^6$ atoms/cm^2 · yr depending on the method by which they were determined (see Lao (1991) for a summary).

The production rate is influenced by variations of the geomagnetic field intensity as deduced from investigations of sediments covering the Brunhes/Matuyama geomagnetic reversal (Henken-Mellies et al., 1990). These authors suggested that a weakening or even breakdown of the Earth's geomagnetic field during reversals allowed the cosmic rays to produce more ^{10}Be. Recent results showed that the production of cosmogenic radionuclides also varied during periods of smaller excursions of the geomagnetic field. There are indications that there was a 30 % increase of the production of ^{10}Be during the last glacial maximum (Lao et al., 1992a). This was also considered to be the maximum range of variation during the last about 420 kyr, as suggested by Southon et al. (1987).

However, more recently detailed investigations of the production rate variations of ^{14}C during the last 50 kyr were published which show an increase of about 40 % during the period from about 20-30 kyr B.P. as deduced from U/Th mass spectrometric calibrations of ^{14}C ages in corals from Barbados (Bard et al., 1990). Mazaud et al. (1991) calculated an increase of the ^{14}C production rate of up to 90 % above the present-day value from 15 to 24 kyr and from 37 to 46 kyr B.P.. Recent records of the dipole intensity, which has controlled the amount of cosmic rays reaching the earth's atmosphere are extended back to 200 kyr B.P. (Meynadier et al., 1992; Tric et al., 1992, Yamazaki and Ioka, 1994).

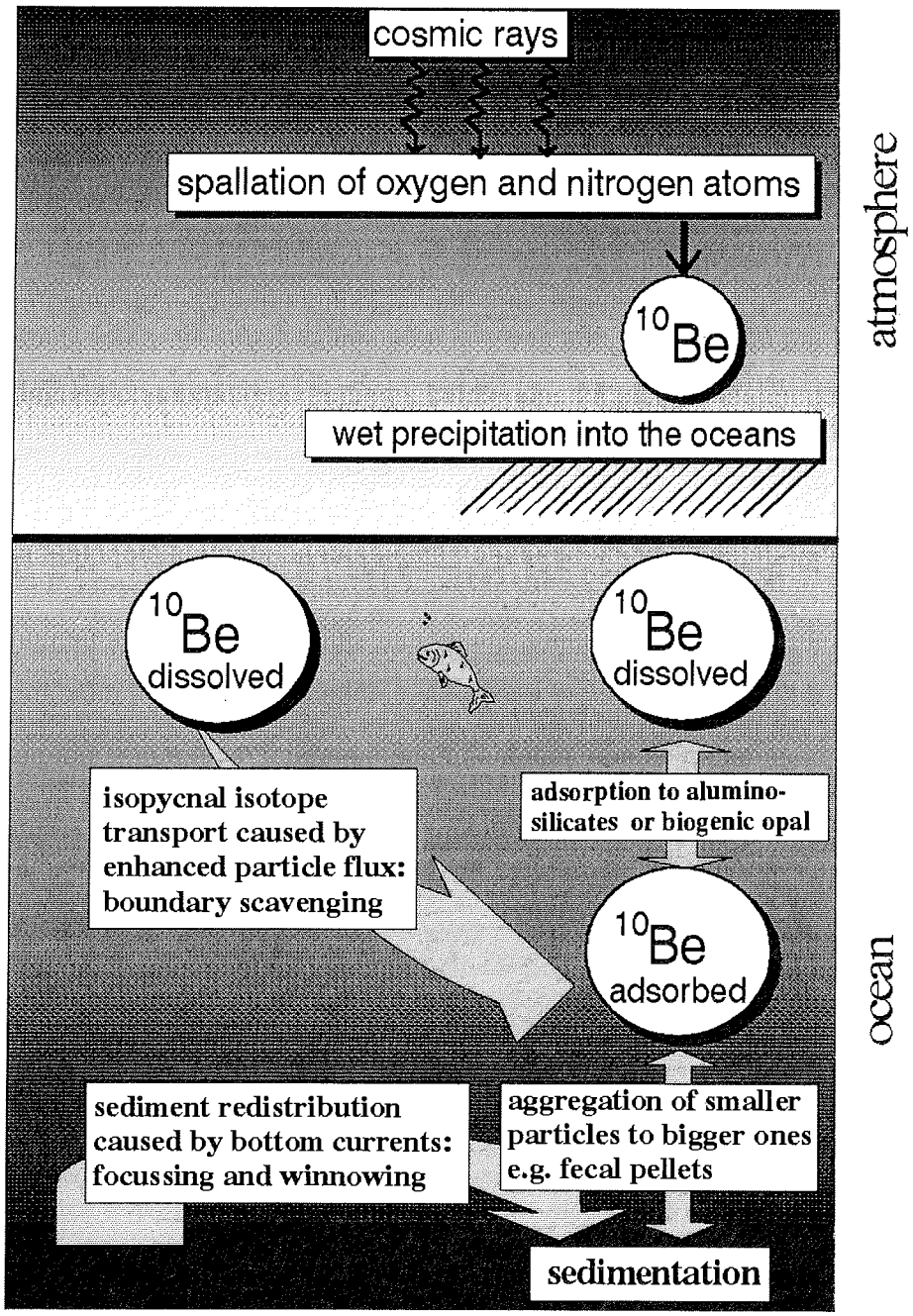

Figure 5: Schematic picture of the path of ^{10}Be from atmospheric production to deposition in the marine sediments.

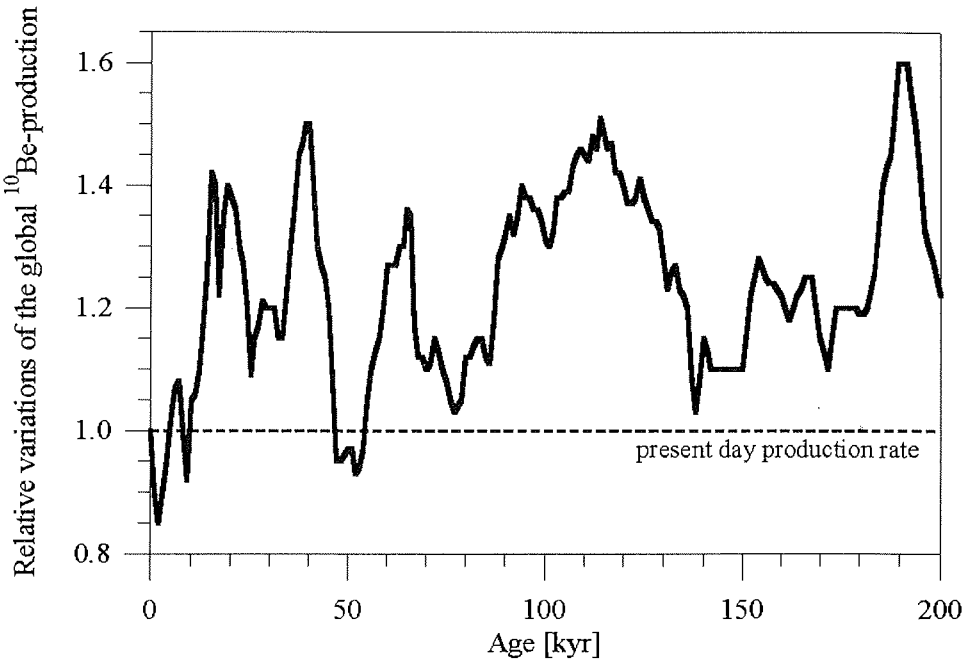

Figure 6: Relative variations of the global ^{10}Be production deduced from variations of the geomagnetic field intensity. The period from 140 kyr B.P. until present was adapted from Mazaud et al. (1994) and from 200 until 140 kyr B.P. variations of the production rate were estimated from the record of Yamazaki and Ioka (1994).

These were converted into a profile of global ^{10}Be production rate for the last 140 kyr (Mazaud et al., 1994) following the calculations of Lal (1988) (Fig. 6). For this study the production rate changes between 200 and 140 kyr B.P. were evaluated from the virtual axis dipole moment (VADM) reconstructions of Yamazaki and Ioka (1994).

Mazaud et al. (1994) showed that their synthetic record correlates very well to a record of the flux of ^{10}Be onto the Antarctic ice sheet measured at the Vostok ice core (Raisbeck et al. 1987; 1992) and thus corroborates the fluctuations of the global production. These results also show that there must be an efficient transport of aerosols loaded with ^{10}Be from low latitudes to Antarctica where significant modulations of the production by changes of the geomagnetic field intensity are not expected due to the vertical field.

Having reached the oceans, ^{10}Be is quickly adsorbed to particles, preferably aluminosilicates (Sharma et al., 1987) (Fig. 5). The biological activity in the surface waters of the ocean produces bigger particles (e.g., fecal pellets) incorporating the clay minerals. The bigger particles have a higher sinking velocity than the smaller ones and partly redissolve in the deeper water column, thus partly releasing the adsorbed ^{10}Be again. This explains the nutrient-like behavior of ^{10}Be in ocean water column profiles (Kusakabe et al., 1987).

From this relation ^{10}Be accumulation in the sediments and biogenic particle fluxes are expected to show a positive correlation. This is indeed observed in sediments from the Arctic Ocean and the Norwegian Sea (Eisenhauer et al. 1990; 1994) and at the Weddell Sea margin (Frank et al., in press), where the ^{10}Be records are applied for stratigraphic purposes.

However, there are still uncertainties concerning the ^{10}Be adsorber phases, as shown by Lao et al. (1993), who did not find a relationship between Al and ^{10}Be in sediment trap samples from off the west coast of the United States. It is proposed that in such a high particle flux area, biogenic opal may be a more important scavenging factor than clay minerals (Lao et al., 1992c; 1993). This was also deduced by Bourlés et al. (1989a) from sequential leaching experiments of natural sediments and by Bourlés et al. (1989b) from the comparison of Be and Si in pore water profiles.

Fe oxihydroxides which are the products of the oxidation of Fe sulphides emanated by hydrothermal activity, may be another scavenging factor for ^{10}Be in the direct neighbourhood of mid-ocean ridges (Valette-Silver et al., 1987; Bourlés et al., 1991). According to Anderson et al. (1990), Mn, for example, released to the bottom water by diagenetic recycling does not scavenge ^{10}Be to any great extent. However, Bourlés et al. (1989a) found a relationship between ^{10}Be and Mn and Fe oxihydroxides in sequential leaching experiments of various sediments and a relationship between Mn and Be in pore waters of the hydrothermally influenced sedimentary environment of the Guayamas Basin (Bourlés et al., 1989b). Nevertheless, the affinity of ^{10}Be for adsorbing to oxihydroxides should be small relative to ^{230}Th and ^{231}Pa (Mangini et al., 1986; Anderson et al., 1990; Lao et al., 1993; Frank et al., 1994). Remobilization of ^{10}Be from the sediments was deduced by Bourlés et al. (1989b; 1991) from the analysis of hydrothermal pore waters emanating from sediment-covered mid ocean ridges. The amount of remobilized ^{10}Be, however, was shown to be very low and negligible compared to the atmospheric supply. The influence of remobilized Be also appeared to be restricted to a small area of a few kilometers around the hydrothermal centers. The authors also demonstrated that remobilization is generally of minor importance for the use of ^{10}Be as a geochronometer in marine sediments. In the water column of the open ocean, the mean residence time of ^{10}Be varies between 400 and 1000 years (Segl et al., 1987; Kusakabe et al., 1991; Ku et al., 1990), but it can be shorter at the ocean boundaries, where high particle fluxes account for very efficient scavenging (Anderson et al., 1990).

1.5.2 ^{230}Th and ^{231}Pa

^{230}Th (T(1/2) = 75,200 years) and ^{231}Pa (T(1/2) = 32,400 years) are produced by decay of ^{234}U and ^{235}U in the water column with a constant rate due to the homogeneous U concentration of 3.3 μg/l in the ocean, which is a result of the relatively long residence time of U in the oceans of about 400 kyr (cf. Mangini et al., 1979) (Fig. 7). The production amounts to 2.6 dpm/cm^2 · kyr · 1000 m water column for ^{230}Th (dpm = disintegrations per minute) and to 0.24 dpm/cm^2 · kyr · 1000 m water column for ^{231}Pa.

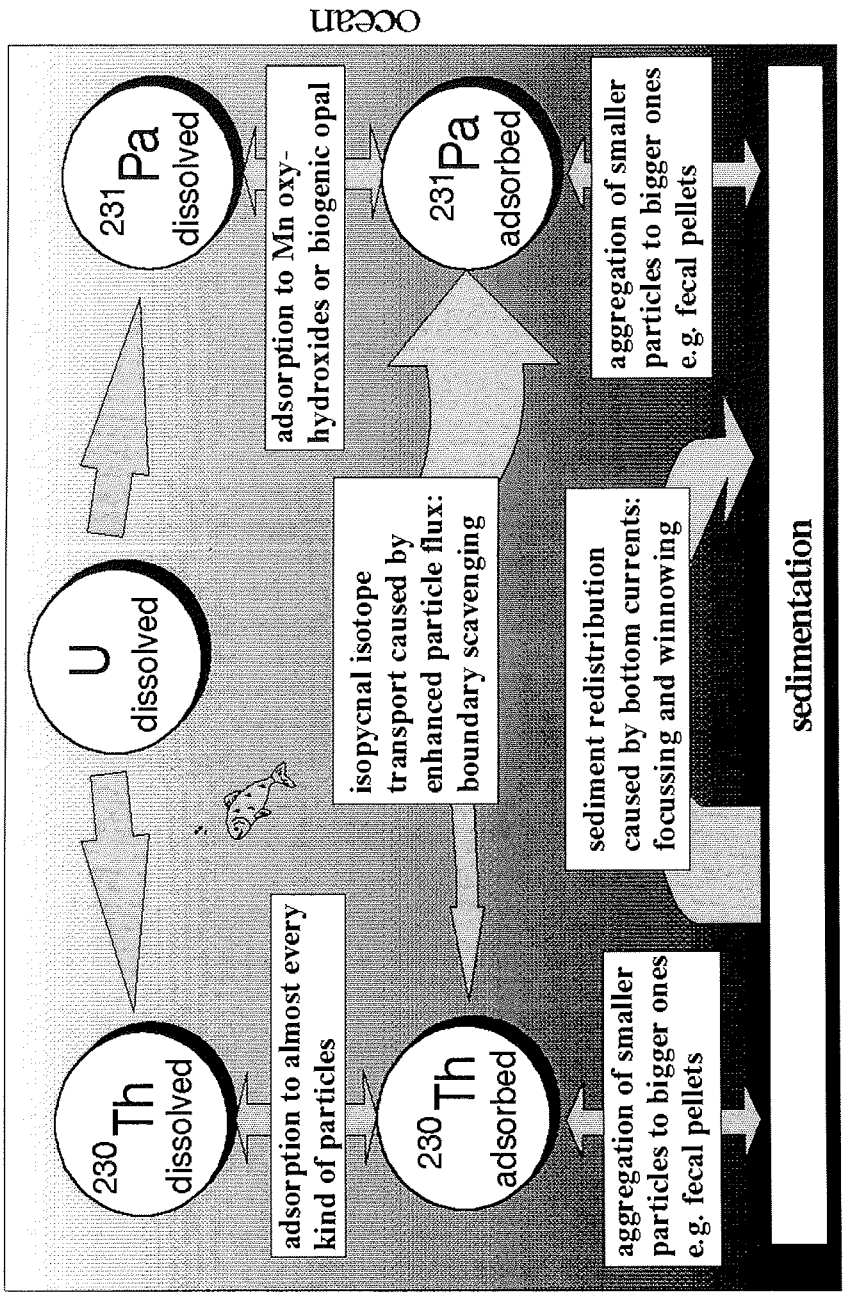

Figure 7: Schematic picture of the path of ^{230}Th and ^{231}Pa from production to deposition in the marine sediments.

Both isotopes are highly particle reactive and are quickly adsorbed to particles in the water column. Important particulate adsorber phases for both isotopes are Mn and Fe oxihydroxides if their abundance is high (Bacon and Anderson, 1982; Hunter et al., 1988), with Mn having been suggested to be more efficient in scavenging ^{231}Pa relative to ^{230}Th (Anderson et al., 1983b). This is, however, very doubtful regarding the fact that MnO_2 coated cartridges adsorb Th appreciably better than Pa (Rutgers van der Loeff and Berger, 1993). The mean residence time of ^{230}Th in the oceans' water column amounts to between 20 and 40 years and the residence time of ^{231}Pa is about 100 years (Anderson et al., 1983a; Nozaki et al., 1981). It is generally accepted that no remobilization of both isotopes in the sediments occurs (e.g., Ivanovich and Harmon, 1992).

The measured concentrations of ^{230}Th and ^{231}Pa have to be corrected for detrital contributions produced by decay of ^{234}U and ^{235}U in the sediment in order to achieve the amount of ^{230}Th and ^{231}Pa originating from scavenging in the oceanic water column (excess concentrations). Additional U may be added to the sediments from the water column if reducing conditions occur close to the sediment water interface (Cochran and Krishnaswami, 1980; Barnes and Cochran, 1990; Klinkhammer and Palmer, 1991). Such a proximity is observed either in areas where bottom waters are low in dissolved oxygen or where a high flux of organic matter consumes the oxygen available and leads to a precipitation of the U from the soluble U^{+6} to the insoluble U^{+4}. These conditions, for example, exist in the sedimentary regimes of coastal upwelling areas. In contrast to Mn, a downward diffusion of U occurs, which is controlled by the gradient between the U concentration in the water column and the sediment pore water. As a consequence, the accumulation of authigenic U occurs very close to the sediment water interface and may thus be assumed to coincide with the deposition of the sediment for studies concerning periods of several hundreds to thousands of years.

For calculating excess ^{230}Th and ^{231}Pa activities (concentrations) the following equations are applied

$$^{230}Th_{ex} = {}^{230}Th_{meas.} - (^{232}Th \cdot 0.75) - (^{238}U_{auth.} \cdot (1 - e^{-\lambda(^{230}Th)\cdot t})) \quad (1)$$

and

$$^{231}Pa_{ex} = {}^{227}Th_{meas.} \cdot e^{13.5\cdot d\cdot\lambda(^{227}Th)} - (^{232}Th \cdot 0.0338) - (^{238}U_{auth.} \cdot 0.045 \cdot (1 - e^{-\lambda(^{231}Pa)\cdot t})) \quad (2)$$

with

$$^{238}U_{auth.} = {}^{238}U_{meas.} - (^{232}Th \cdot 0.75) \quad (3)$$

where

$(^{232}Th \cdot 0.75)$ represents the estimate of the mean activity of detrital ^{238}U in dpm/g

(cf. Wedepohl, 1995),
$(^{232}Th \cdot 0.0338)$ represents the activity of detrital ^{235}U in dpm/g,
λ is the corresponding decay constant of the isotope in brackets in 1/y,
t is the age in years estimated from previous stratigraphic results.

The $^{238}U_{auth.}$ term represents the equilibrium activity of ^{230}Th and ^{231}Pa respectively, which was produced from authigenic U under the assumption of U precipitation during the time of deposition of the sediment. The first exponential term in the ^{231}Pa excess calculation is necessary to correct for decay of ^{227}Th. Decay starts during chemical preparation at the HCl column separation step where the mother nuclide ^{231}Pa is separated from the daughter ^{227}Th. ^{227}Th then decays with a halflife of 18 days and thus has to be decay corrected for the time from separation to measurement d in days.

After the establishment of a stratigraphy the excess activities of the radionuclides may be decay corrected to the time of deposition of the sediment ($^{230}\mathrm{Th}^0_{ex}$, $^{231}\mathrm{Pa}^0_{ex}$ and $^{10}\mathrm{Be}^0$):

$$^{230}Th^0_{ex}(^{231}Pa^0_{ex};^{10}Be^0) = ^{230}Th_{ex}(^{231}Pa_{ex};^{10}Be) \cdot e^{\lambda \cdot t} \quad (4)$$

with λ being the decay constant of the corresponding radionuclide.

1.6 Geochemistry of Mn and Al

In this chapter the geochemistry of the elements Mn and Al and their importance for the problems investigated in this study will briefly be introduced.

Peaks of Mn occurring at the transition from the reduced to the oxidized zone of the sediment column are found in nearly all marine sedimentary settings. They have been caused by remobilization and upward migration of Mn along the redox gradient until it reprecipitates at the base of the oxidized zone (Froelich et al., 1979; Berger et al., 1983; Frank et al., 1994). If the transition between the reduced and oxidized zone (redoxcline) moves upwards at the same speed as sedimentation, the surface Mn peak keeps pace and also moves upwards. If the redoxcline, on the other hand, moves upwards fast, for example caused by a sudden increase of the sedimentation rate, it can not be dissolved fast enough and is buried (Berger et al., 1983). The decreased activity of benthic burrowing organisms may also play a role. Another possibility for the burial of a Mn peak is a downward shift of the redoxcline in the sediment because of a decrease in the supply of organic matter. As a third possibility the supply of Mn from the water column may vary. This may be due to changes in hydrothermal production or due to an increased Mn precipitation in the deep water at the beginning of interglacials, caused by the reestablishment of the global oceanic thermohaline circulation and ventilation system (Mangini et al., 1990).

In order to identify Mn which was reprecipitated after diagenetic remobilization or added by other mechanisms from the water column, the Mn/Al ratio is calculated and was at first compared to the value for average pelagic sediments of 0.06 (Chester and Aston, 1976). The source of the detrital material, and with it the Mn/Al ratio, probably did not

change too much because of the narrow range of the Mn/Al values in crustal material (Best, 1982, Taylor and McLennan, 1985). However, some sedimentary deposits, as for example from the Barents Sea, show Mn/Al ratios below 0.01 (Calvert, 1976). Apparently, the value of 0.06 is too high for Southern Ocean sediments because the measured values in many sections are far lower, which is very difficult to explain.

Taking into account the possible sources of the detrital material, the Mn/Al ratio of 0.004 of the standard granodiorite GSP-1 (Flanagan, 1968) is applied for lithogenic background evaluation. An increase over this value suggests authigenic Mn input. High accumulation rates of aluminosilicates can mask an input of hydrothermal Mn which may only be seen during periods of low aluminosilicate accumulation (Kumar, 1994). Taking into account the high sedimentation rates at the ACC and the high mobility of Mn in the sediments, such a hydrothermal input is very unlikely to be identified.

For these evaluations it is assumed that the Al content is exclusively of terrigenous origin. Various investigations, however, have shown that there may also be a biogenic Al component (MacKenzie et al., 1978). Coale and Bruland (1985) suggested that the intensity of adsorptive scavenging of dissolved Al is likely to be a function of biological productivity. The overall average residence time amounts to between 50 and 150 years (Orians and Bruland, 1985) and thus allows an Al boundary scavenging. Murray et al. (1993) could even demonstrate that the Al/Ti ratio (assuming Ti to be exclusively of terrigenous origin) may be a paleoproductivity tracer in the high productivity area of the central equatorial Pacific ocean. Thus, in high productivity areas the background Mn/Al ratio may even be lower than 0.004 and smaller variations of the Mn/Al ratio may also be caused by changes of biologically enhanced Al boundary scavenging.

In summary, peaks of authigenic Mn probably trace changes of the sedimentary environmental conditions for a number of reasons that will be addressed in detail in the discussion chapter for the setting of each sediment core.

1.7 Boundary Scavenging

The few available open ocean water column data yield dissolved $^{230}Th_{ex}/^{231}Pa_{ex}$ activity ratios of the two radionuclides in the range from 3 to 5, reflecting the stronger affinity of ^{230}Th to particles (Anderson et al., 1983a). Correspondingly, the ratio in deep-sea sediments from the Central Pacific is increased to values between 20 and 30 (Anderson et al., 1983a;b; Yang et al., 1986), whereas in areas of enhanced particle fluxes the situation may be different.

Scavenging effects of ^{230}Th, ^{231}Pa and ^{10}Be resulting from increased particle fluxes at the ocean boundaries have been another important field of research in the recent past (Spencer et al., 1981). Increased ^{231}Pa and ^{10}Be accumulation in the sediments of the oceans' boundaries is explained by transport of isotopes via eddy diffusion along isopycnals through the water column from areas of lower particle fluxes while this effect is negligible for ^{230}Th due to its high particle reactivity (Yang et al., 1986; Anderson et al., 1990; Lao, 1991; Frank et al., 1994).

Additionally, the advective transport may play a major role in redistributing these radionuclides after production. Rutgers van der Loeff and Berger (1993) demonstrated from water column profiles of dissolved and particulate ^{230}Th and ^{231}Pa in the ACC that large amounts of these radionuclides were supplied to the high particle flux areas via upwelling water masses from the north. In a recent study it could be shown that the advective transport probably has been more important than boundary scavenging for the distribution of ^{231}Pa in the sediments of the Atlantic Ocean (Yu, 1994; Yu et al., submitted).

Increased particle fluxes which may lead to enhanced scavenging of radionuclides mainly occur at the ocean margins. Particles originate from terrestrial sources such as fluvial input, for example, in the area of the Congo fan (Jansen et al., 1987) or from aeolian input as in the Mediterranean Sea (Brown et al., 1992). Changes in hydrothermal influence on deep-sea sediments were investigated by comparison of the measured fluxes of $^{231}Pa_{ex}$ and $^{230}Th_{ex}$ to the values expected from production and by comparing the measured $^{230}Th_{ex}/^{231}Pa_{ex}$ ratios to the production ratio in the water column of 10.8 (Shimmield and Price, 1988). These authors found increased fluxes of both radionuclides to the sediments of the East Pacific Rise at 20°S, and they interpreted $^{230}Th_{ex}/^{231}Pa_{ex}$ activity ratios in the range of 3-4 as a consequence of hydrothermal activity.

There are, however, exceptions to the rule. In a study from the Mid Atlantic Bight which is an area of high particle fluxes Anderson et al. (1994) found an expected enhanced deposition of particle reactive radionuclides. However, in contrast to the expectations, a relative enhancement of the deposition of $^{230}Th_{ex}$ compared to $^{231}Pa_{ex}$ and ^{210}Pb was determined. The authors explained this unusual feature by an offshore transport of $^{231}Pa_{ex}$ and ^{210}Pb with resuspended Mn rich particles. The increased amounts of Mn are suggested to originate from a recycling of reduced Mn^{2+} from the organic rich sediments of the Mid Atlantic Bight. This is a process also proposed for increased $^{231}Pa_{ex}$ concentrations in the suboxic sediments of the Panama Basin, where the diagenetically remobilized Mn reprecipitates near the sediment water interface and leads to a near bottom boundary scavenging of ^{231}Pa (Yang et al., submitted).

Another source of high particle fluxes which may lead to radionuclide boundary scavenging effects are areas of high biological production, for example induced by coastal upwelling of nutrient enriched water masses (Mangini and Diester-Haass, 1983). Kumar et al. (1993) were able to trace high biogenic particle fluxes in the area of the Antarctic Polar Front in the Atlantic sector of the Southern Ocean by increased $^{231}Pa_{ex}/^{230}Th_{ex}$ ratios. This corroborated results of Charles et al. (1991) who deduced a northward shift of the high particle flux area during glacials. Francois et al. (1993) could also trace biogenic particle fluxes at the ACC in the Indian sector of the Southern Ocean by $^{231}Pa_{ex}/^{230}Th_{ex}$ ratios.

1.8 $^{230}Th_{ex}$ Constant Flux Modelling: High Resolution Sedimentation Rate and Age Determination

If a constant flux of $^{230}Th_{ex}$ to the sediments is assumed, variations of the concentrations of the initial decay corrected $^{230}Th_{ex}$ in the sediment may be directly interpreted as variations of dilution with accumulating sediment and thus as variations of the sedimentation rates. Using a $^{230}Th_{ex}$ constant flux model, it is possible to calculate high resolution sedimentation rates per sample and thus also ages per sample (e.g. Bacon, 1984; Francois et al., 1990; Frank et al., submitted). For this kind of model it is important to have a continuously sampled record of the sediments to avoid interpolations between single data points. The sedimentation rates and ages calculated by this approach thus represent average values for the corresponding sampled sediment interval.

The flux or accumulation rate F of $^{230}Th_{ex}$ is calculated as

$$F = C_{(x)} \cdot S \cdot \varrho \tag{5}$$

where $C_{(x)}$ is the concentration of $^{230}Th_{ex}$ at a depth x in the sediment, S is the sedimentation rate and ϱ is the dry bulk density. It follows that

$$S = \frac{F}{C_{(x)} \cdot \varrho} = \frac{\Delta x}{\Delta t} \tag{6}$$

where Δx is the depth interval and Δt is the time interval of the corresponding sample. Solved for Δt gives

$$\Delta t = \frac{\Delta x \cdot C_{(x)} \cdot \varrho}{F} \tag{7}$$

With this relation Δt_1 of the first sample of the sediment core is calculated and the $^{230}Th_{ex}$ concentration of the second sample is decay corrected. Δt_2 of the second sample is then

$$\Delta t_2 = \frac{\Delta x \cdot C_{(x)} \cdot e^{\lambda t_1} \cdot \varrho}{F} \tag{8}$$

with
$\lambda\ (^{230}\mathrm{Th}) = 9.24 \cdot 10^{-6}\ 1/y$

All other time intervals may be calculated this way. The age t for a certain depth x is then calculated by adding all Δt's from the top of the core down to x. The sedimentation rate of a sample n is calculated as

$$S_n = \frac{x_n}{t_n} \tag{9}$$

If no additional stratigraphic information on a sediment core is available, the average $^{230}Th_{ex}$ flux is calculated from the average sedimentation rate estimated by $^{230}Th_{ex}$ dating, the average decay corrected $^{230}Th_{ex}$ concentration and the average dry bulk density. This flux F is inserted into the equations 7 and 8. The $^{230}Th_{ex}$ dating method simply works by exponentially fitting the downcore decreasing $^{230}Th_{ex}$ concentrations and thus determining a rough average sedimentations rate and an average flux for the whole sediment core. In case there is more stratigraphic information the flux F is varied within certain age intervals until the sum of the Δt's corresponds to the age previously fixed.

If F deviates significantly from the expected production value within a distinct dated sediment section, particle redistribution processes must have occurred. Nevertheless, assuming constant flux and constant sediment redistribution, sedimentation rates and ages may be calculated this way and yield a better evaluation of the "true" pattern of the sedimentation rates than a linear interpolation between two age fix points.

This method may be considered a reliable and simple dating tool, especially within certain isotope stages. It is also applicable for sediments where standard dating methods like $\delta^{18}O$ and ^{14}C do not work due to missing biogenic carbonate.

1.9 Resedimentation Phenomena: Focusing and Winnowing

One important problem for paleoceanographic reconstructions based on sediment accumulation rates is the quantification of lateral sediment redistribution. This process may either directly affect particles which sink through the water column and are subject to transport by currents, or may cause resedimentation of already deposited particles, especially adjacent to shallow shelf areas. The motors for this process are either bottom current activity or transport in the nepheloid bottom layer, where fine grained particles are preferentially affected. In the case of nepheloid transport, already very low current velocities are sufficient for resedimentation of particles and subsequent transport from morphological highs to lows. That means that sediment accumulation everywhere in the ocean may be influenced.

If applying accumulation rates, for example of C_{org}, biogenic opal or biogenic barium, to calculate proxy fluxes, lateral redistribution of sediments may completely mask original features of vertical particle flux (rain rate). The lateral contributions may amount to more than 10 times the vertical particle flux, as demonstrated for Southern Ocean sediments for example by Francois et al. (1993) and Kumar (1994). A strong lateral contribution to sediment trap material in the Bransfield Strait and at the Maud Rise, which are close to topographic elevations, could be deduced from particle fluxes into sediment traps which were up to a factor of ten higher in the deep traps than in the shallow ones (Abelmann and Gersonde, 1991). A significant part of this laterally transported material had been

resedimented from the shallow water sediments, as documented by the high amounts of lithogenic components. Redistribution of biogenic silica from the Maud Rise was also reported by van Bennekom et al. (1988).

In order to achieve accumulation rates corrected for lateral sediment redistribution, the measured flux of $^{230}Th_{ex}$ (Fa) within an independently dated sediment section is compared to the flux expected from the production in the overlying water column (Fp). Assuming that lateral transport of ^{230}Th along isopycnals is negligible, Fa/Fp ratios < 1 indicate a lateral export of particles loaded with $^{230}Th_{ex}$ (winnowing) and Fa/Fp ratios > 1 indicate an import (focusing) (Cochran and Osmond, 1976; Bacon, 1984; Suman and Bacon, 1989; Francois et al. 1990; 1993; Scholten et al., 1994; Frank et al., in press). Thus, average vertical sediment rain rates $F_{vertical}$ for a certain sediment section may be calculated by dividing the measured sediment accumulation rate F by the Fa/Fp ratio:

$$F_{vertical} = \frac{F}{Fa/Fp} \tag{10}$$

Further assuming that the flux of ^{230}Th and the Fa/Fp ratio were constant during the investigated section in the sediment (Francois et al., 1993), the vertical rain rate Fi of any particulate substance i may be calculated by

$$Fi = \frac{p \cdot z \cdot fi}{C_{(^{230}Th^0_{ex})}} \tag{11}$$

with

p = production of ^{230}Th in the water column
z = water depth
fi = weight fraction or concentration of i in the sediment
$C_{(^{230}Th^0_{ex})}$ = initial decay corrected $^{230}Th_{ex}$ concentration

This approach is limited by some uncertainties: The dissolution of labile biogenic phases in the sediments may alter the ratio between fi and $C_{(^{230}Th^0_{ex})}$ (Yang et al., 1990), which means that the rain rates presented are referred to as "preserved fluxes". Another uncertainty may arise from a grain size fractionation between bigger particles of biogenic origin like radiolarians and fine grained particles like aluminosilicates, especially if transport in the nepheloid layer is responsible for sediment redistribution. The bigger particles may not be affected as strongly as the fine grained fraction. However, if strong bottom currents account for lateral particle transport, this effect of fractionation should be small (Frank et al., in press).

Long range transport of ^{230}Th along isopycnals may be considered negligible, so that regionally the deposition of ^{230}Th should match its production in the water column. This is probably valid for most of the ocean areas. However, there are some exceptions to the rule. Under ideal conditions of a strong upwelling and high mass flux, as given for example at the upwelling areas off West Africa or South America, a lateral supply of ^{230}Th along isopycnals may lead to an increased flux of ^{230}Th to the sediments (Mangini

and Diester-Haass, 1983). From sediment trap data Francois et al. (1990) deduced that this contribution may amount to maximum 50 % excess of the production in the Panama Basin, corresponding to a high particle flux of about 10 $g/cm^2 \cdot kyr$. At particle fluxes of 5 $g/cm^2 \cdot kyr$ or below no excess of the production was observed.

Such a process may also be important in the Atlantic sector of the Southern Ocean, where upwelling of deep and ^{230}Th-enriched water masses, as well as accumulation of ^{230}Th in the Weddell Sea, which is charcterized by extremely low particle flux rates (Fischer et al., 1988), cause enhanced concentrations of ^{230}Th in the water column (Rutgers van der Loeff and Berger, 1993). When these water masses are supplied to the high biogenic particle flux areas south of the Polar Front (PF) regional ^{230}Th scavenging and accumulation may excceed local production. However, the maximum lateral contribution should also be about 50 % in excess over production. This was measured for example in sediment traps from the high particle flux area in the Bransfield Strait and the King George Basin, where a large contribution by laterally transported material, besides from the $^{230}Th_{ex}$ flux, could also be deduced from the ^{210}Pb content of the trap material (Rutgers van der Loeff and Berger, 1991).

2 Core Material

Five gravity cores and the corresponding multicores which deliver undisturbed surface sediments forming a transect over the ACC from 56°S to 43°S were analyzed in this study (Tab. 2, Fig. 8). All cores and multicores were recovered during German research vessel RV Polarstern Cruise ANT VIII-3 (Gersonde and Hempel, 1990), except the northernmost core PS2082-1 and the multicore PS2082-3, which were recovered during RV Polarstern Cruise ANT IX-4 (Bathmann et al., 1992).

In choosing the cores, it was important that all frontal zones of the ACC were covered and, additionally, that a good sedimentological, micropaleontological and stratigraphical data base produced at the SFB 261 was available to calibrate the results of this study, and to improve further the results achieved within the SFB 261.

Name,	Instrument,	Location,	Water Depth, m	Total Recovery, cm	Sampled Core Length, cm
PS1772-8	GC	55°27.5'S, 1°09.8'E	4135	1329	640
PS1772-6	MUC	55°27.5'S, 1°10.0'E	4136	24.5	24.5
PS1768-8	GC	52°35.6'S, 4°28.5'E	3270	896	896
PS1768-1	MUC	52°35.5'S, 4°27.6'E	3298	34	34
PS1756-5	GC	48°43.9'S, 6°42.8'E	3787	862	862
PS1756-6	MUC	48°53.7'S, 6°43.7'E	3803	27	27
PS1754-1	GC	46°46.2'S, 7°36.7'E	2471	356	200
PS1754-2	MUC	46°46.0'S, 7°36.1'E	2476	25	25
PS2082-1	GC	43°13.2'S, 11°44.3'E	4610	1391	1091
PS2082-3	MUC	43°13.1'S, 11°45.5'E	4661	26	26

Table 2: Locations of the gravity cores (GC) and multicores (MUC) from the transect over the ACC

The gravity cores were sampled continuously and then split with a resolution between 2 and 25 cm per sample depending on macroscopical changes in lithology and previously determined stratigraphies. The measurement of each sample thus represents the average value for the corresponding core section. The age resolution ranges from about 100 years to about 10000 years per sample. For the multicore measurements between 8 and 10 of the already freeze fried 1 cm sections were mixed to carry out average measurements. The only exception is multicore PS1754-2, where six 1 cm sections were analyzed. In Fig. 9 the lithologies of the cores, as described in the cruise reports, are displayed (Gersonde and Hempel, 1990; Bathmann et al., 1992).

2.1 Description of the Cores

The transect starts at 56°S in the Antarctic Zone with gravity core PS1772-8 and multicore PS1772-6, which were recovered at a position roughly corresponding to the present day

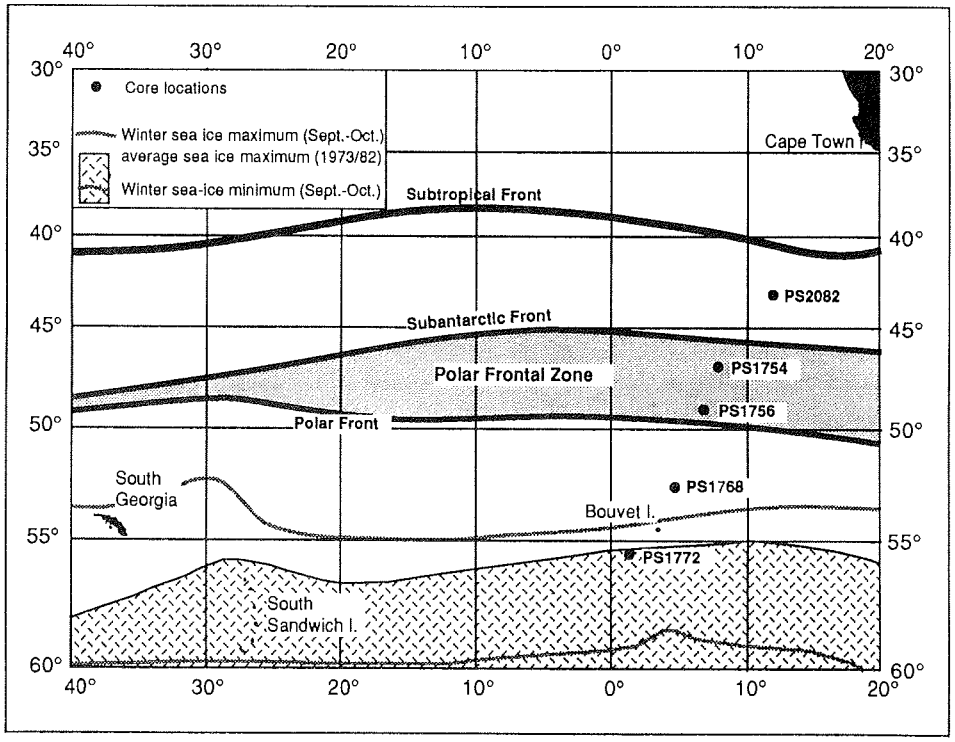

Figure 8: Locations of the five sediment cores forming the transect over the eastern Atlantic sector of the ACC. The present day position of the fronts is taken from Peterson and Stramma (1991) and the data of the sea ice distribution are from the Sea Ice Climatic Atlas (1985).

average sea ice maximum (Sea Ice Climatic Atlas, 1985). The location of the cores is on the southern slope of the SW Indian Ridge. The gravity core mainly consists of diatomaceous mud with two layers of lightly coloured diatomaceous ooze (150-360 cm and 600-675cm). Only the upper 640 cm of the core are included in this study due to the expected limitation of the $^{230}Th_{ex}$ measurements.

About 2° north of the present day average sea ice maximum, gravity core PS1768-8 and multicore PS1768-1 were recovered north of Bouvet Island in the permanently sea ice free Antarctic Zone (Fig. 8). This core also consists of the typical sedimentary components of the opal belt, which are alternating layers of diatomaceous muds and diatomaceous oozes (0-138 cm, 595-625 cm, 640-695 cm and 730-830 cm), respectively.

From the Polar Frontal Zone two sediment cores were analyzed. Gravity core PS1756-5 and multicore PS1756-6 were recovered from a location about 1° north of the present day position of the Polar Front, and south of Meteor Rise. The core shows a monotonous record of diatomaceous mud with only one layer of diatomaceous ooze (673-760 cm). The top of the piston core (0-12 cm) and the multicore consist of foraminiferal ooze and

siliceous foraminiferal ooze.

The second location from the Polar Frontal Zone is represented by gravity core PS1754-1 and multicore PS1754-2 from a location about 1° south of the Subantarctic Front. These cores were recovered at the bottom of a morphological depression at the foot of a submarine mountain on Meteor Rise, close to ODP site 704. The mountain reaches a water depth of about 1000 m. The sediment consists of a siliceous foraminiferal ooze with the upper 20 cm being a foraminferal ooze.

The transect is finished at 43°S in the Agulhas Basin with gravity core PS2082-1 and multicore PS2082-3 from a position north of the Subantarctic Front in the Subantarctic Zone. The core site is located at the bottom of a small morphological depression. Several layers of calcareous muds consisting of calcareous nannoplankton appear in the diatomaceous mud. The top of the core (upper 50 cm) is enriched in nannofossils and from 6-19 cm a foraminiferal ooze was deposited. The section from 33-39 cm is coloured in dark brown, caused by an enrichment in Mn and Fe. Only the upper 1091 cm of the entire recovery of 1391 cm were analyzed due to the expected limitation of the $^{230}Th_{ex}$ measurements.

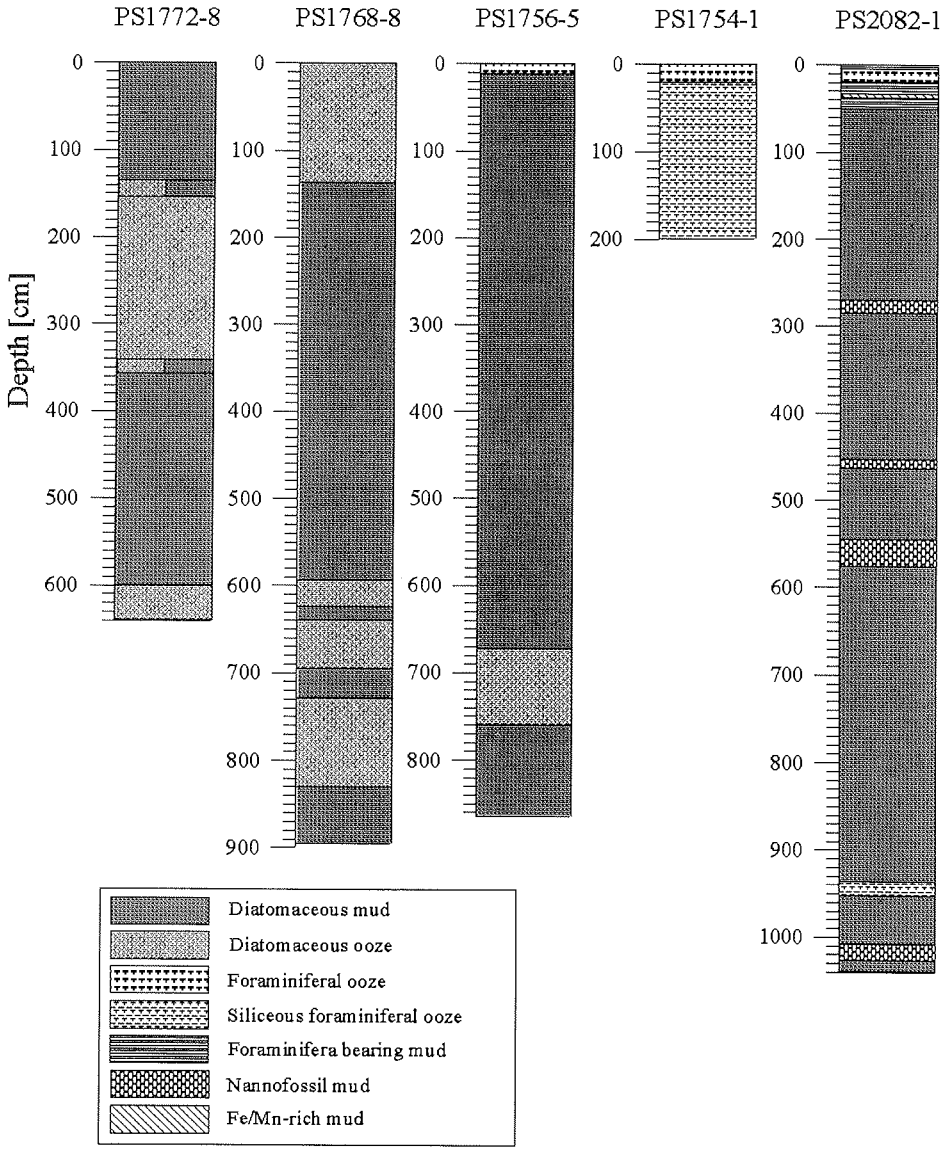

Figure 9: Lithological description of the gravity cores taken from the cruise reports (Gersonde and Hempel, 1990; Bathmann et al., 1992).

3 Results

3.1 Dating and Stratigraphy

In Fig. 10 the results of the $^{230}Th_{ex}$ dating are shown. The drastic decreases of the $^{230}Th_{ex}$ concentrations from 360 cm to 150 cm core depth in core PS1772-8 and from 20 to 160 cm and 780 to 830 cm core depth in core PS1768-8 are omitted for the exponential fitting because the sedimentation rates in these sections were significantly different. From the exponential fits average sedimentation rates for the whole cores may be calculated.

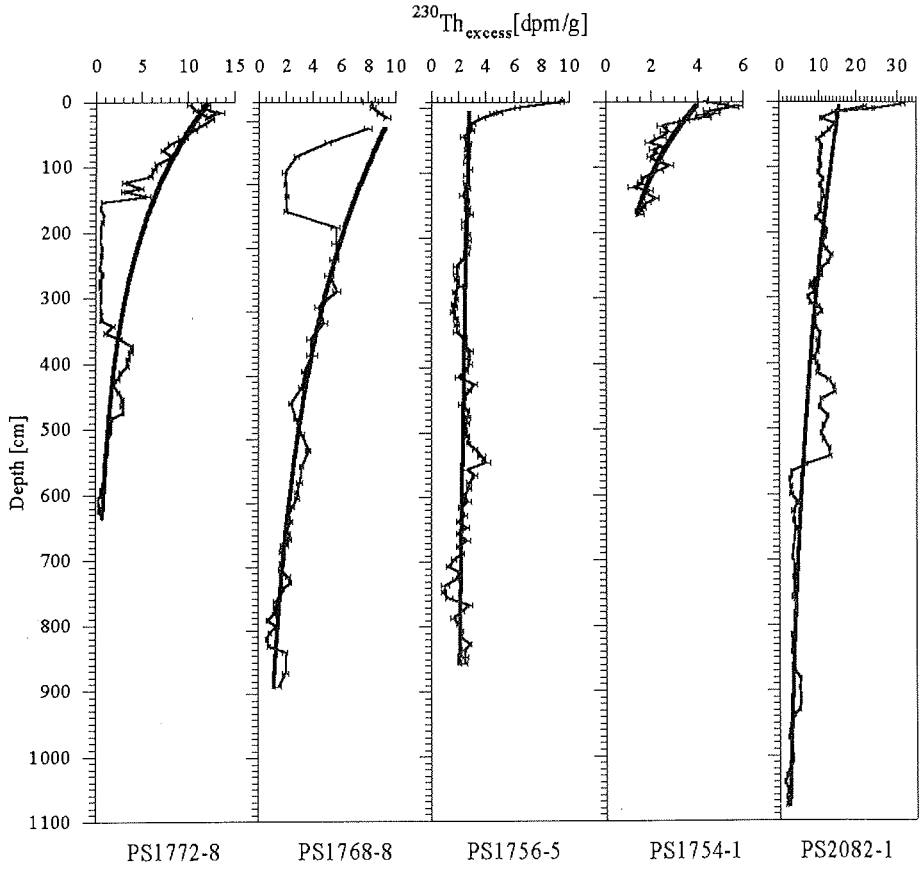

Figure 10: Results of the $^{230}Th_{ex}$ dating of the five cores: The uncorrected $^{230}Th_{ex}$ concentrations are plotted versus depth. The bold black curves are the exponential fits to the downcore decreasing $^{230}Th_{ex}$ concentrations. The error bars represent the statistical errors of one standard deviation from the mean.

The higher the differences between the fit and the $^{230}Th_{ex}$ profile are, the higher is the

uncertainty. It turned out that these rough estimates corroborate previous stratigraphic work for all cores (Tab. 3).

Core	Previous work, cm/kyr	$^{230}Th_{ex}$ dating, cm/kyr
PS1772-8	1.9	2.2
PS1768-8	6.4	4.4
PS1756-5	6.1	-
PS1754-1	1.2	1.4
PS2082-1	4.3	4.8

Table 3: Comparison of previously fixed average sedimentation rates and the $^{230}Th_{ex}$ datings.

The only exception is PS1756-5, where no significant downcore decrease of the $^{230}Th_{ex}$ concentrations can be determined. This may have two causes: Either the sedimentation rates were extremely high so that no significant decay of $^{230}Th_{ex}$ has occurred or the sedimentation rates were constantly increasing with time. This is discussed in more detail in chapter 3.2.3.

Baseline stratigraphic age interpretation was focused on the determination of isotopic stage and substage boundaries using integrated lithostratigraphic, isotope stratigraphic and and siliceous microfossil biofluctuation stratigraphies (Mackensen et al., 1994; Zielinski, 1993; Niebler, 1995; Fischer et al., submitted; and unpublished results of A. Abelmann, G. Bohrmann, R. Gersonde, H.-W. Hubberten, A. Mackensen and G. Kuhn). The absolute age assignment of isotope stage boundaries back to 300 kyr B.P. is after Martinson et al. (1987). The topmost section of core PS1768-8 was dated by AMS-^{14}C at three core depths (Tab. 4). The raw ^{14}C ages were reservoir corrected according to Bard (1988) and recalibrated versus U/Th ages after Bard et al. (1990). The stratigraphic results are also displayed on an age/depth plot of all cores (Fig. 11). More detailed results on age determinations and paleoenvironmental changes during the past 20,000 years in the Southern Ocean are reported by Gersonde et al. (in prep.).

3.2 Individual Core Results

As described in chapter 1.8, a high resolution record of the sedimentation rates and thus also of the ages within certain climatic stages can be achieved by $^{230}Th_{ex}$ modelling (Fig. 17). Additionally, the depth of climatic transitions which can not be fixed by other methods may be evaluated.

Rutgers van der Loeff and Berger (1993) did not find the expected depletion of ^{230}Th in the water column of the ACC. They concluded from the calculation of a mixing/advection model that deep and ^{230}Th enriched water masses from the north flow upwelling into the Weddell Sea, where they get additionally enriched in ^{230}Th due to very low particle fluxes and therefore low scavenging intensity (Fischer et al., 1988). The average residence time

Age, kyr	Depth, cm				
	PS1772-8	*PS1768-8*	*PS1756-5*	*PS1754-1*	*PS2082-1*
10.06	-	54(^{14}C)	-	-	-
11.26	-	78(^{14}C)	-	-	-
12	17	97	12	22	33
14.16	-	142(^{14}C)	-	-	
24	55	244	240	54	245
44	-	-	-	-	300
59	80	469	440	78	370
74	100	585	530	88	440
111	(136)	730	720	(140)	523
130	360	830	770	160	570
153	-	-	-	-	730
190	460	-	-	-	900
225	-	-	-	-	980
244	528	-	-	-	1040
300	588	-	-	-	-

Table 4: Age models of the cores. Depths in brackets indicate that these values were only fixed by $^{230}Th_{ex}$ constant flux modelling. Three ages of core PS1768-8 were determined by ^{14}C AMS measurements of organic matter, which were reservoir corrected and U/Th-calibrated (see text).

of ^{230}Th in the water column (20-40 years) is in about the same range as the residence time of CDW in the Weddell Sea Gyre, which amounts to about 30 years. In this low particle flux regime the ^{230}Th may then build up in the water column. For the $^{230}Th_{ex}$ constant flux modelling this means that the total sedimentation rates and accumulation rates calculated between certain independently fixed isotope stages, assuming a constantly increased lateral advection of ^{230}Th are still reliable (chapter 4.2). In the case of dating stage 5e in the three southern cores by $^{230}Th_{ex}$ constant flux modelling (chapter 3.2), the total sedimentation rates, the sediment accumulation rates and the core length corresponding to isotope stage 5e represent minimum estimates. Maximum estimates, however, are not higher than a factor of 1.5 above the minimum estimates, as deduced from the maximum lateral supply of ^{230}Th along isopycnals.

The measured concentrations of $^{230}Th_{ex}$, $^{231}Pa_{ex}$ and ^{10}Be are decay corrected to the time of deposition of the sediment, applying the final ages derived from the $^{230}Th_{ex}$ constant flux modelling (Fig. 11). In this chapter these initial decay corrected radionuclide concentrations are plotted versus core depth together with the authigenic ^{238}U concentrations and the Mn/Al ratio. The $^{231}Pa_{ex}$ concentrations represent three point running means. The dashed vertical lines on the figures mark the Mn/Al ratio of the standard granodiorite GSP-1 of 0.004 (Flanagan, 1968). The lightly shaded sections mark the interglacial isotope stages and the darkly shaded ones mark the stage 5e following Martinson

et al. (1987). The error bars represent the statistical errors of one standard deviation from the mean, except the authigenic ^{238}U, where the error bars mark an estimated range of the lithogenic $^{238}U/^{232}Th$ activity ratio between 0.5 and 1.

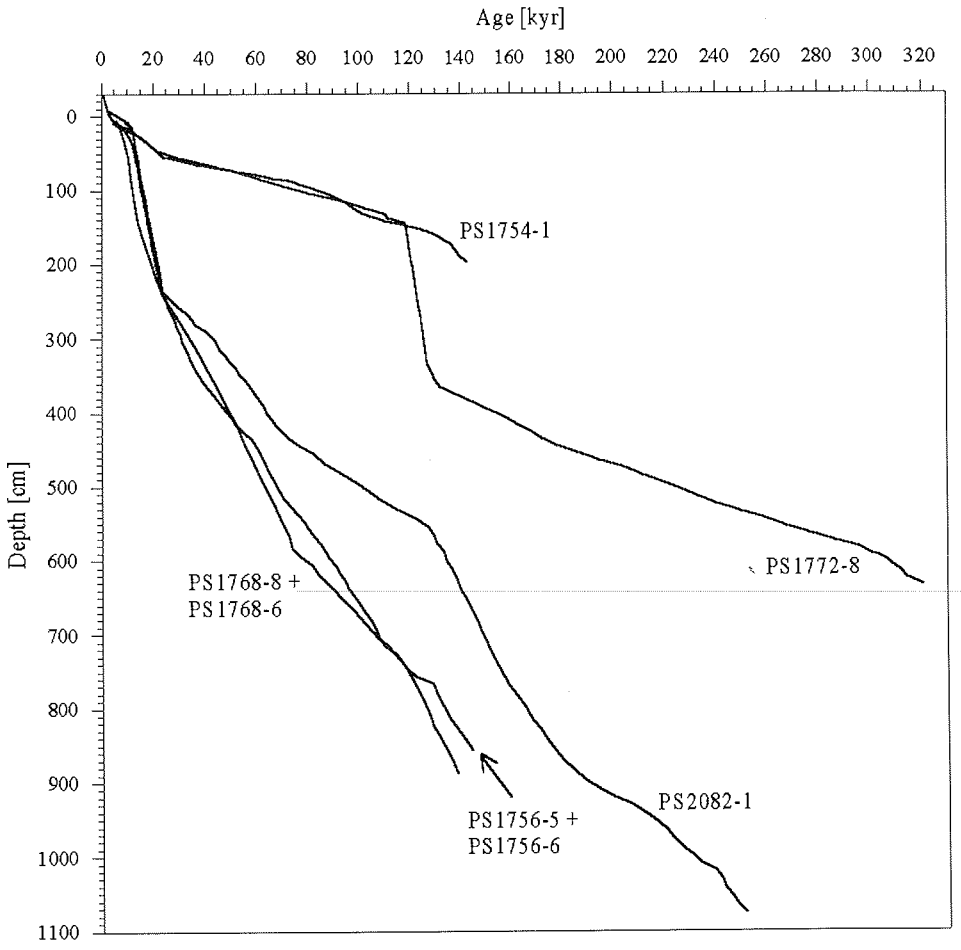

Figure 11: Age/depth plot for all cores of the transect.

3.2.1 Piston Core PS1772-8 and Multicore PS1772-6

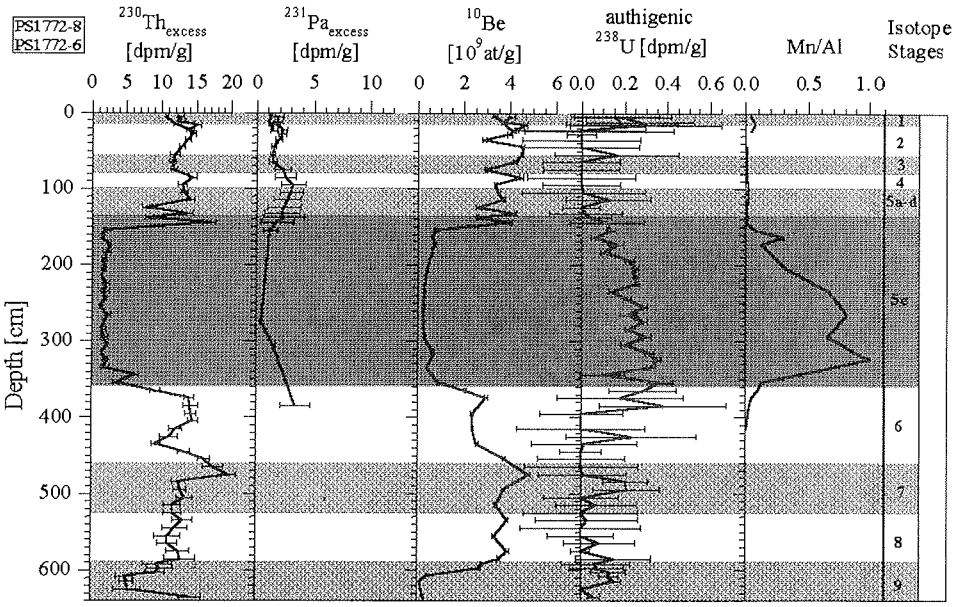

Figure 12: Profiles of the initial radionuclide and the authigenic ^{238}U concentrations and the Mn/Al ratio of cores PS1772-8 and PS1772-6 versus core depth.

In the area south of the APF, the deep water has been highly corrosive for carbonate which results in a severe dissolution of foraminifera. For the sediments of core PS1772-8 which therefore do not contain sufficient biogenic carbonate for oxygen isotope analysis, the stratigraphy is based on the interpretation that the diatomaceous ooze sections represent at least the beginning of the warm stages of the paleoclimate. Diatom biofluctuation stratigraphic results corroborate and complete this interpretation by fixing the 2/3 and 4/5 stage boundaries (Gersonde, unpub. results). These stage boundaries at are verified by the results of the $^{230}Th_{ex}$ dating (Fig. 10).

The decay corrected $^{230}Th_{ex}$ values decrease from an average of 13 dpm/g to about 2 dpm/g in the upper ooze section and to about 5 dpm/g in the lower ooze section. The last value at 640 cm shows an increase although it is still in the ooze section. These variations, which are interpreted as changes of the sedimentation rates by $^{230}Th_{ex}$ constant flux modelling, only show small variations between 1 and 2 cm/ky in the diatomaceous mud sections and increase to values of up to 32 cm/ky in the stage 5 ooze section and up to 3.5 cm/ky in the stage 9 ooze section.

It may be deduced from the record of the sedimentation rates that the diatomaceaous ooze section between 150 and 360 cm core depth was deposited in only about 8 kyr (during about the period from 127-119 kyr B.P., if 360 cm is the correct depth of the stage 6/5 transition at 130 kyr B.P.), thus representing just the beginning of interglacial substage 5e.

During the isotope stages 2-4 no significant sedimentological changes occurred. Isotope stage seven is not clearly seen in the record and the lower ooze section is attributed to isotope stage 9. As in the stage 5e ooze section, the upper boundary of this ooze at 600 cm core depth certainly does not correspond to the transition between stage 9 and 8, which can only be roughly evaluated in this case because the ooze section was not analyzed for $^{230}Th_{ex}$ completely. The approximate boundaries of the other isotope stages may be evaluated, taking into account the poor age resolution of the samples.

The $^{231}Pa_{ex}$ profile shows relative maxima in the core sections representing the stages 2 and 5a-d and a minimum in the stage 5e section. The ^{10}Be profile shows the same features as the $^{230}Th_{ex}$ profile decreasing from an average of $3 - 4 \cdot 10^9$ at/g to $0.5 \cdot 10^9$ at/g. The sediment contains only very small amounts of authigenic ^{238}U, which are mainly found in the ooze section and reach maximum values of 0.4 dpm/g. The Mn/Al ratios are mostly in the range of the assumed lithogenic background value of 0.004, with the exception of a very strong enrichment in the stage 5e ooze section where values up to 1 are reached. A small peak appears at the beginning of the Holocene section.

A comparison between the multicore and the piston core results shows no strong offsets suggesting that no significant loss of sediment of the topmost sediment sequence occurred while recovering PS1772-8.

3.2.2 Piston Core PS1768-8 and Multicore PS1768-1

For this core a dating by a $\delta^{18}O$ record of the planktonic foraminferal species *Neogloboquadrina pachyderma sin.* (Niebler, 1995) could be achieved, which is corroborated by the exponential decrease of the $^{230}Th_{ex}$ concentrations. Additionally, 3 AMS ^{14}C datings were performed to achieve a more detailed picture of the Holocene sedimentation history. After reservoir correction and calibration to the U/Th ages of Bard et al. (1990) the ^{14}C datings suggest that the changes of the opal increase at 168 cm core depth occurred at an age of about 16 kyr B.P. (Gersonde et al., in prep.). The diatomaceous ooze sections in the lower part of the core are attributed to the 3 warm substages of interglacial stage 5.

The initial $^{230}Th_{ex}$ concentrations show significant decreases from 5-10 dpm/g to about 2 dpm/g during the end of the last glacial and at the beginning of the Holocene and during the isotope substage 5e. Applying the $^{230}Th_{ex}$ constant flux model, a huge increase of the sedimentation rates from about 5-8 cm/kyr to up to 25 cm/kyr during the Holocene climate optimum is determined. This increased sedimentation rate does not have a comparably intense counterpart at the transition from stage 6 to stage 5e, where the maximum rates amount to 11 cm/kyr, although the lithology is equivalent. A slight decrease in sedimentation rate from 5-8 cm/kyr to 3-5 cm/kyr, rather than an increase is observed in the ooze sections representing the warm interglacial substages 5a and 5c.

As deduced from the $^{230}Th_{ex}$ constant flux model, the section between 140 cm and about 60 cm core depth was deposited in only 4 kyr (14-10 kyr B.P.), which is corroborated by the ^{14}C datings. There is a discrepancy between the end glacial and Holocene sedimentation rates, which increased by a factor of about 5, and $^{230}Th_{ex}$ concentrations

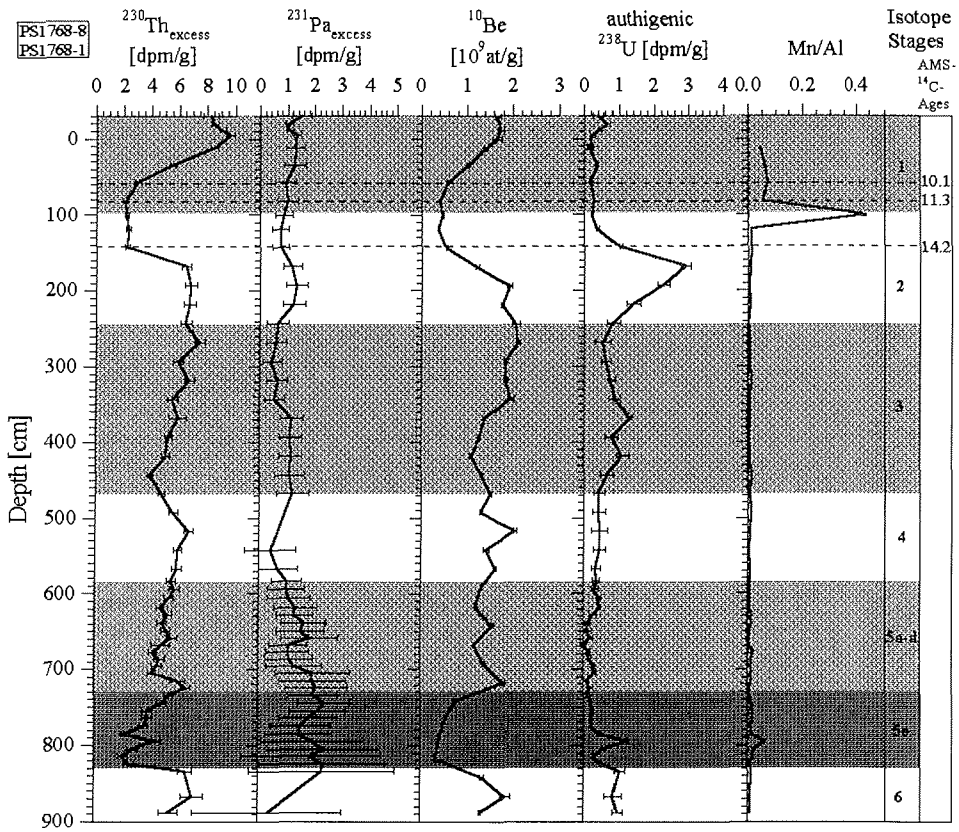

Figure 13: Profiles of the initial radionuclide and the authigenic ^{238}U concentrations and the Mn/Al ratio versus core depth of cores PS1768-8 and PS1768-1. The dotted horizontal lines mark the depths of the ^{14}C AMS datings.

only diluted by a factor of 2 to 3. This will be discussed in more detail in chapter 4.1. The diatomaceous ooze sections representing the warm substages of interglacial stage 5 were not deposited as rapidly. The model shows that the core section from 755 to 830 cm was deposited during about 10 kyr (130-120 kyr B.P.).

The $^{231}Pa_{ex}$ concentrations are relatively constant at about 1 dpm/g and rise to about 1.5 dpm/g in the stage 5e section. Again the pattern of the ^{10}Be profile is similar to the $^{230}Th_{ex}$ profile and varies from about $2 \cdot 10^9$ at/g to $0.4 \cdot 10^9$ at/g. The values of authigenic ^{238}U vary between 0 and 1 dpm/g and show a marked peak of up to 3 dpm/g during the last glacial maximum. The Mn/Al ratios are in the range of 0.004 throughout the core, with the exception of a small peak at the beginning of stage 5e and a marked peak of 0.45 at the beginning of the Holocene.

A significant loss of sediment representing about 3 kyr at the core top occurred while recovering PS1768-8 (M. Rutgers van der Loeff, pers. com.). The values of PS1768-1

could not be adjusted to the top of PS1768 implying that the loss amounted to at least the length of the multicore. Therefore the multicore values are interpreted as representing the upper 30 cm of PS1768-8.

3.2.3 Piston Core PS1756-5 and Multicore PS1756-6

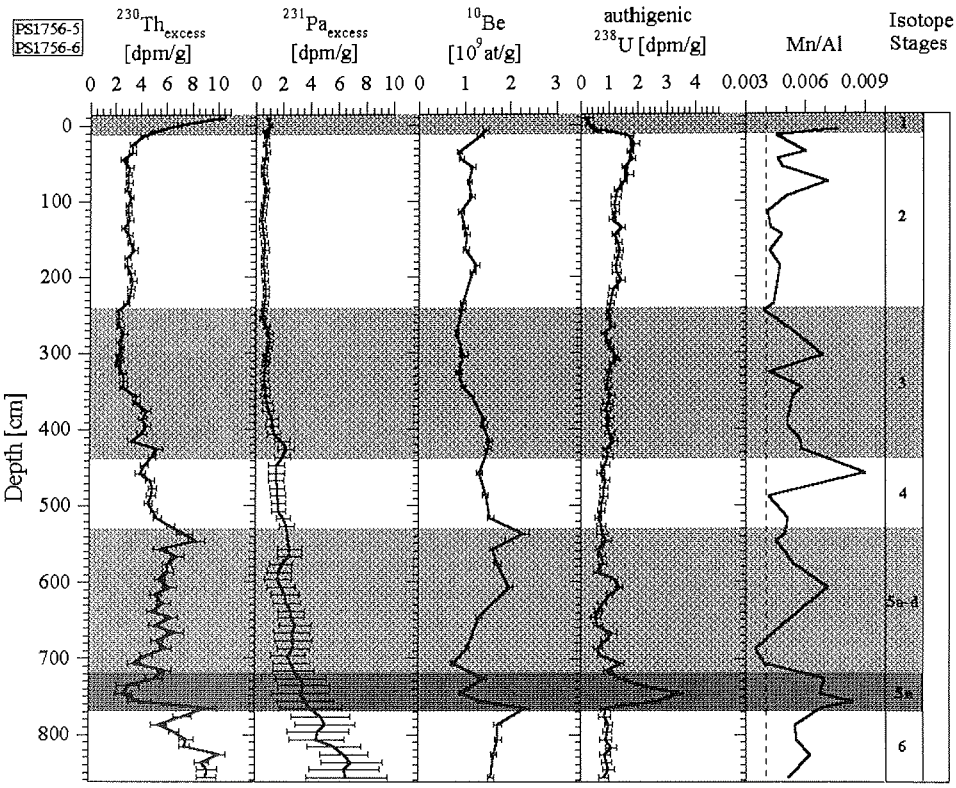

Figure 14: Profiles of the initial radionuclide and the authigenic ^{238}U concentrations and the Mn/Al ratio versus core depth of cores PS1756-5 and PS1756-6.

Due to the lack of lithological changes and biogenic carbonate the establishment of a stratigraphy was very difficult in this core. The stratigraphy is mainly based on a $\delta^{13}C$ profile measured at the organic matter of the sediment (Fischer et al., in prep.) and diatom biofluctuation stratigraphy (Gersonde, unpub. res.). It was planned to achieve further information by the expected decrease of the $^{230}Th_{ex}$ concentrations which, unfortunately, was not possible due to the insignificant decrease below 10 cm core depth (Fig. 10). With all results, the diatomaceous ooze layer is interpreted to be part of interglacial substage 5e.

The $^{230}Th_{ex}$ profile shows highest values of about 10 dpm/g during the Holocene and in the sections representing stages 5 and 6. Decreased concentrations around 3 dpm/g

occur during stages 2, 3 and 5e. The section representing isotope stage 2 is thus marked by increased sedimentation rates between 14 and 24 cm/kyr, compared to 1-7 cm/kyr in the stage 1 and 3 sections. The rates during stage 4 show an increase to values of 7-12 cm/kyr and there is another increase to values of up to 11 cm/kyr in the stage 5e diatomaceous ooze section.

Keeping in mind the doubts concerning the stratigraphy, the $^{230}Th_{ex}$ constant flux model showed that there was a continuous decrease of the sedimentation rates at the beginning of the Holocene from about 14 cm/kyr to about 1 cm/kyr within a period of about 3.5 kyr (12-8.5 kyr B.P.). The section corresponding to stage 5e could be fixed between 680 and 790 cm where the sedimentation rates are increased by a factor of about 2 compared to the sections above and below. No significant changes of the sedimentation rates occurred during the other isotope stages.

The $^{231}Pa_{ex}$ shows a continuous downcore increase from about 1 dpm/g at the core top to about 7 dpm/g at the bottom, which could be the result of a too high estimate of the age in the lower sections of the core. The ^{10}Be profile shows only small variations with a slight increase from about 1 to $2 \cdot 10^9$ at/g during stage 5 and a decrease during stage 5e, similar to the $^{230}Th_{ex}$ profile. The sediment contains authigenic ^{238}U, which decreases continuously downcore from about 2 dpm/g at 10 cm core depth to about 1 dpm/g at the bottom. Very low concentrations of about 0.3 dpm/g were measured in the Holocene section of the core and a peak of more than 3 dpm/g was measured at the beginning of stage 5e. The Mn/Al ratio is homogenously about equal to the lithogenic background value.

When comparing the multicore results to the piston core, a loss at the core top of PS1756-5 of about 15 cm was evaluated and adjusted by the multicore results.

3.2.4 Piston Core PS1754-1 and Multicore PS1754-2

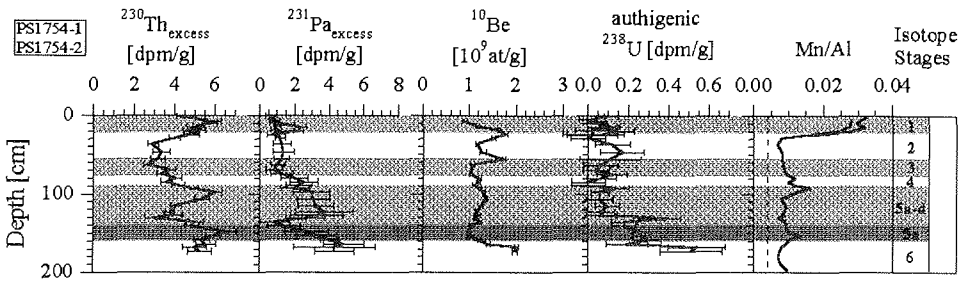

Figure 15: Profiles of the initial radionuclide and the authigenic ^{238}U concentrations and the Mn/Al ratio versus core depth of cores PS1754-1 and PS1754-2.

For this core $\delta^{18}O$ stratigraphies of the foraminiferal species *Neogloboquadrina pachyderma sin., Globigerina bulloides* and *Globigerina inflata* could be established (Niebler, 1995). Due to severe disturbances in the lower part of the core (pers. com. R. Gersonde,

H.-S. Niebler) only the section above 200 cm core depth was included in the interpretations. The possibility of similar disturbances in the upper part of the core cannot be ruled out, which renders the conclusions concerning this core more uncertain than the other ones. The core material is relatively coarse grained, which may indicate bottom current activities.

The initial $^{230}Th_{ex}$ concentrations vary between 3 and 6 dpm/g and show peaks during the Holocene, at the beginning of stage 5e and at the end of stage 5. The generally low sedimentation rates show only slight variations with a tendency towards higher values of about 2 to 3.5 cm/kyr in the stage 2 and 6 sections compared to 0.5 to 2 cm/kyr in the stages 1 and 3 to 5. The $^{230}Th_{ex}$ constant flux model showed that the decrease of the sedimentation rates at the end of the glacial stages preceded the glacial/interglacial isotope stage boundary by about 7 kyr at the transition from stage 6 to 5 and by about 4 kyr at the transition from stage 2 to 1. There is also a small increase of the sedimentation rates in the middle of stage 5.

The $^{231}Pa_{ex}$ profile shows a steady downcore increase from about 1 dpm/g to about 4 dpm/g with a marked minimum at the end of interglacial substage 5e. The ^{10}Be concentrations vary between 1 and $2.5 \cdot 10^9$ at/g with maxima during glacial stages 2 and 6. Authigenic ^{238}U concentrations are negligible until 170 cm core depth and then increase drastically to about 2 dpm/g which probably must be seen in the context of the above mentioned disturbances. The Mn/Al ratio is slightly higher than 0.004 throughout the core. It is significantly increased to 0.03 during the Holocene and shows two small peaks at the beginning and at the end of stage 5. With the exception of the $^{231}Pa_{ex}$ concentrations, the records of multicore and piston core do not show significant deviations, which implies that no loss occurred during the recovery of core PS1754-1.

3.2.5 Piston Core PS2082-1 and Multicore PS2082-3

The northernmost cores of the investigated transect were recovered in the Agulhas Basin in the Subantarctic Zone of the ACC, where the CCD is today located at a water depth below 5000 m and the foraminiferal lysocline is located at about 4000 m water depth. Nearly continuous $\delta^{18}O$ stratigraphies of the benthic foraminiferal species *Fontbotia wuellerstorfi* and *Cibcidoides spp.* and the planktonic species *Globigerina bulloides* and *Neogloboquadrina pachyderma sin.* were established (Mackensen et al., 1994). Additionally, a *C. davisiana* biofluctuation stratigraphy (U. Brathauer, unpub. results) corroborates the $\delta^{18}O$ stratigraphic results where there were uncertainties due to the lack of biogenic carbonate (e.g. the stage 2/3 boundary).

The profile of the initial $^{230}Th_{ex}$ concentration shows relatively high values between 10 and 40 dpm/g with maxima in the interglacial core sections. Correspondingly the sedimentation rates are increased to up to 21 cm/kyr in the glacial stage 2 and to up to 9 cm/kyr in the glacial stage 6, while the interglacial values range from 2 to 5 cm/kyr. The $^{230}Th_{ex}$ constant flux model also shows a continuous increase of the sedimentation rates within the stage 6 from about 1 cm/kyr at the beginning to about 4 cm/kyr at the transition to isotope stage 5.

The $^{231}Pa_{ex}$ profile shows only small variations but increases from values of about 2 dpm/g to about 5 dpm/g in the section below 450 cm which corresponds to the stages 5 and 6. The ^{10}Be values vary between 4 and $5 \cdot 10^9$ at/g with two distinct minima of about $2 \cdot 10^9$ at/g in the Holocene core section and at the end of glacial stage 6. Authigenic ^{238}U concentrations are only found in the glacial core sections with maxima of 2 and 3 dpm/g at the end of the glacial cores sections 2 and 6 respectively. Mn/Al ratios significantly above 0.004 are determined at the transitions from the isotope stages 6 to 5 and 2 to 1. Minor peaks are observed during the interglacial stages 3, 5 and 7.

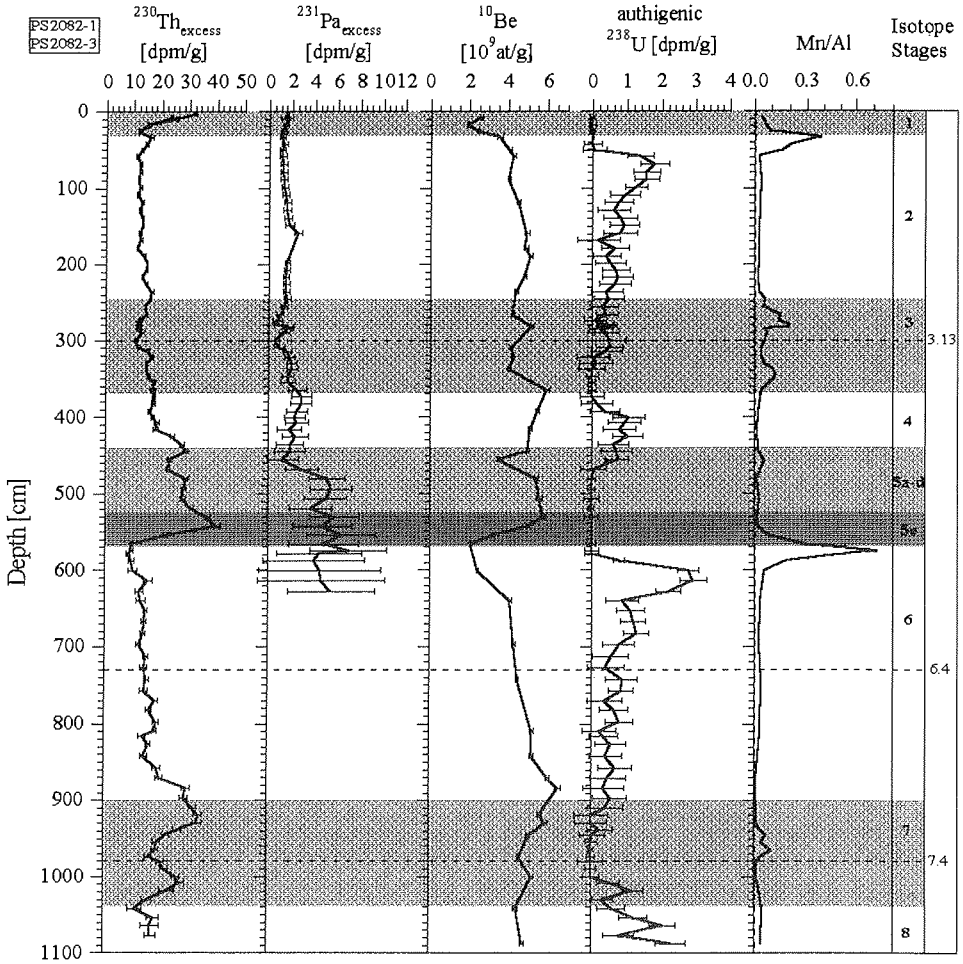

Figure 16: Profiles of the initial radionuclide and the authigenic ^{238}U concentrations and the Mn/Al ratio versus core depth of cores PS2082-1 and PS2082-3. The dashed horizontal lines mark isotope events which could unambiguously be identified from the $\delta^{18}O$ stratigraphy (Mackensen et al., 1994).

4 Discussion

4.1 Sediment Redistribution Versus Vertical Particle Flux

As stated in chapter 1, it is important to distinguish between laterally supplied material and vertical particle flux, which is particularly important in the Southern Ocean with its strong bottom currents. Francois et al. (1993) demonstrated at a core from the Antarctic Zone of the Indian sector of the Southern Ocean that the interglacial sections 1 and 3 were strongly affected by lateral supply of biogenic material. Up to 12 times the amount derived from vertical particle rain was added laterally to the sediments. Kumar (1994) obtained results from the Antarctic Zone of the Atlantic sector of the ACC, where some sediment sections received up to 17 times more material laterally than from the water column above.

In Fig. 17 the sediment accumulation rates (sedimentation rate derived from $^{230}Th_{ex}$ constant flux modelling multiplied by dry bulk density) and the vertical particle rain rates (eq. 11) are plotted versus age for the five cores.

The sediments of core PS1772-8 were not significantly affected by sediment redistribution. The vertical rain rates are only slightly higher than the sediment accumulation rates suggesting a weak winnowing with the exception of isotope stage 2 where a weak focusing is observed. The contrast between the winnowing of 70 % during stage 3 and the focusing of about 70 % during stage 2 may represent an artifact caused by a small mistake of the position of the transition from stage 3 to stage 2, which is possible due to the relatively low sedimentation rates in these sections. In the stage 9 section, where dating is questionable, the vertical rain rates are about twice as high as the accumulation rates.

Further north, however, in core PS1768-8 the deglacial and Holocene sediments received about 4.5 to 5 times more particles by focusing than by vertical supply, which is about the same range as observed in the Antarctic Zone by Francois et al. (1993) and Kumar (1994). During stage 2 the factor even rises to about 6.5. Focusing intensity then decreases downcore and in the stage 5e section it amounts to about a factor of 2. The correction for focusing yields equally high rain rates for the sections representing stage 5e and the last glacial/Holocene transition (about 14-9 kyr B.P.).

In the stage 3 and 5e sections of core PS1756-5 only about 50 % of the vertical rain rate reached the sediments which means that an export of particles occurred, probably due to increased bottom current velocities. During stage 2 and 6 a weak sediment focusing (factor 1.4) is observed while during the other periods, no significant sediment redistribution occurred at this location.

Almost throughout the core sections representing stages 3 to 6, the location of core PS1754 was a region of export of sediment particles. Only during the stages 1 and 2 no export occurred.

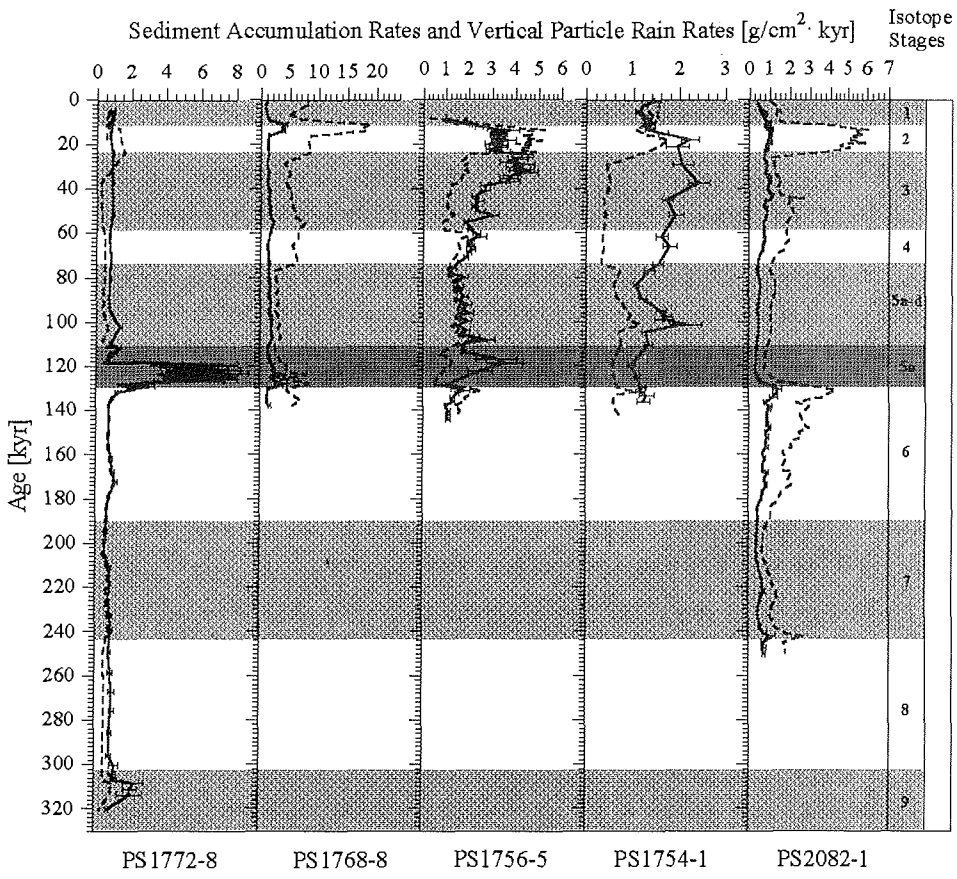

Figure 17: Sediment accumulation rates (dashed line) and vertical particle rain rates which were corrected for sediment redistribution effects (solid line). Due to the calculation of the accumulation rates and vertical rain rates by the $^{230}Th_{ex}$ constant flux model, the error bars represent the statistical errors of one standard deviation from the mean of the $^{230}Th_{ex}$ measurements. Note the different scales of the profiles.

The sediments of core PS2082-1 were affected by focusing almost throughout the investigated period of time with strongest lateral supply of about the 6 fold vertical rain rate during glacial stage 2 and up to the 3 fold vertical rain rate during glacial stage 6, where an increase in focusing intensity during the stage may be deduced.

Both, the sediment accumulation rates and the vertical particle rain rates have to be taken into account for the calculation of paleoenvironmental proxy accumulation rates like biogenic barium or C_{org}. The vertical rain rates yield a reconstruction of the particle supply from the surface water and the sediment accumulation rates serve as a measure for preservation rates. If this lateral component of sediment supply is not addressed, drastic misinterpretations may be the result.

4.2 Vertical Sediment Rain Rates

Low vertical sediment rain rates around 1 $g/cm^2 \cdot kyr$ in the southern core PS1772-8 are caused by the sea ice cover preventing the production of biogenic particles (Fig. 17). Seasonally sea ice free conditions only occurred during the beginning of isotope substage 5e and isotope stage 9. At the beginning of isotope stage 5e, up to 8 $g/cm^2 \cdot kyr$ of mainly biogenic particles were deposited, which represents the by far highest value reached in the sediment cores of the transect. During the climate optimum at the beginning of stage 9, as far as it was analyzed, about 2 $g/cm^2 \cdot kyr$ were deposited. The conditions during the climate optima at the beginning of stage 7 and the Holocene obviously were not sufficient to cause a significantly less dense sea ice cover at the location of core PS1772-8 to allow a stronger increase in biogenic particle production.

In core PS1768-8 which is located north of the present day winter sea ice maximum, sea ice free conditions occurred during the Holocene and during isotope stage 5, as deduced from the abundance distribution of the sea ice indicator diatom species *N. curta* and *N. cylindrus* (Gersonde, unpub. res.). These periods are represented by rain rates of up to 4 $g/cm^2 \cdot kyr$, while values between 1 and 2 $g/cm^2 \cdot kyr$ in the other core sections indicate that the sea ice cover was not as dense during the cold periods as at the location of core PS1772-8. The differences between the other warm and cold substages of interglacial stage 5 are not resolved in the vertical rain rate record.

At the location of core PS1756-5 from the Polar Frontal Zone, which was not covered by sea ice during the last 150 kyr, maxima of the rain rates of 3-4 $g/cm^2 \cdot kyr$ are observed in the glacial stages 2 and 3, while the interglacial stages 1 and 5 are represented by values between 1 and 2 $g/cm^2 \cdot kyr$. No increased values are observed at the end of the stage 6 section. During stage 5e the rates were increased to values of up to 3.5 $g/cm^2 \cdot kyr$.

The second core from the Polar Frontal Zone, PS1754-1, which was influenced by winnowing processes, shows a pattern of the rain rates similar to PS1756-1. However, the amounts of deposited sediment are much lower. The interglacial stages 2 and 3 and also 6 are represented by maxima of up to 2.5 $g/cm^2 \cdot kyr$, while the interglacial values of stage 1 and 5 amount to between 1 and 1.5 $g/cm^2 \cdot kyr$ with a minimum below 1 $g/cm^2 \cdot kyr$ during interglacial stage 5e. In the middle of stage 5 a maximum of about 2 $g/cm^2 \cdot kyr$ is observed.

In the Subantarctic Zone, as in the PFZ, higher sediment rain rates during the glacial stages 2, 3 and especially the end of stage 6 are found. There is a trend of slow increase of the vertical rain rates during glacials followed by a sharp decline at the transitions from stage 6 to 5 and 2 to 1. The amounts of the rain rates, however, are as low as 1 $g/cm^2 \cdot kyr$, which is comparable to the values observed during sea ice cover in the Antarctic Zone. In the interglacial core sections the rates decrease to values of 0.35 $g/cm^2 \cdot kyr$.

With the knowledge of these discrepancies between sediment accumulation rates and vertical rain rates, the paleoproductivity reconstructions of Mackensen at al. (1994) for this core have to be reinterpreted. The basic pattern of higher glacial productivity remains the same after the focusing correction. The amount of productivity, however, is lower by

about a factor of 5 during glacial stage 2 and by about a factor 3 during glacial stage 6 after the correction.

4.3 Rain Rates of Biogenic Material

4.3.1 Biogenic Opal

The pattern of the biogenic opal rain rates (Fig. 18) is very similar to the total vertical rain rate pattern, which is no surprise because the sediments of the three southern cores consist of up to 95 % of biogenic opal. The maximum opal rain rate amounts to 6 g/cm^2 · kyr

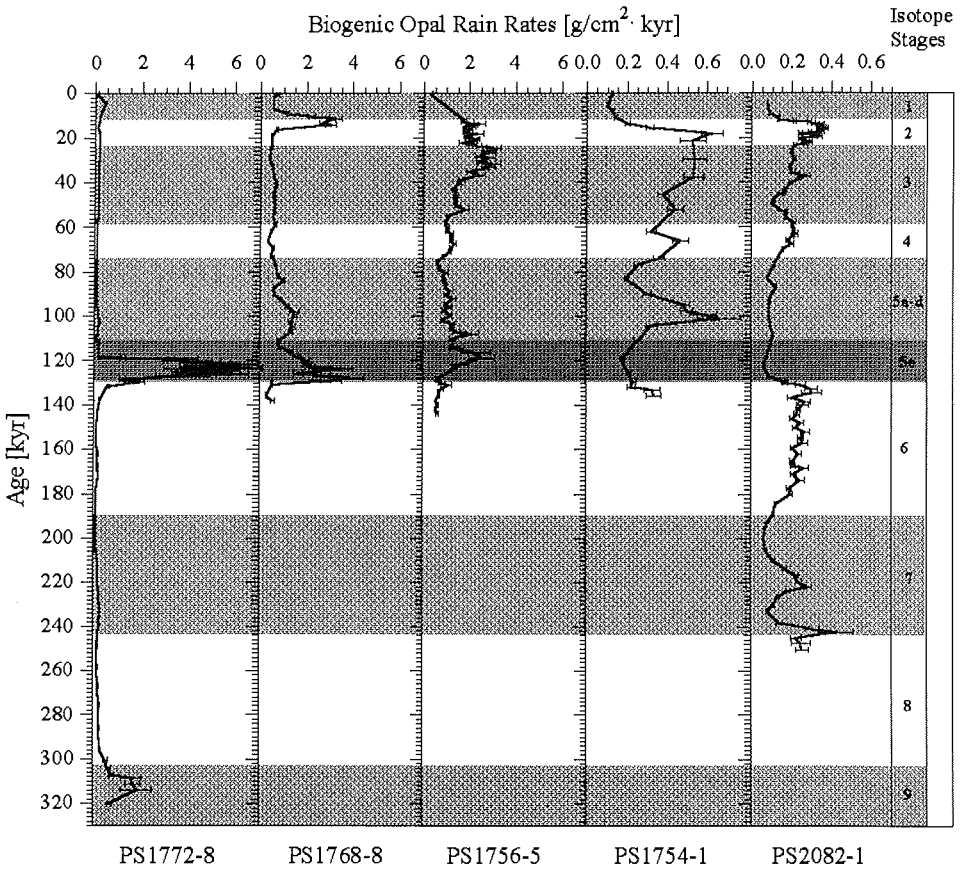

Figure 18: Profiles of the biogenic opal rain rates in g/cm^2 · kyr versus age in kyr B.P. The error bars represent the statistical errors of one standard deviation from the mean of the $^{230}Th_{ex}$ measurements. Note the different scales for the two northern cores. All opal concentrations are from G. Bohrmann (unpub. res.).

in the stage 5e section of core PS1772-8. High values between 2 and 4 g/cm^2 · kyr are determined in the stage 1 and 5e core sections of PS1768-8 and in the stage 2, 3 and 5e sections of PS1756-5.

There are, however, some differences. In core PS1772-8 very low amounts of biogenic opal (0.1-0.2 g/cm^2 · kyr) accumulated during the periods with dense sea ice cover, while in core PS1768-8 about 0.5 g/cm^2 · kyr accumulated, clearly indicating a less dense sea ice cover at the location of core PS1768-8. The two cold and three warm substages of stage 5 are resolved in the opal record.

The two northern cores show low opal rain rates, which are in the range of the ice covered sections in the south, indicating either a low production or a high dissolution. Nevertheless, their glacial rain rates (0.3 to 0.6 g/cm^2 · kyr) are about a factor of 3 higher than the interglacial ones (0.05 to 0.2 g/cm^2 · kyr).

4.3.2 Biogenic Barium

In the two cores from the Antarctic Zone the biogenic barium rain rates (Fig. 19) perfectly resemble the pattern of biogenic opal with maximum values of 3.5 to 4 mg/cm^2 · kyr in the interglacial stages 5e and in the Holocene core section of core PS1768-8. In contrast to the pattern of the opal rain rate, the 5e maximum of the biogenic barium rain in core PS1772-8 amounts to the same value as the maxima of core PS1768-8. Additionally, the transition from glacial stage 2 to the Holocene in core PS1772-8 is clearly visible in the biogenic barium record. In the core sections representing sea ice coverage, rain rates of around 0.4 mg/cm^2 · kyr (PS1772-8) and 0.9 mg/cm^2 · kyr (PS1768-8) are calculated. As in the biogenic opal record, the cold and warm substages of interglacial stage 5 can be identified. In core PS1756-5 the biogenic barium also follows the pattern of biogenic opal with peak values in the glacial stages 2 and 3 and interglacial substage 5e of about 2 mg/cm^2 · kyr.

In contrast to biogenic opal, the biogenic barium rain rates in core PS1754-1 are as high as in the Antarctic Zone, reaching peak values of 3 mg/cm^2 · kyr in the glacial stages 3 and 6. Interglacial values amount to around 1.5 mg/cm^2 · kyr. This inconsistency might indicate an increased opal dissolution in the sediments of the northern Polar Frontal Zone, leading to a glacial decoupling of the biogenic barium and opal rain rates.

In core PS2082-1 there are pronounced maxima of the generally low biogenic barium rain rates of about 1 mg/cm^2 · kyr in the glacial stages 2, 4 and 6. Interglacial values amount to about 0.2 to 0.5 mg/cm^2 · kyr. These features again are in accordance with the biogenic opal record suggesting that there have been no glacial biogenic particle fluxes in the Subantarctic Zone during the last 250 kyr comparable to the interglacial ones in the Antarctic Zone. Thus, the high particle flux area of the opal belt did not extend to 43°S. The decrease of the biogenic barium rain rate at the end of glacial stage 6 precedes the stage transition by about 8 kyr. There is no difference between the younger part of isotope stage 7 and stage 6. Both of these features are not observed in the biogenic

opal record and thus can only be explained by variations of dissolution intensity for both sedimentary components.

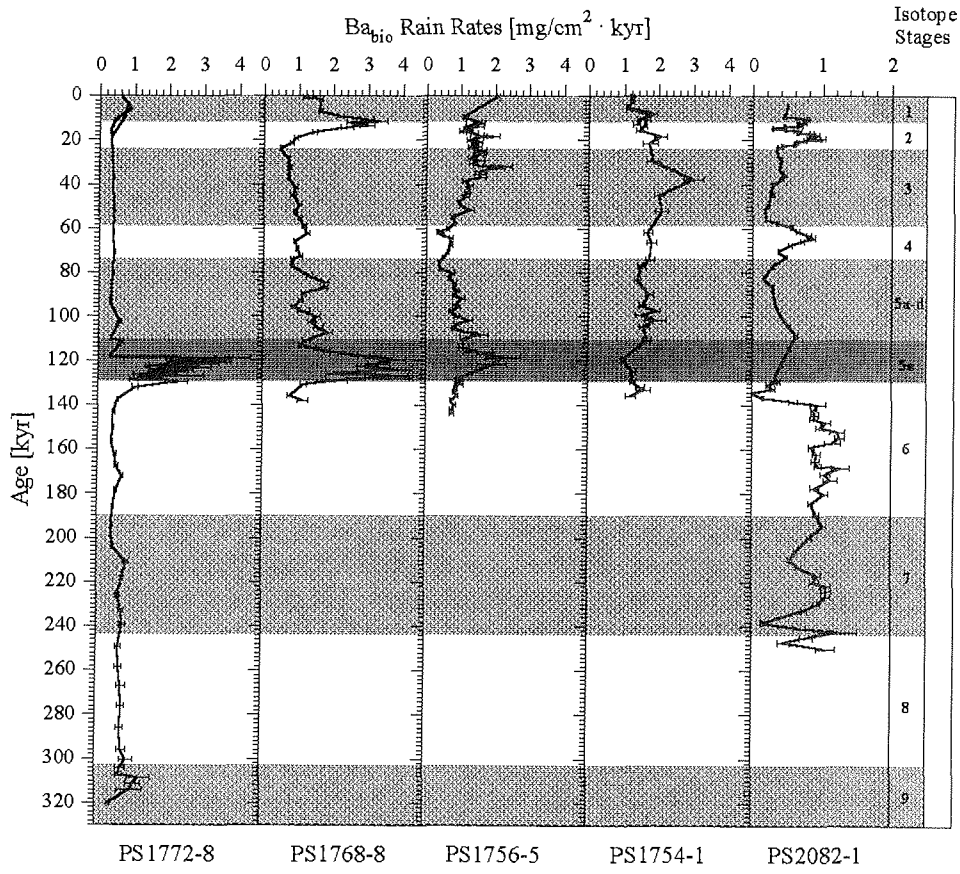

Figure 19: Profiles of the biogenic barium rain rates in mg/cm^2 · kyr versus age in kyr B.P. The error bars represent the statistical errors of one standard deviation from the mean of the $^{230}Th_{ex}$ measurements. Note the different scale of the PS2082-1 profile. All biogenic barium concentrations are from Nürnberg (1995), except core PS1754-1, for which the concentrations were measured as a part of this study.

4.3.3 Export Paleoproductivity

The rain rates of biogenic barium may be translated into export paleoproductivity rates (P_{new}) applying the following transfer function (Nürnberg, 1995; Nürnberg et al., in prep.), which is a combination of a relation between C_{org} and biogenic barium (Francois et al., 1995) and of a relation between export productivity and C_{org} flux to the sea floor (Sarnthein et al., 1988; Dymond et al., 1992):

$$P_{new} = 3.56 \cdot \left(\frac{AR_{\,Ba_{bio}}}{0.209 \cdot log\ (SR_{\,tot.} - 0.213)} \right)^{1.504} \cdot z^{-0.0937} \qquad (1)$$

with
$AR_{\,Ba_{bio}}$ = biogenic barium rain rate [$\mu g \cdot cm^{-2} \cdot year^{-1}$]
$SR_{\,tot.}$ = total sediment accumulation rate [$\mu g \cdot cm^{-2} \cdot year^{-1}$]
z = water depth [m]

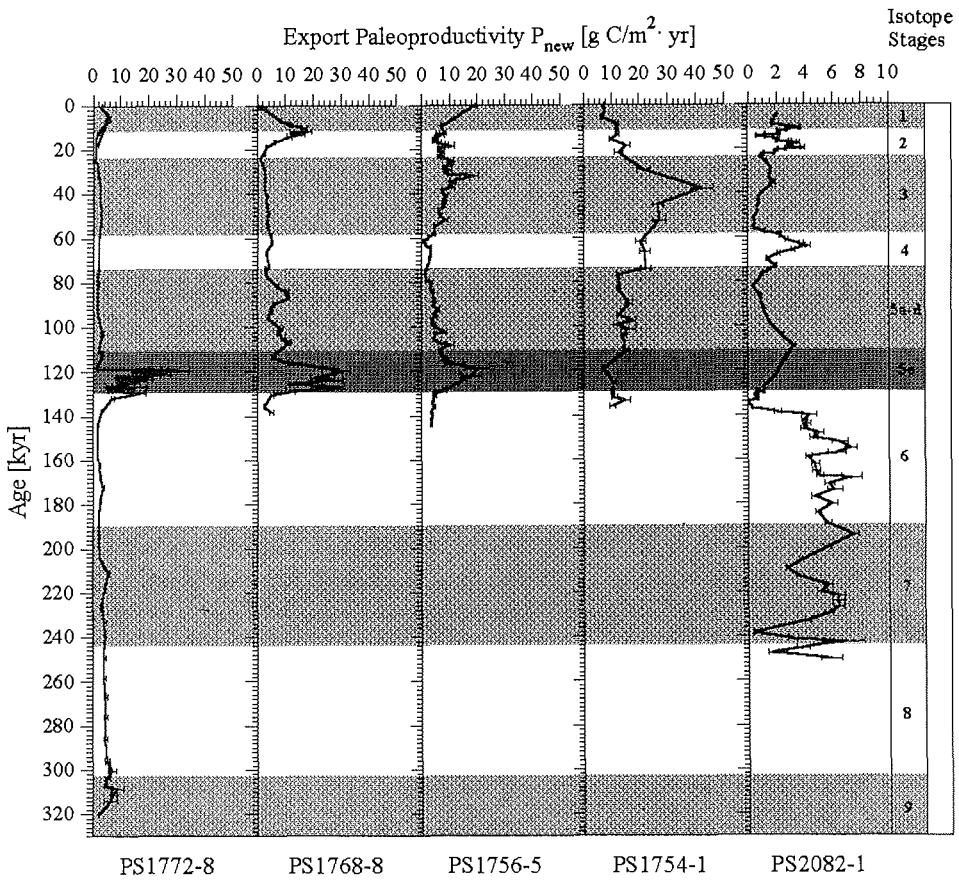

Figure 20: Profiles of the export paleoproductivity calculated from the biogenic barium rain rates following equation 12 in $gC/m^2 \cdot yr$ versus age in kyr B.P. The error bars represent the statistical errors of one standard deviation from the mean of the $^{230}Th_{ex}$ measurements. Note the different scales for the northern and southern cores.

These paleoproductivity values were calculated with the focusing and winnowing corrected biogenic barium rain rates on the one hand and the non corrected total sediment

accumulation rates on the other. This has to be done to account for the degree of barium preservation which is positively correlated to the total sediment accumulation rate. The values are presented in Fig. 20 and resemble the pattern of the biogenic barium rain rate.

However, there are some differences. The paleoproductivity maximum during stage 5e in core PS1768-8 is more pronounced than the Holocene maximum (30 compared to 20 $gC/m^2 \cdot yr$), which is caused by the higher Holocene barium preservation due to the higher total sediment accumulation rates. In core PS1772-8 the total sediment accumulation rates were slightly lower during stage 5e compared to PS1768-8 yielding maximum values of paleoproductivity of about 20-30 $gC/m^2 \cdot yr$.

In core PS1756-5 paleoproductivity maxima are in general about a factor of 2 lower than south of the APF (values around 10 $gC/m^2 \cdot yr$) and the stage 3 paleoproductivity is calculated higher than in stage 2 due to the sediment winnowing with a peak value of 20 $gC/m^2 \cdot yr$ at about 32 kyr B.P.. In core PS1754-1 the paleoproductivity values during the stages 3 and 4 amount to about the same values as in the Antarctic Zone and also reach a marked peak of 42 $gC/m^2 \cdot yr$ at about 40 kyr B.P., which may be synchronous with the peak in core PS1756-5 due to the low time resolution in this section. No significant differences compared to the biogenic barium record are observed in the northernmost core where productivity was very low (maxima between 4 and 7 $gC/m^2 \cdot yr$).

4.3.4 $^{231}Pa_{ex}$

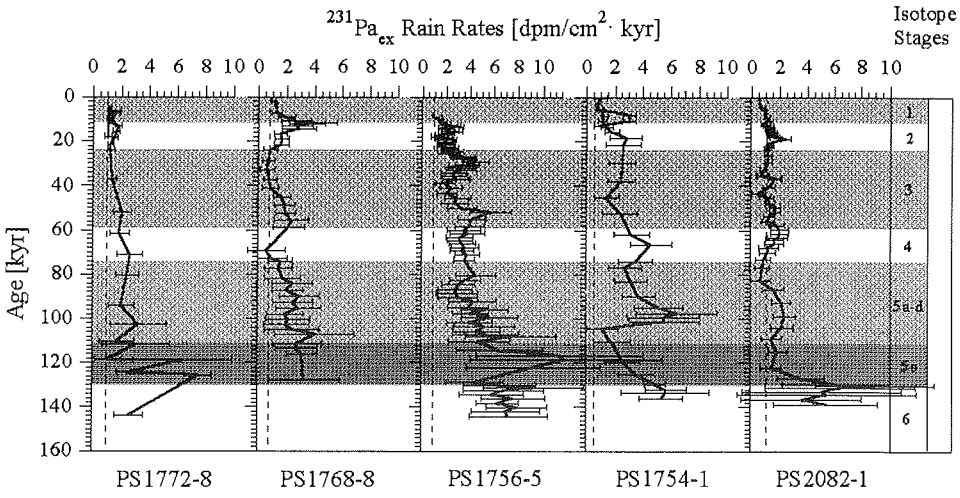

Figure 21: Profiles of the $^{231}Pa_{ex}$ rain rates in $dpm/cm^2 \cdot kyr$ versus age in kyr B.P.. The error bars represent the statistical errors of one standard deviation from the mean of the $^{230}Th_{ex}$ and the $^{231}Pa_{ex}$ measurements.

The rain rates of $^{231}Pa_{ex}$ are, more or less throughout all cores, significantly increased compared to the value expected from production, with the exception of PS2082-1. This

corroborates the high biogenic particle fluxes in the AZ and PFZ of the ACC (Kumar et al., 1993).

Due to the very high statistical uncertainties the indirect measurements of ^{231}Pa in the stage 5e sections of the two AZ cores were not included in the interpretation. Instead, direct reference measurements of Rutgers van der Loeff and Walter, AWI Bremerhaven, were carried out, which are reliable. These direct ^{231}Pa measurements corroborate a high $^{231}Pa_{ex}$ rain rate of up to 7.5 dpm/cm^2 · kyr in core PS1772-8 during stage 5e with a statistical uncertainty of about 10 %. In core PS1768-8 the stage 5e value is increased to 3.3 dpm/cm^2 · kyr, which is about equal to the increased $^{231}Pa_{ex}$ rain rate (up to 4 dpm/cm^2 · kyr) during the last deglaciation. The glacial $^{231}Pa_{ex}$ rain rates are close to the value expected from production and thus are still higher than in central ocean gyres, where rain rates lower than the production are observed. This suggests that, although restricted by the sea ice cover, particle fluxes were significantly higher than in central ocean gyres.

The pattern of the $^{231}Pa_{ex}$ rain rates in the two AZ cores is quite similar to the biogenic opal and biogenic barium rates suggesting that the variations of the paleoproductivity are also mirrored by $^{231}Pa_{ex}$ (Fig. 21). From the two cores of this study alone, this correlation to paleoproductivity would be quite weak. However, a comparison to the results of Kumar (1994) obtained from AZ sediments corroborates this suggestion.

A different picture is observed in core PS1756-5, where the values show a more or less continuous downcore decrease with peak values in the stages 3, 4 and 5e. In this core where the statistical uncertainties are relatively low (in the order of 20 %), the peak values in the stage 5e section exceed production by an order of magnitude. This either means that the observed decrease is realistic or that it might be caused by too high estimates of the ages in the lower part of the core. Assuming that the stratigraphy is correct, a decreasing biogenic particle flux with time at the location of this core is concluded from the $^{231}Pa_{ex}$ record. This feature is not observed at the other paleoproductivity indicators, except a peak value during stage 5e, which exceeds the ^{231}Pa production by a factor of 10, and the minimum during the Holocene.

Core PS1754-1, similar to PS1756-5, yields a decreasing trend of the $^{231}Pa_{ex}$ rain rates with time, however, with a minimum at the beginning of stage 5e. The amounts of the accumulated $^{231}Pa_{ex}$ are comparable to PS1756-5 during most of the time, with the exception of the stages 5 and 6 where they are significantly lower. The multicore PS1754-2, where the age could only be estimated from the $^{230}Th_{ex}$ constant flux model, shows a questionable $^{231}Pa_{ex}$ rain rate maximum, about corresponding to the Holocene climate optimum.

In core PS2082-1 only a very low variability around the production value with small maxima in the stages 2, 4 and in the middle of stage 5 occurred. It may be argued that the low rain rates of $^{231}Pa_{ex}$ in this core were caused by the very efficient scavenging in the south. However, the water column investigations of Rutgers van der Loeff and Berger (1993) showed that today there is no depletion of ^{231}Pa in the water column of the area

of this study, which suggests that the supply of ^{231}Pa did also reach the northern part of the ACC, where particle fluxes obviously were too low for a strong increase in scavenging.

In summary, it may be stated that $^{231}Pa_{ex}$ rain rates higher than the production corroborate high biogenic particle fluxes in the AZ and PFZ and low ones north of the SAF. Thus, keeping in mind the high statistical uncertainties of the measurements of this study, the rain rates of $^{231}Pa_{ex}$ may be a suitable tracer for paleoproductivity at the ACC. This is in accordance with previous results (Francois et al., 1993; Kumar et al., 1993; Kumar , 1994).

4.4 Potential Sources for Additional ^{231}Pa at the Southern ACC

The accumulation rates of $^{231}Pa_{ex}$ during the beginning of stage 5 are increased by up to a factor of 7.5 in the southern core PS1772-8 and up to a factor of 10 compared to production in core PS1756-5 taking into account statistical uncertainties (Fig. 21). Such an increase in the $^{231}Pa_{ex}$ accumulation rate can hardly be reached simply by boundary scavenging effects. (The results of Kumar showed a maximum increase of the $^{231}Pa_{ex}$ rain rate over production by a factor of 3 and Francois et al. found a maximum increase of a factor of 2). It is therefore reasonable to ask where the additional supply of $^{231}Pa_{ex}$ comes from. The definite answer to this question may certainly not be given due to a lack of knowledge of the geochemical behaviour of the radionuclide and to the as yet relatively small data set. Nevertheless, a scenario is developed that covers the observed features.

As demonstrated by Rutgers van der Loeff and Berger (1993), the advectional supply of ^{231}Pa with water masses from the north contributes today to a ^{231}Pa excess in the AZ and the PFZ sediments. The mixing pattern at the ACC probably was about comparable to the present day conditions at the beginning of stage 5 giving way to an upwelling of a water mass at the ACC which was enriched in ^{231}Pa. This, however, can not be the reason for the observed enhancement because the $^{231}Pa_{ex}$ rain rates presented, were normalized to $^{230}Th_{ex}$. As discussed in chapter 3.2, the ^{230}Th is stronger enriched by this advection effect than the ^{231}Pa and thus this explanation may be excluded.

Results of Yu (1994) show that $^{231}Pa_{ex}$ is depleted in the sediments of the whole Atlantic Ocean including the ocean margins in the Holocene and the LGM sections, with the exception of the Southern Ocean south of the Polar Front. This suggests an export of ^{231}Pa from the Atlantic into the Southern Ocean, which possibly may have occurred via NADW.

Coinciding with the stage 5e peak of $^{231}Pa_{ex}$ in core PS1772-8, a strong peak of authigenic Mn (Mn/Al ratio about 1 compared to a value of 0.004 of the standard granodiorite GSP-1) is observed (Figs. 12 and 21). No other measured parameter shows a comparatively strong increase. In core PS1756-5 no increase of authigenic Mn is observed parallel to the $^{231}Pa_{ex}$ increase during stage 5e, as discussed in chapter 4.8.

The key to understanding the feature of core PS1772-8 may be the strong affinity of ^{231}Pa to adsorb to MnO_2. In the suboxic sedimentary regimes of the Panama and

Guatemala Basins the increased presence of Mn oxides was shown to contribute to the boundary scavenging of $^{231}Pa_{ex}$ (Anderson et al. 1983b). Yet unpublished data of Yang et al. (1994) corroborate these results. The remobilization of Mn from the suboxic sediments into the bottom water column and the following reprecipitation as Mn oxides (Mn cycling (Spencer et al., 1981)) may lead to an enhancement of the scavenging of $^{231}Pa_{ex}$. $^{231}Pa_{ex}$ may be stronger enriched in the sediments compared to $^{230}Th_{ex}$ due to its higher residence time in the water column and thus larger supply area for boundary scavenging.

Anderson et al. (1994) report anomalous boundary scavenging in sediment traps from the Mid Atlantic Bight (MAB), where ^{230}Th is stronger enriched in the investigated trap material than ^{231}Pa and ^{210}Pb suggesting a selective enhancement of ^{230}Th scavenging. However, the authors conclude that the opposite is the case: A selective scavenging enhancement of ^{231}Pa and ^{210}Pb relative to ^{10}Be and ^{230}Th by fine grained MnO_2 coated particles, which are subsequently transported downslope by current activity have led to a relative depletion compared to ^{10}Be and ^{230}Th in the water column of the MAB.

It must be pointed out here, that such a geochemical behaviour of ^{231}Pa and ^{230}Th is in contradiction to results of Frank et al. (submitted to Geochim. Cosmochim. Acta), who are able to demonstrate that during the growth of Mn encrustations a fractionation occurs, which clearly prefers ^{230}Th. That means that the affinity of ^{230}Th to adsorb to Mn oxides is higher than that of ^{231}Pa, which is shown by a comparison of the fluxes of $^{231}Pa_{ex}$ and $^{230}Th_{ex}$ to two Mn crusts from the Pacific Ocean. A preferential scavenging of Pa by MnO_2 is also very doubtful regarding the fact that MnO_2 coated cartridges adsorb Th appreciably better than Pa (Rutgers van der Loeff and Berger, 1993).

If, nevertheless, it is assumed that there is a process by which $^{231}Pa_{ex}$ and Mn are added to the NADW and if it is further assumed that the situation described at the MAB is not a single event but occurs at various localities along the continental margin of North and South America, it be may be argued that the NADW becomes enriched in Mn and ^{231}Pa on its way south. This is also reasonable with respect to the mean oceanic residence time of ^{231}Pa of about 100 to 150 years and especially the one in the North Atlantic of about 70 years. Both values are in the same range as the residence time of the NADW in the Atlantic of about 80 years (Broecker and Peng, 1982). A model which demonstrates the possible enrichment of the NADW with $^{231}Pa_{ex}$ and subsequent supply to the Southern Atlantic south of the APF was first suggested by Yu et al. (submitted).

In the western Atlantic the NADW is admixed to the CDW (Reid et al., 1977). Without losing too much ^{231}Pa and Mn this water mass may then reach the area of strongly enhanced biogenic opal fluxes north of the sea ice cover and south of the APF, where the ^{231}Pa and Mn may be scavenged to the sediments.

Additionally, these sediments may, as in the Panama Basin, have become suboxic due to the high oxygen consumption. This can be caused by the high flux of organic matter, which can also be deduced from the laminations of the opal rich sediments representing the beginning of substage 5e which is an indication for oxygen poor conditions restricting benthic living and bioturbation. It is thus reasonable to infer a Mn cycling similar to the observations in the Panama Basin which also may contribute to the $^{231}Pa_{ex}$ enrichment.

In summary, the combination of NADW enrichment with $^{231}Pa_{ex}$ and Mn and a subsequent exposition of this water mass to the high biogenic particle flux area of the opal belt, where a Mn-cycling caused a near bottom scavenging enhancement, may be a reasonable explanation for the strong $^{231}Pa_{ex}$ enrichment in the stage 5e sediments. Due to the above described scenario, the absolute values of the $^{231}Pa_{ex}$ rain rates at the ACC may not be applied as direct tracers for biogenic particle fluxes in the past, whereas relative variations of the rain rates of $^{231}Pa_{ex}$ in the sediments are certainly related to past particle fluxes.

4.5 NADW Input into the Southern Ocean

The increased supply of carbonate poor, and nutrient and ΣCO_2 enriched Pacific Deep Water during glacials was suggested to cause stronger dissolution of calcium carbonate in the Southern Ocean (Howard and Prell, 1994). As mentioned previously, the three southern cores only have very low concentrations of biogenic carbonate, if any. That means, that this hypothesis may only be checked on the two northern cores of the transect, where biogenic carbonate is one of the main components of the sediment. A positive correlation between the $CaCO_3$ content and the $^{230}Th_{ex}$ concentrations was shown to be the result of carbonate dissolution (Francois et al., 1990), which can be resolved by the calculation of the (decay corrected) $^{230}Th_{ex}/CaCO_3$ ratio (Riediger, 1994; Rühlemann et al., in prep.). High carbonate dissolution increases this ratio, while low dissolution leaves it unaffected. In the $^{230}Th_{ex}/CaCO_3$ record of the cores PS1754-1 and PS2082-1 different intensities of the carbonate dissolution are recorded assuming a more or less constant $CaCO_3$ production (Fig. 22).

At the location of the shallower core PS1754-1 (water depth 2471 m) two small increases at the end of the glacial stages 6 and 2 are observed, which might not have been caused by a diminished admixture of NADW to the CDW, but as well by an increased supply of organic material. In the deep core PS2082-1 a strong dissolution signal caused by near zero carbonate concentrations during the glacial stages 2, 4 and 6, as well as in the cold substage 7d of interglacial stage 7 is seen. During these periods the carbonate compensation depth (CCD) was clearly raised above a water depth of 4600 m. During glacial stage 6 peak dissolution was active at the beginning and then decreased towards the end. The features of core PS2082-1 are in accordance with the results of Howard and Prell (1994) suggesting that the diminished glacial NADW input causes strong carbonate dissolution in the Southern Ocean. Core PS1754-1 might be too shallow to be severely influenced by the changes of the deep water chemistry but, nevertheless, a slightly increased glacial carbonate dissolution occurred as well.

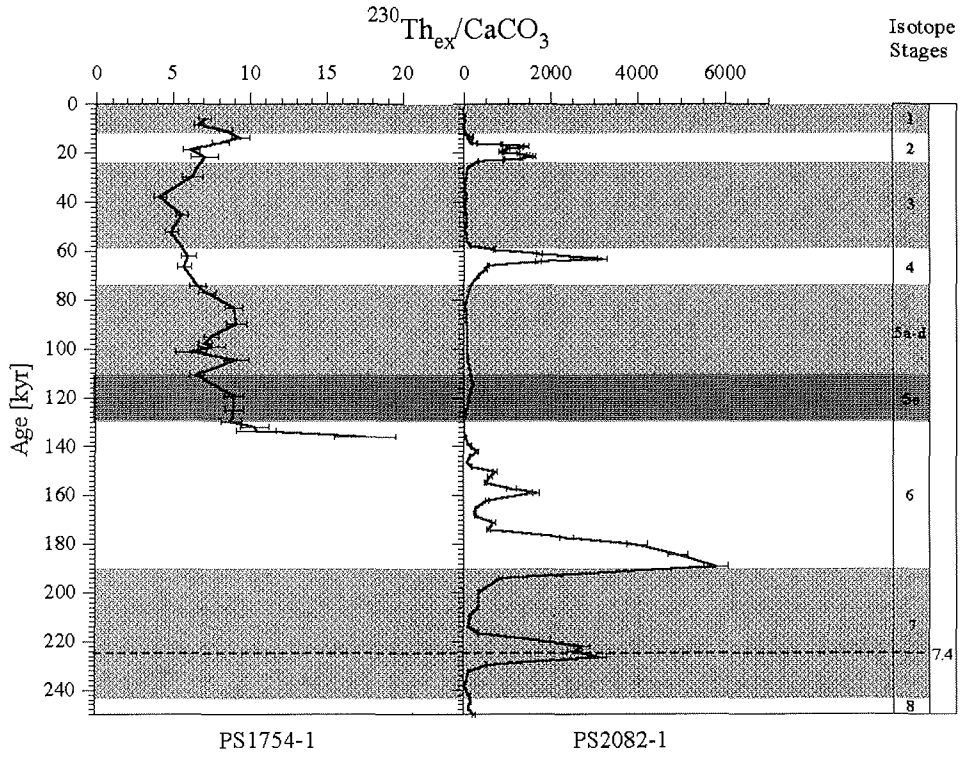

Figure 22: The $^{230}Th_{ex}/CaCO_3$ ratio as a measure for carbonate dissolution versus age in kyr. The error bars represent the statistical errors of one standard deviation from the mean of the $^{230}Th_{ex}$ measurements.

How do these results fit to other investigations? Mackensen et al. (1994) suggested a high input of northern component water into the ACC during the stages 3 and 5.1 to 5.3, which is in accordance with the above derived results. A rejection of northern component water by northward advancing AABW during stage 5e, suggested by Mackensen et al. (1994), contradicts the above results because no carbonate dissolution is observed. Results of Yu et al. (submitted) deduce no significant difference between Holocene and last glacial maximum NADW input into the Southern Ocean from a sedimentary $^{231}Pa_{ex}/^{230}Th_{ex}$ ratios, which also contradicts the results of this study.

The above results are in very good accordance with the results of Raymo et al. (1990) and Howard and Prell (1994) from the Cape Basin and the Indian sector of the ACC. Peak dissolution and thus lowest NADW input was found during stage 8 and and at the beginning of stage 6, whereas the minima during stages 4 and 2 apparently were not as strong. The NADW history reconstructed in this study is also in accordance with the strong increases of the $^{231}Pa_{ex}$ rain rate during the beginning of interglacial stages 5e and 1 in the AZ, which may have been caused by an enhanced input of NADW into the Southern Ocean compared to the glacials (Charles and Fairbanks, 1992). Altogether,

the results of this study suggest that the NADW input into the Southern Ocean during glacials was at least diminished.

More data are required, especially because today the main input of NADW into the ACC takes place in the western part of the South Atlantic at intermediate water depths (Reid et al., 1977). Further investigations of the $^{231}Pa_{ex}$ rain rate on a set of sediment cores recovered on RV Polarstern Cruise XI-2 (Gersonde, 1995) at relatively shallow water depths on the Mid Atlantic Ridge in the area of the Polar Frontal Zone may deliver a $^{231}Pa_{ex}$ record which shows a NADW fluctuation signal more clearly.

5.2 Rain Rates of Terrigenous Particles

5.2.1 ^{10}Be Rain Rate

In the two cores from the Antarctic Zone the ^{10}Be rain rates do not show any positive correlation to the features previously observed in the records of the other components (Fig. 23). The ^{10}Be rain rate exceeds the production rate by about a factor of 2 to 4 throughout the cores, which is expected in a high particle flux area. However, the pattern of the variations of the ^{10}Be rain rate seems to be random. Especially in the core sections representing the Holocene and the stage 5e climate optimum where the paleoproductivity was increased and biogenic particle fluxes were high, in contrast to the expectations, no maxima but minima of the ^{10}Be rain rates are obtained. There is also a strong minimum in the stage 9 section of core PS1772-8, where the biogenic opal and barium records show peaks of the rain rates. These features indicate that a process other than biogenic particle flux controlled the ^{10}Be rain rate during the periods of high productivity in the Antarctic Zone.

In core PS1754-1 a variability coinciding with the other components, showing peak values in the stage 2 and 6 sections, can be observed. This feature is even more pronounced in core PS2082-1, where the ^{10}Be rain rates show marked maxima in the sections corresponding to glacial stages 2-4 and 6 and where the value expected from production is exceeded by a factor of 3. Thus, in the two northern cores the expected positive correlation of particle rain rate and ^{10}Be rain rate is given.

Minimum rain rates of ^{10}Be with values slightly lower than the production rate are thus observed in all five cores of the transect during the isotope substage 5e and the Holocene except core PS1756-5. ^{10}Be rain rates exceeding the production by a factor of 2 to 3 are observed during the glacial stages 2-4 and 6. This pattern suggests that a scavenging process independent from the shifts of the high biogenic particle flux area affected the ^{10}Be rain rate. With the well known affinity of ^{10}Be to adsorb to clay minerals (Sharma et al., 1987) the rain rates of terrigenous material are investigated for comparison.

5.2.2 Al_2O_3 and Fe

The rain rates of terrigenous material, either ice rafted debris (IRD) or aeolian dust, are inferred from the rain rates of Al_2O_3 and Fe (Figs. 24 and 25). The two records yield

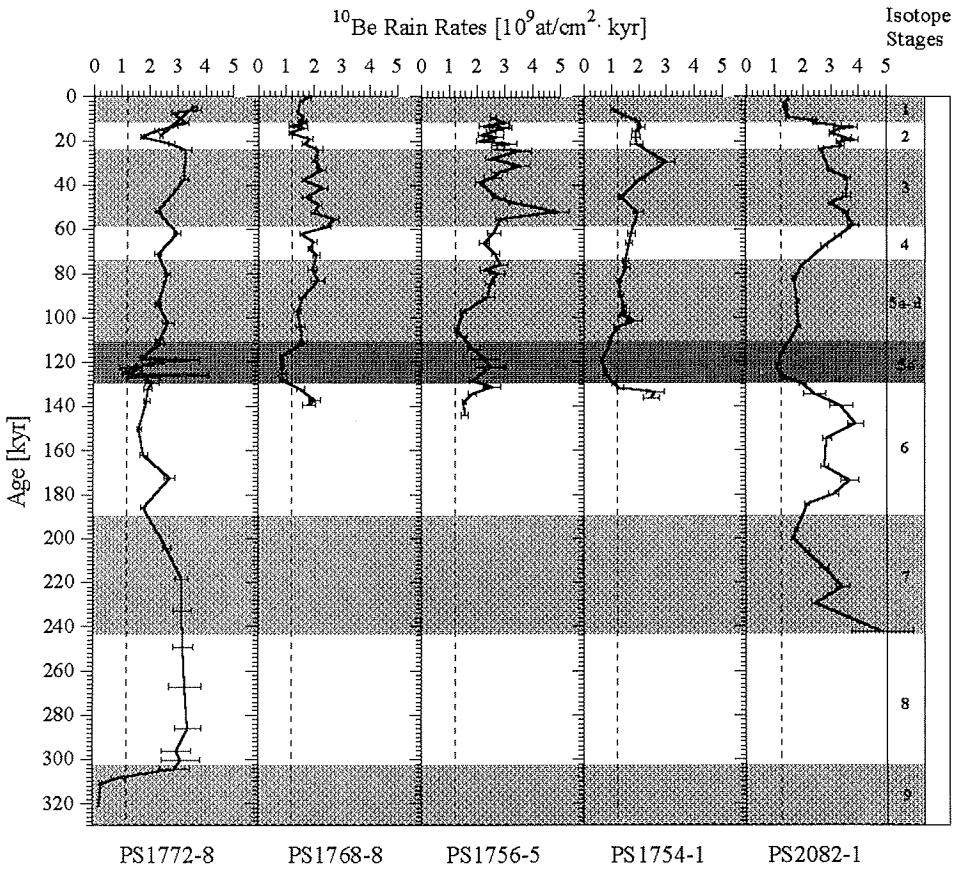

Figure 23: Profiles of the ^{10}Be rain rates in 10^9at/cm^2 · kyr versus age in kyr B.P. The error bars represent the statistical errors of one standard deviation from the mean of the ^{230}Th$_{ex}$ measurements. The rain rates were corrected for variations of the global ^{10}Be production (Fig. 6).

a consistent picture of relatively high terrigenous particle input during glacials and low input during interglacials. The strongest minima are observed in the Holocene and the stage 5e core sections where the values are about a factor of 5 lower than during glacials. The total amounts of glacial detrital fluxes tend to be higher in the AZ and the southern part of the PFZ.

The overall picture is in accordance with the observations of Kumar (1994) who suggested an increased aeolian dust flux to the eastern part of the Atlantic section of the ACC during glacials, probably derived from the Patagonian deserts of Argentina.

This origin of the detrital components was also deduced by investigations in the Vostok ice core (De Angelis et al., 1987), for which Grousset et al. (1992) also suggested a Patagonian source. The eastern Atlantic sector of the ACC is directly located in a zone where the prevailing westerly winds may transport dust from this potential source area.

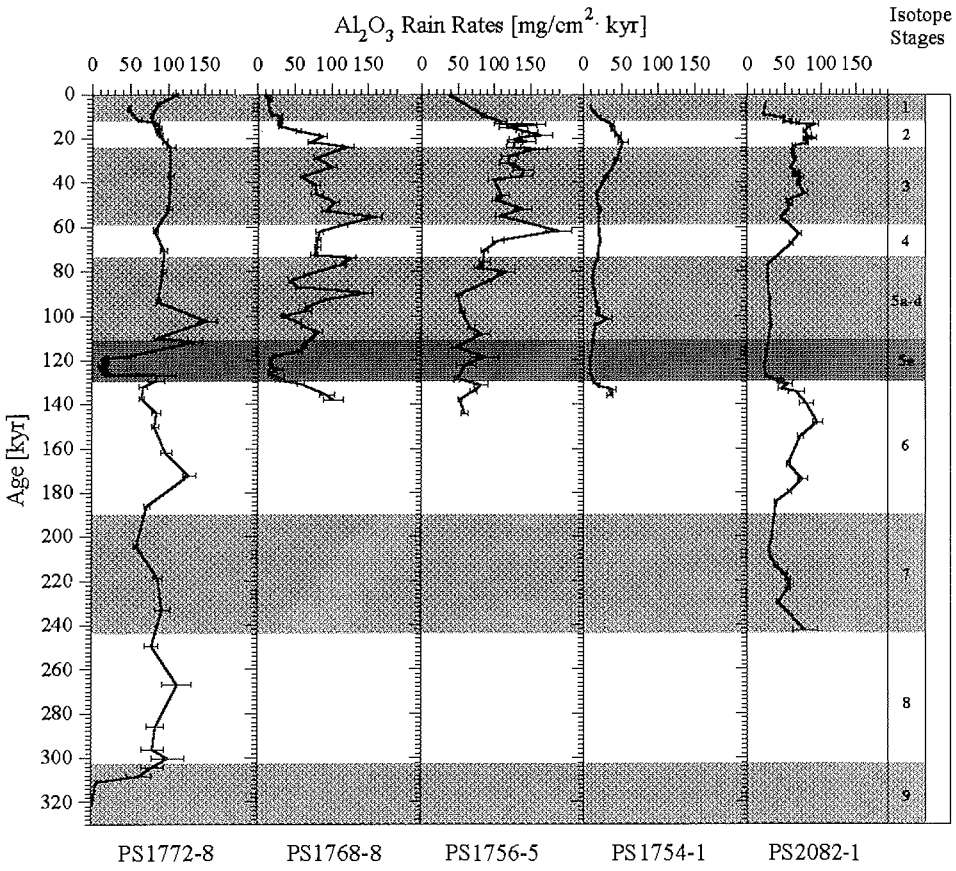

Figure 24: Profiles of the Al_2O_3 rain rates in mg/cm^2 · kyr versus age in kyr B.P. The error bars represent the statistical errors of one standard deviation from the mean of the $^{230}Th_{ex}$ measurements. Note the different scale of the PS2082-1 profile. All Al_2O_3 concentrations are from Nürnberg (1995) except core PS1754-1.

The glacial increase in dust flux may be caused by an increase in wind strength and more arid climatic conditions in Patagonia and, in addition, the lower sea level during glacials may have led to the exposure of a part of the Patagonian and western Atlantic shelves to the atmosphere and thus also made it a potential source for wind blown dust particles.

In the AZ and the southern PFZ a higher amount of IRD compared to the northern part has been released to the water column and the sediments (Labeyrie et al., 1986; Kumar, 1994), which probably has contributed to the higher detrital fluxes.

When comparing the ^{10}Be rain rates to the other investigated components, it is obvious that a correlation is found only with the terrigenous rain rates (Fig. 26). From this, it may be argued that the scavenging of ^{10}Be at the ACC is mainly controlled by clay

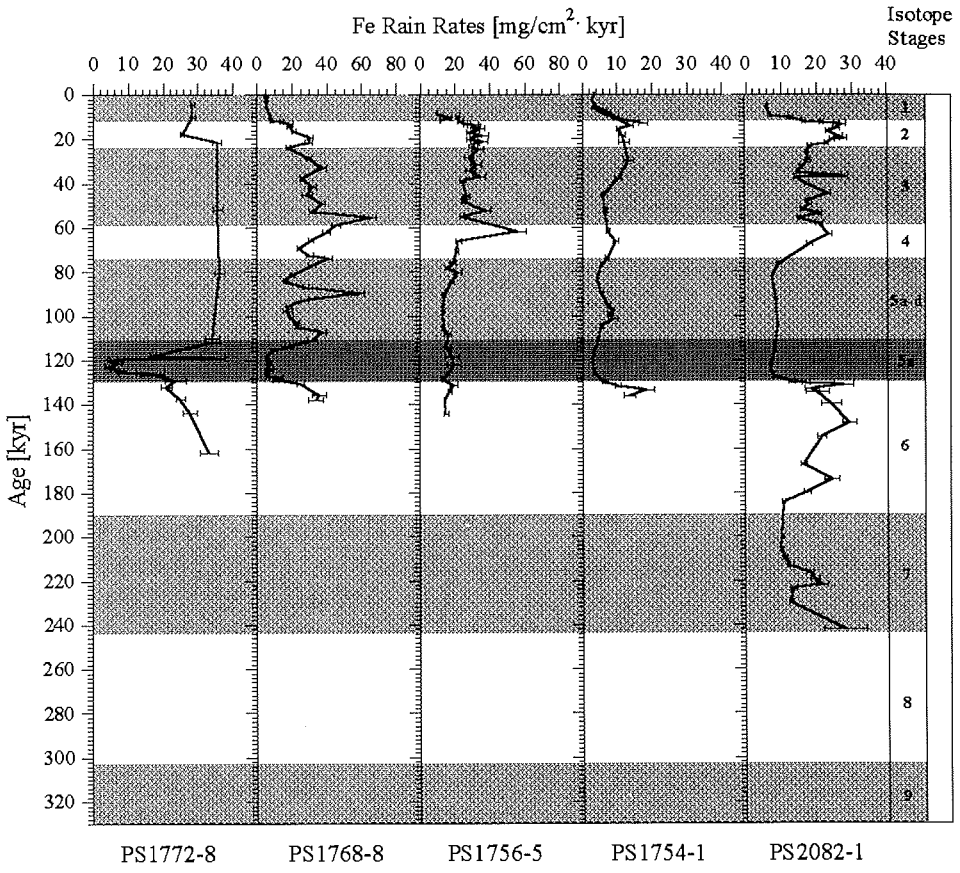

Figure 25: Profiles of the Fe rain rates in mg/cm^2·kyr versus age in kyr B.P. The error bars represent the statistical errors of one standard deviation from the mean of the $^{230}Th_{ex}$ measurements. Note the different scales of the profiles.

particles (Sharma et al., 1987). Additionally the dust particles themselves may transport adsorbed ^{10}Be from the Patagonian deserts. Shengde et al. (1922) report increased rain rates of ^{10}Be with dust particles in Chinese loess during colder and more arid periods of the paleoclimate, which are in about the same range as the rain rates of ^{10}Be in the ACC sediments.

The pattern of maximum and minimum ^{10}Be rain rates at the ACC may, at least partly, also have had its origin at the ocean margin of the Weddell Sea, where only very low amounts of ^{10}Be were deposited in the sediments during glacials and may thus have been transferred to the ACC (Frank et al., in press). On the other hand, in these sediments increased ^{10}Be rain rates are determined in the core sections representing the interglacial stages 7, 5e and 1, which may have contributed to the interglacial minima at the ACC.

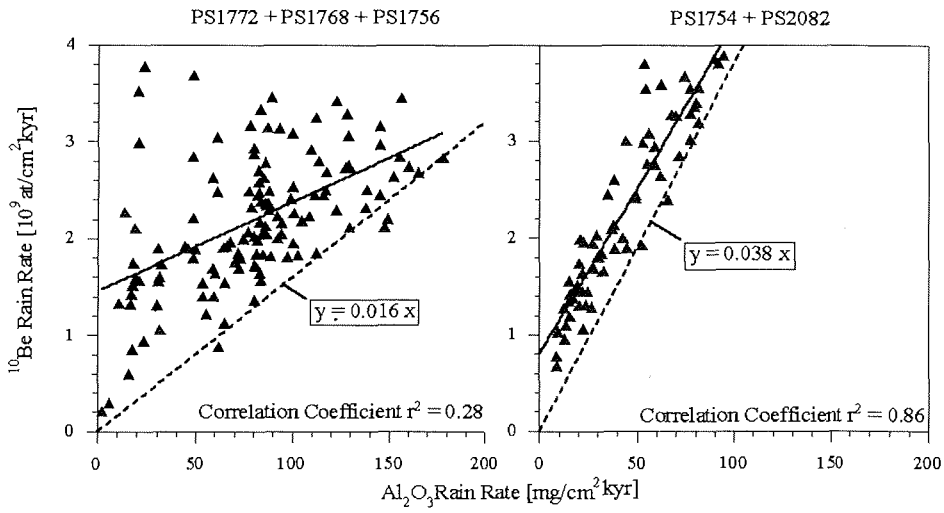

Figure 26: Correlation between the rain rates of Al_2O_3 and ^{10}Be. The solid line represents a linear fit to the three southern cores (left plot) and to the two northern cores (right plot). The dashed line represents the relation of ^{10}Be adsorbed to terrigenous material according to the method of Rutsch et al. (1995).

In order to evaluate biogenic ^{10}Be rain rates, the amount of ^{10}Be adsorbed to terrigenous particles is evaluated by the relations

$$F_{(^{10}Be)}detrital = 0.016 \cdot F_{(Al_2O_3)} \quad (1)$$

for the three southern cores and by

$$F_{(^{10}Be)}detrital = 0.038 \cdot F_{(Al_2O_3)} \quad (2)$$

for the two northern cores, similar to the method of Rutsch et al. (1995). It is obvious that two different terrigenous ^{10}Be background values (Fig. 26) in the two northern and the three southern cores have to be applied for calculating biogenic ^{10}Be. How can this difference be explained?

As mentioned above, in the southern part of the ACC the enhanced release of IRD may have significantly contributed to the observed higher rain rates of terrigenous material. The IRD which tends to be coarser grained has a smaller surface and consequently a lower adsorption capacity for ^{10}Be. In the two northern cores only the fine grained aeolian dust with its larger surface and higher amount of initially adsorbed ^{10}Be seems to have controlled the ^{10}Be scavenging. Additionally, the IRD does not carry ^{10}Be itself. It may, however, be argued that the melting ice with its average concentration of $4 \cdot 10^4$at/g (McHargue and Damon, 1991) and an estimated annual iceberg production of about 2000 Gt (Jacobs et al., 1992) also releases a significant amount of ^{10}Be to the surface water of the ACC (Kumar, 1994). According to the results of this study, the iceberg derived ^{10}Be

contribution obviously was not high enough to account for a significant increase of the ^{10}Be rain in the southern part of the ACC, if compared to the dust controlled scavenging in the northern part.

The biogenic ^{10}Be rain rate is calculated by subtracting the detrital ^{10}Be rain rate from the total rate (Fig. 27). In the two southern cores it is seen that biogenic ^{10}Be rain rate was

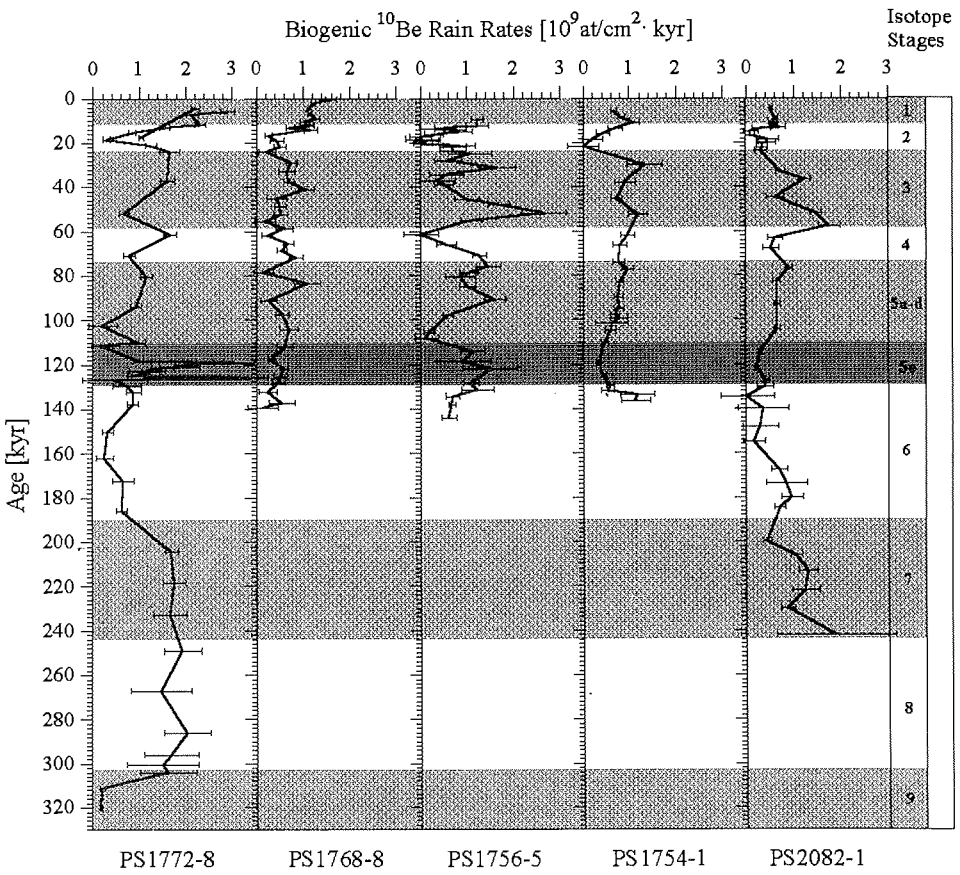

Figure 27: Profiles of the biogenic ^{10}Be rain rates in mg/cm^2 · kyr versus age in kyr B.P. The error bars represent the statistical errors of one standard deviation from the mean of the ^{230}Th$_{ex}$ measurements.

indeed enhanced during the climate optima. In core PS1772-8 an increase of the biogenic ^{10}Be rain rate from glacial values around $1 \cdot 10^9$at/cm^2 · kyr to about $2 \cdot 10^9$at/cm^2 · kyr during stage 5e occurred. In core PS1768 the Holocene climate optimum is also mirrored by increased biogenic ^{10}Be rain rate of about $1 \cdot 10^9$at/cm^2 · kyr, compared to glacial values of about $0.5 \cdot 10^9$at/cm^2 · kyr, whereas in interglacial substage 5e no significant increase is observed.

In the three northern cores paleoproductivity was shown to be increased during gla-

cials. The coinciding biogenic ^{10}Be rain rates, however, are mostly very low. In core PS1756-5 this pattern is most pronounced and even the cold substages of interglacial stage 5 are visible and here is the only exception because the increased stage 5e biogenic ^{10}Be rain rate coincides with increased paleoproductivity.

Apparently, the ratio between settling terrigenous and biogenic material was increased during glacials. This resulted in very low biogenic ^{10}Be rain rates because the ^{10}Be preferentially adsorbed to the offered aluminosilicates. In turn, this may be seen as further support for lower glacial biogenic particle fluxes in the northern PFZ and the SAZ compared to the AZ. If the biogenic particle fluxes had been higher, the amount of biogenic ^{10}Be rain rate would also show increases.

All these features together suggest that in the PFZ and the SAZ the detrital particle fluxes account completely for the increased total ^{10}Be rain rate during glacials and that the biogenic particle fluxes were too low to cause a significant contribution to the total rain rate of ^{10}Be.

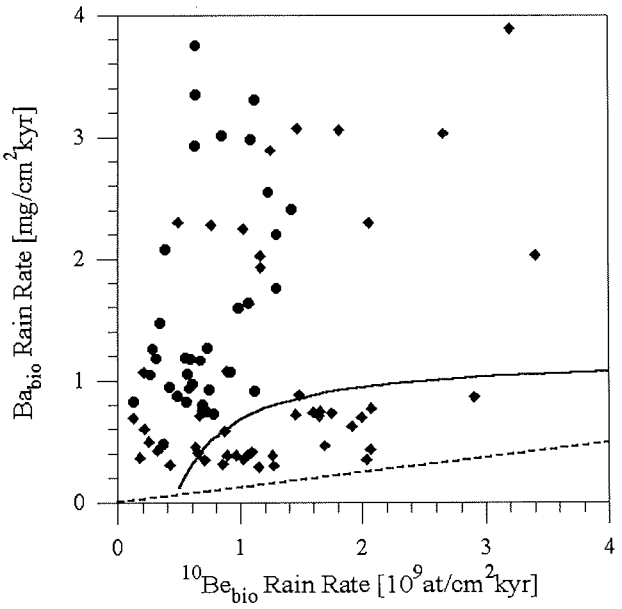

Figure 28: Correlation between the rain rates of biogenic Ba and ^{10}Be in the AZ sediments. The dashed line represents the relation of the rain rates of ^{10}Be (1.2 at/cm^2 · kyr) and Ba (0.12 mg/cm^2 · kyr) in the open ocean. The circles mark the data of core PS1768-8 and the squares mark the data of PS1772-8. The solid line curve represents the modelling results for open ocean fluxes of ^{10}Be and Ba of 0.5 · 10^{9}at/cm^2 · kyr and 0.12 mg/cm^2 · kyr respectively.

5.3 Comparison of Biogenic ^{10}Be and Biogenic Ba

In a recent publication Rutsch et al. (1995) compared the the rain rates of biogenic ^{10}Be and biogenic Ba in sediments from the Angola Basin. They showed that the biogenic Ba deposition exceeds the biogenic ^{10}Be deposition due to the higher residence time of Ba in the oceans, which amounts to about 10,000 years and thus is about 10 times higher than that of ^{10}Be. The measured rain rates of both elements were reproduced by a box model.

If the biogenic Ba and ^{10}Be rain rates of this study are compared to each other, it can be seen that this only makes sense in the two southern cores because, as discussed in the previous chapter, in the three northern cores biogenic ^{10}Be fluxes are masked by aeolian dust flux.

In Fig. 28 the correlation between biogenic ^{10}Be and Ba of the sediments from the AZ is shown. While the biogenic ^{10}Be rain rates are comparable to the ones in the Angola Basin, the corresponding biogenic Ba rain rates are up to three times higher during the climate optima of the stage 5e and the Holocene. For comparison, maximum biogenic Ba rain rates in Angola Basin sediments were in the range of 1.3 mg/cm^2 · kyr. Such an increase can by far not be reached with the residence time model of Rutsch et al. (1995). In addition, if an average ^{10}Be flux of $1.2 \cdot 10^9$at/cm^2 · kyr (as marked by the dashed line in Fig. 28) is applied for the model, the curve marking the modelling results would even be shifted closer to the x-axis. This suggests that there must be an additional source of Ba for the AZ, especially during peak climate optima, which weakens the applicability of biogenic Ba as a paleoproductivity proxy at the ACC. The origin of the additional Ba is not known.

5.4 Authigenic ^{238}U Accumulation and the Mn/Al Ratio: Tracers for Redox Changes in the Sediments

As stated in the chapter 1.5.2, increased deposition of authigenic ^{238}U may be interpreted in terms of more reducing conditions in the surface sediments due to increased accumulation rates of organic matter and thus equates to periods of higher paleoproductivity. Strictly speaking, it does neither make sense to calculate rain rates of authigenic ^{238}U by multiplying the concentration by vertical sediment rain rates nor by total sediment accumulation rates. If authigenic ^{238}U accumulation rates are nevertheless estimated, the total sediment accumulation rates have to be applied (Fig. 29) because the amount of authigenic ^{238}U diffusing into the sediment is only dependent on the total amount of accumulated organic material, no matter whether it originated from the water column above or was supplied laterally.

High oxygen consumption caused by the decomposition of the organic matter leads to the development of reducing conditions close to the sediment water interface. However, if the deposition of organic material was the only factor controlling the accumulation rates of authigenic ^{238}U, they should coincide with the pattern of biogenic barium or opal.

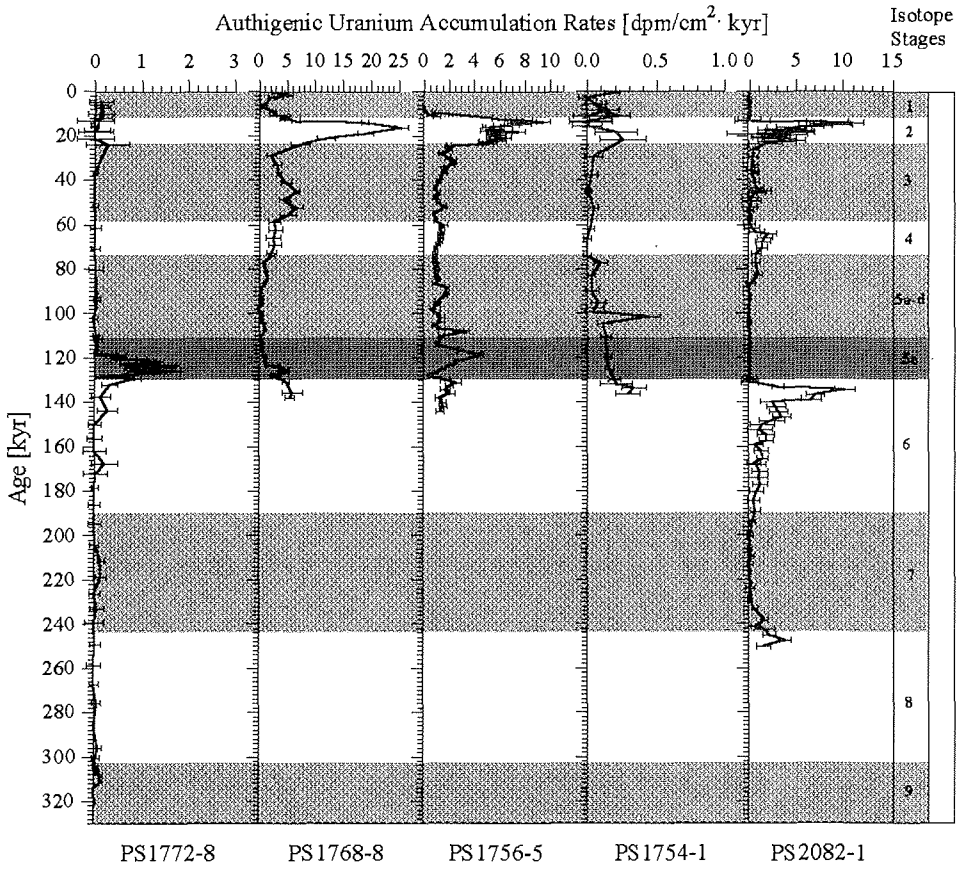

Figure 29: Profiles of the ^{238}U accumulation rates in dpm/cm^2 · kyr versus age in kyr B.P.. The error bars mark the range of the estimates of the lithogenic $^{238}U/^{232}Th$ activity ratio between 0.5 and 1. Note the different scales of the profiles.

Peak accumulation rates of about 2 dpm/cm^2 · kyr are determined in the stage 5e section of core PS1772-8 while, however, the concentrations are very low. In the other sections of core PS1772-8 practically no authigenic ^{238}U was deposited.

In contrast, relatively high values were accumulated during the isotope stages 3 and 2 in core PS1768-8 with a peak value of 25 dpm/cm^2 · kyr in the middle of glacial stage 2. The pattern of the ^{238}U accumulation rates is similar to the one of the concentrations. The glacial stage 2 peak, which was analyzed with a very good time resolution, clearly leads the peaks of biogenic barium and biogenic opal rain rate. This is also the case at the stage 5e enrichment of this core, which does not completely precede the stage 6/5 transition but at least extends into the glacial section.

This feature might be explained by differences in the depth of the redoxcline. While in core PS1772-8 the accumulation rates of organic material were so high that the redoxcline

was about equal to the sediment/water interface, there may have still been an oxygenated layer during peaks of biogenic particle flux in core PS1768-8, leading to a downward migration and subsequent precipitation of authigenic ^{238}U. This clearly shows that the deposition of ^{238}U can not exclusively be related to the deposition of organic matter.

It may be argued that a deposition of about 25 dpm/cm^2 · kyr may even have lowered the U concentration of the water column of the Southern Ocean. If this accumulation rate is compared to the standing crop (an assumed body of water with a base area of 1 cm^2 and a length corresponding to the average water depth of about 3000 m) of ^{238}U in the water column of about 800 dpm/cm^2, even a short-term peak flux of 25 dpm/cm^2 · kyr would not change the ^{238}U concentration in the water column significantly.

Similar to core PS1768-8, in the southern PFZ the pattern of the authigenic ^{238}U accumulation shows high values during isotope stage 2 of up to 9 dpm/cm^2 · kyr which is in accordance with a period of increased biogenic particle flux. However, stage 3 is not represented by equally high values. In this core the concentrations of ^{238}U show a much more homogenous distribution, indicating no significant changes of the redox conditions with the exception of a small peak during stage 5e and very low Holocene values.

Further north, in core PS1754, practically no authigenic ^{238}U was deposited during the investigated period of the last 140 kyr, which probably is a consequence of the low sediment accumulation rate (see next page). In the core from the Agulhas Basin the glacial/interglacial contrasts are very pronounced with zero authigenic ^{238}U accumulation and concentration during the interglacial stages 7, 5 and 1 and peak values of up to 10 dpm/cm^2 · kyr, especially at the end of the glacial sections 6 and 2.

Besides variations of the accumulation of organic matter, another possibility controlling the variations of authigenic ^{238}U is discussed here, which for example may be responsible for the low concentration during the Holocene in core PS1768-8.

A lower oxygen content of the deep water during the glacials caused by a weaker thermohaline circulation may have caused reducing conditions close to the sediment water interface. Such a lower oxygen content of the deep waters of the Southern Ocean is difficult to evaluate. Howard and Prell (1994) suggested low oxygen CDW during glacials and Hodell (1993) found only very small amounts of benthic foraminifera in the glacial sections of DSDP site 704A. On the other hand, Charles and Fairbanks (1991) found that glacial deep water was high enough in oxygen to permit benthic foraminifera to live in a sediment core from the PFZ in the eastern Atlantic sector of the ACC. Presently, the deep water in the area is well oxygenated (Rutgers van der Loeff and Berger, 1991).

In a modelling approach the glacial oxygen concentration of the deep water may be evaluated from the authigenic ^{238}U and C_{org} concentrations (between 0.4 and 0.6 %) of the cores PS2082-1 and PS1756-5. It turned out that during the glacial peak productivity periods a maximum concentration of 0.5-0.7 ppm authigenic ^{238}U may have been reached without changing the oxygen content of the deep-water. To achieve the observed maxima of about 3 ppm, the deep-water oxygen content had to be decreased from the present day values of about 150-200 μmol/kg to values of about 20 μmol/kg (A. Mangini, pers. com.).

Looking at the fact that the authigenic ^{238}U is enriched in the glacial stage 2 sections of the 4 northern cores, no matter whether the paleoproductivity was high or not, suggests that deep-water oxygenation may indeed have played an important role in controlling geochemical conditions in the deep water and the surface sediments of the Southern Ocean. The only exception is core PS1772-8 where no authigenic enrichment in stage 2 is observed. This, however may be explained by a postdepositional burn-down of the uranium enrichment due to the low sedimentation rates. Such a link is confirmed by the almost linear increase of the stage 2 authigenic ^{238}U enrichment with the sediment accumulation rate in the four other cores.

The redox conditions which were reconstructed by authigenic ^{238}U can now be compared to the geochemical information delivered by the Mn/Al ratio in the sediment column.

In core PS2082-1 the peaks of the Mn/Al ratio in excess of the lithogenic background clearly lag the authigenic ^{238}U peaks and exactly mark the transitions from isotope stages 6 to 5 and 2 to 1. Minor peaks of the Mn/Al ratio are found in the middle of stage 7 and during stage 3 also occurring immediately after authigenic ^{238}U maxima. In core PS1754-1 only at the transition from isotope stage 2 to 1 a significant Mn/Al increase occurred.

These features in the two northern cores may well be explained by the drop of the accumulation of biogenic particles at the end of the glacial periods. This led to a higher oxygen level and thus to a burial of the Mn enrichment due to the deepening of the redoxcline on the one hand. On the other, the diminished supply of C_{org} was not able to reduce the Mn at the surface any more. Additionally, the increase in bottom water oxygenation caused by the enhanced circulation at the beginning of the interglacials contributed to the reprecipitation of the MnO_2. In turn, the high authigenic ^{238}U concentrations during glacials are consistent with a diminished oxygenation and a contemporaneous high supply of organic matter to the deep water.

In core PS1756-5 conditions were more or less reducing throughout the last about 140 kyr, except the Holocene, as inferred from the relatively high rates of authigenic ^{238}U. This is corroborated by Mn/Al ratios which are about equal to the lithogenic background throughout the core. The redoxcline was probably located above the sediment/water interface and permitted a release of remobilized Mn to the water column. At this location, the continuous high supply of organic matter apparently was the main controlling factor for sediment geochemistry throughout the last 140 kyr. No significant changes in deep-water oxygenation or supply of organic matter are recorded, with the exception of the Holocene, where the deposition of authigenic ^{238}U decreased.

In the AZ the geochemical and sedimentary conditions must have been different because peaks of biogenic particle fluxes occurred during the beginning of the interglacial stages 5 and 1. The peaks of the Mn/Al ratio appear in the core sections representing high biogenic particle fluxes. It may be argued that the sudden increase of the sedimentation rates caused the burial of the Mn/Al peak (Berger et al., 1983), which is not very reasonable because the increase of organic matter supply would probably keep conditions reducing.

A more reasonable explanation which would also be able to explain the authigenic ^{238}U enrichment described before, is a cycling of Mn remobilization in the sediments and reprecipitation at the sediment water interface. This is consistent with an oxygenated water column during these periods which prevented the deposition of large amounts of authigenic ^{238}U.

An increased Mn inventory in the water column which was built up during periods of diminished glacial circulation with corresponding lower oxygen content in the Atlantic Ocean may also have been an additional source of Mn. The Mn may have been precipitated and deposited during the reestablishment of the circulation at the beginning of the interglacials (Mangini et al., 1990).

5 Reconstruction of the Paleoenvironmental Conditions at the ACC during the last 330 kyr

5.1 Interglacial Isotope Stage 9 and Glacial Stage 8 (330-244 kyr B.P.)

As only core PS1772-8 covers the complete period of the last 330 kyr, the reconstruction is started with isotope stage 9 at the location of the present day average sea ice maximum. During the beginning of interglacial stage 9, the winter sea ice boundary was shifted to a position south of the present one, giving way to an increased production and accumulation of biogenic opal. This is consistent with the results of Hodell (1993) who found the interglacial optima of the stages 9 and 11 to represent the warmest interglacial conditions in the Southern Ocean. However, only a small export paleoproductivity increase (maximum 10 $gC/m^2 \cdot yr$) is deduced from the biogenic barium rain and accumulation rates. The rain rates of ^{10}Be were very low, coinciding with the minimum of the rain of terrigenous material.

During the rest of stage 9 and during glacial stage 8, the location was ice covered during summer and winter, which strongly restricted biological production and particle fluxes. Export productivity values ranged at 5 $gC/m^2 \cdot yr$, which is only slightly higher than the very low values determined in sediment traps below permanent sea ice cover in the Weddell Sea (Wefer and Fischer, 1991). ^{10}Be rain rates exceeded the production by a factor of 2.5, indicating a terrigenous particle flux which was sufficient to cause boundary scavenging of ^{10}Be.

5.2 Interglacial Stage 7 (244-190 kyr B.P.)

During isotope stage 7 a continuous summer and winter sea ice cover still kept particle flux low at the location of core PS1772-8.

At the beginning of stage 7 an export paleoproductivity minimum is observed in the Subantarctic Zone from the beginning of the isotope stage 7 until about isotope event 7.4, followed by a period of full glacial conditions during the period from about 225 to 210 kyr B.P. (Full glacial conditions in the three northern cores are characterized by relative maxima of the rain rates of terrigenous material, ^{10}Be and the proxies for paleoproductivity. In contrast, in the two cores from the AZ full glacial conditions are characterized by low rain rates of the paleoproductivity proxies, caused by the extension of the sea ice cover). From 210 kyr B.P. until the end of stage 7, the results again indicate a lower biological activity in the surface waters. The contrasts between the interglacial conditions in stage 7 and the glacial ones in the following stage 6 were, however, not very strong, as deduced from the biogenic barium and the ^{10}Be rain rate records. This implies that the interglacial stage 7 was a period with intermediate paleoenvironmental conditions, contradicting results of Hodell (1993) who deduced strong interglacial conditions in the Southern Ocean

from a study of oxygen and carbon isotopes in ODP core 704A. Paleoproductivity ranges from almost 0 $gC/m^2 \cdot yr$ at the beginning of the stage to values of about 7 $gC/m^2 \cdot yr$ during the middle of the stage 7. The very beginning of stage 7 is also marked by a small peak of paleoproductivity (7 $gC/m^2 \cdot yr$).

An interpretation of the maxima and minima of the Subantarctic Zone records in terms of shifts of the high particle flux area in the south suggests conditions at the beginning and the end of stage 7 about equal or slightly colder relative to the present. A northward shift of the high particle flux area may have occurred from about 225 to 210 kyr B.P.

5.3 Glacial Stage 6 (190-130 kyr B.P.)

The end of interglacial stage 6 is covered by all 5 cores of the transect, permitting a more detailed paleoenvironmental reconstruction. An overview of the results of this study is given by six time slices representing the average values of each tracer for the interglacial optima of the Holocene and the isotope substage 5e and for the glacial stages 2-4 and 6 (Fig 30).

Full glacial conditions with peak paleoproductivity values of 7.5 $gC/m^2 \cdot yr$ in core PS2082-1 and still very low values around 3 $gC/m^2 \cdot yr$ in core PS1772-8 are observed. In these cores the entire stage 6 sections were analyzed. This suggests a northward shift of the high particle flux area by about 3 to 5° degrees. At the end of glacial stage 6, winter sea ice extended to the location of core PS1768-8, indicated by relatively low rain rates of biogenic opal (about 0.5 $g/cm^2 \cdot kyr$) and increased amounts of the sea ice indicating diatom species *N. curta* and *N. cylindrus* (Gersonde and Pätzold, 1992).

Throughout the transect, sediment rain rates amounted to about 1-1.5 $g/cm^2 \cdot kyr$ at the very end of isotope stage 6. At this time a decrease in the two northern cores resulted in an export productivity of about 3 to 10 $gC/m^2 \cdot yr$ in all cores of the transect, except PS2082-1 where productivity was almost zero. It can be argued that the winter sea ice cover already had started to retreat from the locations of the two southern cores. The end glacial export productivity was 2-3 times lower than the present day values at the Polar Front (Wefer and Fischer, 1991).

In summary, the data of this study suggest that, during the end of glacial stage 6, no high productivity area comparable to other periods was developed (taking into account the uncertainties of the mentioned decoupling between biogenic opal and barium). This period of low biological activity, which was clearly leading the transition from stage 6 to stage 5, suggests that the reorganisation of the ACC towards an interglacial mode was already beginning about 9 kyr before the end of glacial stage 6. This may also be deduced from the gradual increase of the productivity at the end of stage 6 in core PS1772-8.

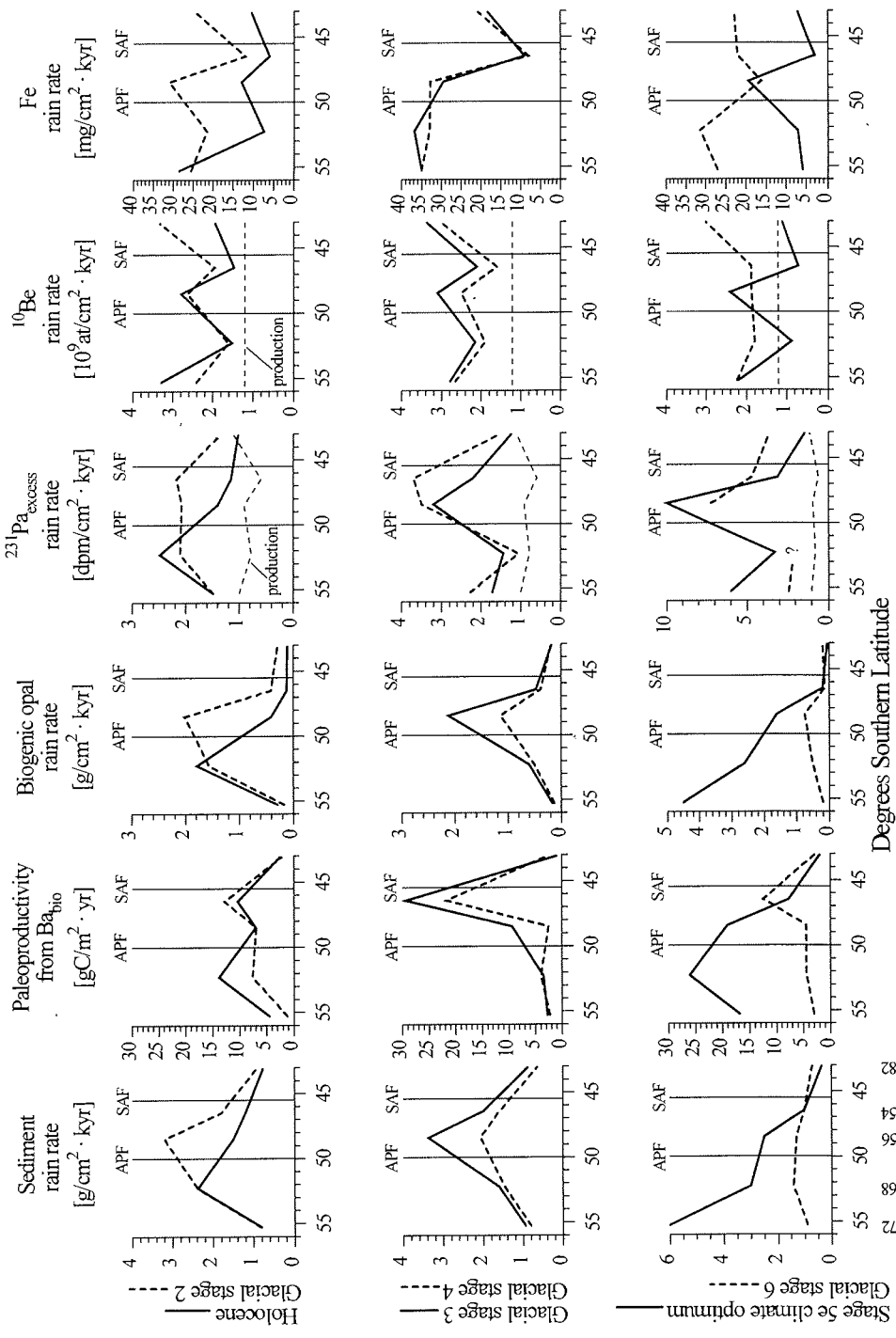
Sediment rain rate [g/cm² · kyr]
Paleoproductivity from Ba_bio [gC/m² · yr]
Biogenic opal rain rate [g/cm² · kyr]
231Pa_excess rain rate [dpm/cm² · kyr]
10Be rain rate [10⁹at/cm² · kyr]
Fe rain rate [mg/cm² · kyr]
APF
SAF
production
?
Holocene
Glacial stage 2
Glacial stage 3
Glacial stage 4
Stage 5e climate optimum
Glacial stage 6
PS1772
PS1768
PS1756
PS1754
PS2082
Degrees Southern Latitude

Figure 30: Time slices of the rain rates of total sediment, paleoproductivity, biogenic opal, $^{231}Pa_{ex}$, ^{10}Be and Fe as a measure for terrigenous material from 56°S to 43°S. The solid line time slices represent average values for the Holocene, the stage 3 and 5e, whereas the dashed line time slices represent the glacial stages 2, 4, and 6, as far as they are covered by the cores. The thin dashed lines at the $^{231}Pa_{ex}$ and ^{10}Be rain rate plots mark the values expected from production. The vertical lines at 50°S and 45.5°S mark the present day positions of the APF and the SAF, respectively.

5.4 Interglacial Substage 5e (130-111 kyr B.P.)

Most drastic changes in paleoenvironmental conditions at the ACC occurred at the transition from glacial stage 6 to interglacial substage 5e. Paleoproductivity reaches maximum values of 31 $gC/m^2 \cdot yr$ in core PS1772-8 and 30 $gC/m^2 \cdot yr$ in core PS1768-8, which is about double the present day value (Wefer and Fischer, 1991). It must, however, be stated that the biogenic barium rain rates were about three times higher than modelling calculations of Rutsch et al. (1995) allow (chapter 4.7), suggesting that there may have been an additional source of Ba for the AZ, at least during the climate optima. This additional contribution renders the applicability of biogenic Ba as a paleoproductivity tracer more uncertain. This aspect will be subject of future studies.

Peaks of $^{231}Pa_{ex}$ (up to 8 times higher than production) and biogenic opal rain rates (up to 6.5 $g/cm^2 \cdot kyr$), as well as the decrease of sea ice diatoms (Gersonde and Pätzold, 1992) and an abundance maximum of the radiolarian species *Antarctissa* (Abelmann, unpubl. results in Müller, 1992) indicate a shift of the winter sea ice boundary and thus also of the high biogenic particle flux area to a position south of core PS1772-8. The position of the winter sea ice boundary, however, probably was not shifted too far south of the location of PS1772-8. The maximum increase in biogenic particle flux of the transect in this core suggests that the productivity increase was caused by the proximity to the ice edge.

In the southern part of the Polar Frontal Zone a contemporaneous increase of the export productivity was also clearly developed, which means that the high biogenic particle flux area also extended to the north into the Polar Frontal Zone during stage 5e. Very low paleoproductivity is deduced from all parameters in the cores PS1754-1 and PS2082-1, which means that the high productivity area was located south of 48°S.

Within the isotope stage 5e, which was investigated at a very high time resolution of only a few hundred years per sample in cores PS1772-8 and PS1768-8, some variations of the paleoenvironmental conditions are recorded that might corroborate the strong paleotemperature variations recorded in the GRIP ice core (GRIP members, 1993; Taylor et al., 1993). The rain rate record of ^{10}Be in core PS1772-8 and the biogenic barium and biogenic opal records in the more northerly located core PS1768-8 might suggest that the period of high biogenic particle flux did not pass as undisturbed as for example the sediment rain rate record shows.

However, the significance of these variations is low and in many cases within the uncertainties of the data. It is also difficult to correlate these variations from core to core due to the too low precision of the dating within the isotope substage 5e in core

PS1768-8. The sedimentary records of this study can thus not decide wether the ice core record represents an artifact, caused by ice tectonics, or wether the observed variations in the GRIP ice core represent real paleoclimatic variations. More detailed investigation of these variations will be subject of a continuation of this study on high sedimentation rate cores from the Mid Atlantic Ridge area of the Southern Ocean.

The minimum ^{10}Be rain rate in all five cores of the transect and especially in the three southern cores, where export productivity was shown to have been relatively high, was probably caused by a drop of the supply of terrigenous material to the ACC. However, there was a biogenic contribution to the ^{10}Be rain rate in core PS1772-8 (Fig. 27).

The features of the Mn/Al ratios and authigenic ^{238}U concentrations suggest an improved ventilation of the deep water which started at the beginning of interglacial stage 5. This increase in oxygen may have been linked to an increased inflow of NADW into the Southern Ocean, as also indicated by the low carbonate dissolution in the two northern cores. In the southern part of the AZ the high accumulation rate of biogenic silica probably led to suboxic conditions in the sediments, caused by which a Mn cycling occurred, as indicated by high amounts of authigenic Mn.

5.5 Interglacial Substages 5d-a (111-74 kyr B.P.)

During the rest of isotope stage 5 the contrasts between the paleoenvironmental conditions in the northern and the southern part of the ACC were much less pronounced than during substage 5e. While the particle flux at the location of core PS1772-8 was again restricted by the permanent sea ice cover, paleoproductivity, biogenic opal and the $^{231}Pa_{ex}$ rate indicate relatively high biogenic particle fluxes at the location of core PS1768-8, where at the same time the existance of a seasonal sea ice cover is indicated by increased abundances of *N. curta* and *N. cylindrus*. The biogenic opal and the paleoproductivity record show a subdivision into the substages 5a to 5d, where paleoproductivity varies from 10 $gC/m^2 \cdot yr$ in the warmer substages to 4 $gC/m^2 \cdot yr$ in the colder substages. These values are in good agreement with the present day export productivity at the Polar Front determined by Wefer and Fischer (1991).

In the southern Polar Frontal Zone biogenic opal accumulation was comparable to the Antarctic Zone and then decreased sharply towards the north. In the middle of stage 5 a small excursion of higher biogenic particle fluxes is developed in core PS1754-1. Productivity decreased to quite low values between 2 and 10 $gC/m^2 \cdot yr$ in the southern Polar Frontal Zone but showed relatively high values of around 16 $gC/m^2 \cdot yr$ in the northern Polar Frontal Zone. All indicators suggest a relatively high particle flux in the Polar Frontal Zone and a low one in the Subantarctic Zone. Still relatively low rain rates of ^{10}Be and correspondingly low terrigenous supply is observed in the three northern cores. The paleoenvironmental conditions probably were intermediate between the glacial and interglacial extrema.

5.6 Glacial Stages 3 and 4 (74-24 kyr B.P.)

A northward shift of the high productivity area by about 3 to 5° from a position south of the Polar Front into the Polar Frontal Zone may be deduced from the proxy records in glacial stage 4 and even more pronounced in glacial stage 3. The maximum opal accumulation of the transect is found in the southern Polar Frontal Zone (up to 3 g/cm^2 · kyr), whereas the paleoproductivity maximum is more located in the northern Polar Frontal Zone. High particle fluxes are indicated by the $^{231}Pa_{ex}$ rain rates in the whole Polar Frontal Zone. The ^{10}Be rain rates were increased to values exceeding production by a factor of 2-3 in all cores caused by the increased terrigenous supply. Peak paleoproductivity values reach 42 gC/m^2 · yr in stage 3 during the period from about 30 to 40 kyr B.P. at the location of core PS1754-1 and about 19 gC/m^2 · yr at the location of PS1756-5, while at the same time paleoproductivity values between 2 and 5 gC/m^2 · yr are observed in the cores PS1768-8 and PS1772-8. These low values south of the Polar Front were caused by the northward extension of the winter sea ice cover, indicated by abundance maxima of *N. curta* and *N. cylindrus* (Gersonde and Pätzold, 1992). The amount of the paleoproductivity values implies that the high productivity area was shifted to the north during stages 4 and 3, and reached about the intensity of the paleoclimate optima in the Antarctic Zone.

During stage 4 high carbonate dissolution probably indicates a diminished admixture of oxygen rich NADW to the ACC, which subsequently was increased again during stage 3.

5.7 Glacial Stage 2 (24-12 kyr B.P.)

At the beginning of the last glacial, the winter sea ice boundary was shifted to the north by about 5-6° compared to the present day position. Productivity decreased to a minimum value of about 2 gC/m^2 · yr in the northern Antarctic Zone and was almost zero at the location of core PS1772-8, indicating a permanent sea ice cover during summer and winter. Relatively high paleoproductivity values between 5 and 16 gC/m^2 · yr are observed in the Polar Frontal Zone and a maximum of about 4 gC/m^2 · yr is observed in core PS2082-1.

Starting at about the LGM (about 18 kyr B.P.) the paleoenvironmental conditions changed in the Antarctic Zone. A gradual increase of the rain rates of biogenic barium and opal as well as $^{231}Pa_{ex}$ is observed, which is accompanied by a drop in the abundance of sea ice diatoms, significantly preceding the glacial/Holocene transition. At the same time the particle flux proxies do not show a significant decrease north of the APF, suggesting that the high particle flux area was enlarged. The intensity of particle flux during this period, however, was relatively low and about equal to the glacial values north of the APF. In the northern AZ the paleoproductivity increase starts at about 16 kyr B.P. and reaches full interglacial values of about 20 gC/m^2 · yr already at 14 kyr B.P., which indicates full deglaciation at about this period.

The ^{10}Be accumulation profiles show relatively high values throughout the whole transect, which are caused by the persisting high terrigenous input. Marked peaks of authi-

genic ^{238}U throughout the transect and high carbonate dissolution in the northern part suggest reduced NADW input and lower deep water oxygenation of the Southern Ocean.

5.8 Interglacial Stage 1 (12 kyr-B.P. to Present)

At the beginning of the stage 1 the peak warm climate forced the sea ice to retreat and the high productivity area shifted to a position south of the Polar Front again. Export productivity values of up to 20 $gC/m^2 \cdot yr$ and biogenic opal rain rates of up to 3 $g/cm^2 \cdot kyr$ were reached at the location of core PS1768-8. At the same time the proxy records only indicate a slight improvement of the conditions at core PS1772-8, suggesting that even the Holocene climate optimum was not strong enough to force the winter sea ice boundary far enough south to give way to a productivity increase comparable to the stage 5e. The Holocene climate optimum was again mirrored by a high rate of $^{231}Pa_{ex}$ and also a slight increase of biogenic ^{10}Be accumulation, caused by the increased biogenic particle fluxes.

In the Polar Frontal Zone and the Subantarctic Zone, very low productivity and particle fluxes were determined during the Holocene climate optimum, corroborating that the opal belt was again located south of the Polar Front. The record of core PS1756-5 which is located in the southern part of the PFZ suggests that siliceous particle fluxes were relatively high at the location of this core throughout the last 150 kyr, except the Holocene, when the particle fluxes drastically decreased.

When comparing the average values of the proxies for the stages 1 and 2 north and south of the Polar Front, it can be seen that the glacial stage 2 maxima north of the Polar Front are only slightly lower than the Holocene maximum south of the Polar Front, thus favouring a shift of the high productivity zone by about 3 to 5°.

Peaks of the Mn/Al ratio at the beginning of the Holocene core sections of all cores except PS1756-5 again indicate a better deep water ventilation, possibly linked to a restarting input of NADW into the ACC. This may also be deduced from the low carbonate dissolution intensity in the northern part of the transect.

After the Holocene climate optimum, productivity decreased again south of the Polar Frontal Zone, leading to the present day situation with moderate export productivity and biogenic particle fluxes at the APF and in the AZ on one hand and low biological activity in the northern PFZ and the SAZ on the other, which is about comparable to the overall situation during isotope stages 5a-d.

5.9 The Southern Ocean: The Missing Sink of Glacial CO_2?

Which are the conclusions concerning an increased Southern Ocean paleoproductivity and thus also a glacial CO_2 sink, that may be drawn from this study? Can the results of Mortlock et al. (1991) and Charles et al. (1991) of a lower glacial productivity be supported or does the hypothesis of Martin (1990) which was recently strengthened by

the results of the iron experiment in the equatorial Pacific (Martin et al., 1994) revive the modelling results of Sarmiento and Toggweiler (1984) and Keir (1988), as suggested by Kumar (1994)?

The hypothesis of Kumar (1994) is based on the assumption that an increased supply of aeolian dust and thus also of iron, originating from the Patagonian deserts, during glacials enhances paleoproductivity following the hypothesis of Martin (1990). However, there is a fundamental discrepancy in the interpretation of glacial productivity north of the APF, deduced from the accumulation of authigenic uranium, between this study and the one of Kumar (1994). In both studies, high authigenic uranium contents were determined in the glacial core sections of the Polar Frontal Zone and the Subantarctic Zone. Interpreting high authigenic uranium contents in terms of high accumulation of C_{org}, led Kumar to the conclusion that there was a decoupling of the biogenic opal fluxes from the C_{org} fluxes during the glacials in the Polar Frontal Zone and the Subantarctic Zone. Kumar inferred an overall higher glacial productivity referring to the northward shift of the high particle flux area and the C_{org} accumulation rates calculated from the authigenic uranium contents.

The authigenic uranium hypothesis remains highly questionable because in the cores of this study no higher glacial authigenic ^{238}U accumulation rates than in the AZ could be determined in the northern PFZ and the SAZ. In contrast, highest values were determined in the glacial stage 2 section of core PS1768-8, where productivity was shown to be lower in the glacials than in the Holocene.

In this study, as in the study of Kumar, a higher glacial supply of aeolian dust may be deduced from the iron and Al_2O_3 rain rates, which show very low values in the peak interglacial sections and are increased in the sections representing lower glacial sea level. If, however, the iron input really was the biolimiting factor for Southern Ocean productivity, the glacial periods throughout the transect should yield higher export productivity values, which they do not. Only the cores from the PFZ and the SAZ show an increased glacial productivity, which, however, probably was caused by the northward shift of the high productivity area. As demonstrated in chapter 4.3.3, the amount was equal or slightly lower compared to the values calculated for the interglacial sediments south of the APF.

In the Antarctic Zone pronounced maxima of the paleoproductivity coincide with strong minima of the aeolian dust and iron supply. This strongly suggests that the iron limitation (Martin, 1990; Martin et al. 1994) is not valid for the Antarctic Zone of the ACC, as also suggested by Kumar (1994). There are probably other processes such as sea ice dynamics and the pattern of upwelling of deep waters, loaded with iron in the PFZ and not in the AZ (de Baar et al., 1994), which control paleoproductivity and biogenic particle flux in the AZ of the ACC.

In summary, the results of this study favour an interpretation of an overall slightly lower glacial productivity of the eastern Atlantic sector of the Southern Ocean during the last 150,000 years, and thus do not support the hypothesis of a glacial Southern Ocean CO_2 sink.

This is consistent with the lower glacial $\delta^{13}C$ values of planktonic foraminifera in the Southern Ocean (Charles and Fairbanks, 1990) and thus resolves the contradiction that a higher glacial paleoproductivity caused by a more efficient nutrient utilization would have increased the planktonic $\delta^{13}C$. The northern Atlantic may have played a more important role in controlling the global CO_2 dropdown as recently proposed by Heinze and Broecker (1995) who modelled a close off of the Southern Ocean surface for gas exchange and carbon export. In their model the unexpected increase of atmospheric CO_2 after a close off could be compensated by an increase in nutrient utilization in the northern Atlantic, consistent with observations of a higher glacial $\delta^{13}C$ gradient in the northern Atlantic, reported for example by Boyle and Keigwin (1987). However, even a complete surface water nutrient consumption in the northern Atlantic is not able to reduce glacial atmospheric CO_2 by the observed 90 ppmV (Barnola et al., 1987). Thus, the missing sink of glacial CO_2 has still not been found.

5.10 Reliability of the Results

Although the different tracers yield a more or less consistent scenario of the paleoenvironmental conditions there are still discrepancies. As stated above, the overall patterns and relative variations of proxy rain rates mostly agree with the results of Kumar (1994) who analyzed sediments from comparable locations at the ACC. His absolute values of the ^{230}Th normalized rain rates of total sediment, the biogenic barium and opal and the lithogenic material are corroborated by this study.

However, there are differences in the absolute values of the rain rates, especially ^{10}Be and $^{231}Pa_{ex}$. For the $^{231}Pa_{ex}$ results of this study it may be argued that the statistical uncertainties of the measurement account for the discrepancies. For the ^{10}Be concentrations and consequently also for the ^{10}Be rain rates, where the results of Kumar are higher throughout all zones of the ACC, this is certainly not the case. The ^{10}Be rain rates in two cores from the AZ, not very far from the two cores of this study, are a factor of 2 to 3 higher, which certainly can not be explained by differences in scavenging intensity or differences in the paleoenvironmental conditions at such a small distance. Comparatively high $^{230}Th_{ex}$ normalized ^{10}Be rain rates have never previously been reported. If these values are indeed too high, as the results of this study suggest, then also the interpretation concerning the ^{10}Be geochemistry of Kumar (1994) would be different. If on the other hand, the results of this study are too low, scavenging of ^{10}Be by biogenic material plays a more important role in accumulating ^{10}Be at the ACC then estimated.

An interlaboratory comparison will show whether any differences in chemical preparation are responsible for the systematic offset, because the measurement procedure of the ^{10}Be concentrations at the ETH Zürich AMS facility was exactly the same.

5.11 Outlook to Future Work

With this study it was possible to add some parts to the puzzle of the Late Quaternary paleoenvironmental conditions in the Atlantic sector of the Southern Ocean. Some questions, however, remain still unsolved or were even raised by the results:

- The spatial density of data concerning the ^{10}Be and biogenic Ba rain rates has to be increased in order to understand the transport and burial processes of both elements.
- Detailed modelling of the authigenic uranium accumulation rates in connection with C_{org} and bulk sediment accumulation rates must be provided to achieve further information on glacial deep water oxygen content and thus also on the intensity of glacial NADW input into the Southern Ocean.
- Further, it is necessary to find more suitable sediment cores with a sufficient time resolution of the sections representing isotope stage 5e. A sedimentary proof for a possible stage 5e climate variability will significantly contribute to the understanding of the processes that run global climate change. Such sediment material was recovered during RV Polarstern Cruise XI-2 (Gersonde, 1995) on the Mid Atlantic Ridge in the eastern Atlantic sector of the ACC and will be subject to further investigations. In addition, some of these cores are nowadays bathed in NADW and it is planned to compare glacial/interglacial $^{231}Pa_{ex}$ rain rates to evaluate the paleointensity of NADW input in the past.
- Probably the most important result: for reconstructions of paleoenvironmantal conditions by means of proxy tracer rain rates lateral sediment redistribution by normalization to $^{230}Th_{ex}$ has to be considered. Unfortunately this normalization to $^{230}Th_{ex}$ is only possible for the last about 250 kyr. Future efforts should focus on the finding of other more stable parameters that provide a quantification of sediment redistribution. This will permit reliable reconstructions also for sediments older than 250 kyr.

6 Summary

$^{230}Th_{ex}$ High Resolution Dating

Applying the $^{230}Th_{ex}$ dating method, average sedimentation rates for the 5 cores of the transect could be estimated and may serve as a time frame for previous stratigraphic and paleoenvironmental investigations. It turned out that earlier stratigraphies could be mostly corroborated, which implies that the method may also be applied to gain rough estimates on sedimentation rates and ages of sediment cores, where no other stratigraphic information exists and although significant variations of the sedimentation rates within the core may have occurred. Unfortunately, the only core where the method was planned to be applied without detailed additional information on stratigraphy, could not be dated due to an insignificant downcore decrease of the $^{230}Th_{ex}$ concentrations.

After the core depths of the main climatic transitions in the cores were fixed, $^{230}Th_{ex}$ constant flux models were run to achieve a high resolution record of the sedimentation rates within the isotope stages. It could be shown that in the southern core PS1772-8 the diatomaceous ooze section deposited during sea ice free conditions, previously believed to represent the isotope stage 5, was deposited during about 8 kyr at the beginning of isotope stage 5e. Similarly, in the northern AZ and the southern PFZ during stage 5e diatomaceous oozes were deposited within relatively short periods of time. In the northern AZ a drastic increase of the sedimentation rates is observed in the Holocene climate optimum. In the SAZ a continuous increase of the sedimentation rates during isotope stage 6 is determined by $^{230}Th_{ex}$ constant flux modelling.

Quantification of Lateral Sediment Redistribution

A comparison of the accumulation rates of $^{230}Th_{ex}$ to the values expected from production shows that lateral sediment redistribution locally affected the accumulation rates during certain periods severely. During the Holocene, sediment focusing contributed up to six times more sediment than accumulated vertically to the location of core PS1768-8. The same focusing intensity was determined for the glacial stage 2 section of core PS2082-1. During stage 3 winnowing caused by bottom currents only left about 25-50 % of the vertically accumulating sediment at the locations of the two cores from the PFZ. All sediment accumulation rates were corrected for sediment redistribution effects by normalization to the $^{230}Th_{ex}$ concentrations, which enables the calculation of the "true" vertical particle rain rates. Only these vertical rain rates deliver reliable accumulation rates of any proxy tracer, which then may be compared between different locations and which may be applied for the balancing of any constituent in the ocean.

Paleoproductivity Reconstructions

The pattern of the vertical sediment rain rates and the biogenic opal rain rates suggest a glacial northward shift of the high biogenic particle flux area, presently located south

of the APF, by about 3-5°, where the amount of peak particle fluxes was slightly lower in the PFZ than in the AZ. During the isotope stage 5e the high particle flux area was extended to the north as well as to the south, compared to the present day situation.

Export paleoproductivity was calculated applying the vertical biogenic barium rain rates and the total, not redistribution corrected sediment accumulation rates to account for the degree of preservation of biogenic barium. Peak paleoproductivity values around 30 $gC/m^2 \cdot yr$ are calculated for the interglacial climate optima 5e and 1 in the AZ. In the northern cores glacial paleoproductivity was higher than during the interglacials and the peak values are about comparable to the AZ. This suggests that a glacial northward shift of the high productivity area occured, which was possibly accompanied by a weakening of the gradients at the frontal systems. However, as demonstrated by a comparison of biogenic Ba and biogenic ^{10}Be in the two southern cores, there may have been an additional source of excess Ba during the climate optima in the AZ which may render export paleoproductivity deduced from biogenic Ba too high.

Paleoenvironmental Information from $^{231}Pa_{ex}$

Rain rates of $^{231}Pa_{ex}$ higher than the production rate in the AZ and the PFZ throughout most of the last 150 kyr corroborate high biogenic particle fluxes. The $^{231}Pa_{ex}$ rain rate pattern shows a positive correlation to the periods of increased biogenic particle flux with peak values during the climate optima south of the APF. In the PFZ relatively high rain rates of $^{231}Pa_{ex}$ are determined more or less throughout the cores. North of the SAF low $^{231}Pa_{ex}$ rain rates indicate a low biogenic particle flux. Apparently, the rain of biogenic particles primarily controls the scavenging of $^{231}Pa_{ex}$ to the sediments and thus the $^{230}Th_{ex}$ normalized rain rates of $^{231}Pa_{ex}$ may serve as a tracer for paleoproductivity in the Southern Ocean. This pattern is confirmed by investigations of Kumar (1994) with lower statistical uncertainties of the ^{231}Pa measurements.

A diminished admixture of NADW during glacials was suggested to result in a rise of the glacial CCD and thus a severe carbonate dissolution by various investigations. This could also be observed in the pattern of the $^{230}Th_{ex}/CaCO_3$ ratio in the Agulhas Basin sediments of this study. Peak $^{231}Pa_{ex}$ rain rates during the interglacial stage 5e exceed production by up to a factor of 10, keeping in mind the high statistical uncertainties. This can hardly be explained by boundary scavenging effects alone. An increased input of ^{231}Pa with NADW at the beginning of the interglacials may help to explain the observed $^{231}Pa_{ex}$ rain rate peaks.

Paleoenvironmental Information from ^{10}Be

In contrast to expectations, the rain rates of ^{10}Be which were corrected for production rate changes caused by variations of the geomagnetic field intensity, did not show an enhancement of the deposition during the interglacial climate optima in the AZ but, exactly opposite, mimima are observed. North of the APF pronounced peak ^{10}Be rain

rates coinciding with increased biogenic particle fluxes are determined. Minimum ^{10}Be rain rates occurred in all cores of the transect during the Holocene and, with the exception of PS1756-5, during the stage 5e climate optimum.

The rain rates of terrigenous particles are the only parameters which show a good correlation with the ^{10}Be rain rates, which suggests that aluminosilicates are the main factors controlling the scavenging of ^{10}Be at the ACC, no matter how high biogenic particle fluxes may be. The terrigenous material probably originates from aeolian dust flux from the Patagonian deserts with additional amounts of IRD derived from melting icebergs in the southern part of the ACC transect. Calculating a terrigenous background level of ^{10}Be deposition, the biogenic ^{10}Be rain rates may be evaluated. It appears that in the AZ during the climate optima an increased amount of ^{10}Be was deposited, which may be ascribed to scavenging by biogenic particles. North of the APF no such increase may be observed but, opposite, the biogenic ^{10}Be rain rates show pronounced minima during periods of higher biogenic particle fluxes. This may be explained by an increased ratio between fine grained wind blown dust particles and relatively low biogenic particle fluxes in the northern part of the transect. $^{230}Th_{ex}$ normalized ^{10}Be rain rates may thus not be considered a suitable tracer for biogenic particle fluxes but, instead, trace the input of fine grained terrigenous material.

Geochemical Tracers: Authigenic Uranium and Manganese

Authigenic ^{238}U and Mn/Al ratios were applied for tracing past changes of the redox conditions of the surface sediments and the deep water. Reducing conditions, on the one hand caused by enhanced accumulation of organic matter and/or also by a lower deep water oxygen content, caused an accumulation of authigenic ^{238}U during glacial periods in all cores except PS1772-8. In this core and also in core PS1754-1 this is a consequence of the very low sediment accumulation rates which allowed a postdepositional burn-down of the accumulated uranium. At the locations of the cores PS1772-8 and PS1756-5, the stage 5e accumulation of authigenic ^{238}U probably was mainly controlled by the accumulation of organic matter. Peaks of the Mn/Al ratios mark transitions from reducing to oxidizing conditions, i.e. the transitions from glacials to interglacials. There are indications for a Mn cycling during the high productivity periods in the AZ which requires an oxygenation of the deep water.

The Iron Hypothesis

The hypothesis of a fertilization of the glacial Southern Ocean and thus a higher nutrient utilization by the increased supply of biolimiting iron can at least for the high productivity areas south of the APF not be corroborated, if it is assumed that the glacial increase of the rain rate of terrigenous material by a factor of up to 5 also releases a lot of iron to the Southern Ocean surface water. The increase in terrigenous input obviously is not accompanied by an increase of biogenic particle flux and export paleoprodcutivity in the AZ.

Glacial Southern Ocean as CO_2 Sink?

Altogether, the results of the proxy records suggest that the export paleoproductivity in the glacial Southern Ocean was not increased compared to the interglacials. Thus the hypothesis of the Southern Ocean being the glacial sink for atmospheric CO_2 is not supported by the results of this study.

Acknowledgements

First of all, I want to thank my advisor Prof. Augusto Mangini for his support and creative ideas through the last three years. Discussions about scientific problems have always been exciting and encouraging as long as the telephone did not ring.

I want to thank Prof. Dr. German Müller for the second expert opinion.

Michiel Rutgers van der Loeff and Rainer Gersonde at the A.W.I. in Bremerhaven have been enthousiastic and motivating participants in this study, which would not have been possible to be completed in this form without their contribution of unpublished results and discussions. I am also very much indebted to Gerhard Kuhn, A.W.I, for the unpublished physical property and carbonate data and a number of other researchers at the A.W.I. for their unpublished data, which appeared in the Arbeits- und Ergebnisbericht of the SFB 261, 1992. Thanks also to Gerhard Bohrmann, GEOMAR, Kiel, for his unpublished biogenic opal data and Gerhard Fischer, Fachbereich Geowissenschaften, Universität Bremen, for his unpublished $\delta^{13}C$ data of core PS1756-5. Christine Nürnberg, GEOMAR, Kiel, provided the biogenic Ba data.

I would also like to thank Martin Suter, Georges Bonani and all other people of the AMS facility at the Institut für Teilchenphysik of the ETH Zürich for sharing the nights of the measurements with me. Especially, I want to thank Beate Dittrich-Hannen and Peter Kubik for their interest in this work and the Swiss clock work like ^{10}Be data.

It has always been a lot of fun to be a member of the unbeatable "Paläos"-team of the Heidelberger Akademie der Wissenschaften at the Institut für Umweltphysik of the Universität Heidelberg. I also want to thank Achim Walter for full time AAS HiWi activity.

David Peate corrected the manuscript for German English. Katrin Rempp and Martin Jung helped to overcome TEXnical problems.

Last but not least I want to thank my wife Claudia for her support and for bearing quite a large number of lonesome evenings, especially during the last six months of this study.

7 References

Abelmann, A. and Gersonde, R. (1988): Cycladophora davisiana stratigraphy in Plio/ Pleistocene sediment cores from the Antarctic Ocean (Atlantic sector).- Micropaleontology 34, 268-276.

Abelmann, A. and Gersonde, R. (1991): Biosiliceous particle flux in the Southern Ocean.- Mar. Chem. 35, 503-536.

Anderson, R.F., Bacon, M.P. and Brewer, P.G. (1983a): Removal of ^{230}Th and ^{231}Pa from the open ocean.- Earth Planet. Sci. Lett. 62, 7-23.

Anderson, R.F., Bacon, M.P. and Brewer, P.G. (1983b): Removal of ^{230}Th and ^{231}Pa at ocean margins.- Earth Planet. Sci. Lett. 66, 73-90.

Anderson, R.F., Lao, Y., Broecker, W.S., Trumbore, S.E., Hofmann, H.J. and Wölfli, W. (1990): Boundary scavenging in the Pacific Ocean: a comparison of ^{10}Be and ^{231}Pa.- Earth Planet. Sci. Lett. 96, 287-304.

Anderson, R.F., Fleisher, M.Q., Biscaye, P.E., Kumar, N., Dittrich, B., Kubik, P., and Suter, M. (1994): Anomalous boundary scavenging in the Middle Atlantic Bight: evidence from ^{230}Th, ^{231}Pa, ^{10}Be and ^{210}Pb.- Deep-Sea Research II 41, 537-561.

Bacon, M.P. and Anderson, R.F. (1982): Distribution of thorium isotopes between dissolved and particulate forms in the deep-sea.- J. Geophys. Res. 87, 2045-2056.

Bacon, M.P. (1984): Glacial to interglacial changes in carbonate and clay sedimentation in the Atlantic estimated from thorium-230 measurements.- Isot. Geosci. 2, 97-111.

Bard, E. (1988): Correction of accelerator mass spectrometry ^{14}C ages measured in planktonic foraminifera: paleoceanographic implications.- Paleoceanography 3, 635-645.

Bard, E., Hamelin, B., Fairbanks, R.G. and Zindler A. (1990): Calibration of the ^{14}C timescale over the past 30,000 years using mass spectrometric U-Th ages from Barbados corals.- Nature 345, 405-410.

Bareille , G., Labracherie, M., Labeyrie, L., Pichon, J.J. and Turon, L. (1991): Biogenic silica accumulation rate during the Holocene in the southeastern Indian Ocean.- Mar. Chem. 35, 537-551.

Barnes, C.E. and Cochran, J.K. (1990): Uranium removal in oceanic sediments and the oceanic uranium balance.- Earth Planet. Sci. Lett. 97, 94-104.

Barnola, J.M., Raynaud, D. and Korotkevich, Y.S. (1987): Vostok ice core provides 160.000 year record of atmospheric CO_2.- Nature 329, 408-414.

Bathmann, U., Schulz-Baldes, M., Fahrbach, E., Smetacek, V. and Hubberten, H.-W. (1992): Die Expeditionen ANTARKTIS-IX/1-4 des Forschungsschiffes "Polarstern" 1990/91.- Ber. Polarforsch. 100, 403 pp.

Berger, W.H., Fischer, K., Lai, C., Wu, G. (1987): Ocean productivity and organic carbon flux, part 1: Overview and maps of primary production and export production.- SIO Reference Series 87-30, Scripps Institution of Oceanography, 67 pp.

Berger, W.H. (1989): Global maps of ocean productivity.- in: Productivity of the Oceans: Present and Past, edited by Berger, W.H., Smetacek, V.S. and Wefer, G., J. Wiley, NewYork, 429-455.

Berger, W.H. (1991): No change down under.- Nature 351, 186-187.

Berger, W.H., Finkel, R.C., Killingley, J.S. and Marchig, V. (1983): Glacial-Holocene transition in deep-sea sediments: Manganese-spike in the East-Equatorial Pacific.- Nature 303, 231-233.

Best, M.G. (1982): Igneous and Metamorphic Petrology.- W.H. Freeman, San Francisco.

Bhat, S.G., Krishnaswami, S., Lal, D., Rama and Moore, W.S. (1969): $^{234}Th/^{238}U$ ratios in the ocean.- Earth Planet. Sci. Lett. 5, 483-491.

Bishop, J.K.B. (1988): The barite-opal-organic carbon association in oceanic particulate matter.- Nature 332, 341-343.

Bond, G., Heinrich, H., Broecker, W.S., Labeyrie, L., McManus, J., Andrews, J., Huon, S., Jantschik, R., Clasen, S., Simet, C., Tedesco, K., Klas, M., Bonani, G. and Ivy, S. (1993): Evidence for massive discharge of icebergs into the North Atlantic ocean during the last glacial period.- Nature, 360, 245-249.

Bourlés, D.L., Raisbeck, G.M. and Yiou, F. (1989a): ^{10}Be and ^{9}Be in marine sediments and their potential for dating.- Geochim. Cosmochim. Acta 53, 443-452.

Bourlés, D.L., Klinkhammer, G., Campbell, A.C., Measures, C.I., Brown, E.T. and Edmond, J.M. (1989b): Beryllium in marine pore waters: Geochemical and geochronological implications.- Nature 341, 731-733.

Bourlés, D.L., Raisbeck, G.M., Brown, E.T., Yiou, F., and Edmond, J.M. (1991): Beryllium isotope systematics of submarine hydrothermal sediments.- Earth Planet. Sci. Lett. 105, 534-542.

Boyle, E.A. (1988a): The role of vertical chemical fractionation in controlling late Quaternary atmospheric carbon dioxide.- J. Geophys. Res. 93, 15701-15714.

Boyle, E.A. (1988b): Cadmium: chemical tracer of deep-water paleoceanography.- Paleoceanography 3, 471-489.

Boyle, E.A. (1992): Cadmium and $\delta^{13}C$ paleochemical ocean distributions during the stage 2 glacial maximum.- Annual Review of Earth and Planetary Sciences 20, 245-287.

Boyle, E.A. and Keigwin, L. (1987): North Atlantic thermohaline circulation during the past 20,000 years linked to high latitude surface temperature.- Nature 330, 35-40.

Boyle, E.A. and Weaver, A. (1994): Conveying past climates.- Nature 372, 41-42.

Broecker, W.S. (1984): Terminations, Milankovitch and Climate.- Lamont Doherty Geological Observatory, NY, D. Reidel Publishing Company.

Broecker, W.S. (1993): An oceanographic explanation for the apparent carbon isotope-cadmium discrepancy in the glacial Antarctic.- Paleoceanography 8, 137-139.

Broecker, W.S. and Peng, T.-H. (1982): Tracers in the Sea.- Lamont- Doherty Earth Obs., Columbia University, USA.

Broecker, W.S. and Denton, G.H. (1989): The role of ocean atmosphere reorganisations in glacial cycles.- Geochim. Cosmochim. Acta 53, 2465-2501.

Broecker, W.S. and Peng, T.-H. (1989): The cause of the glacial to interglacial atmospheric CO_2 change: A polar alkalinity hypothesis.- Global Biochem. Cycles 3, 215-239.

Brown, E.T., Measures, C.I., Edmond, J.M., Bourlés, D.L., Raisbeck, G.M. and Yiou, F. (1992): Continental inputs of beryllium to the oceans.- Earth Planet. Sci. Lett. 114, 101-111.

Burckle, L.H. and Cooke, D.W. (1983): Late Pleistocene Eucampia antarctica abundance stratigraphy in the Atlantic sector of the Southern Ocean.- Micropaleontology 29, 6-10.

Calvert, S.E. (1976): The mineralogy and geochemistry of near shore sediments.- in: Chemical Oceanography, 2nd ed., Vol. 6, edited by Riley, J.P. and Chester, R., New York, Academic, chapter 33, cited in Holland (1984).

Calvert, S.E., Nielsen, B. and Fontugne, M.R. (1992): Evidence from nitrogen isotope ratios for enhanced productivity during formation of eastern Mediterranean sapropels.- Nature 359, 223-225.

Carmack, E.C. and Foster, T.D. (1975): On the flow of water out of the Weddell Sea.- Deep-Sea Res. 22, 711-724.

Charles, C.D. and Fairbanks, R.G. (1990): Glacial to interglacial changes in the isotopic gradients of the Southern Ocean surface water.- in: Geological History of the Polar Oceans: Arctic versus Antarctic, edited by Bleil, U. and Thiede, J., Kluwer Academic, Norwell, Mass., 519-538.

Charles, C.D., Froelich, P.N., Zibello , A., Mortlock, R.A. and Morley, J.J. (1991): Biogenic opal in Southern Ocean sediments over the last 450,000 years: implications for surface water chemistry and circulation.- Paleoceanography 6, 697-728.

Charles, C.D. and Fairbanks, R.G. (1992): Evidence from Southern Ocean sediments for the effect of North Atlantic deep-water flux on climate.- Nature 355, 416-419.

Chester, R. and Aston, S.R. (1976): The geochemistry of deep-sea sediments.- in: Chemical Oceanography, 2nd ed. vol. 6, edited by Riley, J.P. and Chester, R., New York, Academic, chapter 34, cited in Holland (1984).

CLIMAP Project Members (1976): The surface of the ice-age earth.- Science 191, 1131-1137.

CLIMAP-Members (1984): The last interglacial ocean.- Quat. Res. 21, 123-224.

Coale, K.H. and Bruland, K.W. (1985): ^{234}Th :^{238} U disequilibria within the California Current.- Limnol. Oceanogr. 30, 22-33.

Cochran, J.K. and Osmond J.K. (1976): Sedimentation patterns and accumulation rates in the Tasman Basin.- Deep-Sea Research 23, 193-210.

Cochran, J.K. and Krishnaswami, S. (1980): Radium, thorium, uranium and Pb-210 in deep-sea sediments and sediment pore waters from the North Equatorial Pacific.- Am. J. Sci. 280, 849-889.

Dansgaard, W., Clausen, H.B., Gundestrup, N., Hammer, C.U., Johnsen, S.J., Kristindottir, P. and Reeh, N. (1982): A new Greenland deep ice core.- Science 218, 1273-1277.

De Angelis, M., Barkov, N.I. and Petrov, V.N. (1987): Aerosol concentrations over the last climatic cycle (160 kyr) from an Antarctic ice core.- Nature 325, 318-321.

De Baar, H.J.W., de Jong, J.T.M., Bakker, D.C.E., Löscher, B.M., Veth, C., Bathmann, U. and Smetacek, V. (1995): Importance of iron for plankton blooms and carbon dioxide drawdown in the Southern Ocean.- Nature 373, 412-415.

Dehairs, F., Chesselet, R. and Jedwab, J. (1980): Discrete suspended particles of barite and the barium cycle in the open ocean.- Earth Planet. Sci. Lett. 49, 528-550.

De Master, D. (1981): The supply and accumulation of silica in the marine environment.- Geochim. Cosmochim. Acta 45, 1715-1732.

Duce, R.A. and Tindale, N.W. (1991): Atmospheric transport of iron and its.deposition in the ocean.- Limnol. Oceanogr. 36, 1715-1726.

Dymond, J., Suess, E. and Lyle, M. (1992): Barium in deep-sea sediment: A geochemical indicator of paleoproductivity.- Paleoceanography 7, 163-181.

Eisenhauer, A. (1989): ^{10}Be und ^{230}Th: Eine Zwei Tracer Studie mariner Sedimente.- Ph.D. thesis, Univ. Heidelberg, Heidelberg, Germany, 113 pp.

Eisenhauer, A., Mangini, A., Botz, R., Walter, P., Beer, J., Bonani, G., Hofmann, H.-J., Suter, M. and Wölfli, W. (1990): High resolution ^{10}Be und ^{230}Th stratigraphy of late Quaternary sediments from the Fram Strait (core 23235).- in: Geological History of the Polar Oceans: Arctic versus Antarctic, edited by Bleil, U. and Thiede, J., Kluwer Academic, Norwell, Mass., 475-487.

Eisenhauer, A., Spielhagen, R.F., Frank, M., Hentzschel, G., Mangini, A., Kubik, P.W., Dittrich-Hannen, B., Billen, T. (1994): ^{10}Be records of sediment cores from high northern latitudes: Implications for environmental and climatic changes.- Earth Planet. Sci. Lett. 124, 171-184.

Fichefet, T., Hovine, S. and Duplessy, J.-C. (1994): A model study of the Atlantic thermohaline circulation during the last glacial maximum.- Nature 372, 252-255.

Field, M. H., Huntley, B. and Muller, H. (1994): Eemian climate fluctuations observed in a European pollen record.- Nature 371, 779-783.

Fischer, G., Fütterer, D., Gersonde R., Honjo, S., Ostermann, D. and Wefer, G. (1988): Seasonal variability of particle flux in the Weddell Sea and its relation to ice cover.- Nature 335, 426-428.

Fischer, G., Bohrmann, G. and Gersonde, R. (1995): The Late Quaternary δ^{13}C record in the Antarctic Circumpolar Current (eastern Atlantic sector): paleoceanographic implications.- submitted to Geol. Rundsch.

Flanagan, F.J. (1968): U.S. Geological Survey Standards II: First Compilation of data for the U.S.G.S. rocks.- Geochim. Cosmochim. Acta 33, 81-120.

Foldvik, A. and Gammelsrød, T. (1988): Notes on Southern Ocean hydrography, sea-ice and bottom water formation.- Paleogeogr., Paleoclimatol., Paleoecol. 67, 3-17.

Foster, T.D., Foldvik, A. and Middleton, J.H. (1987): Mixing and bottom water foramtion in the shelf break region of the southern Weddell Sea.- Deep-Sea Res. 34, 1771-1794.

Francois, R., Bacon, M.P. and Suman, D. (1990): Thorium 230 profiling in deep-sea sediments: High resolution records of flux and dissolution of carbonate in the equatorial Atlantic during the last 24,000 years.- Paleoceanography 5, 761-787.

Francois, R., Altabet, M.A. and Burckle L.D. (1992): Glacial to interglacial changes in surface nitrate utilization in the Indian sector of the Southern Ocean as recorded by sediment δ^{15}N.- Paleoceanography 7, 589-606.

Francois, R., Bacon, M.P., Altabet, M.A. and Labeyrie, L.D. (1993): Glacial/interglacial changes in sediment rain rate in the SW Indian sector of Subantarctic waters as recorded by ^{230}Th, ^{231}Pa, U, and δ^{15}N.- Paleoceanography 8, 611-629.

Francois, R., Honjo, S., Manganini, S.J. and Ravizza, G.E. (1995): Biogenic barium fluxes to the deep-sea: Implications for paleoproductivity reconstruction.- Global Biochemical Cycles 9, 289-303.

Frank, M., Eckhardt, J.-D., Eisenhauer, A., Kubik, P.W., Dittrich-Hannen, B. and Mangini, A. (1994): Beryllium 10, thorium 230 and protactinium 231 in Galapagos Microplate sediments: Implications for hydrothermal activity and paleoproductivity changes during the last 100.000 years.- Paleoceanography 9, 559-578.

Frank, M., Eisenhauer, E., Bonn, W.J., Walter, P., Grobe, H., Kubik, P.W., Dittrich-Hannen, B. and Mangini, A. (1995): Sediment redistribution versus paleoproductivity change: Weddell Sea Margin sediment stratigraphy for the last 250,000 years deduced from $^{230}Th_{ex}$, ^{10}Be and biogenic barium profiles.- Earth Planet. Sci. Lett. in press

Frank, M., Gersonde, R., Rutgers van der Loeff, M., Kuhn, G. and Mangini, A. (1995): Late Quaternary sediment dating and quantification of lateral sediment redistribution applying $^{230}Th_{ex}$: A study from the eastern Atlantic sector of the Southern Ocean.- submitted to Geol. Rundsch.

Frank, N. and Mangini, A. (1995): A simplified procedure for the determination of ^{231}Pa in Mn encrustations.- Nucl. Instrum. Meth. Phys. Res. B 101, 258-262.

Frank, N., Scholz, A., Eisenhauer, A. and Mangini, A. (1995): High resolution $^{230}Th/^{231}Pa$ activity ratios in two Mn crusts from the Pacific Ocean.- submitted to Geochim. Cosmochim. Acta.

Froelich, P. N., Klinkhammer, G.P., Bender, M.L., Luedtke, N.A., Heath, G.R., Cullen D., Dauphin, P., Hammond, D., Hartman, B., Maynard, V. (1979): Early oxydation of organic matter in pelagic sediments of the eastern equatorial Atlantic: suboxic diagenesis.- Geochim. Cosmocim. Acta 43, 1075-1090.

Frost, B.W. (1991): The role of grazing in nutrient-rich areas of the open sea.- Limnology and Oceanography 36, 1616-1630.

Gersonde, R. and Hempel, G. (1990): Die Expeditionen ANTARKTIS VIII/3 und VIII/4 mit FS "Polarstern" 1989.- Ber. Polarforsch. 74, 173 pp.

Gersonde, R. and Pätzold, J. (1992): Bericht über Teilprojekt B1: Paläotemperaturverteilung des Oberflächenwassers.- in: Der Südatlantik im Spätquartär: Rekonstruktion von Stoffhaushalt und Stromsystemen, Arbeits- und Ergebnisbericht 1989-1992, Universität Bremen, 209-270.

Gersonde, R. (1993): Die Expedition ANTARKTIS-X/5 mit FS "Polarstern" 1992.- Ber. Polarforsch. 131, 167 pp.

Gersonde, R. (1995): Die Expedition ANTARKTIS-XI/2 mit FS "Polarstern" 1993/94.- Ber. Polarforsch. 163, 133 pp.

Gersonde, R. and Zielinski, U. (1995): Significance of diatoms as indicators of past Antarctic sea ice extent.- in prep.

Gersonde, R., Abelmann, A., Bohrmann, G., Frank, M., Heinemeier, J., Rutgers van der Loeff, M.M., Niebler, H.-S., Mangini, A., Rud, N. and Zielinski, U. (1995) Southern Ocean paleoenvironmental changes during the last 20,000 years (Atlantic sector).- in prep.

Gingele, F. and Dahmke, A. (1994): Discrete barite particles and barium as tracers of paleoproductivity in South Atlantic sediments.- Paleoceanography 9, 151-168.

GRIP-Members (1993): Climate instability during the last interglacial period recorded in the GRIP ice core.- Nature 364, 203-207.

Grousset, F.P., Biscaye, B.E., Revel, M., Petit, J.R., Pye, K., Joussaume, S. and Jouzel, J. (1992): Antarctic (Dome C) ice-core dust at 18 k.y. B.P.: Isotopic constraints on origins.- Earth Planet. Sci. Lett. 111, 175-182.

Hays, J.D., Imbrie, J. and Shackleton, N.J. (1976): Variations in the earth's orbit: pacemaker of the ice ages.- Science 194, 1121-1132.

Heinze, C. and Broecker, W.S. (1995): Closing off the Southern Ocean surface.- Paleoceanography 10, 49-58.

Henken-Mellies, W.-U., Beer, J., Heller, F., Hsü, K.-J., Shen, C., Bonani, G., Hofmann, H.-J., Suter, M. and Wölfli, W. (1990): ^{10}Be and ^{9}Be in South Atlantic DSDP site 519: Relation to geomagnetic reversals and to sediment composition.- Earth Planet. Sci. Lett. 98, 267-276.

Hodell, D.A. (1993): Late Pleistocene paleoceanography of the south Atlantic sector of the Southern Ocean: Ocean Drilling Program Hole 704A.- Paleoceanography 8, 47-67.

Hofmann, H.-J., Beer, J., Bonani, G., von Gunten, H.R., Raman, S., Suter, M., Walker, R.L., Wölfli, W. and Zimmermann, D. (1987): ^{10}Be: half-life and AMS-standards.- Nucl. Instrum. Methods Phys. Res. B29, 2-36.

Holland, H.D. (1984): The chemical evolution of the atmosphere and oceans.- Princeton University Press, Princeton, N.J., 582 pp.

Howard, W.R. and Prell, W.L. (1994): Late Quaternary $CaCO_3$ production and preservation in the Southern Ocean: Implications for oceanic and atmosheric carbon cycling.- Paleoceanography 9, 453-482.

Hunter, K.A., Hawke, D.J. and Choo, L.K. (1988): Equilibrium adsorption of thorium by metal oxides in marine electrolytes.- Geochim. Cosmochim. Acta 52, 627-636.

Imbrie, J., Hays, J.D., Martinson, D.G., McIntyre, A., Mix, A.C., Morley, J.J., Pisias, N.G., Prell, W.L. and Shackleton, N.J. (1984): The orbital theory of the Pleistocene climate: Support from a revised chronology of the marine δ^{18}O record.- in Milankovitch and Climate, Part 1, edited by Berger, A.L. et al., D. Riedel, Hingham Mass., 269-305.

Ivanovich, M. and Harmon, R.S. (eds.) (1992): Uranium Series Disequilibrium, 2nd ed., Clarendon, Oxford, 910 pp.

Jacobs, S.S., Hellmar, H.H., Doake, C.S.M., Jenkins, A. and Frolich, R. (1992): Melting of ice shelves and the mass balance of Antarctica.- Journal of Glacialogy 38, 375-387.

Jansen, J.H.F., Alderliesten, C., van Bennekom, A.J., van der Borg, K. and De Jong, A.F.M. (1987): Terrigenous supply of ^{10}Be and dating with ^{14}C and ^{10}Be in sediments of the Angola Basin (SE Atlantic).- Nucl. Instrum. Methods Phys. Res. B29, 311-316.

Keigwin, L.D. and Boyle, E.A: (1989): Late Quaternary paleochemistry of high latitude surface waters.- Paleogeogr. Paleoclimatol. Palaeoecol. 73, 85-106.

Keigwin, L.D., Curry, W. B., Lehman, S. J. und Johnsen, S. (1994): The role of the deep ocean in North Atlantic climate change between 70 and 130 kyr ago.- Nature, 371 323-325.

Keir, R.S. (1988): On the late pleistocene ocean geochemistry and circulation.- Paleoceanography 3, 413-445.

Klinkhammer, G. and Palmer, M.R. (1991): Uranium in the oceans, where it goes and why.- Geochim. Cosmochim. Acta 55, 1799-1806.

Kolber, Z.S., Barber, R.T., Coale, K.H., Fitzwater, S.E., Greene, R.M., Johnson, K.S., Lindley, S. and Falkowski, P.G. (1994): Iron limitation of phytoplankton photosynthesis in the equatorial Pacific Ocean.- Nature 371, 145-149.

Kroopnick, P.M. (1985): The distribution of ^{13}C of CO_2 in the world oceans.- Deep-Sea Res. 32, 57-84.

Ku, T. L., Kusakabe, L., Measures, C.I., Southon, J.R., Vogel, J.S., Nelson, D.E. and Nakaya, S. (1990): Be isotope distribution in the western North Atlantic: A comparison to the Pacific.- Deep-Sea Res. 37, 795-808.

Kumar, N. (1994): Trace metals and natural radionuclides as tracers of ocean productivity.- Ph.D. thesis, Columbia University, New York, 317 pp.

Kumar, N., Gwiazda, R., Anderson, R.F. and Froelich, P.N. (1993): $^{231}Pa/^{230}Th$ ratios in sediments as a proxy for past changes in Southern Ocean productivity.- Nature 362, 45-48.

Kusakabe, L., Ku, T.L., Southon, J.R., Vogel, J.S., Nelson, D.E., Measures, C.I. and Nozaki, Y. (1987): The distribution of ^{10}Be and ^{9}Be in ocean water.- Nucl. Instrum. Methods Phys. Res. B29, 306-310.

Kusakabe, L., Ku, T.L., Southon, J.R., Liu, S., Vogel, J.S., Nelson, D.E., Nakaya, S. and Cusinmano, G.L. (1991): Be isotopes in rivers/estuaries and their oceanic budgets.- Earth Planet. Sci. Lett. 102, 265-276.

Labeyrie, L.D., Pichon, J.J., Labracherie, M., Ippolito, P., Duprat, J. and Duplessy, J.-C. (1986): Melting history of Antarctica during the past 60,000 years.- Nature 322, 701-706.

Lal, D. and Peters, B. (1967): Cosmic ray produced radioactivity on the Earth.- in: Encyclopedia of Physics 46 (2), Springer-Verlag, New York, 581-588.

Lal, D. (1988): Theoretically expected variations in the terrestrial cosmic ray production rates of isotopes.- Soc. Italiana di Fisica-Bologna-Italy, XCV corso, 216-233.

Lao, Y. (1991): Transport and burial rates of ^{10}Be and ^{231}Pa in the Pacific Ocean.- Ph.D. thesis, Columbia University., New York, 246 pp.

Lao, Y., Anderson, R.F., Broecker, W.S., Trumbore, S.E., Hofmann, H.-J. and Wölfli, W. (1992a): Increased production of cosmogenic ^{10}Be during the last glacial maximum.- Nature 357, 576-578.

Lao, Y., Anderson, R.F. and Broecker, W.S. (1992b): Boundary scavenging and deep-sea sediment dating: Constraints from excess ^{230}Th and ^{231}Pa.- Paleoceanography 7, 783-798.

Lao, Y., Anderson, R.F., Broecker, W.S., Trumbore, S.E., Hofmann, H.J. and Wölfli, W. (1992c): Transport and burial rates of ^{10}Be and ^{231}Pa in the Pacific ocean during the Holocene period.- Earth Planet. Sci. Lett. 113, 173-189.

Lao, Y., Anderson, R.F., Broecker, W.S., Hofmann, H.J. and Wölfli, W. (1993): Particulate fluxes of ^{230}Th, ^{231}Pa und ^{10}Be in the northeastern Pacific Ocean.- Geochim. Cosmochim. Acta 57, 205-217.

Lehman, S.J. and Keigwin, L.D. (1992): Sudden changes in North Atlantic circulation during the last deglaciation.- Nature 356, 757-762.

Levitus, S., Conkright, M.E., Reid, J.L., Najjar, R.C. and Mantyla, A. (1993): Distribution of nitrate, phosphate and silicate in the world oceans.- Progress in Oceanography 31, 245-273.

MacKenzie, F.T., Stoffyn, M. and Wollast, R. (1978): Aluminium in seawater: Control by biological activity.- Science 199, 680-682.

Mackensen, A., Hubberten, H.-W., Bickert, T., Fischer, G. and Fütterer, D.K. (1993): The $\delta^{13}C$ in benthic foraminifera tests of Fontbotia Wuellerstorfi (Schwager) relative to the $\delta^{13}C$ of dissolved inorganic carbon in Southern Ocean deep water: implications for glacial ocean circulation models.- Paleoceanography, 8 587-610.

Mackensen, A., Grobe, H., Hubberten, H.-W. and Kuhn, G. (1994): Benthic foraminiferal assemblages and the $\delta^{13}C$-Signal in the Atlantic Sector of the Southern Ocean: Glacial-to-interglacial contrasts.- in: Carbon Cycling in the Glacial Ocean: Constraints on the Ocean's Role in Global Change, NATO ASI-Series, Vol. I 17, edited by Zahn, R. et al., 105-144.

Mangini, A. (1984): Datierung von Sedimenten und andere Anwendungen der Radionuklide ^{230}Th, ^{231}Pa und ^{10}Be in der marinen Geologie.- Habilitationsschrift, Univ. Heidelberg, 63 pp.

Mangini, A., and Sonntag, C. (1977): ^{231}Pa dating of deep-sea cores via ^{227}Th counting.- Earth Planet. Sci. Lett. 37, 251-256.

Mangini, A., Sonntag, C., Bertsch, G. and Müller, E. (1979): Evidence for a higher, natural U-content in world rivers.- Nature 79, 337-339.

Mangini, A. and Diester-Haass, L. (1983): Excess ^{230}Th in N.W. African sediments traces upwelling in the past.- in: Coastal Upwelling: Its Sediment Record, edited by Suess, E. and Thiede, J., NATO Conf. Ser., Ser. IV, 10a, 455-470.

Mangini, A., Segl, M., Bonani, G., Hofmann, H.J., Morenzoni, E., Nessi, M., Suter, M., Wölfli, W. and Turekian, K.K. (1984): Mass spectrometric Beryllium dating of deep-sea sediments applying the Zürich tandem accelerator.- Nucl. Instrum. Methods Phys. Res. B5, 353-357.

Mangini, A., Segl. M., Kudrass, H., Wiedicke, M., Bonani, G., Hofmann, H.J., Morenzoni, E., Nessi, M., Suter, M. and Wölfli, W. (1986): Diffusion and supply rates of ^{10}Be and ^{230}Th radioisotopes in two Mn encrustations from the South China Sea.- Geochim. Cosmochim. Acta 50, 149-156.

Mangini, A., Eisenhauer, A. and Walter, P. (1990): Response of Mn in the ocean to the climatic cycles in the Quaternary.- Paleoceanography 5, 811-821.

Mangini, A., Rutsch, H.J., Frank, M., Eisenhauer, A., and Eckhardt, J.D. (1993): Is there a relationship between atmospheric CO_2 and manganese in the ocean.- in: Carbon Cycling in the Glacial Ocean: Constraints on the Ocean's Role in Global Change, edited by Zahn, R. et al., NATO ASI Ser., Ser. I, 17, 87-104.

Martin, J. H. (1990): Glacial-Interglacial CO_2 change: The iron hypothesis.- Paleoceanography 5, 1-13 .

Martin, J.H., Coale, K.H., Johnson, K.S., Fitzwater, S.E., Gordon, R.M., Tanner, S.J., Hunter, C.N., Elrod, V.A., Nowicki, J.L., Coley, T.L., Barber, R.T., Lindley, S., Watson, A.J., Van Scoy, K., Law, C.S., Liddicoat, M.I., Ling, R., Stanton, T., Stockel, J., Collins, C., Anderson, A., Bidigare, R., Ondrusek, M., Latasa, M., Millero, F.J., Lee, K., Yao, W., Zhang, J.Z., Friederich, G., Sakamoto, C., Chavez, S., Buck, K., Kolber, Z.S., Greene, R.M., Falkowski, P., Chisholm, S.W., Hoge, F., Swift, R., Yungel, J., Turner, S., Nightingale, P., Hatton, A., Liss, P. and Tindale, N.W. (1994): Testing the iron hypothesis in ecosystems of the equatorial Pacific Ocean.- Nature 371, 123-129.

Martinson, D.G., Pisias, N.G., Hays, J.D., Imbrie, J., Moore jr., T.C. and Shackleton, N.J. (1987): Age dating and the orbital theory of the ice ages: development of a high-resolution 0 to 300,000 year chronostratigraphy.- Quat. Res. 27, 1-29.

Mazaud, A., Laj, C., Bard, E., Arnold, M. and Tric, E. (1991): Geomagnetic field control of ^{14}C production over the last 80 ky: Implications for the radiocarbon time-scale.- Geophys. Res. Lett. 18, 1885-1888.

Mazaud, A., Laj, C. and Bender, M. (1994): A geomagnetic chronology for Antarctic ice accumulation, Geophys. Res. Lett. 21, 337-340.

McCorkle, D. C., Martin, P.A., Lea, D.W. and Klinkhammer, G.P. (1994): Evidence of a dissolution effect on benthic foraminiferal Cd/Ca and Ba/Ca.- EOS, 75, AGU Spring Meeting Supplement, p. 54.

McHargue, L.R. and Damon, P.E. (1991): The global Beryllium 10 cycle.- Reviews of Geophysics 29, 141-158.

McManus, J.F., Bond, G.C., Broecker, W.S., Johnsen, S., Labeyrie, L. and Higgins, S. (1994): High-resolution climate records from the North Atlantic during the last interglacial.- Nature 371, 326-329.

Meynadier, L., Valet, J.P., Weeks, R., Shackleton, N.J. and Hagee, V.L. (1992): Relative geomagnetic intensity of the field during the last 140 ka.- Earth Planet. Sci. Lett. 114, 39-57.

Milankovitch, M. (1930): Mathematische Klimalehre und astronomische Theorie der Klimaschwankungen, Gebrüder Bornträger, Berlin, 176 pp.

Monaghan, M., Krishnaswami, S. and Turekian, K.K. (1985/86): The global-average production rate of ^{10}Be.- Earth Planet. Sci. Lett. 76, 279-287.

Mortlock, R.A., Charles, C.D., Froehlich, P.N., Zibello, M.A., Saltzman, J., Hays, J.D. and Burckle, L.H. (1991): Evidence for lower productivity in the Antarctic Ocean during the last glaciacion.- Nature 351, 220-223.

Mosby, H. (1934): The waters of the Atlantic Antarctic Ocean.- Scientific Results of the Norwegian Antarctic Expedition 1927-1928, 11, 1-131.

Müller, P.J. and Suess, E. (1979): Productivity, sedimentation rate, and sedimentary organic matter in the oceans - I. Organic carbon preservation.- Deep-Sea Res. 26, 1347-1362.

Müller, P.J. (1992): Bericht über Teilprojekt A4: Produktivitätsänderungen im Spätquartär.- in: Der Südatlantik im Spätquartär: Rekonstruktion von Stoffhaushalt und Stromsystemen, Arbeits- und Ergebnisbericht 1989-1992, Universität Bremen, 159-208.

Murray, R.W., Leinen, M. and Isern, A.R. (1993): Biogenic flux of Al to sediment in the central equatorial Pacific Ocean: Evidence for increased productivity during glacial periods.- Paleoceanography 8, 651-670.

Niebler, S., (1995): Rekonstruktion von Paläo-Umweltparametern anhand von stabilen Isotopen und Faunenvergesellschaftungen planktischer Foraminiferen.- Ber. Polarforsch. 167, 198.

Nowlin jr., W.D., Whitworth III, T. and Pillsbury R.D. (1977): Structure and transport of the Antarctic Circumpolar Current at Drake Passage from short-term measurements.- J. Phys. Oceanogr. 7, 788-802.

Nozaki, Y., Horibe, Y. and Tsubota, H. (1981): The water column distributions of thorium isotopes in the western North Pacific.- Earth Planet. Sci. Lett. 54, 203-216.

Nürnberg, C.C. (1995): Bariumfluß und Sedimentation im südlichen Südatlantik - Hinweise auf Produktivitätsänderungen im Quartär.- Ph.D. thesis, Univ. Kiel, Germany, 117 pp.

Nürnberg, C.C., Bohrmann, G., Frank, M., Schlüter, M. and Suess, E. (1995): Barium accumulation in the Atlantic sector of the Southern Ocean: Evidence for productivity changes during the last 190,000 years.- in prep.

Orians, K.J and Bruland, K.W (1986): The biogeochemistry of aluminium in the Pacific Ocean.- Earth Planet. Sci. Lett. 78, 397-410.

Peterson, R.G., Nowlin jr., W.D. and Whitworth III, T. (1982): Generation and evolution of a cyclonic ring at Drake Passage in early 1979.- J. Phys. Oceanogr. 12, 712-719.

Peterson, R.G. and Whitworth III, T. (1989): The Subantarctic and Polar fronts in relation to deep water masses through the Southwestern Atlantic.- J. Geophys. Res. 94, 10817-10838.

Peterson, R.G. and Stramma, L. (1991): Upper-level circulation in the South Atlantic Ocean.- Progress in Oceanography 26, 1-73.

Pichon, J.J., Bareille, G., Labracherie, M., Labeyrie, L.D., Baudrimont, A. and Turon, J. (1992): Quantification of the biogenic silica dissolution in Southern Ocean sediments.- Quaternary Research 37, 361-378.

Raisbeck, G.M., Yiou, F., Bourlés, D., Lorius, C., Jouzel, J. and Barkov, N.I. (1987): Evidence for two intervals of enhanced ^{10}Be deposition in Antarctic ice during the last glacial period.- Nature 326, 273-277.

Raisbeck, G.M., Yiou, F., Jouzel, J., Petit, J.R., Barkov, N.I. and Bard, E. (1992): ^{10}Be deposition in Vostok, Antarctica, during the last 50,000 years and its relationship to possible cosmogenic production variation during this period.- in: The Last Deglaciation: Absolute and Radiocarbon Chronologies, NATO ASI Series Vol. 12, edited by Bard, E. and Broecker, W.S., 127-137.

Raymo, M.E., Ruddiman, W.F., Shackleton, N.J. and Oppo, D.W. (1990): Evolution of Atlantic-Pacific δ^{13}C gradients over the last 2.5 m.y.- Earth Planet. Sci. Lett. 97, 353-368.

Reid, J.L., Nowlin, W.D. and Patzert, W.C. (1977): On the characteristics and circulation of the southwestern Atlantic Ocean.- J. Phys. Oceanogr. 7, 62-91.

Riediger, M. (1995): Uran-Thorium-Messung an einem Sedimentkern des mittelatlantischen Ceara-Rückens.- unpubl. Staatsexamensarbeit, Univ. Heidelberg, Heidelberg, Germany, 44 pp.

Rühlemann, C., Frank, M., Hale, W., Mangini, A., Mulitza, S. and Müller, P.J. (1995): Late Quaternary productivity changes in the western equatorial Atlantic: Evidence from ^{230}Th normalized carbonate and organic carbon accumulation rates.- in prep.

Rutgers van der Loeff, M.M. and Berger, G.W. (1991): Scavenging and particle flux: Seasonal and regional variations in the Southern Ocean (Atlantic Sector).- Mar. Chem. 35, 553-567.

Rutgers van der Loeff, M.M. and Berger, G.W. (1993): Scavenging of ^{230}Th and ^{231}Pa near the Antarctic Polar Front in the South Atlantic.- Deep-Sea Res. I 40, 339-357.

Rutsch, H.J., Mangini, A., Bonani, G., Dittrich-Hannen, B., Kubik, P.W., Suter, M. and Segl, M. (1995): ^{10}Be and Ba concentrations in W. African sediments trace productivity in the past.- Earth Planet. Sci. Lett. 133, 129-143.

Saager, P.M. (1994): On the relationships between dissolved trace metals and nutrients in seawater: implications for the use of cadmium as a paleoceanographic tracer.- Ph.D. thesis, Free University, Amsterdam, Niederlande.

Sarmiento, J.L. and Toggweiler, R. (1984): A new model for the role of the oceans in determining atmospheric pCO_2.- Nature 308, 621-624.

Sarnthein, M., Winn, K., Duplessy, J.-C. and Fontugne, M.R. (1988): Global variations of surface ocean productivity in low and mid latitudes: Influence on CO_2 reservoirs of the deep ocean and atmosphere during the last 21,000 years.- Paleoceanography 3, 361-399.

SEA ICE CLIMATIC ATLAS, Vol. 1, Antarctica (1985): Naval Oceanography Command Detachment, Ashville, North Carolina, 131 pp.

Scholten, J.C., Botz, R., Paetsch, H. and Stoffers, P. (1994): $^{230}Th_{ex}$ flux into Norwegian-Greenland Sea sediments: Evidence for lateral sediment transport during the past 300,000 years.- Earth Planet. Sci. Lett. 121, 111-124.

Segl, M., Mangini, A., Beer, J., Bonani, G., Suter, M., Wölfli, W. and Measures, C.I. (1987): ^{10}Be in the Atlantic Ocean, a transect at 25°N.- Nucl. Instrum. Methods Phys. Res. B5, 332-334.

Sharma, P., Mahannah, P., Moore, W.S., Ku, T.L. and Southon, J.R. (1987): Transport of ^{10}Be and ^{9}Be in the ocean.- Earth Planet. Sci. Lett. 86, 69-76.

Shen, C., Beer, J., Liu, T.S., Oeschger, H., Bonani, G., Suter, M. and Wölfli, W. (1992): ^{10}Be in Chinese loess.- Earth Planet. Sci. Lett. 109, 169-177.

Shimmield, G.B. and Price, N.B. (1988): The scavenging of U, ^{230}Th and ^{231}Pa during pulsed hydrothermal activity at 20°S, East Pacific Rise.- Geochim. Cosmochim. Acta 52, 669-677.

Shimmield, G.B., Derrick, S., Mackensen, A., Grobe, H. and Pudsey, C. (1994): The history of barium, biogenic silica and organic carbon accumulation in the Weddell Sea and Antarctic Ocean over the last 150,000 years.- in: Carbon Cycling in the Glacial Ocean: Constraints on the Ocean's Role in Global Change, edited by Zahn, R. et al., NATO ASI Ser., Ser. I, 17, 555-574.

Siegenthaler, U. (1990): Glacial-Interglacial atmospheric CO_2 variations.- in: Global changes in the past, edited by Bradley, R.S., Boulder, Colorado, 245-260.

Southon, J.R., Ku, T.L., Nelson, D.E., Reyss, J.L., Duplessy, J.-C. and Vogel, J.S. (1987): ^{10}Be in a deep-sea core: Implications regarding ^{10}Be production changes over the past 420 ka.- Earth Planet. Sci. Lett. 85, 356-364.

Spencer, D.W., Bacon, M.P. and Brewer, P.G. (1981): Models of the distribution of ^{210}Pb in a section across the north equatorial Atlantic ocean.- J. Mar. Res. 39, 119-138.

Stramma, L. and Peterson, R.G. (1990): The South Atlantic Current.- J. Phys. Oceanogr. 20, 846-859.

Suman, D.O. and Bacon, M.P. (1989): Variations in Holocene sedimentation in the North American basin determined from ^{230}Th measurements.- Deep-Sea Res. 36, 869-878.

Suter, M., Balzer, R., Bonani, G., Hofmann, H.J., Morenzoni, E., Nessi, M. and Wölfli, W. (1984): Precision measurements of ^{14}C in AMS - some results and prospectus.- Nucl. Instrum. Methods Phys. Res. B5, 117-122.

Taylor, K.C., Lamorey, G.W., Doyle, G.A., Alley, R.B., Grootes, P.M., Mayewski, P.A., White, J.W.C. and L.K. Barlow (1993): The "flickering switch" of late Pleistocene climate change.- Nature 361, 432-436.

Taylor, K.C., Hammer, U., Alley, R.B., Clausen, H.B., Dahl-Jensen, D., Gows, A.J., Gundestrup, N.S., Kipfstuhl, J., Moore, J.C. and Waddlington, E.D. (1993): Electrical conductivity measurements from the GISP2 and GRIP Greenland ice cores.- Nature 366, 549-552.

Taylor, S.R. and McLennan, S.M. (1985): The Continental Crust: Its Composition and Evolution.- Blackwell, Oxford, 312 pp.

Tric, E., Valet, J.P., Tucholka, P., Paterne, M., Labeyrie, L., Guichard, F., Tauxe, L. and Fontugne, M. (1992): Paleointensity of the geomagnetic field during the last eighty thousand years.- J. Geophys. Res. 97, 9337-9351.

Tucholke, B.E., Wright, W.R. and Hollister, C.D. (1973): Abyssal circulation over the greater Antilles Outer Ridge.- Deep-Sea Res. 20, 973-975.

Turekian, K.K., Benneinger, L.K. and Dion, E.P. (1983): ^{7}Be and ^{210}Pb total depositional fluxes at New Haven, Connecticut, and at Bermuda.- J. Geophys. Res. 88, 5411-5415.

Valette-Silver, J.N., Tera, F., Klein, J. and Middleton, R. (1987): Beryllium 10 in hydrothermal vent deposits from the east Pacific ridges: Role of sediments in the hydrothermal processes.- J. Geophys. Res. 92, 11364-11372.

Van Bennekom, A.J., Berger, G.W., Van der Gaast, S.J. and De Vries, R.T.P. (1988): Primary productivity and the silica cycle in the in the southern ocean (Atlantic Sector).- Paleogeogr. Paleoclimatol. Paleoecol. 67, 19-30.

Van Geen, A., Mc Corckle, D.C. and Klinkhammer, G.P. (1995): Sensitivity of the phosphate-cadmium-carbon isotope relation in the ocean to cadmium removal by suboxic sediments.- Paleoceanography 10, 159-169.

Wedepohl, K.H. (1995): The composition of the continental crust.- Geochim. Cosmochim. Acta 59, 1217-1232.

Wefer, G. and Fischer, G. (1991): Annual primary production and export flux in the Southern Ocean from sediment trap data.- Mar. Chem. 35, 597-613.

Whitworth III, T. and Peterson, R.G. (1985): The volume transport of the Antarctic Circumpolar Current from bottom pressure measurements.- J. Phys. Oceanogr. 15, 810-816.

Whitworth III, T. and Nowlin jr., W.D. (1987): Water masses and currents of the Southern Ocean at the Greenwich Meridian.- J. Geophys. Res. 92, 6462-6476.

Winograd, I.J., Coplen, T.B., Landwehr, J.M., Riggs, A.C., Ludwig, K.R., Szabo, B.J., Kolesar, P.T. and Revesz, K.M. (1992): Continuous 500,000-year climate record from vein calcite in Devil's Hole, Nevada.- Science 258, 255-260.

Wölfli, W. (1987): Advances in accelerator mass spectrometry.- Nucl. Instrum. Methods Phys. Res. B29, 1-13.

Wüst, G. (1935): Schichtung und Zirkulation des Atlantischen Ozeans. Die Stratosphäre.- Wissenschaftliche Ergebnisse der Deutschen Atlantischen Expedition auf dem Forschungs und Vermessungsschiff 'Meteor' 1925-1927 6, Teil 1, Lieferung 2, 1-288.

Yamazaki, T. and Ioka, N. (1994): Long-term secular variations of the geomagnetic field during the last 200 kyrs recorded in sediment cores from the western equatorial Pacific.- Earth Planet. Sci. Lett. 128, 527-544.

Yang, H.-S., Nozaki, Y., Sakai, Y. and Masuda, A. (1986): The distribution of ^{230}Th and ^{231}Pa in the deep surface sediments of the Pacific Ocean.- Geochim. Cosmochim. Acta 50, 2499-2507.

Yang, Y.L., Elderfield, H. and Ivanovich, M. (1990): Glacial to Holocene changes in the carbonate and clay sedimentation in the equatorial Pacific Ocean estimated from ^{230}Th profiles.- Paleoceanography 5, 789-809.

Yang, Y.L., Elderfield, H., Ivanovich, M. and Pedersen, T.F. (1994): Enhanced uranium, excess ^{230}Th and ^{231}Pa accumulation fluxes associated with the "carbon event" during the Last Glacial Maximum in the Panama Basin.- submitted to Paleoceanography.

Yu, E.-F. (1994): Variations in the particulate flux of ^{230}Th and ^{231}Pa and paleoceanographic applications of the ^{231}Pa/^{230}Th ratio.- Ph.D. thesis, Massachusetts Institute of Technology, USA.

Yu, E.-F., Francois, R. and Bacon, M.P. (1995): Radiochemical constraints on ocean circulation during the last glacial maximum.- submitted to Nature.

Zielinski, U. (1993): Quantitative Bestimmung von Paläoumweltparametern des Antarktischen Oberflächenwassers im Spätquartär anhand von Transferfunktionen mit Diatomeen.- Ber Polarforsch 126, 148 pp.

A Methods

A.1 Chemical Preparation of ^{230}Th and ^{231}Pa

For the chemical preparation of the radionuclides Th, Pa and U, the method described by Mangini (1984) and Eisenhauer (1989) with minor modifications was applied. The sample material is dried and homogenized. For the measurement of the radioisotopes by α-spectroscopy, 0.5 to 1.5 g sample material depending on the expected activity is weighed and a ^{228}Th/^{232}U spike in radioactive equilibrium is added. The sample material is then dissolved in HF conc. (30 %) and evaporated to dryness twice. After melting the residues with $LiBO_2$, they are dissolved in 8 N HCl and loaded onto a Dowex 1 X 8 ion exchange column to separate U/Fe from Th/Ca. The solution containing Th is evaporated to dryness again and then dissolved in 8 N HNO_3 and loaded onto a Dowex 1 X 8 ion exchange column to separate Ca. Th is then back-extracted from the column with 8 N and 10 N HCl and evaporated to dryness again. After being evaporated to dryness and dissolved in a mixture of ammonium acetate and acetic acid (ca. 50 %) with a pH of about 4.5-5, the solution containing U is loaded onto a ion exchange column to separate Fe (Bhat et al., 1969). After back-extraction of the U with warm 1N HCl and H_2O, the solution is evaporated to dryness as well.

For the electroplating procedure 2ml HNO_3 conc. and about 10 drops of HCl conc. are added and evaporated to near dryness in order to get rid of organic matter originating from the ion exchange resin. The solution is then, having added a suitable indicator solution, titrated to a basic pH with NH_4OH and backtitrated to an acidic pH. A buffer solution consisting of 3.5 ml 0.01 N HNO_3, 4.5 ml saturated ammonium oxalate solution and 4.5 ml 2 M NH_4Cl solution is added and titrated to a pH of 4-4.5 with 3.5 N HNO_3.

In a copper electrolysis cell the radionuclides are then electrodeposited onto stainless steel plates using a platinum wire as anode and the steel plate as cathode for about 1 h at 12 V and 0.7 A. At the end of the electroplating procedure 2 ml of NH_4OH are added and the electrolysis is stopped.

A.2 Measurement of the ^{230}Th and ^{231}Pa Activities

A.2.1 ^{230}Th

The steel plates with the electrodeposited U and Th isotopes are put into the vacuum chamber ($p < 5$ Torr) of a silicon surface barrier detector with a distance of 1 to 2 mm to the detector. Only 30 % of the α-decay events are registered due to the geometry of the detector, with the plates having a diameter of 10 mm and an area of 450 mm^2. The simple principle of the measurement is that the emitted α-particles of each isotope which have a characteristic energy are completely stopped in the barrier. They loose their entire energy and produce an electronic signal proportional to the energy loss at the detector. The signal is transmitted to a computer after amplification via an ADC.

For calculation of the activity of ^{230}Th it has to be considered that the decay spectra comprise a number of other alpha emitting isotopes like ^{232}Th and ^{227}Th, as well as a number of daughter nuclides of the ^{228}Th spike, the energies of which partly overlap. The background intensity (counts per unit of time), the radioactive equilibrium amount of ^{228}Th produced by decay of the ^{232}Th in the sample and overlapping 5 % of the ^{224}Ra intensity have to be subtracted from the measured intensity of the ^{228}Th. The chemical efficiency is then calculated by:

$$chemical\ efficiency = \frac{^{228}Th\ intensity \cdot 3.3}{time\ of\ measurement \cdot spike\ activity \cdot spike\ volume} \quad (15)$$

with the factor 3.3 representing the geometrical efficiency of 30 %. The ^{230}Th activity is then calculated by

$$^{230}Th\ \left[\frac{dpm}{g}\right] = \frac{^{230}Th\ intensity}{A} \quad (16)$$

with $A = sample\ weight \cdot time\ of\ measurement \cdot chemical\ efficiency$

The error of the ^{230}Th activity is calculated as the quadratic sum of the 1σ statistical uncertainties of the ^{230}Th and ^{228}Th intensities:

$$error\ ^{230}Th\ \left[\frac{dpm}{g}\right] = \frac{1}{\sqrt{^{230}Th\ intensity\ +\ ^{228}Th\ intensity}} \quad (17)$$

A.2.2 ^{231}Pa

The ^{231}Pa activities were determined by α-counting of ^{227}Th (Mangini and Sonntag, 1977). ^{231}Pa decays into ^{227}Th via ^{227}Ac, which both are in radioactive equilibrium with their mother in the samples due to their short half lives of 18 days and 21.6 years respectively. The peak of the ^{227}Th intensity is located at the same energy of 6 MeV as the one of ^{212}Bi (a daughter nuclide of the ^{228}Th spike) and thus has to be corrected for the intensity of this isotope. The ^{212}Bi intensity corresponds to 56 % of the intensity of the ^{212}Po intensity which is also a part of the spectrum (at 8.76 MeV). A further correction is necessary because only 45% of the ^{227}Th decay events occur at an energy of 6 MeV.

$$^{231}Pa\ \left[\frac{dpm}{g}\right] = \frac{^{227}Th\ intensity\ -\ 0.56 \cdot\ ^{212}Po\ intensity}{0.45 \cdot A} \quad (18)$$

The error of the ^{231}Pa activity is calculated by

$$error\ ^{231}Pa\ \left[\frac{dpm}{g}\right] = \frac{\sqrt{^{227}Th\ intensity\ +\ 0.56^2 \cdot\ ^{212}Po\ intensity}}{0.45 \cdot A} \quad (19)$$

The procedure was improved by correcting the spectra for peak tailing, which occurs at detectors with a low energy resolution and may result in too high ^{231}Pa activities. The overall chemical yields for the measurement of ^{230}Th and ^{231}Pa range from 50 to 90 %.

The measurement of ^{231}Pa by this method yields high statistical uncertainties. This was especially important in the core sections corresponding to the isotope stages 4 to 6, where after 3 to 4 half lives of ^{231}Pa the initial activity is already strongly lowered. Reference measurements by direct α-counting of ^{231}Pa were carried out on aliqout samples and compared to the results of the indirect measurements following Frank and Mangini (1995) (Tab. 5). Additionally, the decay corrected $^{231}Pa_{ex}$ results of core PS1768-8 could be compared to a directly measured $^{231}Pa_{ex}$ profile of M. Rutgers van der Loeff (Bremerhaven) which, however, was performed on different sample intervals.

Core	Depth, cm	^{231}Pa via ^{227}Th, dpm/g	^{231}Pa direct, dpm/g
PS1772-8	270 - 280*	0.19 ± 0.17	0.05 ± 0.01
	300 - 310*	0.15 ± 0.14	0.12 ± 0.01
	380 - 390	0.10 ± 0.14	0.19 ± 0.16
PS1756-5	762 - 772	0.32 ± 0.08	0.38 ± 0.06
	842 - 852	0.38 ± 0.07	0.31 ± 0.04
PS2082-1	94 - 104	1.00 ± 0.15	1.32 ± 0.17
	513 - 525	0.49 ± 0.12	0.25 ± 0.06
		Initial $^{231}Pa_{ex}$ via ^{227}Th	Initial $^{231}Pa_{ex}$ direct
PS1768-8	0 - 25	1.81 ± 0.37	1.5 ± 0.15
	25 - 45	0.71 ± 0.30	0.90 ± 0.10
	70 - 95	0.80 ± 0.34	0.40 ± 0.08
	107 - 131	0.83 ± 0.33	0.45 ± 0.05
	156 - 181	0.88 ± 0.29	0.90 ± 0.30
	181 - 206	2.09 ± 0.43	1.00 ± 0.10
	231 - 256	0.68 ± 0.36	1.10 ± 0.40
	281 - 306	0.80 ± 0.40	1.00 ± 0.30
	306 - 331	0.18 ± 0.31	0.90 ± 0.50
	331 - 356	0.92 ± 0.41	1.20 ± 0.30
	381 - 406	1.40 ± 0.40	0.90 ± 0.50
	431 - 456	1.18 ± 0.40	0.70 ± 0.60
	589 - 599	1.04 ± 0.60	1.55 ± 0.80
	624 - 634	1.80 ± 0.64	1.50 ± 0.70
	729 - 740	2.40 ± 0.95	1.50 ± 0.50
	810 - 820	2.37 ± 1.57	0.80 ± 0.60

Table 5: Comparison between directly and indirectly measured ^{231}Pa. The values of core PS1768-8 represent initial $^{231}Pa_{ex}$ concentrations. The errors represent statistical errors of one standard deviation from the mean (1 σ). The two values of PS1772-8 marked with * were measured by H.J. Walter, AWI Bremerhaven.

Within the high statistical uncertainties both methods deliver the same results with

a trend of the indirectly measured samples towards higher values. Because of the uncertainties the records of the indirect ^{231}Pa measurements are shown in this study as three-point running means within the isotope stages and no ^{231}Pa data older than 140 kyrs are included in the interpretations. In the sections corresponding to the isotope stages 5e (110-130 kyrs B.P.) of the cores PS1772-8 and PS1768-8 only the available directly measured values were included in the interpretations.

A.2.3 ^{238}U and ^{234}U

The activities of ^{238}U and ^{234}U are calculated from the ratio of the measured intensity to the intensity of the ^{232}U spike. Again, the background intensity and 5 % of the ^{224}Ra have to be subtracted from the ^{232}U spike intensity. The chemical efficiency is calculated equivalent to the ^{230}Th efficiency and the ^{238}U activity is then

$$^{238}U \left[\frac{dpm}{g}\right] = \frac{^{238}U\ intensity}{A} \tag{20}$$

The error of ^{238}U is calculated by

$$error\ ^{238}U \left[\frac{dpm}{g}\right] = \frac{1}{\sqrt{^{232}U\ intensity\ +\ ^{238}U\ intensity}} \tag{21}$$

The activity of ^{234}U is calculated from the intensity ratio between ^{234}U and ^{238}U (AU)

$$AU = \frac{^{234}U\ intensity}{^{238}U\ intensity} \tag{22}$$

with the error

$$error\ AU = \frac{1}{\sqrt{^{234}U\ intensity\ +\ ^{238}U\ intensity}} \cdot AU \tag{23}$$

This error corresponds to the statistical error of one standard deviation from the mean (1 σ) of the ^{234}U activity.

A.3 Chemical Preparation and Measurement of ^{10}Be

For the chemical preparation of ^{10}Be the leaching method described by Henken-Mellies et al. (1990) was applied with minor modifications:

About 0.5 to 1 g of the dried and homogenized material are weighed in a teflon beaker and some drops of distilled water and 1 to 2 ml of a ^{9}Be spike (concentration = 1000 ppm) in nitric acid solution are added. 5 ml of H_2O_2, about 25 ml of 8 N HCl are added to desorb the ^{10}Be from the sediment particles during the night. On the next day the

solution is separated from the sediment and another 15 ml of 8 N HCl are added to complete the desorption. After some hours the solution is separated from the sediment again, the solutions are poured together and are evaporated to dryness during the night.

The residue is dissolved in 2 ml of HNO_3 conc. and 2 ml of HCl conc. (about 30 min.) and is then titrated with a NaOH solution until pH 2.5. 2 ml EDTA solution are added and after another hour it is titrated until pH 7-8. During the night Be and Fe precipitate as hydroxides while Al and other alkali metals remain in solution as EDTA complexes.

The residue is separated from the solution and is dissolved in NaOH conc. During the night Be dissolves again, while Fe and other metals stay precipitated. On the next day the Al complexation step is repeated with the solution and is finally titrated until pH 8-9. On the last two days the $Be(OH)_3$ precipitate is rinsed with distilled water and a drop of ammonia to get rid of boron which disturbs the measurement at the accelerator. Finally the precipitate is filtered (0.4 μm) and put into a quartz crucible. In the oven it is then oxidized to BeO at about 1100 °C.

The BeO is mixed with Cu powder and pressed into Cu targets. The ^{10}Be concentrations were measured by accelerator mass spectrometry (AMS), applying the Zürich tandem accelerator. A detailed description of the AMS facility in Zürich and the measurement technique is given for example by Mangini et al. (1984), Suter et al. (1984) and Wölfli (1987) and will only be discussed very briefly here.

The samples are brought into the ion source chamber and with a Cs^+ ion beam, BeO^- ions are produced which are subsequently accelerated in an electric field. At the positive pole the BeO^- ions pass a stripper where the molecule is destroyed and the Be ions loose a part of their electron shell resulting in Be^{3+} ions. These Be cations are again accelerated in a 4.5 MeV electric field and then are deviated by an electromagnet according to their mass. ^{10}Be and ^{10}B can not be separated due to their similar mass and thus the boron is absorbed in a argon filled gas absorption cell before counting at a semiconductor detector. Typical $^{10}Be/^{9}Be$ ratios in sediment samples amount to between 10^{-12} and 10^{-13}.

The ^{10}Be results were calibrated to the internal standard S555 of the ETH Zürich with a $^{10}Be/^{9}Be$ ratio of $95.5 \cdot 10^{-12}$. Blank corrections are negligible and the statistical error represents one standard deviation of the mean (1σ).

A.4 Chemical Preparation and Measurement of the Other Components

Mn and Fe concentrations of all cores and the Ba and Al concentrations of the cores PS1754-1 and PS1754-2 were measured by AAS after $LiBO_2$ melting and complete dissolution applying standard techniques. The Al and Ba concentrations of the other cores were determined by atomic emission spectroscopy (ICP-AES) at the GEOMAR in Kiel (Nürnberg, 1995). Unpublished biogenic opal data of the five investigated cores were kindly put to disposal for comparison as paleoproductivity proxies by G. Bohrmann, GEOMAR Kiel (pers. com.). Carbonate contents for the cores PS1754-1 and PS2082-1 and physical property data (wet bulk density in g/cm^3 and porosity in %) for all five cores were determined by G. Kuhn, AWI Bremerhaven, and put to disposal for dry bulk density determination:

$$dry\ bulk\ density = wet\ bulk\ density - (1.026 \cdot \frac{porosity}{100}) \qquad (24)$$

B Data

B.1 Average Rain Rates

	Isotope Stages									
Core	1	Holocene Climate Optimum	Last Glacial Maximum	2	3	4	5a-d	5e	Stage 5e Climate Optimum	6
				Sediment Rain Rate [g/cm^2 · *kyr*]						
PS1772-8	0.80	0.72	0.79	0.82	0.94	0.80	0.94	4.00	6.00	0.90
PS1768-8	2.37	2.83	1.30	2.38	1.60	1.46	1.70	2.60	3.00	1.40
PS1756-5	1.50	1.90	3.20	3.20	3.37	2.07	1.75	2.47	2.50	1.29
PS1754-1	1.20	1.25	2.20	1.80	2.00	1.60	1.40	1.00	1.00	1.00
PS2082-1	0.77	0.90	1.00	0.93	0.87	0.64	0.45	0.60	0.35	0.70
				Biogenic Barium Rain Rate [mg/cm^2 · kyr]						
PS1772-8	0.69	0.43	0.35	0.35	0.43	0.43	0.44	1.68	2.43	0.57
PS1768-8	2.50	2.79	0.94	1.65	0.91	1.00	1.35	2.85	3.20	1.05
PS1756-5	-	1.20	1.50	1.38	1.40	0.60	0.90	1.60	2.00	0.86
PS1754-1	1.47	1.65	1.90	1.68	2.25	1.70	1.56	1.06	1.10	1.21
PS2082-1	0.62	0.61	0.85	0.64	0.31	0.60	0.37	0.41	0.35	0.47
				Export Paleoproductivity [gC/m^2 · yr]						
PS1772-8	4.5	2.3	1.2	1.2	2.7	2.3	2.5	14.4	16.8	3.0
PS1768-8	13.8	15.5	3.3	7.6	3.5	4.0	7.5	20.1	26.0	4.4
PS1756-5	7.0	6.1	7.0	6.9	9.4	2.5	4.9	13.3	19.0	4.3
PS1754-1	10.4	12.0	14.4	12.8	29.4	21.7	14.6	9.7	7.6	12.4
PS2082-1	2.6	2.7	3.2	2.2	1.0	2.7	1.5	2.0	1.9	2.8
				Biogenic Opal Rain Rate [g/cm^2 · kyr]						
PS1772-8	0.29	0.20	0.19	0.17	0.17	0.13	0.15	2.80	4.50	0.20
PS1768-8	1.78	2.18	0.48	1.56	0.60	0.50	1.06	2.30	2.60	0.50
PS1756-5	0.40	0.50	2.00	2.01	2.12	1.14	1.11	1.68	1.61	0.73
PS1754-1	0.12	0.14	0.60	0.41	0.47	0.38	0.37	0.19	0.20	0.14
PS2082-1	0.11	0.12	0.30	0.29	0.18	0.19	0.10	0.10	0.06	0.19

Average rain rates of the tracers of the five studied cores. The Holocene climate optimum represents the average values for the period from 12 to 9 kyrs B.P., the last glacial maximum represents the period from 18 to 20 kyrs B.P. and the stage 5e climate optimum represents the period from 124 to 120 kyrs B.P.

	Isotope Stages									
Core	1	Holocene Climate Optimum	Last Glacial Maximum	2	3	4	5a-d	5e	Stage 5e Climate Optimum	6
				$^{231}Pa_{ex}$ Rain Rate [dpm/cm^2 · kyr]						
PS1772-8	1.48	1.25	1.51	1.48	1.72	2.28	2.38	5.00	6.00	2.40
PS1768-8	2.48	3.87	1.66	2.10	1.44	1.06	2.40	3.30	3.30	-
PS1756-5	1.40	1.60	1.90	2.07	3.20	3.50	4.40	8.70	9.90	7.20
PS1754-1	1.15	1.20	2.70	2.17	2.20	3.70	3.72	3.30	3.10	4.70
PS2082-1	1.02	1.10	2.50	1.36	1.24	1.54	1.58	3.25	1.40	3.60
				^{10}Be Rain Rate [10^9at/cm^2 · kyr]						
PS1772-8	3.29	3.30	1.72	2.41	2.78	2.65	2.51	2.14	2.20	2.23
PS1768-8	1.52	1.56	1.84	1.61	2.15	1.90	1.70	0.87	0.87	1.80
PS1756-5	2.79	2.80	2.42	2.64	3.10	2.50	2.13	2.14	2.40	1.87
PS1754-1	1.47	1.80	1.91	1.95	2.10	1.60	1.33	0.77	0.70	1.87
PS2082-1	1.94	1.90	3.56	3.33	3.37	3.00	1.79	1.42	1.10	3.00
				Fe [mg/cm^2 · kyr]						
PS1772-8	28.5	28.5	25.5	25.5	35.0	35.0	35.0	15.0	5.8	27.0
PS1768-8	7.4	7.7	30.0	21.5	36.8	33.0	26.7	8.8	7.0	31.3
PS1756-5	13.0	13.0	31.9	31.0	29.5	32.8	16.1	16.6	19.3	16.3
PS1754-1	6.0	9.8	11.6	12.0	9.0	8.0	6.4	4.0	2.9	22.0
PS2082-1	10.5	12.0	27.0	24.3	18.3	20.7	8.4	8.9	7.0	22.8

Average rain rates of the tracers of the five studied cores (continued).

B.2 PS1772-8 and PS1772-6

Depth, cm	Age, kyr	DBD, g/cm^3	$^{230}Th_{ex}$, dpm/g	$^{230}Th^0_{ex}$, dpm/g	SR, cm/kyr	SAR, g/cm^2 · kyr	VRR, g/cm^2 · kyr
			Multicore PS1772-6				
0 – 9.5	4.58	0.35	10.19 ± 0.25	10.63 ± 0.27	2.08 ± 0.05	0.73 ± 0.02	1.02 ± 0.03
9.5 – 19.5	10.07	0.36	10.82 ± 0.28	11.87 ± 0.30	1.82 ± 0.05	0.66 ± 0.02	0.92 ± 0.02
19.5 – 29.5	17.82	0.43	12.16 ± 0.26	14.34 ± 0.30	1.29 ± 0.03	0.55 ± 0.01	0.76 ± 0.02
			Gravity Core PS1772-8				
0 – 11.5	6.16	0.35	11.91 ± 0.46	12.61 ± 0.48	1.87 ± 0.07	0.65 ± 0.03	0.86 ± 0.03
11.5 – 13.5	7.26	0.34	11.93 ± 0.48	12.76 ± 0.51	1.82 ± 0.07	0.62 ± 0.02	0.85 ± 0.03
13.5 – 20	11.72	0.37	13.51 ± 0.47	15.05 ± 0.52	1.46 ± 0.05	0.54 ± 0.02	0.72 ± 0.02
20 – 25	13.20	0.40	12.32 ± 0.38	13.92 ± 0.43	3.37 ± 0.11	1.35 ± 0.04	0.78 ± 0.02
25 – 32	15.60	0.45	12.50 ± 0.38	14.43 ± 0.44	2.91 ± 0.09	1.31 ± 0.04	0.75 ± 0.02
32 – 40	18.38	0.48	11.58 ± 0.37	13.73 ± 0.44	2.88 ± 0.09	1.38 ± 0.04	0.79 ± 0.03
40 – 50	21.49	0.46	10.54 ± 0.39	12.85 ± 0.47	3.22 ± 0.12	1.48 ± 0.05	0.85 ± 0.03
50 – 60	24.08	0.42	9.48 ± 0.55	11.84 ± 0.69	3.86 ± 0.22	1.60 ± 0.09	0.92 ± 0.05
60 – 70	37.17	0.41	8.18 ± 0.33	11.53 ± 0.47	0.76 ± 0.03	0.31 ± 0.01	0.94 ± 0.04
70 – 80	51.86	0.46	7.25 ± 0.27	11.71 ± 0.44	0.68 ± 0.03	0.31 ± 0.01	0.93 ± 0.04
80 – 90	61.62	0.48	8.19 ± 0.33	14.48 ± 0.59	1.02 ± 0.04	0.49 ± 0.02	0.75 ± 0.03
90 – 100	70.96	0.51	6.73 ± 0.32	12.97 ± 0.61	1.07 ± 0.05	0.55 ± 0.03	0.84 ± 0.04
100 – 110	80.55	0.52	6.29 ± 0.26	13.23 ± 0.54	1.04 ± 0.04	0.54 ± 0.02	0.82 ± 0.03
110 – 120	94.08	0.53	5.94 ± 0.25	14.17 ± 0.60	0.74 ± 0.03	0.39 ± 0.02	0.77 ± 0.03
120 – 130	102.49	0.56	3.09 ± 0.26	7.95 ± 0.68	1.19 ± 0.10	0.67 ± 0.06	1.37 ± 0.12
130 – 136	110.27	0.50	4.93 ± 0.28	13.65 ± 0.77	0.77 ± 0.04	0.39 ± 0.02	0.80 ± 0.04
136 – 140	111.65	0.35	2.93 ± 0.20	8.21 ± 0.57	2.89 ± 0.20	1.01 ± 0.07	1.32 ± 0.09
140 – 150	118.41	0.35	5.64 ± 0.30	16.85 ± 0.89	1.48 ± 0.08	0.52 ± 0.03	0.65 ± 0.03
150 – 160	119.05	0.27	0.66 ± 0.06	1.98 ± 0.19	15.72 ± 1.54	4.17 ± 0.41	5.49 ± 0.54
160 – 169	119.35	0.18	0.50 ± 0.06	1.52 ± 0.19	30.15 ± 3.82	5.43 ± 0.69	7.18 ± 0.91
169 – 179	119.91	0.18	0.85 ± 0.08	2.56 ± 0.25	17.86 ± 1.75	3.21 ± 0.31	4.24 ± 0.41
179 – 190	120.43	0.18	0.72 ± 0.19	2.18 ± 0.58	20.97 ± 5.57	3.77 ± 1.00	4.98 ± 1.32
190 – 200	120.81	0.17	0.61 ± 0.12	1.85 ± 0.36	26.14 ± 5.12	4.44 ± 0.87	5.87 ± 1.15
200 – 210	121.23	0.20	0.56 ± 0.12	1.73 ± 0.36	23.80 ± 5.01	4.76 ± 1.00	6.29 ± 1.32
210 – 220	121.67	0.24	0.48 ± 0.06	1.49 ± 0.20	23.00 ± 3.07	5.52 ± 0.74	7.29 ± 0.97
220 – 230	122.23	0.22	0.68 ± 0.13	2.09 ± 0.39	17.90 ± 3.38	3.94 ± 0.74	5.20 ± 0.98
230 – 240	122.72	0.21	0.62 ± 0.18	1.92 ± 0.55	20.42 ± 5.89	4.29 ± 1.24	5.66 ± 1.63
240 – 250	123.15	0.19	0.60 ± 0.09	1.87 ± 0.27	23.14 ± 3.30	4.40 ± 0.63	5.81 ± 0.83
250 – 260	123.45	0.18	0.45 ± 0.06	1.39 ± 0.17	32.76 ± 4.08	5.90 ± 0.73	7.80 ± 0.97
260 – 270	123.99	0.19	0.74 ± 0.15	2.33 ± 0.47	18.62 ± 3.77	3.54 ± 0.72	4.67 ± 0.95
270 – 280	124.43	0.20	0.57 ± 0.06	1.79 ± 0.18	22.94 ± 2.35	4.59 ± 0.47	6.06 ± 0.62

Results of gravity core PS1772-8 and multicore PS1772-6. Abreviations: DBD = dry bulk density, SR = sedimentation rate, SAR = total sediment accumulation rate, VRR = vertical rain rate. All errors represent the statistical errors of one standard deviation from the mean (1σ) of the $^{230}Th_{ex}$ measurement. The age of each sample represents the age of the mean depth of the sampled core section.

Depth, cm	Age, kyr	DBD. g/cm^3	$^{230}Th_{ex}$, dpm/g	$^{230}Th^0_{ex}$, dpm/g	SR, cm/kyr	SAR, g/cm^2 · kyr	VRR, g/cm^2 · kyr
280 – 290	124.79	0.18	0.52 ± 0.12	1.65 ± 0.38	27.73 ± 6.31	4.99 ± 1.14	6.60 ± 1.50
290 – 300	125.21	0.19	0.57 ± 0.15	1.83 ± 0.48	23.70 ± 6.26	4.50 ± 1.19	5.95 ± 1.57
300 – 310	125.74	0.20	0.68 ± 0.05	2.18 ± 0.17	18.92 ± 1.50	3.78 ± 0.30	4.99 ± 0.39
310 – 320	126.09	0.19	0.47 ± 0.05	1.50 ± 0.17	28.80 ± 3.22	5.47 ± 0.61	7.23 ± 0.81
320 – 330	126.50	0.17	0.62 ± 0.12	1.99 ± 0.37	24.28 ± 4.55	4.13 ± 0.77	5.45 ± 1.02
330 – 340	126.97	0.20	0.60 ± 0.19	1.94 ± 0.61	21.25 ± 6.66	4.25 ± 1.33	5.61 ± 1.76
340 – 349	128.57	0.24	1.88 ± 0.21	6.17 ± 0.68	5.62 ± 0.62	1.35 ± 0.15	1.76 ± 0.19
349 – 360	129.57	0.21	1.08 ± 0.13	3.58 ± 0.44	11.01 ± 1.37	2.31 ± 0.29	3.04 ± 0.38
360 – 370	132.16	0.28	2.68 ± 0.20	9.10 ± 0.69	3.86 ± 0.29	1.08 ± 0.08	1.19 ± 0.09
370 – 380	137.70	0.40	3.92 ± 0.20	13.99 ± 0.71	1.81 ± 0.09	0.72 ± 0.04	0.78 ± 0.04
380 – 390	143.85	0.44	3.76 ± 0.28	14.20 ± 1.07	1.63 ± 0.12	0.72 ± 0.05	0.77 ± 0.06
390 – 400	150.30	0.46	3.56 ± 0.19	14.28 ± 0.78	1.55 ± 0.08	0.71 ± 0.04	0.76 ± 0.04
400 – 410	156.60	0.44	3.43 ± 0.17	14.59 ± 0.72	1.59 ± 0.08	0.70 ± 0.03	0.75 ± 0.04
410 – 420	162.13	0.46	2.71 ± 0.21	12.13 ± 0.92	1.81 ± 0.14	0.83 ± 0.06	0.90 ± 0.07
420 – 430	167.73	0.51	2.36 ± 0.28	11.11 ± 1.32	1.78 ± 0.21	0.91 ± 0.11	0.98 ± 0.12
430 – 440	172.28	0.49	1.89 ± 0.13	9.30 ± 0.65	2.20 ± 0.15	1.08 ± 0.07	1.17 ± 0.08
440 – 450	178.53	0.48	2.54 ± 0.16	13.24 ± 0.85	1.60 ± 0.10	0.77 ± 0.05	0.82 ± 0.05
450 – 460	186.08	0.48	2.90 ± 0.16	16.19 ± 0.88	1.32 ± 0.07	0.64 ± 0.03	0.67 ± 0.04
460 – 470	194.81	0.46	2.89 ± 0.24	17.48 ± 1.42	1.15 ± 0.09	0.53 ± 0.04	0.62 ± 0.05
470 – 480	204.39	0.45	2.99 ± 0.15	19.77 ± 1.01	1.04 ± 0.05	0.47 ± 0.02	0.55 ± 0.03
480 – 490	211.21	0.49	1.79 ± 0.14	12.60 ± 0.97	1.47 ± 0.11	0.72 ± 0.06	0.86 ± 0.07
490 – 500	218.66	0.53	1.70 ± 0.12	12.81 ± 0.89	1.34 ± 0.09	0.71 ± 0.05	0.85 ± 0.06
500 – 510	226.47	0.53	1.66 ± 0.13	13.45 ± 1.09	1.28 ± 0.10	0.68 ± 0.06	0.81 ± 0.07
510 – 520	233.07	0.51	1.36 ± 0.14	11.70 ± 1.21	1.51 ± 0.16	0.77 ± 0.08	0.93 ± 0.10
520 – 530	239.41	0.49	1.28 ± 0.14	11.65 ± 1.30	1.58 ± 0.18	0.77 ± 0.09	0.93 ± 0.10
530 – 540	249.40	0.50	1.31 ± 0.15	13.15 ± 1.49	1.00 ± 0.11	0.50 ± 0.06	0.83 ± 0.09
540 – 550	258.62	0.50	1.10 ± 0.16	12.05 ± 1.79	1.08 ± 0.16	0.54 ± 0.08	0.90 ± 0.13
550 – 560	267.23	0.51	0.93 ± 0.16	10.97 ± 1.89	1.16 ± 0.20	0.59 ± 0.10	0.99 ± 0.17
560 – 570	276.00	0.52	0.86 ± 0.11	10.97 ± 1.46	1.14 ± 0.15	0.59 ± 0.08	0.99 ± 0.13
570 – 580	286.08	0.53	0.89 ± 0.12	12.52 ± 1.71	0.99 ± 0.14	0.53 ± 0.07	0.87 ± 0.12
580 – 590	296.18	0.52	0.83 ± 0.15	12.80 ± 2.27	0.99 ± 0.18	0.51 ± 0.09	0.85 ± 0.15
590 – 595	300.61	0.48	0.60 ± 0.13	9.61 ± 2.08	1.13 ± 0.24	0.54 ± 0.12	1.13 ± 0.24
595 – 600	304.30	0.38	0.60 ± 0.11	10.04 ± 1.89	1.36 ± 0.25	0.52 ± 0.10	1.08 ± 0.20
600 – 605	307.22	0.32	0.55 ± 0.08	9.36 ± 1.35	1.72 ± 0.25	0.55 ± 0.08	1.16 ± 0.17
605 – 610	308.56	0.28	0.28 ± 0.07	4.86 ± 1.26	3.72 ± 0.96	1.04 ± 0.27	2.24 ± 0.58
610 – 620	311.32	0.27	0.30 ± 0.05	5.24 ± 0.97	3.63 ± 0.67	0.98 ± 0.18	2.08 ± 0.38
620 – 630	314.02	0.26	0.29 ± 0.11	5.32 ± 1.93	3.71 ± 1.34	0.96 ± 0.35	2.04 ± 0.74
630 – 640	320.50	0.24	0.74 ± 0.08	14.33 ± 1.60	1.54 ± 0.17	0.37 ± 0.04	0.76 ± 0.08

Results of gravity core PS1772-8 and multicore PS1772-6 (continued).

Age, kyr	^{232}Th, ppm	^{238}U, dpm/g	$^{231}Pa^{0}_{ex}$, dpm/g	$^{10}Be^{0}$, 10^{9}at/g	Mn, ppm	Fe, ppm
			Multicore PS1772-6			
4.58	3.33 ± 0.25	0.77 ± 0.08	1.16 ± 0.13	3.33 ± 0.11	2250	27820
10.07	4.24 ± 0.28	0.97 ± 0.09	1.16 ± 0.16		3620	31160
17.82	5.64 ± 0.30	1.12 ± 0.09	1.42 ± 0.32	4.12 ± 0.08	2810	33660
			Gravity Core PS1772-8			
6.16	3.71 ± 0.45	0.88 ± 0.12	1.86 ± 0.39	4.055 ± 0.170		
7.26	4.06 ± 0.50	1.02 ± 0.13	1.85 ± 0.33	3.671 ± 0.081		
11.72	5.76 ± 0.48	1.36 ± 0.18	1.73 ± 0.31	4.641 ± 0.070		
13.20	6.95 ± 0.49	1.15 ± 0.14	2.29 ± 0.31	4.206 ± 0.063		
15.60	6.53 ± 0.46	0.87 ± 0.11	2.17 ± 0.32	3.969 ± 0.095		
18.38	6.06 ± 0.43	1.02 ± 0.15	1.90 ± 0.29	2.857 ± 0.094		
21.49	5.22 ± 0.40	0.91 ± 0.15	1.46 ± 0.24	4.533 ± 0.077	1121	42140
24.08	4.69 ± 0.39	1.03 ± 0.29	1.36 ± 0.26	4.501 ± 0.068		
37.17	5.44 ± 0.39	0.85 ± 0.11	1.42 ± 0.36	4.214 ± 0.097		
51.86	4.99 ± 0.39	0.79 ± 0.07	2.26 ± 0.72	2.935 ± 0.062	1108	38500
61.62	5.36 ± 0.40	0.91 ± 0.11	2.52 ± 0.91	4.467 ± 0.094		
70.96	5.52 ± 0.45	0.86 ± 0.11	3.17 ± 1.04	3.355 ± 0.060		
80.55	4.65 ± 0.35	0.87 ± 0.10	3.00 ± 1.01	3.495 ± 0.049	1324	44200
94.08	3.18 ± 0.30	0.71 ± 0.10	2.68 ± 1.17	3.735 ± 0.052		
102.49	2.30 ± 0.28	0.37 ± 0.08	2.39 ± 1.41	2.647 ± 0.122		
110.27	2.71 ± 0.34	0.52 ± 0.10	2.19 ± 1.52	4.213 ± 0.059	1226	42940
111.65	1.41 ± 0.21	0.31 ± 0.07	2.34 ± 1.79	2.587 ± 0.060	1188	25860
118.41	2.83 ± 0.34	0.64 ± 0.11	1.75 ± 1.44	4.008 ± 0.072	447	26740
119.05	0.33 ± 0.05	0.20 ± 0.03	1.17 ± 0.63	0.738 ± 0.034	178	6280
119.35	0.35 ± 0.06	0.13 ± 0.03		0.665 ± 0.031	450	1076
119.91	0.58 ± 0.06	0.27 ± 0.05		0.732 ± 0.033	230	1068
120.43	0.28 ± 0.07	0.16 ± 0.06				
120.81	0.36 ± 0.08	0.29 ± 0.06		0.506 ± 0.030		
121.23	0.23 ± 0.07	0.29 ± 0.05			490	1074
121.67	0.21 ± 0.03	0.29 ± 0.03		0.338 ± 0.037		
122.23	0.17 ± 0.06	0.29 ± 0.05				
122.72	0.30 ± 0.09	0.20 ± 0.05		0.329 ± 0.031	664	836
123.15	0.31 ± 0.08	0.27 ± 0.03				
123.45	0.20 ± 0.03	0.33 ± 0.03		0.271 ± 0.023		
123.99	0.66 ± 0.15	0.34 ± 0.06			1232	1312
124.43	0.24 ± 0.05	0.34 ± 0.02	0.43 ± 0.14	0.288 ± 0.037		

Results of gravity core PS1772-8 and multicore PS1772-6 (continued). All errors represent the statistical errors of one standard deviation from the mean (1σ). The $^{231}Pa_{ex}$ data from 0-160 cm core depth represent three times running means.

Age, kyr	^{232}Th, ppm	^{238}U, dpm/g	$^{231}Pa^{0}_{ex}$, dpm/g	$^{10}Be^{0}$, 10^{9}at/g	Mn, ppm	Fe, ppm
124.79	0.27 ± 0.04	0.27 ± 0.04				
125.21	0.38 ± 0.14	0.37 ± 0.06		0.324 ± 0.038	974	1632
125.74	0.37 ± 0.07	0.27 ± 0.02	1.51 ± 0.15			
126.09	0.34 ± 0.04	0.38 ± 0.03		0.699 ± 0.046		
126.50	0.30 ± 0.08	0.41 ± 0.05			1903	3136
126.97	0.41 ± 0.07	0.40 ± 0.09		0.438 ± 0.029		
128.57	1.68 ± 0.16	0.41 ± 0.07				
129.57	0.93 ± 0.11	0.54 ± 0.06		0.924 ± 0.034	1891	7792
132.16	2.57 ± 0.19	0.76 ± 0.09		2.086 ± 0.054	2940	17600
137.70	4.76 ± 0.21	1.06 ± 0.11		2.965 ± 0.059	2151	32340
143.85	4.82 ± 0.27	1.27 ± 0.17	3.42 ± 1.31		1712	36460
150.30	5.19 ± 0.25	0.83 ± 0.10		2.383 ± 0.067		
156.60	5.90 ± 0.28	0.50 ± 0.08				
162.13	5.30 ± 0.26	0.95 ± 0.12		2.391 ± 0.057	703	37180
167.73	4.92 ± 0.25	1.14 ± 0.17				
172.28	3.93 ± 0.19	0.74 ± 0.08		2.577 ± 0.067		
178.53	4.10 ± 0.27	0.60 ± 0.08				
186.08	4.87 ± 0.30	0.80 ± 0.08		3.757 ± 0.060		
194.81	4.94 ± 0.38	0.87 ± 0.11				
204.39	3.31 ± 0.21	0.62 ± 0.07		4.811 ± 0.077		
211.21	1.69 ± 0.17	0.52 ± 0.08				
218.66	2.54 ± 0.17	0.68 ± 0.09		3.732 ± 0.097		
226.47	3.31 ± 0.24	0.58 ± 0.07				
233.07	3.03 ± 0.19	0.63 ± 0.08		3.417 ± 0.058		
239.41	4.36 ± 0.32	0.80 ± 0.08				
249.40	3.86 ± 0.23	0.74 ± 0.09		3.885 ± 0.074		
258.62	5.94 ± 0.27	1.01 ± 0.12				
267.23	4.29 ± 0.21	0.68 ± 0.12		3.324 ± 0.066		
276.00	2.67 ± 0.20	0.58 ± 0.08				
286.08	3.14 ± 0.23	0.43 ± 0.06		3.914 ± 0.070		
296.18	2.82 ± 0.22	0.67 ± 0.13		3.526 ± 0.060		
300.61	2.56 ± 0.19	0.54 ± 0.08		2.784 ± 0.056		
304.30	2.04 ± 0.20	0.45 ± 0.06		2.714 ± 0.057		
307.22	1.26 ± 0.13	0.36 ± 0.05				
308.56	0.70 ± 0.09	0.26 ± 0.05		0.403 ± 0.012		
311.32	0.46 ± 0.04	0.24 ± 0.04		0.148 ± 0.008		
314.02	1.56 ± 0.15	0.10 ± 0.02				
320.50	0.48 ± 0.07	0.15 ± 0.03		0.287 ± 0.011		

Results of gravity core PS1772-8 and multicore PS1772-6 (continued).

Age, kyr	rel, PRC,	VRR ^{10}Be, 10^9at/ cm^2 · kyr	VRR ^{231}Pa$_{ex}$, dpm/ cm^2 · kyr	VRR biog. opal, g/ cm^2 · kyr	VRR Ba_{bio}, mg/ cm^2 · kyr	VRR Al_2O_3, mg/ cm^2 · kyr	^{238}U auth., dpm/g
			Multicore PS1772-6				
4.58	0.95	3.59 ± 0.09	1.18 ± 0.14	0.45 ± 0.01	0.83 ± 0.02	86.59 ± 2.16	0.16 ± 0.20
10.07	1.05		1.07 ± 0.15		0.69 ± 0.02	77.49 ± 1.97	0.19 ± 0.26
17.82	1.3	2.40 ± 0.05	1.08 ± 0.25		0.38 ± 0.01	85.57 ± 1.80	0.08 ± 0.35
			Gravity Core PS1772-6				
6.16	0.95	3.68 ± 0.14	1.61 ± 0.34	0.38 ± 0.01	0.86 ± 0.03	48.65 ± 1.86	0.19 ± 0.23
7.26	1.08	2.90 ± 0.12	1.58 ± 0.29	0.30 ± 0.01	0.77 ± 0.03	48.08 ± 1.93	0.27 ± 0.25
11.72	1.02	3.29 ± 0.11	1.25 ± 0.23	0.20 ± 0.01	0.43 ± 0.01	61.13 ± 2.11	0.30 ± 0.35
13.20	1.13	2.91 ± 0.09	1.79 ± 0.25	0.15 ± 0.00	0.39 ± 0.01	85.21 ± 2.66	0.00 ± 0.30
15.60	1.33	2.25 ± 0.07	1.63 ± 0.25	0.14 ± 0.00	0.33 ± 0.01	87.82 ± 2.70	0.00 ± 0.07
18.38	1.32	1.72 ± 0.05	1.51 ± 0.23	0.19 ± 0.01	0.34 ± 0.01	89.37 ± 2.85	0.00 ± 0.27
21.49	1.38	2.78 ± 0.10	1.24 ± 0.20	0.19 ± 0.01	0.34 ± 0.01	95.46 ± 3.51	0.00 ± 0.27
24.08	1.25	3.31 ± 0.19	1.25 ± 0.25	0.20 ± 0.01	0.37 ± 0.02	103.59 ± 6.00	0.16 ± 0.29
37.17	1.22	3.26 ± 0.13	1.34 ± 0.35	0.17 ± 0.01	0.41 ± 0.02	102.88 ± 4.16	0.00 ± 0.18
51.86	1.18	2.31 ± 0.09	2.10 ± 0.68	0.17 ± 0.01	0.44 ± 0.02	102.18 ± 3.86	0.00 ± 0.18
61.62	1.12	3.00 ± 0.12	1.89 ± 0.69	0.13 ± 0.01	0.41 ± 0.02	83.33 ± 3.37	0.00 ± 0.25
70.96	1.22	2.31 ± 0.11	2.66 ± 0.88	0.13 ± 0.01	0.44 ± 0.02	94.60 ± 4.49	0.00 ± 0.18
80.55	1.08	2.66 ± 0.11	2.46 ± 0.83	0.13 ± 0.01	0.41 ± 0.02	94.26 ± 3.87	0.01 ± 0.29
94.08	1.23	2.33 ± 0.10	2.05 ± 0.90	0.12 ± 0.01	0.36 ± 0.02	87.27 ± 3.68	0.12 ± 0.20
102.49	1.35	2.68 ± 0.23	3.27 ± 1.95	0.22 ± 0.02	0.62 ± 0.05	154.21 ± 13.21	0.00 ± 0.09
110.27	1.42	2.36 ± 0.13	1.74 ± 1.22	0.13 ± 0.01	0.38 ± 0.02	86.88 ± 4.90	0.02 ± 0.17
111.65	1.44	2.38 ± 0.16	3.10 ± 2.38	0.21 ± 0.01	0.69 ± 0.05	136.88 ± 9.43	0.05 ± 0.09
118.41	1.47	1.76 ± 0.09	1.13 ± 0.93	0.19 ± 0.01	0.35 ± 0.02	48.53 ± 2.57	0.12 ± 0.17
119.05	1.42	2.85 ± 0.28	6.43 ± 3.52	1.21 ± 0.12	3.02 ± 0.30	20.65 ± 2.03	0.14 ± 0.02
119.35	1.42	3.36 ± 0.43		3.95 ± 0.50	3.88 ± 0.49	20.24 ± 2.57	0.07 ± 0.02
119.91	1.40	2.22 ± 0.22		3.48 ± 0.34	2.29 ± 0.22	13.56 ± 1.33	0.16 ± 0.04
120.43	1.39			3.99 ± 1.06	2.69 ± 0.72		0.11 ± 0.02
120.81	1.37	2.17 ± 0.42		4.52 ± 0.89	3.05 ± 0.60	18.77 ± 3.68	0.22 ± 0.02
121.23	1.37			4.84 ± 1.02	3.14 ± 0.66	17.73 ± 3.73	0.25 ± 0.01
121.67	1.37	1.80 ± 0.24		6.20 ± 0.83	3.06 ± 0.41	17.82 ± 2.38	0.25 ± 0.01
122.23	1.37			4.83 ± 0.91	1.82 ± 0.34		0.26 ± 0.01
122.72	1.38	1.35 ± 0.39		5.15 ± 1.49	1.93 ± 0.56	10.65 ± 3.07	0.14 ± 0.02
123.15	1.38			4.76 ± 0.68	1.97 ± 0.28		0.21 ± 0.02
123.45	1.39	1.52 ± 0.19		6.39 ± 0.80	2.89 ± 0.36	17.59 ± 2.19	0.29 ± 0.01
123.99	1.41			3.74 ± 0.76	1.82 ± 0.37	13.17 ± 2.67	0.22 ± 0.04
124.43	1.40	1.25 ± 0.13	2.61 ± 0.89	4.79 ± 0.49	2.24 ± 0.23	17.09 ± 1.75	0.29 ± 0.01

Results of gravity core PS1772-8 and multicore PS1772-6 (continued). PRC = relative production rate changes of cosmogenic radionuclides following Mazaud et al. (1994). Biogenic barium and Al_2O_3 data are from Nürnberg (1995). Biogenic opal data are from G. Bohrmann (unpub. res.). All errors represent the statistical errors of one standard deviation from the mean (1σ) of the ^{230}Th$_{ex}$ measurement except the ^{231}Pa$_{ex}$ errors where it represents the quadratic sum of the 1σ uncertainties of the ^{230}Th$_{ex}$ and ^{231}Pa$_{ex}$ measurements. The error of the authigenic ^{238}U concentrations represents the range of the lithogenic ^{238}U/^{232}Th activity ratio between 0.5 and 1.

Age, kyr	rel, PRC,	VRR ^{10}Be, 10^9at/ cm^2 · kyr	VRR $^{231}Pa_{ex}$, dpm/ cm^2 · kyr	VRR biog, opal, g/ cm^2 · kyr	VRR Ba_{bio}, mg/ cm^2 · kyr	VRR Al_2O_3, mg/ cm^2 · kyr	^{238}U auth., dpm/g
124.79	1.39			5.08 ± 1.16	2.24 ± 0.51		0.22 ± 0.02
125.21	1.38	1.40 ± 0.37		4.52 ± 1.19	2.02 ± 0.53	16.77 ± 4.43	0.30 ± 0.02
125.74	1.36		7.54 ± 0.96	3.90 ± 0.31	1.70 ± 0.13		0.20 ± 0.02
126.09	1.36	3.72 ± 0.42		5.93 ± 0.66	2.03 ± 0.23	23.12 ± 2.59	0.32 ± 0.02
126.50	1.35			4.09 ± 0.77	1.25 ± 0.24	19.48 ± 3.65	0.35 ± 0.02
126.97	1.34	1.84 ± 0.57		3.82 ± 1.20	2.30 ± 0.72	84.41 ± 26.44	0.32 ± 0.03
128.57	1.33			1.20 ± 0.13	1.04 ± 0.11		0.10 ± 0.10
129.57	1.33	2.11 ± 0.26		1.91 ± 0.24	2.28 ± 0.28	85.66 ± 10.64	0.37 ± 0.06
132.16	1.27	1.96 ± 0.15		0.57 ± 0.04	1.08 ± 0.08	67.40 ± 5.13	0.29 ± 0.16
137.70	1.20	1.92 ± 0.10		0.23 ± 0.01	0.58 ± 0.03	65.75 ± 3.32	0.18 ± 0.29
143.85	1.10		2.62 ± 1.02	0.15 ± 0.01	0.44 ± 0.03	84.93 ± 6.39	0.38 ± 0.30
150.30	1.10	1.65 ± 0.09		0.11 ± 0.01	0.43 ± 0.02	83.01 ± 4.52	0.00 ± 0.19
156.60	1.25			0.13 ± 0.01	0.42 ± 0.02		0.00 ± 0.00
162.13	1.18	1.82 ± 0.14		0.18 ± 0.01	0.50 ± 0.04	97.75 ± 7.44	0.00 ± 0.30
167.73	1.25			0.18 ± 0.02	0.55 ± 0.07		0.23 ± 0.30
172.28	1.10	2.74 ± 0.19		0.20 ± 0.01	0.71 ± 0.05	129.70 ± 9.03	0.01 ± 0.24
178.53	1.20			0.13 ± 0.01	0.54 ± 0.03		0.00 ± 0.10
186.08	1.40	1.80 ± 0.10		0.12 ± 0.01	0.46 ± 0.02	73.23 ± 4.00	0.00 ± 0.20
194.81	1.40			0.11 ± 0.01	0.44 ± 0.04		0.00 ± 0.26
204.39		2.65 ± 0.13		0.11 ± 0.01	0.47 ± 0.02	58.94 ± 3.00	0.01 ± 0.20
211.21				0.21 ± 0.02	0.86 ± 0.07		0.21 ± 0.10
218.66		3.17 ± 0.22		0.20 ± 0.01	0.74 ± 0.05	87.80 ± 6.09	0.21 ± 0.16
226.47				0.23 ± 0.02	0.61 ± 0.05		0.00 ± 0.17
233.07		3.18 ± 0.33		0.28 ± 0.03	0.72 ± 0.07	94.35 ± 9.78	0.07 ± 0.19
239.41				0.25 ± 0.03	0.75 ± 0.08		0.00 ± 0.26
249.40		3.21 ± 0.36		0.18 ± 0.02	0.64 ± 0.07	79.28 ± 8.99	0.03 ± 0.24
258.62				0.16 ± 0.02	0.66 ± 0.10		0.00 ± 0.28
267.23		3.30 ± 0.57		0.20 ± 0.03	0.73 ± 0.13	113.70 ± 19.63	0.00 ± 0.15
276.00				0.24 ± 0.03	0.74 ± 0.10		0.09 ± 0.16
286.08		3.40 ± 0.46		0.24 ± 0.03	0.71 ± 0.10	84.89 ± 11.56	0.00 ± 0.04
296.18		2.99 ± 0.53		0.29 ± 0.05	0.76 ± 0.14	81.44 ± 14.42	0.15 ± 0.17
300.61		3.15 ± 0.68		0.52 ± 0.11	0.91 ± 0.20	102.10 ± 22.09	0.07 ± 0.16
304.30		2.94 ± 0.55		0.65 ± 0.12	0.76 ± 0.14	81.42 ± 15.28	0.07 ± 0.13
307.22				0.79 ± 0.11	0.70 ± 0.10		0.13 ± 0.08
308.56		0.90 ± 0.23		1.63 ± 0.42	1.25 ± 0.32	63.09 ± 16.32	0.13 ± 0.04
311.32		0.31 ± 0.06		1.70 ± 0.32	1.10 ± 0.20	5.85 ± 1.08	0.16 ± 0.03
314.02				1.84 ± 0.67	1.00 ± 0.36		0.00 ± 0.00
320.50		0.22 ± 0.02		0.69 ± 0.08	0.38 ± 0.04	2.14 ± 0.24	0.06 ± 0.03

Results of gravity core PS1772-8 and multicore PS1772-6 (continued).

B.3 PS1768-8 and PS1768-6

Depth, cm	Age, kyr	DBD, g/cm^3	$^{230}Th_{ex}$, dpm/g	$^{230}Th^0_{ex}$, dpm/g	SR, cm/kyr	SAR, g/cm^2 · kyr	VRR, g/cm^2 · kyr
			Multicore PS1768-6				
0.5 – 10.5	0.86	0.81	8.18 ± 0.54	8.25 ± 0.54	10.00 ± 0.66	8.10 ± 0.53	1.04 ± 0.07
10.5 – 20.5	1.75	0.81	8.36 ± 0.24	8.49 ± 0.25	10.00 ± 0.29	8.10 ± 0.23	1.01 ± 0.03
20.5 – 27.5	2.41	0.81	8.88 ± 0.24	9.08 ± 0.24	10.00 ± 0.27	8.10 ± 0.22	0.95 ± 0.03
27.5 – 33.5	3.01	0.80	9.40 ± 0.27	9.66 ± 0.28	10.00 ± 0.29	8.00 ± 0.23	0.89 ± 0.03
			Gravity Core PS1768-8				
1 – 2	3.00						1.00 ± 0.05
0 – 25	7.04	0.81	7.97 ± 0.27	8.51 ± 0.29	6.19 ± 0.21	5.02 ± 0.17	1.01 ± 0.03
25 – 45	9.21	0.80	5.08 ± 0.21	5.53 ± 0.23	9.22 ± 0.39	7.38 ± 0.31	1.55 ± 0.07
45 – 70	10.66	0.78	2.73 ± 0.18	3.01 ± 0.20	17.24 ± 1.15	13.45 ± 0.90	2.85 ± 0.19
70 – 95	11.66	0.77	1.89 ± 0.17	2.11 ± 0.19	24.84 ± 2.20	19.13 ± 1.69	4.07 ± 0.36
95 – 107	12.17	0.78	1.96 ± 0.12	2.20 ± 0.13	23.47 ± 1.43	18.31 ± 1.12	3.92 ± 0.24
107 – 131	13.26	0.79	2.05 ± 0.15	2.32 ± 0.17	22.02 ± 1.64	17.40 ± 1.30	3.70 ± 0.28
131 – 156	14.32	0.76	1.97 ± 0.16	2.24 ± 0.18	23.69 ± 1.88	18.01 ± 1.43	3.83 ± 0.30
156 – 181	16.61	0.80	5.58 ± 0.29	6.51 ± 0.34	10.89 ± 0.57	8.71 ± 0.46	1.32 ± 0.07
181 – 206	19.13	0.84	5.70 ± 0.36	6.80 ± 0.43	9.94 ± 0.62	8.35 ± 0.52	1.26 ± 0.08
206 – 231	21.54	0.81	5.54 ± 0.34	6.76 ± 0.42	10.36 ± 0.64	8.40 ± 0.52	1.27 ± 0.08
231 – 256	23.94	0.84	5.19 ± 0.32	6.48 ± 0.40	10.43 ± 0.65	8.76 ± 0.54	1.33 ± 0.08
256 – 281	28.96	0.83	5.72 ± 0.30	7.48 ± 0.39	4.98 ± 0.26	4.13 ± 0.21	1.15 ± 0.06
281 – 306	33.08	0.85	4.38 ± 0.28	5.94 ± 0.38	6.07 ± 0.39	5.16 ± 0.33	1.45 ± 0.09
306 – 331	37.59	0.82	4.78 ± 0.27	6.77 ± 0.38	5.54 ± 0.31	4.54 ± 0.25	1.27 ± 0.07
331 – 356	41.28	0.81	3.79 ± 0.26	5.55 ± 0.38	6.78 ± 0.46	5.49 ± 0.38	1.55 ± 0.11
356 – 381	45.25	0.82	3.90 ± 0.40	5.93 ± 0.60	6.29 ± 0.64	5.16 ± 0.52	1.45 ± 0.15
381 – 406	49.00	0.87	3.34 ± 0.15	5.26 ± 0.24	6.67 ± 0.30	5.81 ± 0.27	1.64 ± 0.07
406 – 431	52.58	0.86	3.13 ± 0.19	5.08 ± 0.30	6.97 ± 0.42	6.00 ± 0.36	1.69 ± 0.10
431 – 456	55.55	0.91	2.36 ± 0.14	3.95 ± 0.23	8.44 ± 0.49	7.68 ± 0.45	2.18 ± 0.13
456 – 480	58.95	0.91	2.75 ± 0.16	4.75 ± 0.27	7.05 ± 0.40	6.41 ± 0.36	1.81 ± 0.10
480 – 505	62.19	0.86	3.17 ± 0.17	5.63 ± 0.31	7.73 ± 0.43	6.65 ± 0.37	1.53 ± 0.08
505 – 530	65.95	0.84	3.66 ± 0.17	6.73 ± 0.32	6.65 ± 0.31	5.59 ± 0.26	1.28 ± 0.06
530 – 555	69.29	0.84	3.14 ± 0.15	5.97 ± 0.29	7.47 ± 0.36	6.28 ± 0.31	1.44 ± 0.07

Results of gravity core PS1768-8 and multicore PS1768-6. Abreviations: DBD = dry bulk density, SR = sedimentation rate, SAR = total sediment accumulation rate, VRR = vertical rain rate. All errors represent the statistical errors of one standard deviation from the mean (1σ) of the $^{230}Th_{ex}$ measurement. The age of each sample represents the age of the mean depth of the sampled core section.

Depth, cm	Age, kyr	DBD, g/cm^3	$^{230}Th_{ex}$, dpm/g	$^{230}Th^0_{ex}$, dpm/g	SR, cm/kyr	SAR, g/cm^2 · kyr	VRR, g/cm^2 · kyr
555 – 580	72.67	0.86	3.01 ± 0.19	5.89 ± 0.37	7.40 ± 0.47	6.36 ± 0.40	1.46 ± 0.09
579 – 589	73.96	0.86	2.77 ± 0.16	5.49 ± 0.31	7.01 ± 0.39	6.02 ± 0.34	1.57 ± 0.09
589 – 599	77.26	0.87	2.82 ± 0.18	5.76 ± 0.36	3.03 ± 0.19	2.63 ± 0.17	1.49 ± 0.09
599 – 614	81.72	0.85	2.52 ± 0.15	5.36 ± 0.33	3.36 ± 0.21	2.86 ± 0.18	1.60 ± 0.10
614 – 624	84.28	0.81	2.18 ± 0.13	4.75 ± 0.28	3.91 ± 0.23	3.17 ± 0.19	1.81 ± 0.11
624 – 634	87.22	0.84	2.37 ± 0.14	5.29 ± 0.32	3.40 ± 0.20	2.85 ± 0.17	1.62 ± 0.10
634 – 644	89.95	0.85	2.11 ± 0.13	4.84 ± 0.30	3.67 ± 0.23	3.12 ± 0.20	1.78 ± 0.11
644 – 654	92.84	0.85	2.18 ± 0.15	5.14 ± 0.34	3.45 ± 0.23	2.94 ± 0.20	1.67 ± 0.11
654 – 663	95.62	0.84	2.29 ± 0.17	5.54 ± 0.40	3.24 ± 0.23	2.72 ± 0.20	1.55 ± 0.11
663 – 672	97.99	0.83	1.93 ± 0.28	4.77 ± 0.69	3.80 ± 0.55	3.15 ± 0.45	1.80 ± 0.26
672 – 682	100.36	0.84	1.68 ± 0.10	4.24 ± 0.27	4.22 ± 0.26	3.55 ± 0.22	2.03 ± 0.13
682 – 691	102.72	0.84	1.82 ± 0.15	4.69 ± 0.38	3.81 ± 0.31	3.20 ± 0.26	1.83 ± 0.15
691 – 700	105.00	0.84	1.72 ± 0.14	4.54 ± 0.36	3.94 ± 0.32	3.31 ± 0.27	1.90 ± 0.15
700 – 710	107.34	0.85	1.54 ± 0.11	4.14 ± 0.29	4.27 ± 0.30	3.63 ± 0.25	2.08 ± 0.14
710 – 721	111.08	0.86	2.15 ± 0.19	6.01 ± 0.53	2.95 ± 0.26	2.53 ± 0.22	1.43 ± 0.13
721 – 729	113.53	0.83	2.32 ± 0.09	6.62 ± 0.26	3.26 ± 0.13	2.70 ± 0.11	1.30 ± 0.05
729 – 740	116.10	0.78	1.83 ± 0.09	5.36 ± 0.28	4.29 ± 0.22	3.35 ± 0.17	1.61 ± 0.08
740 – 750	118.19	0.77	1.63 ± 0.11	4.85 ± 0.31	4.78 ± 0.31	3.68 ± 0.24	1.77 ± 0.12
750 – 760	119.83	0.77	1.25 ± 0.12	3.79 ± 0.37	6.09 ± 0.59	4.69 ± 0.46	2.27 ± 0.22
760 – 770	121.50	0.78	1.24 ± 0.12	3.81 ± 0.35	5.99 ± 0.56	4.67 ± 0.44	2.26 ± 0.21
770 – 780	123.04	0.77	1.14 ± 0.10	3.55 ± 0.31	6.50 ± 0.58	5.00 ± 0.44	2.42 ± 0.21
780 – 790	123.99	0.77	0.69 ± 0.10	2.18 ± 0.30	10.52 ± 1.45	8.10 ± 1.12	3.94 ± 0.54
790 – 800	125.87	0.78	1.34 ± 0.15	4.28 ± 0.49	5.33 ± 0.61	4.16 ± 0.48	2.01 ± 0.23
800 – 810	127.08	0.78	0.85 ± 0.12	2.75 ± 0.40	8.25 ± 1.21	6.44 ± 0.95	3.13 ± 0.46
810 – 820	127.98	0.77	0.63 ± 0.10	2.07 ± 0.32	11.09 ± 1.70	8.54 ± 1.31	4.16 ± 0.64
820 – 830	129.05	0.76	0.76 ± 0.11	2.50 ± 0.36	9.32 ± 1.35	7.08 ± 1.03	3.45 ± 0.50
830 – 840	130.84	0.83	1.96 ± 0.15	6.56 ± 0.51	5.60 ± 0.44	4.65 ± 0.36	1.31 ± 0.10
855 – 880	135.77	0.88	2.01 ± 0.22	7.04 ± 0.77	8.11 ± 0.89	7.13 ± 0.78	1.22 ± 0.13
880 – 896	138.20	0.87	1.49 ± 0.19	5.34 ± 0.69	6.60 ± 0.86	5.75 ± 0.74	1.61 ± 0.21

Results of gravity core PS1768-8 and multicore PS1768-6 (continued).

Age, kyr	^{232}Th, ppm	^{238}U, dpm/g	$^{231}Pa^{0}_{ex}$, dpm/g	$^{10}Be^{0}$, 10^{9}at/g	Mn, ppm	Fe, ppm
			Multicore PS1768-6			
0.86	2.33 ± 0.54	0.84 ± 0.09	1.51 ± 0.36	1.587 ± 0.052		
1.75	1.15 ± 0.13	0.88 ± 0.10	1.04 ± 0.13		383	5520
2.41	0.99 ± 0.13	0.63 ± 0.08	1.05 ± 0.12	1.643 ± 0.062	562	6457
3.01	1.15 ± 0.17	0.46 ± 0.05	1.34 ± 0.14		488	5860
			Gravity Core PS1768-6			
3.00				1.665 ± 0.097		
7.04	1.30 ± 0.19	0.40 ± 0.07	1.28 ± 0.34	1.399 ± 0.048	407	6060
9.21	0.78 ± 0.14	0.50 ± 0.06	1.26 ± 0.38	1.020 ± 0.034	416	4940
10.66	0.71 ± 0.14	0.32 ± 0.07	0.92 ± 0.38	0.561 ± 0.020	412	2640
11.66	0.20 ± 0.09	0.31 ± 0.06	0.99 ± 0.37	0.410 ± 0.015	218	1980
12.17	0.41 ± 0.09	0.30 ± 0.04	0.87 ± 0.32	0.465 ± 0.017	1882	3540
13.26	0.66 ± 0.13	0.50 ± 0.06	0.75 ± 0.30	0.377 ± 0.012	69	5160
14.32	0.58 ± 0.09	1.15 ± 0.08	0.74 ± 0.31	0.543 ± 0.020	64	4880
16.61	2.25 ± 0.23	3.32 ± 0.14	1.17 ± 0.34	1.226 ± 0.044	215	15860
19.13	2.84 ± 0.30	2.79 ± 0.18	1.32 ± 0.40	1.945 ± 0.053	346	23960
21.54	3.17 ± 0.35	2.00 ± 0.14	1.24 ± 0.42	1.798 ± 0.040	386	23260
23.94	3.10 ± 0.36	1.41 ± 0.13	0.64 ± 0.39	2.101 ± 0.086	242	13460
28.96	3.71 ± 0.36	1.22 ± 0.13	0.61 ± 0.37	2.150 ± 0.045	402	25760
33.08	2.29 ± 0.28	1.05 ± 0.11	0.44 ± 0.35	1.874 ± 0.039	378	25800
37.59	1.56 ± 0.23	1.07 ± 0.11	0.63 ± 0.37	1.887 ± 0.040	350	20340
41.28	2.53 ± 0.31	1.35 ± 0.14	0.55 ± 0.36	1.993 ± 0.066	350	20380
45.25	1.08 ± 0.18	1.52 ± 0.20	1.16 ± 0.41	1.413 ± 0.031	305	19660
49.00	3.00 ± 0.18	1.35 ± 0.07	1.13 ± 0.43	1.314 ± 0.033	292	22880
52.58	2.96 ± 0.21	1.65 ± 0.10	1.14 ± 0.42	1.129 ± 0.024	367	18640
55.55	3.01 ± 0.18	1.21 ± 0.07	1.08 ± 0.55	1.373 ± 0.025	536	29740
58.95	2.63 ± 0.24	0.92 ± 0.06	1.20 ± 0.60	1.575 ± 0.027	442	24800
62.19	2.98 ± 0.16	0.99 ± 0.09		1.353 ± 0.034	412	26000
65.95	3.84 ± 0.26	1.16 ± 0.07		2.120 ± 0.036	395	24000
69.29	2.84 ± 0.20	0.97 ± 0.06	0.42 ± 0.92	1.482 ± 0.062	268	16800

Results of gravity core PS1768-8 and multicore PS1768-6 (continued). All errors represent the statistical errors of one standard deviation from the mean (1σ). The $^{231}Pa_{ex}$ data represent three times running means.

Age, kyr	^{232}Th, ppm	^{238}U, dpm/g	$^{231}Pa^{0}_{ex}$, dpm/g	$^{10}Be^{0}$, 10^{9}at/g	Mn, ppm	Fe, ppm
72.67	2.19 ± 0.17	0.75 ± 0.09	0.69 ± 0.72	1.691 ± 0.034	364	20500
73.96	1.53 ± 0.17	0.64 ± 0.07	1.01 ± 0.55		448	25860
77.26	1.50 ± 0.19	0.60 ± 0.07	0.99 ± 0.66	1.380 ± 0.030	390	21060
81.72	1.04 ± 0.14	0.63 ± 0.06	1.10 ± 0.77		256	12360
84.28	0.69 ± 0.11	0.58 ± 0.05	1.35 ± 0.79	1.258 ± 0.031	171	8620
87.22	1.58 ± 0.16	0.57 ± 0.06	1.30 ± 0.67		292	16980
89.95	1.65 ± 0.16	0.41 ± 0.06	1.64 ± 0.81	1.647 ± 0.035	588	32480
92.84	1.80 ± 0.18	0.45 ± 0.07	1.50 ± 0.86		320	16220
95.62	1.56 ± 0.21	0.48 ± 0.07	1.86 ± 1.03		209	11540
97.99	2.94 ± 0.60	0.43 ± 0.06	1.08 ± 0.69	1.229 ± 0.027	173	9620
100.36	0.97 ± 0.12	0.32 ± 0.05	1.06 ± 0.78		206	9600
102.72	1.03 ± 0.17	0.36 ± 0.06	1.11 ± 0.87		267	12080
105.00	0.87 ± 0.14	0.45 ± 0.08	1.29 ± 1.01	1.463 ± 0.033	243	12380
107.34	1.00 ± 0.20	0.50 ± 0.06	1.96 ± 1.37		337	17860
111.08	1.46 ± 0.25	0.36 ± 0.04	1.96 ± 1.23	1.914 ± 0.037	397	22140
113.53	1.21 ± 0.10	0.42 ± 0.05	2.10 ± 1.13		261	15040
116.10	0.92 ± 0.11	0.32 ± 0.03	1.98 ± 0.89		119	5320
118.19	0.57 ± 0.10	0.30 ± 0.03	2.38 ± 0.95	0.809 ± 0.023	94	3460
119.83	0.48 ± 0.12	0.33 ± 0.03	2.15 ± 1.03		80	2560
121.50	0.62 ± 0.12	0.32 ± 0.04	1.80 ± 1.06	0.548 ± 0.022	81	3480
123.04	0.44 ± 0.11	0.32 ± 0.03	1.52 ± 1.11		62	2600
123.99	0.46 ± 0.10	0.53 ± 0.04	1.46 ± 1.22		69	2140
125.87	0.52 ± 0.12	1.35 ± 0.06	1.95 ± 1.87	0.437 ± 0.018	269	2560
127.08	0.84 ± 0.10	0.73 ± 0.06	2.37 ± 2.02		91	1960
127.98	0.48 ± 0.09	0.36 ± 0.05	1.92 ± 2.52	0.363 ± 0.015	75	3100
129.05	0.44 ± 0.08	0.60 ± 0.06	2.33 ± 2.28		49	3100
130.84	2.25 ± 0.16	1.45 ± 0.09	2.31 ± 2.64	1.439 ± 0.046	355	19100
135.77	3.97 ± 0.29	1.57 ± 0.11		1.975 ± 0.122	486	29060
138.20	2.32 ± 0.21	1.40 ± 0.09	0.34 ± 2.70	1.397 ± 0.032	384	20860

Results of gravity core PS1768-8 and multicore PS1768-6 (continued).

Age, kyr	rel, PRC,	VRR ^{10}Be, 10^9at/ cm^2 · kyr	VRR $^{231}Pa_{ex}$, dpm/ cm^2 · kyr	VRR biog. opal, g/ cm^2 · kyr	VRR Ba_{bio}, mg/ cm^2 · kyr	VRR Al_2O_3, mg/ cm^2 · kyr	^{238}U auth., dpm/g
			Multicore PS1768-6				
0.86	1.00	1.65 ± 0.08		0.73 ± 0.05	1.16 ± 0.08	10.78 ± 0.71	0.41 ± 0.14
1.75			1.05 ± 0.14		1.63 ± 0.05	16.00 ± 0.46	0.67 ± 0.07
2.41	0.86	1.81 ± 0.09	1.00 ± 0.12			20.00 ± 0.53	0.45 ± 0.06
3.01			1.19 ± 0.13			15.00 ± 0.43	0.25 ± 0.07
			Gravity Core PS1768-8				
3.00	1.00	1.66 ± 0.08					
7.04	1.07	1.32 ± 0.07	1.29 ± 0.35	0.58 ± 0.02	1.62 ± 0.06	16.34 ± 0.56	0.16 ± 0.08
9.21	1.00	1.58 ± 0.08	1.96 ± 0.60	1.13 ± 0.05	2.18 ± 0.09	19.00 ± 0.80	0.36 ± 0.05
10.66	1.03	1.55 ± 0.08	2.63 ± 1.09	2.20 ± 0.15	2.94 ± 0.20	30.03 ± 2.00	0.19 ± 0.04
11.66	1.05	1.59 ± 0.08	4.03 ± 1.54	3.22 ± 0.28	3.26 ± 0.29	30.64 ± 2.71	0.27 ± 0.01
12.17	1.06	1.72 ± 0.09	3.42 ± 1.29	3.02 ± 0.18	2.51 ± 0.15	31.67 ± 1.93	0.22 ± 0.02
13.26	1.07	1.30 ± 0.07	2.76 ± 1.14	2.70 ± 0.20	2.96 ± 0.22	29.24 ± 2.18	0.38 ± 0.04
14.32	1.10	1.89 ± 0.09	2.84 ± 1.22	3.03 ± 0.24	2.38 ± 0.19	30.27 ± 2.40	1.04 ± 0.04
16.61	1.33	1.22 ± 0.06	1.54 ± 0.46	0.71 ± 0.04	1.45 ± 0.08	54.67 ± 2.88	2.90 ± 0.14
19.13	1.35	1.82 ± 0.09	1.66 ± 0.52	0.48 ± 0.03	0.94 ± 0.06	87.96 ± 5.52	2.27 ± 0.17
21.54	1.34	1.71 ± 0.09	1.58 ± 0.54	0.51 ± 0.03	0.81 ± 0.05	71.75 ± 4.46	1.42 ± 0.19
23.94	1.20	2.33 ± 0.12	0.85 ± 0.52	0.49 ± 0.03	0.48 ± 0.03	122.32 ± 7.60	0.84 ± 0.19
28.96	1.20	2.06 ± 0.10	0.70 ± 0.42	0.41 ± 0.02	0.72 ± 0.04	79.97 ± 4.14	0.54 ± 0.23
33.08	1.18	2.30 ± 0.11	0.63 ± 0.51	0.54 ± 0.03	0.75 ± 0.05	100.65 ± 6.45	0.63 ± 0.14
37.59	1.43	1.68 ± 0.08	0.80 ± 0.47	0.60 ± 0.03	0.74 ± 0.04	59.71 ± 3.34	0.78 ± 0.10
41.28	1.30	2.37 ± 0.12	0.85 ± 0.56	0.70 ± 0.05	0.91 ± 0.06	78.59 ± 5.38	0.88 ± 0.16
45.25	1.16	1.77 ± 0.09	1.68 ± 0.61	0.59 ± 0.06	0.87 ± 0.09	80.14 ± 8.11	1.32 ± 0.07
49.00	0.96	2.24 ± 0.11	1.84 ± 0.70	0.62 ± 0.03	1.05 ± 0.05	104.51 ± 4.77	0.80 ± 0.18
52.58	0.93	2.05 ± 0.10	1.93 ± 0.71	0.62 ± 0.04	0.93 ± 0.06	92.21 ± 5.51	1.10 ± 0.18
55.55	1.06	2.82 ± 0.14	2.36 ± 1.21	0.57 ± 0.03	1.05 ± 0.06	159.69 ± 9.33	0.65 ± 0.19
58.95	1.13	2.53 ± 0.13	2.17 ± 1.09	0.67 ± 0.04	1.16 ± 0.07	115.79 ± 6.53	0.43 ± 0.16
62.19	1.28	1.62 ± 0.08		0.47 ± 0.03	1.25 ± 0.07	83.31 ± 4.59	0.44 ± 0.18
65.95	1.32	2.05 ± 0.10		0.36 ± 0.02	0.92 ± 0.04	81.73 ± 3.83	0.45 ± 0.24
69.29	1.12	1.91 ± 0.10	0.61 ± 1.33	0.58 ± 0.03	0.97 ± 0.05	81.30 ± 3.96	0.45 ± 0.17

Results of gravity core PS1768-8 and multicore PS1768-6 (continued). PRC = relative production rate changes of cosmogenic radionuclides following Mazaud et al. (1994). Biogenic barium and Al_2O_3 data are from Nürnberg (1995). Biogenic opal data are from G. Bohrmann (unpub. res.). All errors represent the statistical errors of one standard deviation from the mean (1σ) of the $^{230}Th_{ex}$ measurement except the $^{231}Pa_{ex}$ errors where it represents the quadratic sum of the 1σ uncertainties of the $^{230}Th_{ex}$ and $^{231}Pa_{ex}$ measurements. The error of the authigenic ^{238}U concentrations represents the range of the lithogenic $^{238}U/^{232}Th$ activity ratio between 0.5 and 1.

Age, kyr	rel, PRC,	VRR ^{10}Be, 10^9at/ cm^2 · kyr	VRR $^{231}Pa_{ex}$, dpm/ cm^2 · kyr	VRR biog. opal, g/ cm^2 · kyr	VRR Ba_{bio}, mg/ cm^2 · kyr	VRR Al_2O_3, mg/ cm^2 · kyr	^{238}U auth., dpm/g
72.67	1.15	2.15 ± 0.11	1.01 ± 1.05	0.48 ± 0.03	1.07 ± 0.07	76.92 ± 4.88	0.35 ± 0.13
73.96			1.58 ± 0.87	0.58 ± 0.03	0.83 ± 0.05	126.70 ± 7.13	0.36 ± 0.09
77.26	1.07	1.93 ± 0.10	1.48 ± 0.99	0.70 ± 0.04	0.82 ± 0.05	112.34 ± 7.10	0.32 ± 0.09
81.72			1.76 ± 1.25	0.79 ± 0.05	1.33 ± 0.08	66.36 ± 4.08	0.44 ± 0.06
84.28	1.14	2.00 ± 0.10	2.44 ± 1.44	1.05 ± 0.06	1.76 ± 0.10	44.28 ± 2.63	0.45 ± 0.04
87.22			2.11 ± 1.09	0.63 ± 0.04	1.75 ± 0.10	54.96 ± 3.28	0.28 ± 0.10
89.95	1.32	2.22 ± 0.11	2.91 ± 1.44	0.64 ± 0.04	1.16 ± 0.07	147.12 ± 9.26	0.11 ± 0.10
92.84			2.52 ± 1.45	0.90 ± 0.06	1.09 ± 0.07	91.20 ± 6.09	0.12 ± 0.11
95.62			2.88 ± 1.62	1.20 ± 0.09	0.87 ± 0.06	70.04 ± 5.06	0.19 ± 0.10
97.99	1.37	1.62 ± 0.08	1.94 ± 1.28	1.48 ± 0.21	1.17 ± 0.17	64.44 ± 9.30	0.00 ± 0.07
100.36			2.16 ± 1.58	1.50 ± 0.09	1.54 ± 0.10	34.35 ± 2.15	0.14 ± 0.06
102.72			2.03 ± 1.60	1.34 ± 0.11	1.41 ± 0.12	55.15 ± 4.49	0.17 ± 0.06
105.00	1.38	2.01 ± 0.10	2.44 ± 1.92	1.40 ± 0.11	1.59 ± 0.13	64.16 ± 5.16	0.29 ± 0.05
107.34			4.08 ± 2.85	1.35 ± 0.09	1.87 ± 0.13	81.98 ± 5.70	0.32 ± 0.06
111.08	1.48	1.85 ± 0.09	2.81 ± 1.77	0.80 ± 0.07	1.26 ± 0.11	69.98 ± 6.17	0.09 ± 0.09
113.53			2.73 ± 1.47	0.82 ± 0.03	1.08 ± 0.04	63.48 ± 2.51	0.20 ± 0.07
116.10			3.19 ± 1.07	1.36 ± 0.07	1.88 ± 0.10	57.35 ± 2.95	0.15 ± 0.06
118.19	1.44	1.00 ± 0.05		1.53 ± 0.10	2.93 ± 0.19	23.34 ± 1.51	0.19 ± 0.04
119.83				1.98 ± 0.19	3.75 ± 0.36	17.51 ± 1.70	0.24 ± 0.03
121.50	1.36	0.91 ± 0.05		2.08 ± 0.19	3.34 ± 0.31	17.42 ± 1.63	0.21 ± 0.04
123.04				2.18 ± 0.19	2.98 ± 0.26	19.14 ± 1.69	0.24 ± 0.03
123.99				3.55 ± 0.49	3.79 ± 0.52	31.15 ± 4.30	0.45 ± 0.03
125.87	1.38	0.64 ± 0.03		1.69 ± 0.19	2.07 ± 0.24	15.87 ± 1.82	1.25 ± 0.03
127.08				2.69 ± 0.39	3.66 ± 0.54	22.94 ± 3.37	0.58 ± 0.05
127.98	1.34	1.13 ± 0.06	3.33 ± 2.55	3.91 ± 0.60	3.74 ± 0.57	31.29 ± 4.80	0.27 ± 0.03
129.05				3.10 ± 0.45	2.14 ± 0.31	27.22 ± 3.95	0.52 ± 0.03
130.84	1.26	1.50 ± 0.07		0.52 ± 0.04	1.18 ± 0.09	59.12 ± 4.60	1.03 ± 0.14
135.77	1.1	2.19 ± 0.11		0.33 ± 0.04	0.79 ± 0.09	94.11 ± 10.31	0.84 ± 0.24
138.20	1.15	1.96 ± 0.10		0.57 ± 0.07	1.18 ± 0.15	102.94 ± 13.33	0.97 ± 0.14

Results of gravity core PS1768-8 and multicore PS1768-6 (continued).

B.4 PS1756-5 and PS1756-6

Depth, cm	Age, kyr	DBD, g/cm^3	$^{230}Th_{ex}$, dpm/g	$^{230}Th^0_{ex}$, dpm/g	SR, cm/kyr	SAR, g/cm^2 · kyr	VRR, g/cm^2 · kyr
			Multicore PS1756-6				
0 – 1	0.50			11.00 ± 0.20		1.00 ± 0.20	0.91 ± 0.02
2 – 9	8.33	0.35	9.52 ± 0.16	10.29 ± 0.18	0.84 ± 0.01	0.29 ± 0.01	0.97 ± 0.02
10 – 19	10.60	0.32	6.26 ± 0.15	6.91 ± 0.17	3.97 ± 0.10	1.27 ± 0.03	1.45 ± 0.03
21 – 27	11.48	0.26	4.39 ± 0.13	4.89 ± 0.14	6.82 ± 0.20	1.77 ± 0.05	2.05 ± 0.06
			Gravity Core PS1756-5				
4 – 10	9.75	0.26	5.01 ± 0.21	5.48 ± 0.23	4.00 ± 0.17	1.04 ± 0.04	1.82 ± 0.08
10 – 20	12.17	0.26	3.71 ± 0.25	4.16 ± 0.29	13.25 ± 0.91	3.44 ± 0.24	2.41 ± 0.17
20 – 30	12.72	0.23	2.97 ± 0.24	3.34 ± 0.27	18.30 ± 1.50	4.21 ± 0.34	2.99 ± 0.24
30 – 40	13.24	0.22	2.95 ± 0.24	3.33 ± 0.27	19.19 ± 1.57	4.22 ± 0.35	3.00 ± 0.25
40 – 50	13.66	0.22	2.35 ± 0.25	2.67 ± 0.28	23.92 ± 2.50	5.26 ± 0.55	3.74 ± 0.39
50 – 60	14.17	0.23	2.73 ± 0.25	3.12 ± 0.28	19.63 ± 1.78	4.51 ± 0.41	3.21 ± 0.29
60 – 70	14.64	0.22	2.67 ± 0.21	3.05 ± 0.24	20.95 ± 1.67	4.61 ± 0.37	3.28 ± 0.26
70 – 80	15.12	0.22	2.65 ± 0.25	3.05 ± 0.28	20.95 ± 1.94	4.61 ± 0.43	3.28 ± 0.30
80 – 90	15.59	0.22	2.58 ± 0.20	2.98 ± 0.23	21.48 ± 1.70	4.72 ± 0.37	3.36 ± 0.27
90 – 100	16.14	0.24	2.82 ± 0.17	3.27 ± 0.20	17.92 ± 1.10	4.30 ± 0.26	3.06 ± 0.19
100 – 110	16.68	0.25	2.60 ± 0.21	3.03 ± 0.24	18.54 ± 1.49	4.64 ± 0.37	3.30 ± 0.26
110 – 120	17.24	0.26	2.59 ± 0.19	3.03 ± 0.23	17.85 ± 1.34	4.64 ± 0.35	3.30 ± 0.25
120 – 130	17.84	0.27	2.66 ± 0.22	3.14 ± 0.26	16.61 ± 1.40	4.49 ± 0.38	3.19 ± 0.27
130 – 140	18.39	0.28	2.31 ± 0.23	2.74 ± 0.27	18.34 ± 1.82	5.14 ± 0.51	3.65 ± 0.36
140 – 150	18.99	0.27	2.62 ± 0.20	3.12 ± 0.23	16.71 ± 1.25	4.51 ± 0.34	3.21 ± 0.24
150 – 160	19.57	0.26	2.64 ± 0.21	3.16 ± 0.25	17.11 ± 1.35	4.45 ± 0.35	3.16 ± 0.25
160 – 170	20.19	0.25	2.90 ± 0.21	3.49 ± 0.25	16.13 ± 1.15	4.03 ± 0.29	2.86 ± 0.20
170 – 180	20.74	0.26	2.44 ± 0.20	2.96 ± 0.25	18.29 ± 1.52	4.75 ± 0.40	3.38 ± 0.28
180 – 190	21.25	0.24	2.45 ± 0.21	2.98 ± 0.26	19.66 ± 1.70	4.72 ± 0.41	3.35 ± 0.29
190 – 200	21.82	0.25	2.63 ± 0.22	3.22 ± 0.27	17.51 ± 1.49	4.38 ± 0.37	3.11 ± 0.26
200 – 210	22.42	0.25	2.73 ± 0.22	3.36 ± 0.27	16.75 ± 1.36	4.19 ± 0.34	2.97 ± 0.24
210 – 220	22.92	0.22	2.63 ± 0.22	3.25 ± 0.27	19.69 ± 1.62	4.33 ± 0.36	3.08 ± 0.25
220 – 230	23.38	0.20	2.56 ± 0.20	3.18 ± 0.25	22.10 ± 1.76	4.42 ± 0.35	3.14 ± 0.25
230 – 240	23.81	0.21	2.32 ± 0.19	2.89 ± 0.24	23.19 ± 1.90	4.87 ± 0.40	3.46 ± 0.28
240 – 250	24.80	0.19	1.85 ± 0.20	2.33 ± 0.25	10.12 ± 1.07	1.92 ± 0.20	4.29 ± 0.45
250 – 260	25.84	0.20	1.84 ± 0.20	2.34 ± 0.25	9.60 ± 1.03	1.92 ± 0.21	4.28 ± 0.46

Results of gravity core PS1756-5 and multicore PS1756-6. Abreviations: DBD = dry bulk density, SR = sedimentation rate, SAR = total sediment accumulation rate, VRR = vertical rain rate. All errors represent the statistical errors of one standard deviation from the mean (1σ) of the $^{230}Th_{ex}$ measurement. The age of each sample represents the age of the mean depth of the sampled core section.

Depth, cm	Age, kyr	DBD, g/cm^3	$^{230}Th_{ex}$, dpm/g	$^{230}Th^0_{ex}$, dpm/g	SR, cm/kyr	SAR, g/cm^2 · kyr	VRR, g/cm^2 · kyr
260 – 270	26.98	0.21	1.90 ± 0.20	2.44 ± 0.25	8.76 ± 0.90	1.84 ± 0.19	4.10 ± 0.42
270 – 280	28.25	0.21	2.09 ± 0.19	2.71 ± 0.25	7.88 ± 0.73	1.66 ± 0.15	3.68 ± 0.34
280 – 290	29.33	0.21	1.76 ± 0.19	2.30 ± 0.25	9.27 ± 1.02	1.95 ± 0.21	4.34 ± 0.48
290 – 300	30.57	0.22	1.91 ± 0.17	2.54 ± 0.22	8.04 ± 0.69	1.77 ± 0.15	3.94 ± 0.34
300 – 306	31.34	0.25	1.72 ± 0.17	2.29 ± 0.23	7.80 ± 0.77	1.95 ± 0.19	4.36 ± 0.43
306 – 311	31.96	0.23	1.79 ± 0.20	2.40 ± 0.27	8.08 ± 0.91	1.86 ± 0.21	4.16 ± 0.47
311 – 321	32.96	0.20	1.65 ± 0.18	2.24 ± 0.25	9.99 ± 1.10	2.00 ± 0.22	4.46 ± 0.49
321 – 331	34.29	0.23	1.90 ± 0.19	2.61 ± 0.27	7.49 ± 0.76	1.72 ± 0.18	3.83 ± 0.39
331 – 341	35.55	0.21	1.93 ± 0.20	2.68 ± 0.28	7.97 ± 0.82	1.67 ± 0.17	3.73 ± 0.39
341 – 351	36.91	0.23	1.90 ± 0.22	2.67 ± 0.31	7.32 ± 0.84	1.68 ± 0.19	3.75 ± 0.43
351 – 361	38.86	0.24	2.56 ± 0.20	3.66 ± 0.29	5.14 ± 0.41	1.23 ± 0.10	2.73 ± 0.22
361 – 371	40.97	0.26	2.52 ± 0.19	3.68 ± 0.28	4.73 ± 0.36	1.23 ± 0.09	2.72 ± 0.20
371 – 381	43.59	0.27	2.96 ± 0.22	4.42 ± 0.33	3.81 ± 0.28	1.03 ± 0.08	2.26 ± 0.17
381 – 391	45.79	0.24	2.71 ± 0.22	4.14 ± 0.34	4.56 ± 0.37	1.09 ± 0.09	2.41 ± 0.20
391 – 401	48.05	0.23	2.87 ± 0.18	4.47 ± 0.28	4.41 ± 0.28	1.01 ± 0.06	2.24 ± 0.14
401 – 411	50.22	0.24	2.57 ± 0.22	4.09 ± 0.34	4.62 ± 0.39	1.11 ± 0.09	2.45 ± 0.21
411 – 421	52.05	0.25	2.05 ± 0.18	3.31 ± 0.29	5.45 ± 0.48	1.36 ± 0.12	3.02 ± 0.27
421 – 431	55.21	0.27	3.21 ± 0.21	5.35 ± 0.35	3.17 ± 0.21	0.85 ± 0.06	1.87 ± 0.12
431 – 441	58.32	0.29	2.85 ± 0.17	4.89 ± 0.29	3.22 ± 0.19	0.93 ± 0.06	2.05 ± 0.12
441 – 452	60.30	0.32	2.47 ± 0.17	4.31 ± 0.29	5.54 ± 0.38	1.77 ± 0.12	2.32 ± 0.16
452 – 462	61.61	0.25	2.26 ± 0.21	3.99 ± 0.38	7.62 ± 0.72	1.90 ± 0.18	2.51 ± 0.24
462 – 472	63.18	0.25	2.66 ± 0.20	4.77 ± 0.36	6.38 ± 0.48	1.59 ± 0.12	2.10 ± 0.16
472 – 482	64.67	0.23	2.70 ± 0.18	4.91 ± 0.32	6.73 ± 0.44	1.55 ± 0.10	2.04 ± 0.13
482 – 492	66.13	0.23	2.62 ± 0.21	4.82 ± 0.38	6.86 ± 0.54	1.58 ± 0.12	2.08 ± 0.16
492 – 502	67.60	0.24	2.49 ± 0.17	4.65 ± 0.32	6.81 ± 0.47	1.63 ± 0.11	2.15 ± 0.15
502 – 512	69.11	0.23	2.65 ± 0.15	5.02 ± 0.29	6.58 ± 0.37	1.51 ± 0.09	1.99 ± 0.11
512 – 522	71.00	0.27	2.77 ± 0.15	5.33 ± 0.29	5.30 ± 0.29	1.43 ± 0.08	1.87 ± 0.10
522 – 532	73.50	0.30	3.23 ± 0.16	6.38 ± 0.32	4.01 ± 0.20	1.20 ± 0.06	1.57 ± 0.08
532 – 542	76.02	0.29	3.70 ± 0.30	7.47 ± 0.61	3.97 ± 0.32	1.15 ± 0.09	1.34 ± 0.11
542 – 552	78.63	0.27	4.02 ± 0.31	8.32 ± 0.64	3.83 ± 0.30	1.03 ± 0.08	1.20 ± 0.09
552 – 562	80.38	0.27	2.64 ± 0.26	5.56 ± 0.55	5.69 ± 0.56	1.54 ± 0.15	1.80 ± 0.18

Results of gravity core PS1756-5 and multicore PS1756-6 (continued).

Depth, cm	Age, kyr	DBD, g/cm^3	$^{230}Th_{ex}$, dpm/g	$^{230}Th^0_{ex}$, dpm/g	SR, cm/kyr	SAR, g/cm^2 · kyr	VRR, g/cm^2 · kyr
562 – 572	82.70	0.29	3.20 ± 0.23	6.87 ± 0.50	4.31 ± 0.31	1.25 ± 0.09	1.46 ± 0.11
572 – 582	84.77	0.29	2.78 ± 0.17	6.09 ± 0.38	4.85 ± 0.30	1.41 ± 0.09	1.64 ± 0.10
582 – 592	86.78	0.28	2.76 ± 0.19	6.16 ± 0.42	4.96 ± 0.34	1.39 ± 0.09	1.62 ± 0.11
592 – 602	88.66	0.29	2.43 ± 0.20	5.52 ± 0.46	5.34 ± 0.45	1.55 ± 0.13	1.81 ± 0.15
602 – 612	90.63	0.27	2.71 ± 0.24	6.27 ± 0.55	5.06 ± 0.44	1.37 ± 0.12	1.60 ± 0.14
612 – 622	92.27	0.27	2.21 ± 0.19	5.18 ± 0.44	6.09 ± 0.52	1.65 ± 0.14	1.93 ± 0.16
622 – 635	94.83	0.29	2.43 ± 0.21	5.83 ± 0.52	5.09 ± 0.45	1.48 ± 0.13	1.72 ± 0.15
635 – 642	96.02	0.29	2.04 ± 0.17	4.96 ± 0.41	5.90 ± 0.49	1.71 ± 0.14	2.02 ± 0.17
642 – 652	97.89	0.25	2.60 ± 0.19	6.42 ± 0.46	5.32 ± 0.38	1.33 ± 0.10	1.56 ± 0.11
652 – 662	99.70	0.30	2.04 ± 0.16	5.14 ± 0.40	5.54 ± 0.43	1.66 ± 0.13	1.95 ± 0.15
662 – 672	101.97	0.29	2.62 ± 0.27	6.72 ± 0.68	4.40 ± 0.45	1.28 ± 0.13	1.49 ± 0.15
672 – 682	103.72	0.28	2.04 ± 0.18	5.32 ± 0.46	5.74 ± 0.50	1.61 ± 0.14	1.88 ± 0.16
682 – 692	105.68	0.28	2.26 ± 0.17	6.01 ± 0.45	5.08 ± 0.38	1.42 ± 0.11	1.66 ± 0.12
692 – 702	107.02	0.25	1.69 ± 0.18	4.55 ± 0.49	7.48 ± 0.81	1.87 ± 0.20	2.20 ± 0.24
702 – 712	108.20	0.28	1.32 ± 0.17	3.59 ± 0.47	8.46 ± 1.11	2.37 ± 0.31	2.79 ± 0.37
712 – 722	110.35	0.31	2.14 ± 0.19	5.93 ± 0.53	4.66 ± 0.42	1.45 ± 0.13	1.69 ± 0.15
722 – 732	114.33	0.29	1.79 ± 0.23	5.13 ± 0.66	2.51 ± 0.32	0.73 ± 0.09	1.95 ± 0.25
732 – 742	116.62	0.27	1.06 ± 0.30	3.11 ± 0.87	4.38 ± 1.22	1.18 ± 0.33	3.22 ± 0.90
742 – 752	118.67	0.27	0.93 ± 0.21	2.80 ± 0.61	4.86 ± 1.07	1.31 ± 0.29	3.58 ± 0.79
752 – 762	122.09	0.32	1.28 ± 0.28	3.97 ± 0.87	2.93 ± 0.64	0.94 ± 0.21	2.52 ± 0.55
762 – 772	128.80	0.28	2.79 ± 0.22	9.17 ± 0.72	1.49 ± 0.12	0.42 ± 0.03	1.09 ± 0.09
772 – 782	130.14	0.26	2.19 ± 0.21	7.30 ± 0.70	7.47 ± 0.71	1.94 ± 0.19	1.37 ± 0.13
782 – 792	131.18	0.27	1.63 ± 0.19	5.48 ± 0.65	9.56 ± 1.14	2.58 ± 0.31	1.83 ± 0.22
792 – 802	132.69	0.32	1.96 ± 0.12	6.70 ± 0.39	6.63 ± 0.39	2.12 ± 0.12	1.49 ± 0.09
802 – 812	134.35	0.31	2.20 ± 0.15	7.63 ± 0.53	6.01 ± 0.42	1.86 ± 0.13	1.31 ± 0.09
812 – 822	136.04	0.32	2.14 ± 0.11	7.51 ± 0.40	5.92 ± 0.31	1.89 ± 0.10	1.33 ± 0.07
822 – 832	138.25	0.31	2.84 ± 0.13	10.18 ± 0.47	4.53 ± 0.21	1.40 ± 0.06	0.98 ± 0.05
832 – 842	140.17	0.31	2.42 ± 0.15	8.83 ± 0.55	5.20 ± 0.32	1.61 ± 0.10	1.13 ± 0.07
842 – 852	142.18	0.31	2.48 ± 0.22	9.22 ± 0.81	4.99 ± 0.44	1.55 ± 0.14	1.08 ± 0.10
852 – 862	144.17	0.31	2.42 ± 0.20	9.16 ± 0.77	5.02 ± 0.42	1.56 ± 0.13	1.09 ± 0.09

Results of gravity core PS1756-5 and multicore PS1756-6 (continued).

Age, kyr	^{232}Th, ppm	^{238}U, dpm/g	$^{231}Pa^{0}_{ex}$, dpm/g	$^{10}Be^{0}$, 10^{9}at/g	Mn, ppm	Fe, ppm
			Multicore PS1756-6			
0.50						
8.33	2.49 ± 0.11	0.72 ± 0.07	0.90 ± 0.09		289	10240
10.60	2.43 ± 0.11	0.77 ± 0.07	1.04 ± 0.10		219	12240
11.48	2.33 ± 0.12	1.01 ± 0.06	0.88 ± 0.10		65	5640
			Gravity Core PS1756-5			
9.75	2.90 ± 0.24	1.25 ± 0.09	0.71 ± 0.17	1.452 ± 0.060	190	11820
12.17	2.35 ± 0.21	2.15 ± 0.13	0.78 ± 0.19	1.334 ± 0.077	110	9480
12.72	2.43 ± 0.24	2.34 ± 0.14	0.75 ± 0.21			
13.24	1.75 ± 0.19	2.05 ± 0.13	0.84 ± 0.22	0.877 ± 0.045	116	9020
13.66	1.69 ± 0.20	2.11 ± 0.12	0.68 ± 0.21	0.919 ± 0.052	102	8154
14.17	1.86 ± 0.18	1.91 ± 0.13	0.61 ± 0.21	1.164 ± 0.059	118	9960
14.64	2.55 ± 0.19	2.15 ± 0.13	0.60 ± 0.21			
15.12	2.10 ± 0.20	1.90 ± 0.13	0.69 ± 0.21	1.090 ± 0.057	136	10394
15.59	2.57 ± 0.19	1.79 ± 0.12	0.78 ± 0.19			
16.14	2.75 ± 0.21	1.75 ± 0.08	0.69 ± 0.18	1.146 ± 0.058	120	10580
16.68	2.31 ± 0.16	1.62 ± 0.11	0.58 ± 0.19			
17.24	2.06 ± 0.19	1.62 ± 0.10	0.53 ± 0.21	0.916 ± 0.061	99	8700
17.84	1.99 ± 0.18	1.49 ± 0.11	0.46 ± 0.23			
18.39	1.73 ± 0.18	1.78 ± 0.13	0.48 ± 0.22	1.000 ± 0.068	102	9760
18.99	1.99 ± 0.12	1.58 ± 0.12	0.56 ± 0.25	1.048 ± 0.064	115	9660
19.57	2.11 ± 0.19	1.72 ± 0.13	0.65 ± 0.24			
20.19	2.06 ± 0.17	1.76 ± 0.13	0.68 ± 0.25	1.021 ± 0.065	101	10160
20.74	2.21 ± 0.19	1.73 ± 0.13	0.58 ± 0.22			
21.25	2.29 ± 0.18	1.65 ± 0.11	0.60 ± 0.22	1.263 ± 0.062	109	10720
21.82	2.45 ± 0.20	1.72 ± 0.13	0.63 ± 0.23	1.169 ± 0.062	103	10140
22.42	2.59 ± 0.21	1.88 ± 0.13	0.65 ± 0.24			
22.92	2.61 ± 0.20	1.65 ± 0.12	0.75 ± 0.23			
23.38	2.24 ± 0.18	1.52 ± 0.11	0.72 ± 0.22			
23.81	1.97 ± 0.16	1.43 ± 0.10	0.66 ± 0.21	0.956 ± 0.061	86	8800
24.80	1.68 ± 0.16	1.32 ± 0.10	0.58 ± 0.21	0.933 ± 0.058	77	7680
25.84	1.55 ± 0.11	1.27 ± 0.11	0.53 ± 0.22			

Results of gravity core PS1756-5 and multicore PS1756-6 (continued). All errors represent the statistical errors of one standard deviation from the mean (1σ). The $^{231}Pa_{ex}$ data represent three times running means.

Age, kyr	^{232}Th, ppm	^{238}U, dpm/g	$^{231}Pa^{0}_{ex}$, dpm/g	$^{10}Be^{0}$, 10^{9}at/g	Mn, ppm	Fe, ppm
26.98	1.60 ± 0.14	1.40 ± 0.11	0.82 ± 0.23			
28.25	1.90 ± 0.17	1.17 ± 0.09	0.96 ± 0.25	0.816 ± 0.043	97	7684
29.33	1.78 ± 0.18	1.29 ± 0.09	1.02 ± 0.24			
30.57	1.79 ± 0.15	1.40 ± 0.08	0.95 ± 0.24			
31.34	1.54 ± 0.13	1.51 ± 0.10	0.76 ± 0.24	0.976 ± 0.084	100	7410
31.96	1.81 ± 0.16	1.60 ± 0.12	0.78 ± 0.25			
32.96	1.59 ± 0.15	1.40 ± 0.10	0.72 ± 0.27			
34.29	1.87 ± 0.16	1.35 ± 0.11	0.68 ± 0.27	0.866 ± 0.059	83	7608
35.55	1.95 ± 0.18	1.31 ± 0.11	0.70 ± 0.29			
36.91	2.14 ± 0.18	1.37 ± 0.12	0.75 ± 0.30	0.966 ± 0.054	114	9080
38.86	2.01 ± 0.18	1.45 ± 0.10	0.71 ± 0.30	1.143 ± 0.062	105	8920
40.97	2.75 ± 0.17	1.47 ± 0.10	0.88 ± 0.33			
43.59	2.97 ± 0.22	1.43 ± 0.11	0.92 ± 0.39			
45.79	2.29 ± 0.20	1.47 ± 0.11	1.23 ± 0.45	1.419 ± 0.064	126	10940
48.05	2.74 ± 0.18	1.43 ± 0.10	1.22 ± 0.48	1.418 ± 0.075	125	11260
50.22	2.66 ± 0.23	1.52 ± 0.11	1.36 ± 0.48			
52.05	2.30 ± 0.14	1.60 ± 0.11	1.89 ± 0.54	1.540 ± 0.062	142	12400
55.21	2.45 ± 0.18	1.38 ± 0.11	2.21 ± 0.59	1.510 ± 0.071	179	12920
58.32	2.75 ± 0.15	1.47 ± 0.10	1.95 ± 0.59			
60.30	2.66 ± 0.18	1.36 ± 0.10	1.52 ± 0.60			
61.61	2.12 ± 0.17	1.11 ± 0.15	1.52 ± 0.55	1.315 ± 0.062	360	22120
63.18	2.25 ± 0.17	1.30 ± 0.11	1.50 ± 0.52			
64.67	2.28 ± 0.17	1.23 ± 0.11	1.56 ± 0.51			
66.13	2.41 ± 0.17	1.27 ± 0.11	1.62 ± 0.53	1.463 ± 0.067	112	10520
67.60	2.11 ± 0.14	1.15 ± 0.10	1.67 ± 0.53			
69.11	2.16 ± 0.14	1.13 ± 0.08	1.68 ± 0.51			
71.00	1.97 ± 0.12	1.00 ± 0.08	2.02 ± 0.53	1.571 ± 0.077	125	11220
73.50	2.66 ± 0.18	1.23 ± 0.09	2.28 ± 0.54			
76.02	2.99 ± 0.30	1.32 ± 0.14		2.307 ± 0.104	171	13940
78.63	3.02 ± 0.33	1.48 ± 0.17		1.967 ± 0.090	155	12600
80.38	2.10 ± 0.23	1.04 ± 0.13	2.48 ± 0.88	1.638 ± 0.072	168	11940

Results of gravity core PS1756-5 and multicore PS1756-6 (continued).

Age, kyr	^{232}Th, ppm	^{238}U, dpm/g	$^{231}Pa^{0}_{ex}$, dpm/g	$^{10}Be^{0}$, 10^{9}at/g	Mn, ppm	Fe, ppm
82.70	2.21 ± 0.26	1.17 ± 0.11	2.48 ± 0.87			
84.77	2.25 ± 0.18	1.20 ± 0.10	1.86 ± 0.82	1.725 ± 0.066	160	10940
86.78	2.18 ± 0.17	1.02 ± 0.09	1.74 ± 0.87			
88.66	2.00 ± 0.15	1.56 ± 0.12	1.62 ± 0.96			
90.63	2.00 ± 0.19	1.74 ± 0.14	1.89 ± 1.01	1.986 ± 0.081	122	8580
92.27	1.61 ± 0.16	1.34 ± 0.11	2.19 ± 1.02			
94.83	2.63 ± 0.22	1.26 ± 0.11	2.27 ± 0.96			
96.02	2.32 ± 0.18	1.06 ± 0.09	2.62 ± 0.93			
97.89	2.61 ± 0.21	1.02 ± 0.08	2.62 ± 0.92	1.315 ± 0.062	102	8440
99.70	2.61 ± 0.16	1.09 ± 0.09	2.90 ± 1.16			
101.97	3.35 ± 0.20	1.71 ± 0.18	2.68 ± 1.26			
103.72	2.63 ± 0.17	1.36 ± 0.11	2.78 ± 1.32			
105.68	2.46 ± 0.18	1.07 ± 0.10	2.76 ± 1.18	1.062 ± 0.050	78	7940
107.02	2.47 ± 0.19	1.21 ± 0.10	2.41 ± 1.22			
108.20	1.76 ± 0.16	1.74 ± 0.10	2.65 ± 1.30	0.755 ± 0.042	63	5600
110.35	2.62 ± 0.18	1.45 ± 0.11	2.82 ± 1.48			
114.33	2.19 ± 0.18	1.82 ± 0.14	3.32 ± 1.78	1.422 ± 0.064	90	7900
116.62	1.33 ± 0.14	2.46 ± 0.16	3.54 ± 1.87			
118.67	1.43 ± 0.16	3.74 ± 0.09	3.32 ± 2.06	0.929 ± 0.048	88	5040
122.09	1.91 ± 0.18	3.00 ± 0.16	3.65 ± 2.02	1.371 ± 0.084	109	7640
128.80	2.92 ± 0.21	1.43 ± 0.11	4.05 ± 2.20	2.324 ± 0.100	160	12520
130.14	3.23 ± 0.20	1.45 ± 0.11	4.75 ± 2.12			
131.18	2.34 ± 0.20	1.42 ± 0.10	5.06 ± 2.15	1.736 ± 0.087	131	10680
132.69	2.43 ± 0.11	1.40 ± 0.06	4.57 ± 2.21			
134.35	3.44 ± 0.23	1.53 ± 0.07	4.43 ± 1.98	1.745 ± 0.075	160	12700
136.04	3.17 ± 0.12	1.68 ± 0.07	5.71 ± 1.93			
138.25	3.19 ± 0.14	1.45 ± 0.07	6.42 ± 1.75	1.654 ± 0.071	181	14360
140.17	2.77 ± 0.19	1.43 ± 0.07	6.97 ± 2.17			
142.18	3.29 ± 0.22	1.61 ± 0.13	6.46 ± 2.53			
144.17	3.06 ± 0.19	1.39 ± 0.12	6.61 ± 2.93	1.575 ± 0.065	148	13620

Results of gravity core PS1756-5 and multicore PS1756-6 (continued).

Age, kyr	rel, PRC,	VRR ^{10}Be, 10^9at/ cm^2 · kyr	VRR $^{231}Pa_{ex}$, dpm/ cm^2 · kyr	VRR biog. opal, g/ cm^2 · kyr	VRR Ba_{bio}, mg/ cm^2 · kyr	VRR Al_2O_3, mg/ cm^2 · kyr	VRR ^{238}U auth., dpm/ cm^2 · kyr
			Multicore PS1756-6				
0.50				0.36 ± 0.01	2.09 ± 0.04	39.99 ± 0.73	
8.33			0.87 ± 0.09				0.26 ± 0.15
10.60			1.50 ± 0.15				0.32 ± 0.15
11.48			1.81 ± 0.21	1.19 ± 0.03	1.09 ± 0.03		0.58 ± 0.14
			Gravity Core PS1756-5				
9.75	1.02	2.60 ± 0.11	1.30 ± 0.32		1.09 ± 0.05	85.70 ± 3.65	0.71 ± 0.18
12.17	1.08	2.97 ± 0.20	1.89 ± 0.48		1.52 ± 0.10	109.02 ± 7.48	1.72 ± 0.14
12.72			2.23 ± 0.65	1.73 ± 0.14	1.56 ± 0.13		1.89 ± 0.15
13.24	1.16	2.27 ± 0.19	2.52 ± 0.68	2.00 ± 0.16	1.26 ± 0.10	108.32 ± 8.85	1.73 ± 0.11
13.66	1.21	2.84 ± 0.30	2.56 ± 0.82	2.41 ± 0.25	1.50 ± 0.16	154.88 ± 16.19	1.80 ± 0.10
14.17	1.26	2.97 ± 0.27	1.97 ± 0.71	2.14 ± 0.19	1.22 ± 0.11	144.82 ± 13.10	1.57 ± 0.11
14.64			1.97 ± 0.71	1.95 ± 0.16	1.21 ± 0.10		1.68 ± 0.16
15.12	1.33	2.69 ± 0.25	2.27 ± 0.70	2.04 ± 0.19	1.18 ± 0.11	117.09 ± 10.87	1.51 ± 0.13
15.59			2.62 ± 0.67	1.91 ± 0.15	1.18 ± 0.09		1.32 ± 0.16
16.14	1.4	2.50 ± 0.15	2.10 ± 0.58	1.77 ± 0.11	1.01 ± 0.06	137.92 ± 8.44	1.24 ± 0.17
16.68			1.92 ± 0.65	1.98 ± 0.16	1.25 ± 0.10		1.19 ± 0.14
17.24	1.37	2.21 ± 0.17	1.76 ± 0.70	1.83 ± 0.14	1.39 ± 0.10	148.81 ± 11.19	1.24 ± 0.13
17.84			1.45 ± 0.74	1.96 ± 0.17	1.53 ± 0.13		1.12 ± 0.12
18.39	1.36	2.68 ± 0.27	1.77 ± 0.83	2.34 ± 0.23	1.93 ± 0.19	164.69 ± 16.35	1.46 ± 0.11
18.99	1.37	2.45 ± 0.18	1.80 ± 0.81	1.85 ± 0.14	1.54 ± 0.12	144.64 ± 10.82	1.21 ± 0.12
19.57			2.05 ± 0.77	1.95 ± 0.15	1.36 ± 0.11		1.33 ± 0.13
20.19	1.38	2.12 ± 0.15	1.96 ± 0.73	1.96 ± 0.14	1.26 ± 0.09	129.26 ± 9.20	1.38 ± 0.13
20.74			1.97 ± 0.75	2.22 ± 0.19	1.52 ± 0.13		1.32 ± 0.14
21.25	1.34	3.16 ± 0.27	2.01 ± 0.76	2.15 ± 0.19	1.51 ± 0.13	145.03 ± 12.54	1.23 ± 0.14
21.82	1.32	2.75 ± 0.23	1.95 ± 0.72	1.93 ± 0.16	1.40 ± 0.12	128.63 ± 10.94	1.27 ± 0.15
22.42			1.94 ± 0.73	1.67 ± 0.14	1.40 ± 0.11		1.40 ± 0.16
22.92			2.30 ± 0.74	2.05 ± 0.17	1.48 ± 0.12		1.17 ± 0.16
23.38			2.27 ± 0.71	2.11 ± 0.17	1.32 ± 0.11		1.11 ± 0.14
23.81	1.21	2.74 ± 0.22	2.30 ± 0.75	2.30 ± 0.19	1.35 ± 0.11	127.01 ± 10.43	1.07 ± 0.12
24.80	1.12	3.58 ± 0.38	2.47 ± 0.93	3.03 ± 0.32	1.59 ± 0.17	157.36 ± 16.61	1.01 ± 0.10
25.84			2.25 ± 0.96	2.85 ± 0.30	1.58 ± 0.17		0.98 ± 0.10

Results of gravity core PS1756-5 and multicore PS1756-6 (continued). PRC = relative production rate changes of cosmogenic radionuclides following Mazaud et al. (1994). Biogenic barium and Al_2O_3 data are from Nürnberg (1995). Biogenic opal data are from G. Bohrmann (unpub. res.). All errors represent the statistical errors of one standard deviation from the mean (1σ) of the $^{230}Th_{ex}$ measurement except the $^{231}Pa_{ex}$ errors where it represents the quadratic sum of the 1σ uncertainties of the $^{230}Th_{ex}$ and $^{231}Pa_{ex}$ measurements. The error of the authigenic ^{238}U rain rates represents the range of the lithogenic $^{238}U/^{232}Th$ activity ratio between 0.5 and 1.

Age, kyr	rel, PRC,	VRR ^{10}Be, 10^9at/ cm^2 · kyr	VRR $^{231}Pa_{ex}$, dpm/ cm^2 · kyr	VRR biog, opal, g/ cm^2 · kyr	VRR Ba_{bio}, mg/ cm^2 · kyr	VRR Al_2O_3, mg/ cm^2 · kyr	VRR ^{238}U auth., dpm/ cm^2 · kyr
26.98			3.36 ± 1.02	2.81 ± 0.29	1.52 ± 0.16		1.10 ± 0.10
28.25	1.19	2.53 ± 0.23	3.54 ± 0.97	2.46 ± 0.23	1.33 ± 0.12	121.23 ± 11.21	0.82 ± 0.12
29.33			4.44 ± 1.14	2.79 ± 0.31	1.52 ± 0.17		0.96 ± 0.11
30.57			3.75 ± 0.98	2.52 ± 0.22	1.38 ± 0.12		1.07 ± 0.11
31.34	1.2	3.55 ± 0.35	3.30 ± 1.09	2.62 ± 0.26	1.53 ± 0.15	118.85 ± 11.74	1.23 ± 0.09
31.96			3.23 ± 1.12	3.00 ± 0.34	2.25 ± 0.25		1.27 ± 0.11
32.96			3.20 ± 1.25	2.81 ± 0.31	2.05 ± 0.23		1.11 ± 0.10
34.29	1.18	2.81 ± 0.29	2.61 ± 1.08	2.55 ± 0.26	1.61 ± 0.16	140.51 ± 14.34	1.00 ± 0.12
35.55			2.60 ± 1.12	2.09 ± 0.22	1.57 ± 0.16		0.95 ± 0.12
36.91	1.41	2.57 ± 0.29	2.83 ± 1.16	2.41 ± 0.28	1.57 ± 0.18	137.32 ± 15.77	0.98 ± 0.13
38.86	1.48	2.11 ± 0.17	1.94 ± 0.83	1.64 ± 0.13	1.15 ± 0.09	100.14 ± 7.96	1.08 ± 0.12
40.97			2.39 ± 0.92	1.52 ± 0.11	1.28 ± 0.10		0.96 ± 0.17
43.59			2.07 ± 0.90	1.31 ± 0.10	1.20 ± 0.09		0.88 ± 0.18
45.79	1.23	2.79 ± 0.23	2.96 ± 1.11	1.41 ± 0.12	1.16 ± 0.09	111.22 ± 9.11	1.05 ± 0.14
48.05	0.95	3.34 ± 0.21	2.72 ± 1.09	1.39 ± 0.09	0.96 ± 0.06	103.11 ± 6.45	0.92 ± 0.17
50.22			3.33 ± 1.22	1.47 ± 0.12	1.05 ± 0.09		1.03 ± 0.16
52.05	0.95	4.89 ± 0.44	5.72 ± 1.70	1.81 ± 0.16	1.30 ± 0.12	138.99 ± 12.36	1.18 ± 0.14
55.21	0.99	2.85 ± 0.19	4.14 ± 1.14	1.05 ± 0.07	0.77 ± 0.05	109.00 ± 7.22	0.93 ± 0.15
58.32			3.98 ± 1.23	0.97 ± 0.06	0.82 ± 0.05		0.96 ± 0.17
60.30			3.52 ± 1.40	1.06 ± 0.07	0.60 ± 0.04		0.87 ± 0.16
61.61	1.27	2.60 ± 0.25	3.82 ± 1.44	1.03 ± 0.10	0.30 ± 0.03	188.64 ± 17.83	0.72 ± 0.13
63.18			3.14 ± 1.11	1.22 ± 0.09	0.48 ± 0.04		0.88 ± 0.14
64.67			3.18 ± 1.05	1.18 ± 0.08	0.71 ± 0.05		0.81 ± 0.14
66.13	1.35	2.25 ± 0.18	3.36 ± 1.13	1.20 ± 0.09	0.71 ± 0.06	105.36 ± 8.28	0.83 ± 0.15
67.60			3.60 ± 1.16	1.33 ± 0.09	0.71 ± 0.05		0.76 ± 0.13
69.11			3.33 ± 1.03	1.19 ± 0.07	0.66 ± 0.04		0.73 ± 0.13
71.00	1.11	2.65 ± 0.14	3.79 ± 1.01	1.16 ± 0.06	0.62 ± 0.03	86.35 ± 4.69	0.64 ± 0.12
73.50			3.57 ± 0.87	0.88 ± 0.04	0.47 ± 0.02		0.74 ± 0.16
76.02	1.08	2.86 ± 0.23		0.60 ± 0.05	0.36 ± 0.03	86.52 ± 7.06	0.77 ± 0.18
78.63	1.03	2.30 ± 0.18		0.72 ± 0.06	0.41 ± 0.03	77.99 ± 6.04	0.92 ± 0.19

Results of gravity core PS1756-5 and multicore PS1756-6 (continued).

Age, kyr	rel, PRC,	VRR ^{10}Be, 10^9at/ cm^2 · kyr	VRR $^{231}Pa_{ex}$, dpm/ cm^2 · kyr	VRR biog, opal, g/ cm^2 · kyr	VRR Ba_{bio}, mg/ cm^2 · kyr	VRR Al_2O_3, mg/ cm^2 · kyr	VRR ^{238}U auth., dpm/ cm^2 · kyr
80.38	1.08	2.73 ± 0.27	4.47 ± 1.65	0.97 ± 0.10	0.76 ± 0.07	116.73 ± 11.54	0.65 ± 0.13
82.70			3.60 ± 1.29	0.87 ± 0.06	0.67 ± 0.05		0.76 ± 0.14
84.77	1.15	2.46 ± 0.15	3.06 ± 1.36	0.92 ± 0.06	0.82 ± 0.05	90.71 ± 5.69	0.78 ± 0.14
86.78			2.82 ± 1.42	0.97 ± 0.07	0.81 ± 0.06		0.62 ± 0.13
88.66			2.94 ± 1.76	1.18 ± 0.10	0.91 ± 0.08		1.19 ± 0.12
90.63	1.31	2.42 ± 0.21	3.01 ± 1.64	1.01 ± 0.09	0.83 ± 0.07	51.00 ± 4.44	1.37 ± 0.12
92.27			4.23 ± 2.00	1.31 ± 0.11	1.06 ± 0.09		1.04 ± 0.10
94.83			3.90 ± 1.68	0.99 ± 0.09	0.86 ± 0.08		0.77 ± 0.16
96.02			5.28 ± 1.92	1.17 ± 0.10	0.93 ± 0.08		0.63 ± 0.14
97.89	1.37	1.49 ± 0.11	4.07 ± 1.46	0.90 ± 0.07	0.72 ± 0.05	56.48 ± 4.08	0.54 ± 0.16
99.70			5.64 ± 2.30	1.17 ± 0.09	0.90 ± 0.07		0.61 ± 0.16
101.97			3.98 ± 1.92	0.86 ± 0.09	1.25 ± 0.13		1.09 ± 0.21
103.72			5.23 ± 2.53	1.25 ± 0.11	0.90 ± 0.08		0.87 ± 0.16
105.68	1.38	1.28 ± 0.10	4.60 ± 2.00	1.25 ± 0.09	0.81 ± 0.06	68.79 ± 5.13	0.62 ± 0.15
107.02			5.31 ± 2.74	1.45 ± 0.16	1.12 ± 0.12		0.75 ± 0.15
108.20	1.44	1.46 ± 0.19	7.39 ± 3.76	2.12 ± 0.28	1.62 ± 0.21	83.89 ± 11.00	1.42 ± 0.11
110.35			4.75 ± 2.53	1.30 ± 0.12	1.11 ± 0.10		0.97 ± 0.16
114.33	1.47	1.88 ± 0.24	6.47 ± 3.56	1.35 ± 0.17	1.11 ± 0.14	47.60 ± 6.10	1.42 ± 0.13
116.62			11.38 ± 6.79	2.31 ± 0.64	1.54 ± 0.43		2.21 ± 0.08
118.67	1.44	2.31 ± 0.51	11.87 ± 7.83	2.54 ± 0.56	2.25 ± 0.50	87.44 ± 19.21	3.48 ± 0.09
122.09	1.39	2.49 ± 0.55	9.21 ± 5.49	1.61 ± 0.35	1.94 ± 0.43	61.62 ± 13.51	2.65 ± 0.12
128.80	1.36	1.85 ± 0.15	4.41 ± 2.42	0.60 ± 0.05	0.96 ± 0.07	48.56 ± 3.79	0.89 ± 0.18
130.14			6.51 ± 2.97	0.77 ± 0.07	0.97 ± 0.09		0.85 ± 0.20
131.18	1.25	2.54 ± 0.30	9.24 ± 0.00	1.13 ± 0.14	0.99 ± 0.12	81.70 ± 9.76	0.99 ± 0.14
132.69			6.83 ± 3.33	0.84 ± 0.05	0.90 ± 0.05		0.95 ± 0.15
134.35	1.25	1.83 ± 0.13	5.81 ± 2.63	0.68 ± 0.05	0.85 ± 0.06	71.47 ± 5.00	0.90 ± 0.21
136.04			7.60 ± 2.61	0.69 ± 0.04	0.93 ± 0.05		1.10 ± 0.19
138.25	1.06	1.53 ± 0.07	6.31 ± 1.74	0.57 ± 0.03	0.74 ± 0.03	53.56 ± 2.45	0.86 ± 0.20
140.17			7.89 ± 2.51	0.66 ± 0.04	0.83 ± 0.05		0.92 ± 0.17
142.18			7.01 ± 2.81	0.56 ± 0.05	0.76 ± 0.07		1.00 ± 0.20
144.17	1.1	1.56 ± 0.13	7.22 ± 3.25	0.63 ± 0.05	0.76 ± 0.06	59.53 ± 5.00	0.83 ± 0.19

Results of gravity core PS1756-5 and multicore PS1756-6 (continued).

B.5 PS1754-1 and PS1754-2

Depth, cm	Age, kyr	DBD, g/cm^3	$^{230}Th_{ex}$, dpm/g	$^{230}Th^0_{ex}$, dpm/g	SR, cm/kyr	SAR, g/cm^2 · kyr	VRR, g/cm^2 · kyr
			Multicore PS1754-2				
1	0.55	0.78	4.26 ± 0.20	4.29 ± 0.20	2.00 ± 0.09	1.56 ± 0.07	1.52 ± 0.07
5	2.73	0.78	5.13 ± 0.24	5.26 ± 0.24	2.00 ± 0.09	1.56 ± 0.07	1.24 ± 0.06
10	5.46	0.77	5.50 ± 0.29	5.79 ± 0.31	2.00 ± 0.11	1.54 ± 0.08	1.12 ± 0.06
15	8.20	0.77	4.61 ± 0.33	4.97 ± 0.36	2.00 ± 0.14	1.54 ± 0.11	1.31 ± 0.09
20	10.93	0.70	4.26 ± 0.29	4.71 ± 0.33	2.00 ± 0.14	1.40 ± 0.10	1.38 ± 0.10
25	13.13	0.60	4.27 ± 0.33	4.82 ± 0.38	2.00 ± 0.16	1.20 ± 0.09	1.35 ± 0.11
			Gravity Core PS1754-1				
2 – 12	5.88	0.78	5.66 ± 0.33	5.97 ± 0.35	1.70 ± 0.10	1.33 ± 0.08	1.09 ± 0.06
12 – 17	8.48	0.77	4.79 ± 0.24	5.18 ± 0.26	1.93 ± 0.10	1.48 ± 0.07	1.26 ± 0.06
17 – 22	10.87	0.70	4.74 ± 0.23	5.24 ± 0.25	2.09 ± 0.10	1.46 ± 0.07	1.24 ± 0.06
22 – 27	13.73	0.60	4.31 ± 0.28	4.89 ± 0.31	1.75 ± 0.11	1.05 ± 0.07	1.33 ± 0.09
27 – 32	15.73	0.51	3.45 ± 0.23	3.99 ± 0.27	2.50 ± 0.17	1.28 ± 0.09	1.63 ± 0.11
32 – 42	18.46	0.48	2.46 ± 0.22	2.92 ± 0.26	3.66 ± 0.32	1.76 ± 0.15	2.23 ± 0.19
42 – 52	21.63	0.49	2.73 ± 0.35	3.33 ± 0.42	3.15 ± 0.40	1.55 ± 0.20	1.95 ± 0.25
52 – 59	29.66	0.52	2.39 ± 0.26	3.14 ± 0.35	0.87 ± 0.10	0.45 ± 0.05	2.07 ± 0.23
59 – 67	37.82	0.54	1.90 ± 0.18	2.69 ± 0.26	0.98 ± 0.09	0.53 ± 0.05	2.42 ± 0.23
67 – 72	45.27	0.56	2.47 ± 0.18	3.76 ± 0.27	0.67 ± 0.05	0.38 ± 0.03	1.73 ± 0.13
72 – 77	52.33	0.59	2.08 ± 0.18	3.37 ± 0.30	0.71 ± 0.06	0.42 ± 0.04	1.93 ± 0.17
77 – 83	61.90	0.57	2.28 ± 0.18	4.03 ± 0.33	0.63 ± 0.05	0.36 ± 0.03	1.61 ± 0.13
83 – 86	66.32	0.56	1.96 ± 0.16	3.62 ± 0.30	0.68 ± 0.06	0.38 ± 0.03	1.80 ± 0.15
86 – 91	74.15	0.53	2.11 ± 0.16	4.20 ± 0.32	0.64 ± 0.05	0.34 ± 0.03	1.55 ± 0.12
91 – 95	77.08	0.54	2.36 ± 0.18	4.80 ± 0.37	1.37 ± 0.11	0.74 ± 0.06	1.35 ± 0.10
95 – 102	83.31	0.54	2.79 ± 0.17	6.02 ± 0.37	1.12 ± 0.07	0.61 ± 0.04	1.08 ± 0.07
102 – 111	89.81	0.49	2.36 ± 0.17	5.40 ± 0.38	1.38 ± 0.10	0.68 ± 0.05	1.20 ± 0.09
111 – 121	95.08	0.47	1.69 ± 0.11	4.07 ± 0.26	1.90 ± 0.12	0.89 ± 0.06	1.60 ± 0.10
121 – 126	97.70	0.49	1.53 ± 0.10	3.78 ± 0.24	1.91 ± 0.12	0.93 ± 0.06	1.72 ± 0.11
126 – 129	99.32	0.48	1.57 ± 0.18	3.93 ± 0.46	1.86 ± 0.22	0.89 ± 0.10	1.65 ± 0.19
129 – 134	101.44	0.49	1.19 ± 0.19	3.05 ± 0.50	2.36 ± 0.38	1.16 ± 0.19	2.13 ± 0.35
134 – 138	104.56	0.55	1.91 ± 0.16	5.03 ± 0.43	1.28 ± 0.11	0.71 ± 0.06	1.29 ± 0.11
138 – 145	110.53	0.64	1.75 ± 0.12	4.86 ± 0.33	1.17 ± 0.08	0.75 ± 0.05	1.34 ± 0.09
145 – 152	119.48	0.72	2.21 ± 0.16	6.65 ± 0.47	0.78 ± 0.06	0.56 ± 0.04	0.98 ± 0.07
152 – 157	125.21	0.70	1.87 ± 0.12	5.95 ± 0.39	0.87 ± 0.06	0.61 ± 0.04	1.09 ± 0.07
157 – 162	129.76	0.61	1.62 ± 0.12	5.37 ± 0.40	1.10 ± 0.08	0.67 ± 0.05	1.21 ± 0.09
162 – 166	131.87	0.58	1.65 ± 0.14	5.57 ± 0.49	1.89 ± 0.17	1.10 ± 0.10	1.17 ± 0.10
166 – 170	133.48	0.49	1.46 ± 0.18	5.00 ± 0.62	1.26 ± 0.16	0.62 ± 0.08	1.30 ± 0.16
170 – 177	136.17	0.45	1.49 ± 0.17	5.26 ± 0.60	1.27 ± 0.15	0.57 ± 0.07	1.24 ± 0.14

Results of gravity core PS1754-1 and multicore PS1754-2. Abreviations: DBD = dry bulk density, SR = sedimentation rate, SAR = total sediment accumulation rate, VRR = vertical rain rate. All errors represent the statistical errors of one standard deviation from the mean (1σ) of the $^{230}Th_{ex}$ measurement. The age of each sample represents the age of the mean depth of the sampled core section.

Age, kyr	Ca CO_3, %	^{232}Th, ppm	^{238}U, dpm/g	$^{231}Pa^0_{ex}$, dpm/g	$^{10}Be^0$, 10^9at/g	Mn, ppm	Fe, ppm	Al, ppm	Ba, ppm
				Multicore PS1754-2					
0.55		0.57 ± 0.11	0.22 ± 0.10	0.64 ± 0.31		109	2040	3306	822
2.73		0.87 ± 0.19	0.15 ± 0.03	0.67 ± 0.18		122	2280	3860	1009
5.46		0.80 ± 0.21	0.19 ± 0.05	0.80 ± 0.21		145	3220	4854	998
8.20		1.19 ± 0.32	0.29 ± 0.06	2.31 ± 0.33		240	5920	7462	1427
10.93		1.03 ± 0.27	0.35 ± 0.09	2.19 ± 0.30		229	7140	8100	1106
13.13		2.06 ± 0.36	0.40 ± 0.10	0.67 ± 0.28		291	13060	16868	1109
				Multicore PS1754-2					
5.88	84	0.71 ± 0.21	0.17 ± 0.05	0.97 ± 0.19	0.899 ± 0.048	131	2900	4656	1032
8.48	77	0.84 ± 0.18	0.26 ± 0.06	1.00 ± 0.20	1.170 ± 0.030	186	4680	6728	1372
10.87	62	1.37 ± 0.21	0.27 ± 0.07	0.92 ± 0.28	1.629 ± 0.036	247	7880	9754	1389
13.73	52	2.42 ± 0.35	0.47 ± 0.08	1.10 ± 0.32	1.778 ± 0.039	249	10600	14736	1268
15.73	49	2.72 ± 0.33	0.42 ± 0.07	1.13 ± 0.30	1.509 ± 0.048	101	6474	12519	960
18.46	47	1.41 ± 0.26	0.38 ± 0.06	1.26 ± 0.49	1.168 ± 0.041	74	5220	10674	985
21.63	47	1.75 ± 0.47	0.49 ± 0.10	1.33 ± 0.60	1.284 ± 0.078	119	6227	14266	989
29.66	50	2.44 ± 0.43	0.56 ± 0.10	1.24 ± 0.43	1.740 ± 0.037	93	6500	11312	964
37.82	64	1.39 ± 0.22	0.32 ± 0.07	1.04 ± 0.40	1.051 ± 0.041	56	4340	6462	1286
45.27	67	1.04 ± 0.18	0.23 ± 0.06	0.83 ± 0.50	1.041 ± 0.029	48	3420	5354	1204
52.33	69	1.21 ± 0.21	0.34 ± 0.07	1.25 ± 0.62	1.032 ± 0.035	56	3403	5817	1126
61.90	67	1.16 ± 0.18	0.28 ± 0.08	1.99 ± 0.77	1.221 ± 0.031	81	4560	6736	1088
66.32	63	1.52 ± 0.22	0.27 ± 0.06	2.55 ± 0.80	1.188 ± 0.037	65	5366	6522	1035
74.15	63	1.60 ± 0.22	0.28 ± 0.06	2.24 ± 0.77	1.127 ± 0.059	79	4540	6656	1170
77.08	66	1.05 ± 0.19	0.33 ± 0.06	2.05 ± 0.82	1.221 ± 0.037	99	3940	6030	1143
83.31	67	0.72 ± 0.15	0.19 ± 0.03	2.97 ± 1.05	1.313 ± 0.033	76	3920	6120	1328
89.81	59	1.10 ± 0.20	0.26 ± 0.04	3.09 ± 0.94	1.352 ± 0.034	54	4560	6760	1477
95.08	54	1.01 ± 0.13	0.28 ± 0.04	3.21 ± 1.05	1.245 ± 0.059	57	4648	6016	994
97.70	53	1.13 ± 0.13	0.27 ± 0.03	3.74 ± 1.65	1.161 ± 0.033	53	4949	6286	1160
99.32	52	1.29 ± 0.25	0.31 ± 0.09	3.32 ± 1.52	1.189 ± 0.042	53	4803	5982	957
101.44	49	1.21 ± 0.16	0.61 ± 0.11	2.62 ± 1.11	1.134 ± 0.060	60	4151	7944	942
104.56	55	1.04 ± 0.17	0.37 ± 0.06	0.90 ± 0.83	1.244 ± 0.036	58	4160	6398	1270
110.53	74	0.93 ± 0.11	0.35 ± 0.05	1.39 ± 0.95	1.018 ± 0.030	49	3380	5198	1284
119.48	74	0.70 ± 0.13	0.39 ± 0.07	2.68 ± 1.25	1.007 ± 0.043	49	2940	4852	1032
125.21	66	0.80 ± 0.13	0.41 ± 0.03	3.26 ± 1.16	0.982 ± 0.029	58	3060	4338	1190
129.76	61	1.07 ± 0.12	0.49 ± 0.04	4.03 ± 0.53	1.205 ± 0.036	63	4920	5990	1087
131.87	54	1.68 ± 0.15	0.50 ± 0.05	4.84 ± 1.19	1.411 ± 0.041	85	8760	9290	1329
133.48	48	2.33 ± 0.20	0.97 ± 0.10	4.32 ± 2.34	2.002 ± 0.044	124	14160	15560	1321
136.17	30	2.54 ± 0.20	0.98 ± 0.10	4.32 ± 1.15	1.980 ± 0.044	112	11020	14880	1086

Results of gravity core PS1754-1 and multicore PS1754-2 (continued). All errors represent the statistical errors of one standard deviation from the mean (1σ). The $^{231}Pa_{ex}$ data represent three times running means.

Age, kyr	rel. PRC,	VRR ^{10}Be, 10^9at/ cm^2 · kyr	VRR $^{231}Pa_{ex}$, dpm/ cm^2 · kyr	VRR biog. opal, g/ cm^2 · kyr	VRR Ba_{bio}, mg/ cm^2 · kyr	VRR Al_2O_3, mg/ cm^2 · kyr	^{238}U auth., dpm/g
			Multicore PS1754-2				
0.55	0.95		0.97 ± 0.47	0.12 ± 0.01	1.21 ± 0.06	9.42 ± 0.44	0.11 ± 0.04
2.73	0.98		0.83 ± 0.23		1.21 ± 0.06	8.97 ± 0.42	0.00 ± 0.04
5.46	1.02		0.90 ± 0.24		1.08 ± 0.06	10.25 ± 0.54	0.04 ± 0.05
8.20	1.07		3.02 ± 0.48		1.80 ± 0.13	18.34 ± 1.31	0.07 ± 0.07
10.93	1.1		3.02 ± 0.46		1.45 ± 0.10	21.00 ± 1.45	0.16 ± 0.06
13.13	1.13		0.90 ± 0.39		1.34 ± 0.11	42.76 ± 3.35	0.02 ± 0.13
			Multicore PS1754-2				
5.88	0.95	1.03 ± 0.06	1.06 ± 0.21	0.10 ± 0.01	1.09 ± 0.06	9.52 ± 0.55	0.04 ± 0.04
8.48	1.03	1.43 ± 0.07	1.25 ± 0.26	0.13 ± 0.01	1.67 ± 0.08	15.88 ± 0.79	0.11 ± 0.05
10.87	1.03	1.96 ± 0.10	1.14 ± 0.35	0.14 ± 0.01	1.64 ± 0.08	22.76 ± 1.11	0.02 ± 0.08
13.73	1.13	2.09 ± 0.13	1.46 ± 0.44	0.20 ± 0.01	1.55 ± 0.10	36.80 ± 2.37	0.02 ± 0.15
15.73	1.30	1.89 ± 0.13	1.84 ± 0.50	0.31 ± 0.02	1.43 ± 0.10	38.37 ± 2.56	0.00 ± 0.09
18.46	1.37	1.90 ± 0.17	2.81 ± 1.12	0.62 ± 0.05	2.03 ± 0.18	44.68 ± 3.91	0.12 ± 0.09
21.63	1.30	1.93 ± 0.24	2.60 ± 1.21	0.53 ± 0.07	1.74 ± 0.22	52.34 ± 6.63	0.17 ± 0.11
29.66	1.20	3.00 ± 0.33	2.56 ± 0.93	0.54 ± 0.06	1.84 ± 0.20	44.04 ± 4.85	0.11 ± 0.15
37.82	1.25	2.03 ± 0.19	2.51 ± 1.00	0.53 ± 0.05	3.00 ± 0.29	29.38 ± 2.79	0.06 ± 0.09
45.27	1.30	1.38 ± 0.10	1.44 ± 0.88	0.38 ± 0.03	2.02 ± 0.15	17.40 ± 1.26	0.04 ± 0.06
52.33	1.00	1.99 ± 0.18	2.41 ± 1.21	0.44 ± 0.04	2.09 ± 0.18	21.06 ± 1.86	0.12 ± 0.07
61.90	1.13	1.74 ± 0.14	3.21 ± 1.27	0.32 ± 0.03	1.68 ± 0.14	20.40 ± 1.65	0.07 ± 0.07
66.32	1.30	1.64 ± 0.14	4.58 ± 1.49	0.47 ± 0.04	1.78 ± 0.15	22.04 ± 1.84	0.00 ± 0.08
74.15	1.15	1.52 ± 0.12	3.47 ± 1.22	0.36 ± 0.03	1.74 ± 0.13	19.38 ± 1.50	0.00 ± 0.08
77.08	1.06	1.56 ± 0.12	2.77 ± 1.14	0.26 ± 0.02	1.49 ± 0.12	15.34 ± 1.18	0.14 ± 0.06
83.31	1.11	1.28 ± 0.08	3.21 ± 1.16	0.19 ± 0.01	1.39 ± 0.08	12.43 ± 0.76	0.06 ± 0.04
89.81	1.21	1.35 ± 0.10	3.72 ± 1.17	0.30 ± 0.02	1.72 ± 0.12	15.30 ± 1.09	0.06 ± 0.07
95.08	1.36	1.46 ± 0.10	5.14 ± 1.71	0.48 ± 0.03	1.52 ± 0.10	18.08 ± 1.18	0.09 ± 0.06
97.70	1.37	1.46 ± 0.09	6.42 ± 2.86	0.50 ± 0.03	1.92 ± 0.12	20.30 ± 1.27	0.06 ± 0.07
99.32	1.33	1.48 ± 0.17	5.48 ± 2.60	0.58 ± 0.07	1.52 ± 0.18	18.59 ± 2.19	0.07 ± 0.08
101.44	1.32	1.83 ± 0.30	5.59 ± 2.53	0.66 ± 0.11	1.90 ± 0.31	31.88 ± 5.20	0.39 ± 0.07
104.56	1.35	1.19 ± 0.10	1.17 ± 1.08	0.32 ± 0.03	1.59 ± 0.14	15.55 ± 1.33	0.18 ± 0.06
110.53	1.42	0.96 ± 0.07	1.86 ± 1.28	0.25 ± 0.02	1.67 ± 0.11	13.06 ± 0.89	0.18 ± 0.06
119.48	1.45	0.68 ± 0.05	2.62 ± 1.24	0.18 ± 0.01	0.98 ± 0.07	8.91 ± 0.63	0.26 ± 0.04
125.21	1.38	0.78 ± 0.05	3.56 ± 1.29	0.21 ± 0.01	1.27 ± 0.08	8.90 ± 0.58	0.26 ± 0.05
129.76	1.32	1.11 ± 0.08	4.88 ± 0.74	0.23 ± 0.02	1.27 ± 0.09	13.64 ± 1.02	0.29 ± 0.07
131.87	1.26	1.31 ± 0.11	5.65 ± 1.48	0.22 ± 0.02	1.48 ± 0.13	20.39 ± 1.79	0.19 ± 0.10
133.48	1.25	2.60 ± 0.32	5.61 ± 3.12	0.33 ± 0.04	1.58 ± 0.20	38.03 ± 4.73	0.54 ± 0.14
136.17	1.20	2.45 ± 0.28	5.34 ± 1.54	0.33 ± 0.04	1.22 ± 0.14	34.57 ± 3.95	0.51 ± 0.16

Results of gravity core PS1754-1 and multicore PS1754-2 (continued). PRC = relative production rate changes of cosmogenic radionuclides following Mazaud et al. (1994). Biogenic opal data are from G. Bohrmann (unpub. res.). All errors represent the statistical errors of one standard deviation from the mean (1σ) of the $^{230}Th_{ex}$ measurement except the $^{231}Pa_{ex}$ errors where it represents the quadratic sum of the 1σ uncertainties of the $^{230}Th_{ex}$ and $^{231}Pa_{ex}$ measurements. The error of the authigenic ^{238}U concentrations represents the range of the lithogenic $^{238}U/^{232}Th$ activity ratio between 0.5 and 1.

B.6 PS2082-1 and PS2082-3

Depth, cm	Age, kyr	DBD, g/cm^3	$^{230}Th_{ex}$, dpm/g	$^{230}Th^0_{ex}$, dpm/g	SR, cm/kyr	SAR, g/cm^2 · kyr	VRR, g/cm^2 · kyr
			Multicore PS2082-3				
0.5 – 6.5	1.27	0.43	31.58 ± 0.41	31.95 ± 0.42	2.5 ± 0.03	1.08 ± 0.01	0.38 ± 0.00
6.5 – 14.5	3.82	0.58	24.19 ± 0.35	25.05 ± 0.36	2.5 ± 0.04	1.45 ± 0.02	0.48 ± 0.01
14.5 – 21	6.45	0.62	14.27 ± 0.53	15.14 ± 0.56	2.5 ± 0.09	1.55 ± 0.06	0.80 ± 0.03
			Gravity Core PS2082-1				
4 – 13	4.87	0.50	22.19 ± 0.41	23.21 ± 0.43	2.67 ± 0.05	1.33 ± 0.02	0.52 ± 0.01
13 – 23	9.19	0.60	14.12 ± 0.39	15.37 ± 0.43	2.31 ± 0.06	1.39 ± 0.04	0.79 ± 0.02
23 – 29	10.94	0.52	10.56 ± 0.30	11.69 ± 0.33	3.43 ± 0.10	1.78 ± 0.05	1.04 ± 0.03
29 – 39	12.02	0.45	14.52 ± 0.41	16.22 ± 0.45	9.27 ± 0.26	4.17 ± 0.12	0.75 ± 0.02
39 – 48	12.73	0.37	12.83 ± 0.35	14.43 ± 0.39	12.63 ± 0.34	4.67 ± 0.13	0.84 ± 0.02
48 – 54	13.11	0.33	11.33 ± 0.40	12.79 ± 0.45	15.93 ± 0.56	5.26 ± 0.19	0.95 ± 0.03
54 – 64	13.62	0.31	9.83 ± 0.37	11.15 ± 0.42	19.47 ± 0.73	6.04 ± 0.23	1.09 ± 0.04
64 – 74	14.13	0.28	10.75 ± 0.40	12.26 ± 0.46	19.62 ± 0.73	5.49 ± 0.21	0.99 ± 0.04
74 – 84	14.66	0.29	10.63 ± 0.39	12.17 ± 0.45	19.07 ± 0.70	5.53 ± 0.20	1.00 ± 0.04
84 – 94	15.15	0.28	10.21 ± 0.38	11.74 ± 0.44	20.47 ± 0.77	5.73 ± 0.22	1.03 ± 0.04
94 – 104	15.65	0.28	10.55 ± 0.41	12.20 ± 0.47	19.71 ± 0.76	5.52 ± 0.21	0.99 ± 0.04
104 – 114	16.15	0.29	9.96 ± 0.37	11.56 ± 0.43	20.08 ± 0.75	5.82 ± 0.22	1.05 ± 0.04
114 – 124	16.71	0.29	11.17 ± 0.27	13.04 ± 0.31	17.81 ± 0.42	5.17 ± 0.12	0.93 ± 0.02
124 – 134	17.24	0.29	10.43 ± 0.39	12.23 ± 0.45	18.99 ± 0.70	5.51 ± 0.20	0.99 ± 0.04
134 – 144	17.79	0.28	11.12 ± 0.38	13.11 ± 0.45	18.35 ± 0.63	5.14 ± 0.18	0.92 ± 0.03
144 – 154	18.31	0.27	11.11 ± 0.42	13.16 ± 0.50	18.94 ± 0.72	5.12 ± 0.19	0.92 ± 0.03
154 – 164	18.81	0.27	10.36 ± 0.51	12.33 ± 0.61	20.22 ± 1.00	5.46 ± 0.27	0.98 ± 0.05
164 – 174	19.31	0.27	10.51 ± 0.44	12.56 ± 0.53	19.85 ± 0.84	5.36 ± 0.23	0.96 ± 0.04
174 – 184	19.78	0.28	9.33 ± 0.34	11.21 ± 0.41	21.44 ± 0.78	6.00 ± 0.22	1.08 ± 0.04
184 – 194	20.39	0.30	11.43 ± 0.31	13.80 ± 0.37	16.27 ± 0.44	4.88 ± 0.13	0.88 ± 0.02
194 – 203	21.01	0.31	12.19 ± 0.28	14.80 ± 0.34	14.68 ± 0.33	4.55 ± 0.10	0.82 ± 0.02
203 – 212	21.61	0.31	11.91 ± 0.30	14.54 ± 0.37	14.95 ± 0.38	4.63 ± 0.12	0.83 ± 0.02
212 – 221	22.14	0.30	10.84 ± 0.28	13.31 ± 0.34	16.87 ± 0.44	5.06 ± 0.13	0.91 ± 0.02
221 – 231	22.80	0.30	11.93 ± 0.36	14.72 ± 0.45	15.26 ± 0.46	4.58 ± 0.14	0.82 ± 0.03
231 – 241	23.56	0.31	13.37 ± 0.46	16.62 ± 0.58	13.09 ± 0.45	4.06 ± 0.14	0.73 ± 0.03
241 – 251	26.43	0.32	12.62 ± 0.34	16.12 ± 0.44	3.48 ± 0.09	1.12 ± 0.03	0.75 ± 0.02
251 – 261	29.43	0.38	10.81 ± 0.27	14.19 ± 0.35	3.34 ± 0.08	1.27 ± 0.03	0.85 ± 0.02
261 – 271	33.01	0.44	10.86 ± 0.29	14.73 ± 0.39	2.79 ± 0.07	1.23 ± 0.03	0.82 ± 0.02
271 – 278	35.21	0.45	9.02 ± 0.30	12.49 ± 0.41	3.18 ± 0.10	1.43 ± 0.05	0.97 ± 0.03
278 – 280	35.80	0.45	8.25 ± 0.41	11.48 ± 0.58	3.41 ± 0.17	1.53 ± 0.08	1.06 ± 0.05
280 – 283	36.73	0.44	8.87 ± 0.26	12.46 ± 0.36	3.22 ± 0.09	1.42 ± 0.04	0.97 ± 0.03
283 – 285	37.29	0.43	8.10 ± 0.45	11.43 ± 0.64	3.58 ± 0.20	1.54 ± 0.09	1.06 ± 0.06

Results of gravity core PS2082-1 and multicore PS2082-3. Abreviations: DBD = dry bulk density, SR = sedimentation rate, SAR = total sediment accumulation rate, VRR = vertical rain rate. All errors represent the statistical errors of one standard deviation from the mean (1σ) of the $^{230}Th_{ex}$ measurement. The age of each sample represents the age of the mean depth of the sampled core section.

Depth, cm	Age, kyr	DBD, g/cm^3	$^{230}Th_{ex}$, dpm/g	$^{230}Th^0_{ex}$, dpm/g	SR, cm/kyr	SAR, g/cm^2 · kyr	VRR, g/cm^2 · kyr
285 – 295	40.54	0.44	9.15 ± 0.36	13.31 ± 0.53	3.08 ± 0.12	1.35 ± 0.05	0.91 ± 0.04
295 – 306	43.58	0.45	7.38 ± 0.25	11.04 ± 0.37	3.62 ± 0.12	1.63 ± 0.06	1.10 ± 0.04
306 – 313	44.76	0.45	7.80 ± 0.32	11.79 ± 0.49	5.91 ± 0.24	2.66 ± 0.11	1.03 ± 0.04
313 – 317	45.67	0.46	10.12 ± 0.24	15.43 ± 0.37	4.40 ± 0.10	2.03 ± 0.05	0.79 ± 0.02
317 – 327	48.16	0.47	10.79 ± 0.25	16.83 ± 0.40	4.01 ± 0.09	1.88 ± 0.04	0.72 ± 0.02
327 – 333	49.50	0.48	9.20 ± 0.27	14.53 ± 0.43	4.50 ± 0.13	2.16 ± 0.06	0.83 ± 0.02
333 – 344	51.99	0.49	9.07 ± 0.28	14.67 ± 0.45	4.41 ± 0.13	2.16 ± 0.07	0.83 ± 0.03
344 – 351	53.64	0.48	9.45 ± 0.28	15.51 ± 0.46	4.23 ± 0.13	2.03 ± 0.06	0.78 ± 0.02
351 – 360	55.91	0.46	10.35 ± 0.25	17.34 ± 0.42	3.97 ± 0.10	1.83 ± 0.04	0.70 ± 0.02
360 – 370	57.95	0.38	9.93 ± 0.51	16.95 ± 0.87	4.90 ± 0.25	1.86 ± 0.10	0.71 ± 0.04
370 – 378	59.50	0.35	10.02 ± 0.40	17.37 ± 0.69	5.17 ± 0.21	1.81 ± 0.07	0.70 ± 0.03
378 – 388	61.40	0.35	9.71 ± 0.40	17.12 ± 0.71	5.26 ± 0.22	1.84 ± 0.08	0.71 ± 0.03
388 – 398	63.17	0.35	8.90 ± 0.34	15.95 ± 0.62	5.65 ± 0.22	1.98 ± 0.08	0.76 ± 0.03
398 – 404	64.31	0.35	9.38 ± 0.39	16.99 ± 0.70	5.27 ± 0.22	1.84 ± 0.08	0.71 ± 0.03
404 – 412	65.90	0.34	10.03 ± 0.43	18.45 ± 0.78	5.02 ± 0.21	1.71 ± 0.07	0.66 ± 0.03
412 – 421	67.67	0.34	9.73 ± 0.47	18.19 ± 0.89	5.10 ± 0.25	1.73 ± 0.08	0.67 ± 0.03
421 – 431	70.27	0.34	12.66 ± 0.40	24.24 ± 0.76	3.85 ± 0.12	1.31 ± 0.04	0.50 ± 0.02
431 – 440	73.06	0.36	13.99 ± 0.42	27.49 ± 0.82	3.21 ± 0.10	1.16 ± 0.03	0.44 ± 0.01
440 – 450	77.03	0.43	14.25 ± 0.43	29.03 ± 0.87	2.39 ± 0.07	1.03 ± 0.03	0.42 ± 0.01
450 – 463	82.66	0.55	10.70 ± 0.42	22.97 ± 0.90	2.40 ± 0.09	1.32 ± 0.05	0.53 ± 0.02
463 – 474	86.74	0.49	10.17 ± 0.39	22.66 ± 0.88	2.69 ± 0.10	1.32 ± 0.05	0.53 ± 0.02
474 – 488	92.90	0.46	12.36 ± 0.37	29.16 ± 0.87	2.27 ± 0.07	1.05 ± 0.03	0.42 ± 0.01
488 – 501	98.93	0.50	11.33 ± 0.32	28.27 ± 0.80	2.15 ± 0.06	1.08 ± 0.03	0.43 ± 0.01
501 – 513	104.23	0.48	10.61 ± 0.34	27.80 ± 0.88	2.27 ± 0.07	1.09 ± 0.03	0.44 ± 0.01
513 – 525	109.05	0.39	11.33 ± 0.32	31.05 ± 0.87	2.49 ± 0.07	0.97 ± 0.03	0.39 ± 0.01
525 – 537	114.89	0.40	12.78 ± 0.35	36.95 ± 1.02	2.06 ± 0.06	0.82 ± 0.02	0.33 ± 0.01
537 – 549	122.11	0.46	13.04 ± 0.38	40.28 ± 1.17	1.66 ± 0.05	0.76 ± 0.02	0.30 ± 0.01
549 – 561	127.23	0.59	6.74 ± 0.26	21.84 ± 0.85	2.34 ± 0.09	1.38 ± 0.05	0.55 ± 0.02
561 – 573	129.83	0.66	2.91 ± 0.19	9.66 ± 0.63	4.63 ± 0.30	3.05 ± 0.20	1.26 ± 0.08
573 – 575	130.17	0.65	2.87 ± 0.19	9.56 ± 0.64	5.81 ± 0.39	3.78 ± 0.25	1.27 ± 0.09
575 – 581	131.03	0.62	2.51 ± 0.26	8.42 ± 0.87	6.96 ± 0.72	4.31 ± 0.44	1.44 ± 0.15
581 – 595	132.98	0.54	2.77 ± 0.31	9.46 ± 1.05	7.18 ± 0.80	3.87 ± 0.43	1.28 ± 0.14
595 – 607	134.44	0.44	2.91 ± 0.49	10.09 ± 1.69	8.22 ± 1.38	3.62 ± 0.61	1.20 ± 0.20
607 – 620	136.74	0.42	4.37 ± 0.49	15.46 ± 1.75	5.66 ± 0.64	2.38 ± 0.27	0.78 ± 0.09
620 – 635	138.72	0.39	3.46 ± 0.40	12.45 ± 1.44	7.55 ± 0.87	2.95 ± 0.34	0.97 ± 0.11
635 – 645	140.00	0.36	3.54 ± 0.43	12.90 ± 1.56	7.84 ± 0.95	2.82 ± 0.34	0.94 ± 0.11
645 – 660	142.14	0.36	3.91 ± 0.21	14.53 ± 0.78	7.02 ± 0.38	2.53 ± 0.14	0.83 ± 0.04
660 – 675	144.34	0.38	3.73 ± 0.24	14.17 ± 0.90	6.82 ± 0.44	2.59 ± 0.17	0.86 ± 0.05

Results of gravity core PS2082-1 and multicore PS2082-3 (continued).

Depth, cm	Age, kyr	DBD, g/cm^3	$^{230}Th_{ex}$, dpm/g	$^{230}Th^0_{ex}$, dpm/g	SR, cm/kyr	SAR, g/cm^2 · kyr	VRR, g/cm^2 · kyr
675 – 690	146.48	0.38	3.57 ± 0.24	13.82 ± 0.93	6.99 ± 0.47	2.66 ± 0.18	0.88 ± 0.06
690 – 705	148.24	0.35	3.12 ± 0.22	12.27 ± 0.88	8.52 ± 0.61	2.98 ± 0.21	0.99 ± 0.07
705 – 720	150.37	0.35	3.71 ± 0.22	14.87 ± 0.89	7.05 ± 0.42	2.47 ± 0.15	0.82 ± 0.05
720 – 735	152.33	0.34	3.46 ± 0.31	14.14 ± 1.27	7.62 ± 0.68	2.59 ± 0.23	0.86 ± 0.08
735 – 750	154.87	0.34	3.60 ± 0.22	15.04 ± 0.91	5.91 ± 0.36	2.01 ± 0.12	0.81 ± 0.05
750 – 765	157.22	0.33	3.34 ± 0.34	14.29 ± 1.45	6.39 ± 0.65	2.11 ± 0.21	0.85 ± 0.09
765 – 775	159.24	0.33	4.22 ± 0.21	18.37 ± 0.92	4.96 ± 0.25	1.64 ± 0.08	0.66 ± 0.03
775 – 790	162.12	0.36	3.61 ± 0.22	16.14 ± 0.98	5.21 ± 0.32	1.88 ± 0.11	0.75 ± 0.05
790 – 805	165.52	0.37	4.05 ± 0.25	18.70 ± 1.14	4.40 ± 0.27	1.63 ± 0.10	0.65 ± 0.04
805 – 814	167.54	0.37	3.88 ± 0.19	18.24 ± 0.90	4.45 ± 0.22	1.65 ± 0.08	0.66 ± 0.03
814 – 819	168.35	0.35	2.90 ± 0.29	13.75 ± 1.38	6.18 ± 0.62	2.16 ± 0.22	0.88 ± 0.09
819 – 835	171.37	0.36	3.26 ± 0.22	15.88 ± 1.07	5.30 ± 0.36	1.91 ± 0.13	0.76 ± 0.05
835 – 850	174.01	0.37	2.88 ± 0.26	14.38 ± 1.31	5.68 ± 0.52	2.10 ± 0.19	0.84 ± 0.08
850 – 865	177.37	0.36	3.68 ± 0.26	18.94 ± 1.34	4.46 ± 0.31	1.61 ± 0.11	0.64 ± 0.05
865 – 877	180.14	0.35	3.78 ± 0.22	19.95 ± 1.16	4.33 ± 0.25	1.52 ± 0.09	0.61 ± 0.04
877 – 890	184.51	0.35	5.36 ± 0.25	29.50 ± 1.37	2.97 ± 0.14	1.04 ± 0.05	0.41 ± 0.02
890 – 905	189.15	0.33	5.03 ± 0.24	28.85 ± 1.37	3.23 ± 0.15	1.07 ± 0.05	0.42 ± 0.02
905 – 915	194.29	0.36	5.35 ± 0.24	32.21 ± 1.42	1.94 ± 0.09	0.70 ± 0.03	0.38 ± 0.02
915 – 925	200.11	0.39	5.32 ± 0.23	33.83 ± 1.48	1.72 ± 0.08	0.67 ± 0.03	0.36 ± 0.02
925 – 935	206.04	0.40	5.02 ± 0.24	33.66 ± 1.58	1.69 ± 0.08	0.67 ± 0.03	0.36 ± 0.02
935 – 942	209.80	0.45	3.83 ± 0.21	26.58 ± 1.48	1.86 ± 0.10	0.84 ± 0.05	0.46 ± 0.03
942 – 950	213.35	0.44	3.13 ± 0.19	22.45 ± 1.39	2.25 ± 0.14	0.99 ± 0.06	0.54 ± 0.03
950 – 960	216.73	0.39	2.59 ± 0.15	19.21 ± 1.15	2.96 ± 0.18	1.15 ± 0.07	0.63 ± 0.04
960 – 970	219.85	0.37	2.44 ± 0.17	18.63 ± 1.27	3.21 ± 0.22	1.19 ± 0.08	0.65 ± 0.04
970 – 978	222.04	0.37	2.09 ± 0.15	16.26 ± 1.16	3.65 ± 0.26	1.35 ± 0.10	0.75 ± 0.05
978 – 985	223.91	0.37	2.59 ± 0.17	20.52 ± 1.33	3.75 ± 0.24	1.39 ± 0.09	0.59 ± 0.04
985 – 995	226.72	0.37	2.69 ± 0.17	21.82 ± 1.34	3.56 ± 0.22	1.32 ± 0.08	0.56 ± 0.03
995 – 1005	230.06	0.37	3.11 ± 0.17	26.07 ± 1.39	2.99 ± 0.16	1.11 ± 0.06	0.46 ± 0.02
1005 – 1012	232.93	0.43	3.19 ± 0.19	27.43 ± 1.62	2.44 ± 0.14	1.05 ± 0.06	0.44 ± 0.03
1012 – 1025	238.39	0.54	2.53 ± 0.29	22.91 ± 2.65	2.38 ± 0.28	1.29 ± 0.15	0.53 ± 0.06
1025 – 1037	241.04	0.40	1.71 ± 0.20	15.82 ± 1.89	4.53 ± 0.54	1.81 ± 0.22	0.77 ± 0.09
1037 – 1048	242.49	0.36	1.19 ± 0.27	11.19 ± 2.51	7.55 ± 1.69	2.72 ± 0.61	1.08 ± 0.24
1048 – 1060	245.16	0.38	1.86 ± 0.23	17.95 ± 2.24	4.51 ± 0.56	1.71 ± 0.21	0.68 ± 0.08
1060 – 1070	247.41	0.41	1.71 ± 0.34	16.86 ± 3.32	4.43 ± 0.87	1.82 ± 0.36	0.72 ± 0.14
1070 – 1084	250.42	0.39	1.68 ± 0.21	16.96 ± 2.15	4.66 ± 0.59	1.82 ± 0.23	0.71 ± 0.09
1084 – 1091	254.00	0.37			5.00 ± 1.00		

Results of gravity core PS2082-1 and multicore PS2082-3 (continued).

Age, kyr	$CaCO_3$, %	^{232}Th, ppm	^{238}U, dpm/g	$^{231}Pa^0_{ex}$, dpm/g	$^{10}Be^0$, 10^9at/g	Mn, ppm	Fe, ppm
			Multicore PS2082-3				
1.27		4.44 ± 0.30	0.55 ± 0.07	1.52 ± 0.14	3.744 ± 0.086	1264	15600
3.82		4.41 ± 0.26	0.72 ± 0.10	1.16 ± 0.26	2.715 ± 0.084	1072	11840
6.45		1.81 ± 0.37	0.31 ± 0.05		1.854 ± 0.032	920	8820
			Gravity Core PS2082-1				
4.87	54.0	3.32 ± 0.31	0.49 ± 0.06	1.69 ± 0.29	2.580 ± 0.070	1086	11560
9.19	62.0	2.60 ± 0.33	0.42 ± 0.05	1.40 ± 0.27	1.917 ± 0.059	1012	8680
10.94	47.0	4.00 ± 0.40	0.56 ± 0.10	1.22 ± 0.24	2.443 ± 0.034	2232	12600
12.02	30.0	5.87 ± 0.45	0.75 ± 0.11	1.09 ± 0.26	3.533 ± 0.170	13400	21880
12.73	11.0	5.79 ± 0.40	0.97 ± 0.11	1.33 ± 0.26		7850	25440
13.11	6.0	5.77 ± 0.45	1.13 ± 0.12	1.12 ± 0.27	4.073 ± 0.077	6250	27280
13.62	11.0	6.00 ± 0.40	2.48 ± 0.19	1.15 ± 0.28	4.272 ± 0.094	1246	25160
14.13	7.4	6.65 ± 0.40	3.02 ± 0.19	1.22 ± 0.29			
14.66	6.7	6.36 ± 0.41	2.73 ± 0.18	1.22 ± 0.30			
15.15	7.9	5.90 ± 0.40	2.64 ± 0.17	1.26 ± 0.31	4.026 ± 0.101	1632	24780
15.65	6.0	5.28 ± 0.39	2.24 ± 0.19	1.30 ± 0.32			
16.15	3.7	7.13 ± 0.48	2.24 ± 0.16	1.42 ± 0.31			
16.71	1.5	6.59 ± 0.21	1.99 ± 0.17	1.58 ± 0.32	4.513 ± 0.095	1510	24960
17.24	0.9	7.48 ± 0.47	2.00 ± 0.17	1.53 ± 0.32			
17.79	1.0	7.89 ± 0.44	2.27 ± 0.18	1.64 ± 0.35			
18.31	1.3	6.73 ± 0.48	2.16 ± 0.20	1.78 ± 0.39			
18.81	1.3	7.63 ± 0.51	2.21 ± 0.25	2.52 ± 0.32	4.948 ± 0.104	1282	26780
19.31	1.5	10.10 ± 0.69	2.04 ± 0.16				
19.78	1.3	6.25 ± 0.42	1.81 ± 0.15		4.879 ± 0.132	1314	25680
20.39	1.1	6.46 ± 0.35	1.62 ± 0.14		5.118 ± 0.102	1244	27980
21.01	1.0	7.13 ± 0.33	1.84 ± 0.11	1.59 ± 0.25			
21.61	0.9	6.32 ± 0.37	1.85 ± 0.11	1.55 ± 0.26			
22.14	1.0	7.14 ± 0.33	2.06 ± 0.12	1.46 ± 0.27	4.843 ± 0.097	930	25200
22.80	1.6	7.32 ± 0.47	2.00 ± 0.12	1.49 ± 0.29			
23.56	5.0	7.30 ± 0.60	1.77 ± 0.11	1.50 ± 0.30	4.418 ± 0.093	1234	24780
26.43	16.0	6.93 ± 0.43	1.76 ± 0.11	1.59 ± 0.30		2830	22980
29.43	20.0	6.56 ± 0.34	1.55 ± 0.10	1.36 ± 0.30		2132	20860
33.01	27.0	5.07 ± 0.26	1.36 ± 0.14	1.02 ± 0.31	4.227 ± 0.093	5670	18980
35.21	36.0	5.17 ± 0.31	1.05 ± 0.12	0.74 ± 0.41		4900	15180
35.80	32.0	3.95 ± 0.38	1.10 ± 0.17	0.81 ± 0.42		6950	16940
36.73	25.0	4.81 ± 0.25	1.30 ± 0.14	1.68 ± 0.49	5.159 ± 0.108	6763	28917
37.29	18.0	5.43 ± 0.54	1.26 ± 0.17	1.59 ± 0.46		2040	13800

Results of gravity core PS2082-1 and multicore PS2082-3 (continued). All errors represent the statistical errors of one standard deviation from the mean (1σ). The $^{231}Pa_{ex}$ data represent three times running means.

Age, kyr	$CaCO_3$, %	^{232}Th, ppm	^{238}U, dpm/g	$^{231}Pa^0_{ex}$, dpm/g	$^{10}Be^0$, 10^9at/g	Mn, ppm	Fe, ppm
40.54	26.0	5.52 ± 0.39	1.43 ± 0.14	1.35 ± 0.50		3022	19040
43.58	25.5	7.82 ± 0.31	1.94 ± 0.16	0.46 ± 0.48			
44.76	22.0	6.28 ± 0.36	1.66 ± 0.15	0.91 ± 0.45	4.143 ± 0.099	1652	22540
45.67	25.0	7.22 ± 0.30	1.75 ± 0.12	1.59 ± 0.39			
48.16	26.0	7.61 ± 0.33	1.43 ± 0.10	1.84 ± 0.42	4.231 ± 0.093	1494	23840
49.50	25.0	7.91 ± 0.37	1.57 ± 0.10	2.03 ± 0.44		2040	21560
51.99	28.0	6.65 ± 0.40	1.21 ± 0.08	2.02 ± 0.50	4.069 ± 0.098	3918	19400
53.64	26.0	5.70 ± 0.35	0.87 ± 0.09	1.62 ± 0.53		4256	26800
55.91	26.0	6.80 ± 0.32	0.94 ± 0.10	1.69 ± 0.62		2892	21200
57.95	11.0	6.91 ± 0.60	0.97 ± 0.17	2.51 ± 0.77	5.948 ± 0.125	1514	28940
59.50	2.5	8.54 ± 0.56	1.41 ± 0.18	2.87 ± 0.91			
61.40	1.0	7.20 ± 0.53	1.47 ± 0.21	2.82 ± 0.90			
63.17	0.5	6.70 ± 0.34	1.61 ± 0.17	2.44 ± 0.92	5.493 ± 0.110	994	31020
64.31	1.0	7.60 ± 0.45	2.46 ± 0.21	2.28 ± 0.90			
65.90	3.4	7.77 ± 0.53	2.37 ± 0.18	2.47 ± 1.00			
67.67	3.7	7.53 ± 0.58	2.19 ± 0.19	1.83 ± 1.03	5.122 ± 0.108	866	26900
70.27	7.5	7.27 ± 0.46	2.37 ± 0.20	2.32 ± 1.12			
73.06	13.0	7.07 ± 0.43	1.92 ± 0.18	1.87 ± 1.19			
77.03	27.0	7.03 ± 0.43	2.00 ± 0.19	1.86 ± 1.33	4.990 ± 0.090	880	20820
82.66	49.0	5.51 ± 0.43	1.74 ± 0.15	1.22 ± 1.36	3.499 ± 0.070	1626	14100
86.74	32.5	5.98 ± 0.46	1.16 ± 0.16	2.90 ± 1.46			
92.90	29.0	7.27 ± 0.46	1.01 ± 0.14	5.11 ± 1.57	5.430 ± 0.109	674	20400
98.93	33.0	5.78 ± 0.38	0.81 ± 0.13	5.51 ± 1.84			
104.23	27.0	5.90 ± 0.39	0.94 ± 0.16	5.03 ± 1.86	5.587 ± 0.145	1004	20300
109.05	20.0	6.86 ± 0.40	0.92 ± 0.12	3.71 ± 1.89			
114.89	17.0	7.15 ± 0.45	1.09 ± 0.13	5.77 ± 2.12	5.789 ± 0.110	672	24740
122.11	33.0	7.94 ± 0.49	0.89 ± 0.13	4.73 ± 2.55	5.043 ± 0.096	1000	22720
127.23	54.0	3.95 ± 0.35	0.47 ± 0.08	6.41 ± 3.00	3.261 ± 0.068	2036	13960
129.83	62.0	2.82 ± 0.27	0.48 ± 0.07	4.88 ± 3.10	2.118 ± 0.055	5368	10280
130.17	58.0	3.52 ± 0.31	0.63 ± 0.11	7.01 ± 3.32		13650	13200
131.03	52.0	3.97 ± 0.43	0.69 ± 0.10	4.46 ± 3.72		10610	19220
132.98	47.0	2.67 ± 0.36	1.27 ± 0.18	3.97 ± 4.45		3514	14560
134.44	36.0	4.97 ± 0.46	3.70 ± 0.25	4.52 ± 5.31	2.470 ± 0.057	1668	16760
136.74	26.0	6.44 ± 0.64	4.11 ± 0.22	4.65 ± 5.55			
138.72	14.6	5.92 ± 0.46	3.30 ± 0.21	5.51 ± 3.81			
140.00	7.5	7.60 ± 0.56	2.27 ± 0.22		4.107 ± 0.078	1624	25580
142.14	4.4	6.70 ± 0.28	2.34 ± 0.13				
144.34	9.3	5.86 ± 0.29	2.27 ± 0.13				

Results of gravity core PS2082-1 and multicore PS2082-3 (continued).

Age, kyr	$CaCO_3$, %	^{232}Th, ppm	^{238}U, dpm/g	$^{231}Pa^0_{ex}$, dpm/g	$^{10}Be^0$, 10^9at/g	Mn, ppm	Fe, ppm
146.48	13.6	6.01 ± 0.26	2.38 ± 0.13				
148.24	6.2	7.41 ± 0.32	2.15 ± 0.12		4.325 ± 0.099	1524	29680
150.37	2.0	8.42 ± 0.32	2.10 ± 0.12				
152.33	2.3	8.38 ± 0.34	1.96 ± 0.23				
154.87	3.0	7.34 ± 0.34	2.22 ± 0.12		4.490 ± 0.090	1896	26540
157.22	1.3	5.68 ± 0.60	1.89 ± 0.11				
159.24	1.1	7.97 ± 0.31	1.86 ± 0.11				
162.12	3.0	6.62 ± 0.27	1.86 ± 0.12				
165.52	6.5	6.32 ± 0.31	1.97 ± 0.13				
167.54	7.0	7.77 ± 0.32	1.67 ± 0.09		5.207 ± 0.099	1376	24660
168.35	5.0	6.82 ± 0.46	1.61 ± 0.16				
171.37	2.3	7.20 ± 0.37	1.88 ± 0.12				
174.01	2.5	7.72 ± 0.49	1.84 ± 0.13		5.222 ± 0.089	1006	28800
177.37	0.8	7.89 ± 0.36	2.14 ± 0.15				
180.14	0.5	8.27 ± 0.34	2.00 ± 0.12		6.034 ± 0.103	638	28420
184.51	0.6	9.52 ± 0.45	2.11 ± 0.12		6.552 ± 0.177	508	25360
189.15	0.5	7.65 ± 0.37	1.96 ± 0.13				
194.29	3.8	8.21 ± 0.37	1.93 ± 0.13				
200.11	10.0	9.03 ± 0.40	1.61 ± 0.12		5.655 ± 0.130	706	28040
206.04	10.0	8.64 ± 0.37	1.53 ± 0.12		5.922 ± 0.113	776	27000
209.80	18.0	5.89 ± 0.33	1.33 ± 0.10			1442	23960
213.35	18.0	5.88 ± 0.30	1.13 ± 0.10		5.098 ± 0.102	2712	22740
216.73	5.5	7.57 ± 0.31	1.10 ± 0.08			1752	28320
219.85	1.0	7.35 ± 0.31	0.98 ± 0.09			4252	29800
222.04	0.6	7.10 ± 0.30	0.98 ± 0.08		4.589 ± 0.092	1504	28601
223.91	0.8	6.76 ± 0.28	1.20 ± 0.12			696	22200
226.72	0.7	7.61 ± 0.30	1.09 ± 0.10				
230.06	5.0	7.04 ± 0.28	1.10 ± 0.09		5.219 ± 0.104	864	26910
232.93	26.0	5.19 ± 0.25	1.46 ± 0.09				
238.39	45.0	5.00 ± 0.27	2.10 ± 0.15				
241.04	19.0	4.73 ± 0.28	1.21 ± 0.12				
242.49	8.0	6.36 ± 0.30	1.75 ± 0.18		4.453 ± 0.134	1608	25720
245.16	11.5	6.52 ± 0.28	2.41 ± 0.15				
247.41	14.0	6.22 ± 0.29	3.19 ± 0.22				
250.42	7.0	6.92 ± 0.33	2.07 ± 0.12				
254.00	1.8	7.17 ± 0.29	3.59 ± 0.25		4.749 ± 0.100	1613	26344

Results of gravity core PS2082-1 and multicore PS2082-3 (continued).

Age, kyr	rel, PRC,	VRR ^{10}Be, 10^9at/ cm^2 · kyr	VRR $^{231}Pa_{ex}$, dpm/ cm^2 · kyr	VRR biog. opal, g/ cm^2 · kyr	VRR Ba_{bio}, mg/ cm^2 · kyr	VRR Al_2O_3, mg/ cm^2 · kyr	^{238}U auth., dpm/g
			Multicore PS2082-3				
1.27	0.95	1.495 ± 0.020	0.58 ± 0.05				0.00 ± 0.00
3.82	1.00	1.313 ± 0.019	0.56 ± 0.13				0.00 ± 0.18
6.45	1.05	1.413 ± 0.052					0.00 ± 0.09
			Gravity Core PS2082-1				
4.87	0.93	1.449 ± 0.027	0.88 ± 0.15	0.08 ± 0.00	0.50 ± 0.01	24.54 ± 0.46	0.00 ± 0.08
9.19	1.04	1.453 ± 0.040	1.10 ± 0.22	0.09 ± 0.00	0.44 ± 0.01	22.23 ± 0.62	0.00 ± 0.10
10.94	1.05	2.413 ± 0.068	1.26 ± 0.25	0.13 ± 0.00	0.78 ± 0.02	48.75 ± 1.37	0.00 ± 0.07
12.02	1.08	2.444 ± 0.069	0.81 ± 0.19	0.13 ± 0.00	0.75 ± 0.02	49.16 ± 1.38	0.00 ± 0.02
12.73			1.12 ± 0.22	0.21 ± 0.01	0.63 ± 0.02	58.41 ± 1.59	0.00 ± 0.26
13.11	1.18	3.272 ± 0.115	1.07 ± 0.26	0.28 ± 0.01	0.67 ± 0.02	67.71 ± 2.38	0.07 ± 0.35
13.62	1.22	3.806 ± 0.143	1.24 ± 0.31	0.30 ± 0.01	0.67 ± 0.03	91.95 ± 3.45	1.37 ± 0.37
14.13			1.21 ± 0.29	0.35 ± 0.01	0.45 ± 0.02		1.79 ± 0.41
14.66			1.21 ± 0.30	0.34 ± 0.01	0.28 ± 0.01		1.56 ± 0.39
15.15	1.30	3.196 ± 0.120	1.30 ± 0.32	0.33 ± 0.01	0.45 ± 0.02	81.69 ± 3.07	1.55 ± 0.36
15.65			1.30 ± 0.32	0.36 ± 0.01	0.60 ± 0.02		1.27 ± 0.32
16.15			1.49 ± 0.33	0.37 ± 0.01	0.67 ± 0.03		0.92 ± 0.44
16.71	1.39	3.018 ± 0.072	1.47 ± 0.30	0.33 ± 0.01	0.63 ± 0.01	77.42 ± 1.84	0.77 ± 0.41
17.24			1.52 ± 0.32	0.35 ± 0.01	0.83 ± 0.03		0.62 ± 0.46
17.79			1.51 ± 0.32	0.29 ± 0.01	0.92 ± 0.03		0.81 ± 0.49
18.31			1.64 ± 0.37	0.24 ± 0.01	0.83 ± 0.03		0.92 ± 0.41
18.81	1.37	3.551 ± 0.175	2.48 ± 0.34	0.32 ± 0.02	0.81 ± 0.04	81.69 ± 4.03	0.80 ± 0.47
19.31				0.30 ± 0.01	0.84 ± 0.04		0.18 ± 0.62
19.78	1.37	3.852 ± 0.140		0.34 ± 0.01	0.99 ± 0.04	89.87 ± 3.26	0.66 ± 0.38
20.39	1.37	3.280 ± 0.089		0.24 ± 0.01	0.75 ± 0.02	77.58 ± 2.10	0.43 ± 0.40
21.01			1.30 ± 0.21	0.26 ± 0.01	0.64 ± 0.01		0.52 ± 0.44
21.61			1.29 ± 0.22	0.25 ± 0.01	0.60 ± 0.02		0.68 ± 0.39
22.14	1.30	3.394 ± 0.088	1.33 ± 0.25	0.29 ± 0.01	0.59 ± 0.02	80.49 ± 2.09	0.74 ± 0.44
22.80			1.22 ± 0.24	0.26 ± 0.01	0.41 ± 0.01		0.65 ± 0.45
23.56	1.22	2.640 ± 0.092	1.09 ± 0.22	0.21 ± 0.01	0.35 ± 0.01	61.68 ± 2.14	0.42 ± 0.45
26.43			1.20 ± 0.23	0.20 ± 0.01	0.35 ± 0.01	60.79 ± 1.66	0.48 ± 0.43
29.43			1.16 ± 0.26	0.21 ± 0.01	0.41 ± 0.01	64.23 ± 1.59	0.34 ± 0.40
33.01	1.18	2.948 ± 0.079	0.84 ± 0.26	0.19 ± 0.01	0.39 ± 0.01	58.79 ± 1.58	0.42 ± 0.31
35.21			0.72 ± 0.40	0.19 ± 0.01	0.44 ± 0.01	65.68 ± 2.15	0.10 ± 0.32
35.80			0.85 ± 0.45	0.20 ± 0.01	0.46 ± 0.02	67.50 ± 3.39	0.37 ± 0.24
36.73	1.40	3.585 ± 0.104	1.64 ± 0.48	0.23 ± 0.01	0.43 ± 0.01	62.19 ± 1.80	0.41 ± 0.30
37.29			1.69 ± 0.49	0.28 ± 0.02	0.42 ± 0.02	71.74 ± 4.00	0.26 ± 0.33

Results of gravity core PS2082-1 and multicore PS2082-3 (continued). PRC = relative production rate changes of cosmogenic radionuclides following Mazaud et al. (1994). Biogenic barium and Al_2O_3 data are from Nürnberg (1995). Biogenic opal data are from G. Bohrmann (unpub. res.). All errors represent the statistical errors of one standard deviation from the mean (1σ) of the $^{230}Th_{ex}$ measurement except the $^{231}Pa_{ex}$ errors where it represents the quadratic sum of the 1σ uncertainties of the $^{230}Th_{ex}$ and $^{231}Pa_{ex}$ measurements. The error of the authigenic ^{238}U concentrations represents the range of the lithogenic $^{238}U/^{232}Th$ activity ratio between 0.5 and 1.

Age, kyr	rel, PRC,	VRR ^{10}Be, 10^9at/ cm^2 · kyr	VRR $^{231}Pa_{ex}$, dpm/ cm^2 · kyr	VRR biog. opal, g/ cm^2 · kyr	VRR Ba_{bio}, mg/ cm^2 · kyr	VRR Al_2O_3, mg/ cm^2 · kyr	^{238}U auth., dpm/g
40.54			1.23 ± 0.46	0.19 ± 0.01	0.28 ± 0.01	68.46 ± 2.72	0.41 ± 0.34
43.58			0.51 ± 0.52	0.16 ± 0.01	0.25 ± 0.01		0.50 ± 0.48
44.76	1.20	3.548 ± 0.146	0.93 ± 0.46	0.15 ± 0.01	0.30 ± 0.01	77.29 ± 3.19	0.50 ± 0.39
45.67			1.25 ± 0.31	0.13 ± 0.00	0.25 ± 0.01		0.42 ± 0.44
48.16	1.02	2.987 ± 0.070	1.32 ± 0.30	0.11 ± 0.00	0.24 ± 0.01	52.79 ± 1.24	0.03 ± 0.47
49.50			1.69 ± 0.37	0.10 ± 0.00	0.23 ± 0.01	58.01 ± 1.70	0.11 ± 0.49
51.99	0.95	3.539 ± 0.108	1.67 ± 0.42	0.13 ± 0.00	0.18 ± 0.01	54.37 ± 1.66	0.00 ± 0.39
53.64			1.27 ± 0.42	0.17 ± 0.01	0.19 ± 0.01	50.68 ± 1.51	0.00 ± 0.17
55.91			1.18 ± 0.44	0.16 ± 0.00	0.18 ± 0.00	44.67 ± 1.07	0.00 ± 0.10
57.95	1.12	3.797 ± 0.196	1.79 ± 0.56	0.21 ± 0.01	0.36 ± 0.02	53.76 ± 2.77	0.00 ± 0.12
59.50			2.00 ± 0.64	0.20 ± 0.01	0.56 ± 0.02		0.00 ± 0.36
61.40			2.00 ± 0.64	0.21 ± 0.01	0.64 ± 0.03		0.14 ± 0.44
63.17	1.28	3.261 ± 0.126	1.85 ± 0.70	0.22 ± 0.01	0.80 ± 0.03	70.00 ± 2.71	0.37 ± 0.41
64.31			1.63 ± 0.64	0.20 ± 0.01	0.86 ± 0.04		1.06 ± 0.47
65.90			1.62 ± 0.66	0.18 ± 0.01	0.70 ± 0.03		0.94 ± 0.48
67.67	1.24	2.752 ± 0.134	1.22 ± 0.69	0.20 ± 0.01	0.53 ± 0.03	58.88 ± 2.87	0.80 ± 0.46
70.27			1.16 ± 0.56	0.16 ± 0.00	0.37 ± 0.01		1.03 ± 0.45
73.06			0.82 ± 0.52	0.13 ± 0.00	0.47 ± 0.01		0.62 ± 0.43
77.03	1.07	1.947 ± 0.058	0.77 ± 0.55	0.11 ± 0.00	0.29 ± 0.01	27.47 ± 0.82	0.70 ± 0.43
82.66	1.09	1.694 ± 0.066	0.64 ± 0.72	0.08 ± 0.00	0.16 ± 0.01	27.77 ± 1.09	0.72 ± 0.34
86.74			1.55 ± 0.78	0.12 ± 0.00	0.28 ± 0.01		0.06 ± 0.37
92.90	1.25	1.806 ± 0.054	2.12 ± 0.65	0.09 ± 0.00	0.32 ± 0.01	30.48 ± 0.91	0.00 ± 0.12
98.93			2.36 ± 0.79	0.09 ± 0.00	0.39 ± 0.01		0.00 ± 0.10
104.23	1.33	1.832 ± 0.058	2.19 ± 0.82	0.09 ± 0.00	0.52 ± 0.02	31.15 ± 0.99	0.00 ± 0.21
109.05			1.45 ± 0.74	0.11 ± 0.00	0.62 ± 0.02		0.00 ± 0.08
114.89	1.47	1.292 ± 0.036	1.89 ± 0.70	0.09 ± 0.00	0.52 ± 0.01	26.83 ± 0.74	0.00 ± 0.21
122.11	1.43	1.061 ± 0.031	1.42 ± 0.77	0.06 ± 0.00	0.42 ± 0.01	22.63 ± 0.66	±
127.23	1.38	1.311 ± 0.051	3.56 ± 1.67	0.09 ± 0.00	0.33 ± 0.01	23.99 ± 0.93	±
129.83	1.33	1.999 ± 0.130	6.12 ± 3.91	0.16 ± 0.01	0.38 ± 0.02	42.47 ± 2.76	0.00 ± 0.13
130.17			8.89 ± 4.26	0.16 ± 0.01	0.29 ± 0.02	45.30 ± 3.04	0.00 ± 0.20
131.03			6.43 ± 5.39	0.24 ± 0.03	0.23 ± 0.02	54.15 ± 5.59	0.00 ± 0.20
132.98			5.08 ± 5.73	0.29 ± 0.03	0.29 ± 0.03	45.77 ± 5.09	0.78 ± 0.16
134.44	1.24	2.392 ± 0.400	5.43 ± 6.44	0.30 ± 0.05	0.00 ± 0.00	65.49 ± 10.96	2.78 ± 0.31
136.74			3.65 ± 4.37	0.20 ± 0.02	0.16 ± 0.02		2.92 ± 0.40
138.72			5.36 ± 3.76	0.26 ± 0.03	0.58 ± 0.07		2.21 ± 0.36
140.00	1.15	3.356 ± 0.405		0.25 ± 0.03	0.94 ± 0.11	79.49 ± 9.59	0.87 ± 0.47
142.14				0.23 ± 0.01	0.88 ± 0.05		1.10 ± 0.41
144.34				0.22 ± 0.01	0.90 ± 0.06		1.19 ± 0.36

Results of gravity core PS2082-1 and multicore PS2082-3 (continued).

Age, kyr	rel, PRC,	VRR ^{10}Be, 10^9at/ cm^2 · kyr	VRR ^{231}Pa$_{ex}$, dpm/ cm^2 · kyr	VRR biog. opal, g/ cm^2 · kyr	VRR Ba_{bio}, mg/ cm^2 · kyr	VRR Al_2O_3, mg/ cm^2 · kyr	^{238}U auth., dpm/g
146.48				0.20 ± 0.01	0.88 ± 0.06		1.27 ± 0.37
148.24	1.10	3.883 ± 0.279		0.24 ± 0.02	1.05 ± 0.08	94.71 ± 6.80	0.78 ± 0.46
150.37				0.22 ± 0.01	0.96 ± 0.06		0.55 ± 0.52
152.33				0.27 ± 0.02	1.22 ± 0.11		0.41 ± 0.52
154.87	1.27	2.849 ± 0.172		0.24 ± 0.01	1.25 ± 0.08	71.21 ± 4.30	0.87 ± 0.45
157.22				0.25 ± 0.03	1.14 ± 0.12		0.84 ± 0.35
159.24				0.20 ± 0.01	0.84 ± 0.04		0.39 ± 0.49
162.12				0.23 ± 0.01	0.92 ± 0.06		0.64 ± 0.41
165.52				0.20 ± 0.01	0.91 ± 0.06		0.80 ± 0.39
167.54	1.25	2.768 ± 0.137		0.21 ± 0.01	0.94 ± 0.05	54.96 ± 2.72	0.24 ± 0.48
168.35				0.26 ± 0.03	1.27 ± 0.13		0.35 ± 0.42
171.37				0.21 ± 0.01	1.05 ± 0.07		0.55 ± 0.44
174.01	1.20	3.668 ± 0.335		0.24 ± 0.02	1.12 ± 0.10	74.47 ± 6.80	0.42 ± 0.47
177.37				0.19 ± 0.01	0.90 ± 0.06		0.68 ± 0.49
180.14	1.19	3.080 ± 0.179		0.19 ± 0.01	1.03 ± 0.06	55.96 ± 3.26	0.47 ± 0.51
184.51	1.26	2.136 ± 0.099		0.12 ± 0.01	0.84 ± 0.04	37.85 ± 1.76	0.35 ± 0.59
189.15				0.11 ± 0.01	0.92 ± 0.04		0.55 ± 0.47
194.29				0.07 ± 0.00	1.02 ± 0.04		0.42 ± 0.50
200.11	1.22	1.661 ± 0.073		0.06 ± 0.00	0.82 ± 0.04	32.33 ± 1.42	0.00 ± 0.50
206.04		2.132 ± 0.100		0.07 ± 0.00	0.63 ± 0.03	28.77 ± 1.35	0.00 ± 0.47
209.80				0.11 ± 0.01	0.55 ± 0.03	31.71 ± 1.76	0.24 ± 0.36
213.35		2.752 ± 0.171		0.16 ± 0.01	0.68 ± 0.04	38.57 ± 2.39	0.05 ± 0.36
216.73				0.22 ± 0.01	0.94 ± 0.06	49.81 ± 2.97	0.00 ± 0.17
219.85				0.23 ± 0.02	0.90 ± 0.06	53.80 ± 3.66	0.00 ± 0.08
222.04		3.420 ± 0.244		0.28 ± 0.02	1.06 ± 0.08	57.45 ± 4.10	0.00 ± 0.11
223.91				0.18 ± 0.01	1.06 ± 0.07	54.40 ± 3.54	0.00 ± 0.37
226.72				0.13 ± 0.01	1.06 ± 0.06		0.00 ± 0.15
230.06		2.427 ± 0.130		0.11 ± 0.01	0.93 ± 0.05	41.08 ± 2.19	0.00 ± 0.23
232.93				0.08 ± 0.00	0.75 ± 0.04		0.50 ± 0.32
238.39				0.14 ± 0.02	0.14 ± 0.02		1.18 ± 0.31
241.04				0.30 ± 0.04	0.69 ± 0.08		0.34 ± 0.29
242.49		4.824 ± 1.082		0.42 ± 0.09	1.25 ± 0.28	77.40 ± 17.36	0.58 ± 0.39
245.16				0.22 ± 0.03	0.78 ± 0.10		1.21 ± 0.40
247.41				0.24 ± 0.05	0.46 ± 0.09		2.04 ± 0.38
250.42				0.25 ± 0.03	1.06 ± 0.13		0.79 ± 0.43

Results of gravity core PS2082-1 and multicore PS2082-3 (continued).